

Thermal Characterization of a Gas-gap Heat Switch for Satellite Thermal Control

by

Stefanos Dermenakis

For the degree of Master of Science in Space Systems Engineering
at the Delft University of Technology,
to be defended publically on Friday September 9, 2016 at 09:00 AM

Faculty of Aerospace Engineering – Delft University of Technology
European Space Agency – Mechanical Thermal Division (TEM-MT)



Student number: 4378415
Project duration: January 4, 2016 – September 1, 2016
Thesis committee: Prof. Dr. E.K.A. (Eberhard) Gill – TU Delft Space Systems Engineering Chairholder
Dr. Jian Guo – TU Delft department of Space Systems Engineering (supervisor)
Dr. Marios Kotsonis – TU Delft department of Aerodynamics
Mr. Thierry Tirolien – ESA Thermal Engineer (TEC-MTT)

An electronic version of this thesis is available at <http://repository.tudelft.nl/>

Abstract

A heat switch is a variable thermal conductance device that can act as a thermal conductor or a thermal insulator. A gas-gap heat switch, which is currently in its third design iteration, has been developed by University of Twente in collaboration with the European Space Agency. This device is filled with a gas, whose thermal conductivity varies with temperature and pressure. It is a promising technology that could find extensive applications in Earth Observation and interplanetary missions due to the extreme variations in the thermal environment encountered throughout a mission lifetime. The gas-gap heat switch is manufactured out of a titanium alloy using 3D-printing technology. The main idea is to offer a quick and cheap plug-and-play solution for electronics units thermal control. The main purpose of this thesis is to evaluate the performance of the heat switch by building thermal simulation models and through experimentation, providing a correlation between the experimental and theoretical data. Additionally, the various parameters that affect the performance are identified and quantified. A preliminary analysis to evaluate the impact of the device in future missions has been conducted, using the straw-man concept analysis method. Design and manufacturability improvements and recommendations are also provided in order to facilitate the manufacturing process and improve the attainable tolerances. The experimental data shows a good correlation with the theoretical data with a deviation of less than 20% when adequate manufacturing tolerances are achieved. The experiments showed that the second prototype has an ON-conductance of 2.60 W/K and an OFF-conductance of 0.30 W/K, with an overall ON/OFF ratio of 8.67, when operating with Helium. The third iteration exhibited a degraded performance that is attributed to manufacturing problems. A scale analysis shows that theoretically the performance of the heat switch reaches a plateau at a size of 0.1 m², with an ON-conductance of 241 W/m²·K and an OFF-conductance of 8.5 W/m²·K for an ON/OFF ratio of 27.29. All the mentioned values include a contact heat transfer coefficient of 700 W/m²·K on both sides of the switch. The switch has a surface area density of 8.16 kg/m².

Table of Contents

1	Introduction	1
1.1	General introduction	1
1.2	Research questions	2
1.3	Hypothesis and methodology	3
1.4	Structure of the report	3
2	Fundamentals of Heat Transfer	5
2.1	Modes of heat transfer	5
2.2	Steady-state and Transient Analysis	7
2.3	Spacecraft thermal environment	7
2.4	Geometrical and Thermal Mathematical Model	9
2.5	Summary	10
3	Heat switches technology	11
3.1	Heat switches purpose and measures of effectiveness	11
3.2	Heat switches applications	11
3.3	Gas-gap heat switch	12
3.4	Currently available heat switches	16
3.5	Summary	18
4	Systems Engineering Study	19
4.1	Straw-man concept	19
4.2	Sentinel-2	19
4.3	Thermal environment simulation model	20
4.4	Summary	26
5	Heat switch thermal modeling	27
5.1	Heat switch thermal network	27
5.2	Conductive heat transfer	30
5.3	Gaseous heat transfer	31
5.4	Convective heat transfer	37
5.5	Radiative heat transfer	39
5.6	Summary	40
6	Part inspection	41
6.1	Emissivity measurements	41
6.2	Visual inspection	41

6.3	CT scan inspection.....	45
6.4	Summary.....	50
7	Experimental setup	51
7.1	Test objective.....	51
7.2	Test configuration.....	51
7.3	Test configuration leak inspection.....	56
7.4	Thermal interface resistance.....	57
7.5	Test configuration structural analysis	64
7.6	Test configuration thermal simulation.....	69
7.7	Scale analysis	71
7.8	Test procedure	74
7.9	Test stabilization criteria	74
7.10	Summary.....	79
8	Experimental results & correlation.....	80
8.1	Contact heat transfer coefficient	80
8.2	Real time constant calculations.....	82
8.3	ON/OFF conductances	88
8.4	Conductance dependence on pressure.....	98
8.5	ON/OFF ratio	101
8.6	Summary.....	102
9	Uncertainty analysis.....	104
9.1	Heating power uncertainty	104
9.2	Leaking power uncertainty	105
9.3	Area uncertainty	106
9.4	Thermocouples uncertainty	106
9.5	Sample uncertainty calculations.....	107
9.6	Summary.....	107
10	Correlated straw-man analysis.....	108
10.1	Detailed Geometrical Mathematical Model.....	108
10.2	Detailed Thermal Mathematical Model.....	110
10.3	Heat switch impact on interrelated subsystems.....	114
10.4	Summary.....	114
11	Improvement recommendations	116
11.1	Manufacturing improvements.....	116

11.2	Design improvements	118
11.3	Summary.....	122
12	Conclusion & recommendations	123
12.1	Conclusions	123
12.2	Remarks & recommendations.....	124
Appendix A	Sentinel-2 units.....	126
Appendix B	Orbital heating fluxes	127
Appendix C	Material transport properties.....	129
Appendix D	Gas thermal properties	131
Appendix E	Radiation properties and VF	132
Appendix F	Material properties	136
Appendix G	Structural analysis results.....	138
Appendix H	Reduced TMM code	140
Appendix I	Technical Drawings.....	142

List of Figures

Figure 1: Solar zenith angle.....	8
Figure 2: Heat switches between components and spacecraft structure [13].....	12
Figure 3: Heat switch between spacecraft structure and radiator [13].....	12
Figure 4: First prototype vertical cross-section.....	13
Figure 5: First prototype horizontal cross-section.....	13
Figure 6: Second prototype horizontal cross-section	14
Figure 7: Third prototype design.....	15
Figure 8: Test sample for gap size	15
Figure 9: Paraffin heat switch dimensions	17
Figure 10: Total thermal conductance with temperature.....	17
Figure 11: Starsys pedestal heat switch [13]	17
Figure 12: IberEspacio heat switch.....	18
Figure 13: Artist's rendition of Sentinel-2.....	20
Figure 14: Unit layout of simulation model	21
Figure 15: Visualization of the orbit as seen from the sun at 2800 sec.....	22
Figure 16: Units temperature profile (worst hot, no switch)	25
Figure 17: +Z panel temperature profile (Worst cold, no switch).....	25
Figure 18: +Z panel temperature profile (Worst cold, with switch).....	26
Figure 19: OFF-state thermal network.....	27
Figure 20: ON-state thermal network.....	29
Figure 21: Simplified ON-case thermal network	30
Figure 22: Variation of thermal conductivity of Argon [24]	32
Figure 23: Gas thermal conductivity in the transition regime.....	36
Figure 24: Classification of free-molecular, transition, and continuum regimes for heat conduction across a gas confined between parallel plates [24]	37
Figure 25: Convective currents in a horizontal enclosure [6]	38
Figure 26: A vertical rectangular enclosure with isothermal surfaces [6]	38
Figure 27: Infinitely large parallel plates radiation heat exchange [6]	39
Figure 28: Front view of second prototype	42
Figure 29: Test assembly with no applied torque	42
Figure 30: Test assembly with a 1 N·m torque.....	43
Figure 31: Buckling of iteration 1.....	43
Figure 32: Added stiffeners to prevent buckling	43
Figure 33: Buckling of iteration 3.....	44
Figure 34: Iteration 4 - lattice structure for additional stiffness.....	45
Figure 35: Second prototype thickness and flatness deviation.....	45
Figure 36: Second prototype gap size (edge).....	46
Figure 37: Second prototype gap size (middle)	46
Figure 38: Second prototype support pillars.....	47
Figure 39: Side views of a cracked support pillar.....	47
Figure 40: Remaining powder inside second prototype	48
Figure 41: CT scan setup	48

Figure 42: Third prototype cross-section	49
Figure 43: Third prototype gap size	49
Figure 44: Third prototype pillars side views	49
Figure 45: Third prototype channel clog	50
Figure 46: Third prototype channel clog cross-section	50
Figure 47: Thermoelectric cooler mounting scheme. (From FerroTec).....	51
Figure 48: Test setup sandwich configuration.....	52
Figure 49: Test setup cross-section	52
Figure 50: T/C placement through groove	53
Figure 51: Heat switch covered with MLI.....	54
Figure 52: Pressure sensor calibration curve.....	55
Figure 53: Pressure handling system schematic	56
Figure 54: Bolt thermal resistance against bolt shaft diameter	59
Figure 55: M4 bolt thermal resistance against plate thickness	60
Figure 56: Dimensional correlation of bolted-joint conductance [13]	61
Figure 57: Maximum Von-Mises stresses location	68
Figure 58: Pillar cross-section stresses [5.33 bar]	69
Figure 59: Pillar cross-section stresses [2.3 bar]	69
Figure 60: Switch cross-section near edges (baseplate at 20°C)	70
Figure 61: Switch cross-section middle (baseplate at 20°C)	70
Figure 62: Thermal model couplings and BCs	71
Figure 63: ON-conductance scale analysis	72
Figure 64: OFF-conductance scale analysis	73
Figure 65: Heat switch area density	73
Figure 66: Test setup reduced thermal network	75
Figure 67: Lumped mass test setup transient response at 20°C (ON-case).....	76
Figure 68: FEM test setup transient response at 20°C (ON-case)	76
Figure 69: Lumped mass test setup transient response at 20°C (OFF-case).....	77
Figure 70: FEM test setup transient response at 20°C (OFF-case)	77
Figure 71: Sigraflex contact heat transfer coefficient for second prototype	81
Figure 72: Sigraflex contact heat transfer coefficient for third prototype (OFF-case)	81
Figure 73: Sigraflex contact heat transfer coefficient for third prototype (ON-case)	82
Figure 74: Second prototype real time constant - ON-state (20°C)	83
Figure 75: Second prototype ON-case transient response (20°C).....	83
Figure 76: Second prototype real time constant - OFF-state (20°C)	84
Figure 77: Second prototype OFF-case transient response (20°C).....	85
Figure 78: Third prototype real time constant - ON-state (20°C)	86
Figure 79: Third prototype ON-case transient response (20°C).....	86
Figure 80: Third prototype real time constant - OFF-state (20°C)	87
Figure 81: Third prototype OFF-case transient response (20°C).....	87
Figure 82: Second prototype ON-state heat transfer coefficient ($P = 40$ W)	88
Figure 83: Exaggerated arc-shape deformation of second prototype	89
Figure 84: Second prototype in-plane temperature distribution (ON-case)	89
Figure 85: Second prototype ON-state overall heat transfer coefficient (Plate 1 to Plate 2)	90

Figure 86: Third prototype ON-state heat transfer coefficient ($P = 50$ W)	91
Figure 87: Third prototype ON-state overall heat transfer coefficient (Plate 1 to Plate 2) ...	91
Figure 88: Switch heat transfer coefficient (Neon)	92
Figure 89: Overall heat transfer coefficient (Neon)	93
Figure 90: Effect of temperature on titanium alloys thermal conductivity	94
Figure 91: Second prototype OFF-state heat transfer coefficient ($P = 5$ W)	94
Figure 92: Second prototype OFF-state overall heat transfer coefficient (Plate 1 to Plate 2)	95
Figure 93: Second prototype in-plane temperature distribution (OFF-case)	96
Figure 94: Third prototype OFF-state heat transfer coefficient ($P = 15$ W)	97
Figure 95: Third prototype OFF-state overall heat transfer coefficient (Plate 1 to Plate 2) .	97
Figure 96: Second prototype pressure drop.....	98
Figure 97: Heat transfer coefficient against pressure (second prototype)	99
Figure 98: Transition to continuum regime heat transfer coefficient (second prototype)	100
Figure 99: Third prototype pressure drop.....	100
Figure 100: Heat transfer coefficient against pressure (third prototype)	101
Figure 101: Third prototype ON/OFF ratio.....	102
Figure 102: Third prototype ON/OFF ratio.....	102
Figure 103: T/C temperature difference with calibration points (second prototype).....	106
Figure 104: Combined T/C uncertainty budget.....	107
Figure 105: Worst hot incident solar fluxes	109
Figure 106: Worst cold incident solar fluxes.....	109
Figure 107: Units temperature profile (worst hot, no switch)	111
Figure 108: Units temperature profile (worst cold, no switch)	111
Figure 109: +Z Panel unit temperature profile (worst cold, no switch)	112
Figure 110: Units temperature profile (worst hot, no switch)	112
Figure 111: Units temperature profile (worst cold, no switch)	113
Figure 112: +Z Panel unit temperature profile (worst cold, no switch)	113
Figure 113: JUICE mission trajectory	115
Figure 114: Fine Ti-6Al-4V powder particle size distribution	116
Figure 115: Milling versus grinding process [40].....	117
Figure 116: Mounting hole cross-section	118
Figure 117: Suggested design pillar stresses	119
Figure 118: Suggested design maximum stresses (no pillars, $P_{\text{gauge}} = 0$ bar)	120
Figure 119: Suggested design maximum stresses (no pillars, $P_{\text{gauge}} = 1.5$ bar)	120
Figure 120: Vertical displacement at $P_{\text{gauge}} = 1.5$ bar	121
Figure 121: Side wall thickness.....	121
Figure 122: Mounting of heat switch and unit on honeycomb panel.....	122
Figure 123: Incident Albedo flux in Worst Hot	127
Figure 124: Incident Albedo flux in Worst Cold.....	127
Figure 125: Incident Solar flux in Worst Hot	128
Figure 126: Incident Solar flux in Worst Cold.....	128
Figure 127: Gases thermal conductivity with respect to temperature	131
Figure 128: Gases density with respect to temperature	131

Figure 129: Ratio of hemispherical emissivity to normal emittance	132
Figure 130: Two infinitely long parallel strips of unequal length	133
Figure 131: Second prototype fin profile.....	134
Figure 132: Third prototype fin profile.....	135
Figure 133: Hydrogen permeability versus temperature [42]	137
Figure 134: Bolted connections contact pressure	138
Figure 135: Test setup exaggerated displacement	139
Figure 136: Switch exaggerated displacement [2.3 bar]	139

List of Tables

Table 1: Heat switch performance requirements	14
Table 2: IberEspacio heat switch characteristics.....	18
Table 3: Sentinel-2 orbital parameters [22].....	19
Table 4: Sizing cases	21
Table 5: Average external fluxes on spacecraft.....	22
Table 6: Model optical properties	23
Table 7: View Factors for internal radiation	24
Table 8: Gebhart Factors for internal radiation	24
Table 9: 10x10 cm ² OFF-case thermal conductances	28
Table 10: 20x20 cm ² OFF-case thermal conductances	28
Table 11: Conductive conductances of different prototypes.....	31
Table 12: Gas thermal conductivities at 300 K.....	34
Table 13: Gases accommodation coefficients.....	36
Table 14: Regime pressure limits.....	37
Table 15: Thermocouples channel and location (2 nd prototype)	54
Table 16: Thermocouples channel and location (3 rd prototype.....	54
Table 17: Fillers thermal resistance	58
Table 18: Bolt Thermal Resistance estimate [13].....	59
Table 19: Aluminium-PEEK contact heat transfer coefficient	64
Table 20: Unlubricated M4 class A2-70 socket head cap screw bolt preload parameters.....	65
Table 21: Heating power leak.....	105
Table 22: Solar array thermo-optical properties	108
Table 23: Units node label.....	110
Table 24: Power subsystem components mass	114
Table 25: Units power dissipation and temperature range.....	126
Table 26: Acronyms, dimensions and thermal capacitance of Sentinel-2 units.....	126
Table 27: Lennard-Jones constants and molecular weights of selected species [15].....	129
Table 28: Collision integrals for diffusivity, viscosity, and thermal conductivity based on the Lennard-Jones potential [15]	130
Table 29: Second prototype fin view factors.....	134
Table 30: Third prototype fin view factors.....	135
Table 31: Ti-6Al-4V chemical composition	136
Table 32: Inconel 718® chemical composition.....	136
Table 33: Material thermal properties	136
Table 34: Material structural properties.....	136
Table 35: Classical rule-of-thumb safety factors [30].....	138

Abbreviations

BC	Boundary Conditions
BLT	Bond-Line Thickness
CAD	Computer-Aided Design
CT	Computer Tomography
CTE	Coefficient of Thermal Expansion
EDM	Electrical Discharge Machining
ESA	European Space Agency
ESTEC	European Space Research & Technology Center
FEM	Finite Element Model
GMM	Geometric Mathematical Model
JAXA	Japan Aerospace Exploration Agency
LEO	Low Earth Orbit
LIVAF	Little Vacuum Facility
LN ₂	Liquid Nitrogen
MLI	Multi-Layer Insulation
NASTRAN	NASA Structure Analysis
NIST	National Institute Standards & Technology
NLR	Dutch National Aerospace Laboratory
PCM	Phase Change Material
PEEK	Polyether Ether Ketone
SLM	Selective Laser Melting
SS	Stainless Steel
STC	Satellite Thermal Control
T/C	Thermocouple
TEC	Thermoelectric cooler
TMM	Thermal Mathematical Model
TRP	Thermal Reference Point
VF	View Factor

Preface

As early as my bachelor studies, satellite thermal control has attracted my interest. After my involvement in the thermal analysis of Concordia University's ConSat-1 during my Bachelor's degree and two successful internships in Thermal Engineering, I had found my true passion. My main interest lays in spacecraft mission thermal modeling and in active and passive thermal control systems. My mutual interests with the Thermal Division of ESA offered me the great opportunity to complete my final thesis as a trainee at the European Space Agency. The 9-month thesis work was completed within the Thermal Division (TEC-MT) of ESA under the Directorate of Technical and Quality Management.

Acknowledgments

I would first like to thank my parents for all the support they provided in every decision I made throughout my studies and their faith in me. I would also like to notably thank my TU Delft supervisor, Dr. Guo, my ESA supervisor, Mr. Tirolien, and all the people of the Mechanical Systems Laboratory at ESTEC for the technical support and facilitations they offered throughout the 9 months of my thesis work. My special thanks go to the European Space Agency and its Thermal Division for helping me realize my dreams and aspirations, providing me with the essential skills required to enter the challenging and competitive space industry.

1 Introduction

1.1 General introduction

Space is a very harsh and unforgiving environment. Within a few minutes, the temperature of a spacecraft can vary from -130°C when in eclipse to $+100^{\circ}\text{C}$ when in full illumination [1]. Such variations can cause permanent damage to spacecraft equipment. The Satellite Thermal Control (STC) subsystem is an integral part of a spacecraft architecture, dedicated to managing and controlling such variations. More specifically, STC maintains spacecraft components within their respective temperature limits in the environments encountered during launch and on-orbit, it maintains stable temperatures over time and ensures temperature uniformity for sensitive components by controlling the temperature gradients.

Heat switches are an innovative, variable thermal conductance technology that can ideally provide an adiabatic interface in order to couple or de-couple thermal surfaces according to needs [2]. It is a technology that has not been extensively used in the thermal architecture of past spacecraft due to their bulky structure and complexity.

In collaboration with ESA, University of Twente has developed a gas-gap heat switch that is produced using 3D-printing technology. The suggested heat switch is easier and more economical to produce and contains no moving parts, when compared to its state-of-the-art counterparts. The switch allows for the thermal coupling and the de-coupling of a unit from a heat sink (radiator) depending on the unit's temperature. When the unit exceeds its maximum threshold temperature, the switch is turned on so as to allow for heat to flow from the hot unit to the radiator by conduction through an acting gas (ideally Hydrogen or Helium). Subsequently, the heat is released into space via the radiator. When, the unit is below its minimum threshold, the switch is turned off, being depressurized to high vacuum conditions ($<10^{-3}$ mbar), to thermally isolate the unit from the radiator.

The suggested gas-gap heat switch design is currently in its third design iteration. The first and second prototype have already been tested at an operating temperature of 295 K and the performance has been documented in reference [3]. However, it should be noted that the performance of the switch is dependent on temperature due to radiative effects and the variation of the gases thermal conductivity with temperature. This thesis is dedicated to evaluating the thermal performance of the second and third prototype of the developed gas-gap heat switch with respect to the operating temperature and pressure. The research objective is to evaluate the impact of the developed gas-gap heat switch in Earth-Observation missions and thermally characterize it. This is achieved by using a straw-man concept system analysis and by carrying out performance quantitative tests and correlating the results to theoretical data from Finite Element Models and reduced Thermal Mathematical Models for validation.

This thesis work can be used as a reference for the design improvement of the developed gas-gap heat switch and as a benchmark to conduct further objective testing for the evaluation of the performance of the future iterations. It provides a detailed report of the critical parameters involved in this technology and of the steps taken, starting from the theoretical molecular

analysis, leading to the conduct of the experiment and the correlation of the experimental to the theoretical data. All the mentioned thermal and structural models in the report are reproducible by following the steps and using the codes mentioned in the appendices.

1.2 Research questions

A clear research question is always vital to a research. The following main research question was derived:

Main question: What is the thermal performance of the gas-gap heat switch and how would it impact a future mission in terms of power and mass?

Evaluation criteria are necessary in order to have a set of objective parameters that can help us assess the behavior of a heat switch and allow for the comparison with other similar technologies. There are different evaluation methods for the performance of the switch, both theoretical and experimental. Consequently, representative theoretical models are necessary and their accuracy with respect to the experimental data needs to be established. The experimental setup has to be representative of real-life applications in order to minimize the effect of unwanted parameters, such as convection or heat leaks. Additionally, it would be ideal to determine the operating temperature range of the technology so as to determine the extent of its use in different applications, such as at cryogenic temperatures and the technology's scalability to establish potential limitations in minimum or maximum size. It is also necessary to establish the potential effects, both positive and negative, of the gas-gap heat switch technology in a spacecraft mission. These effects will determine whether such a technology is worth further investments and whether it could be considered for future missions. Based on these remarks, the main research question is eventually analyzed into the following sub-questions.

Sub-questions:

1. What are the evaluation criteria of the performance of the thermal switch?
2. What are the evaluation methods of the performance?
 - a. How accurate is the Thermal Mathematical Model?
 - b. How accurate is the Finite Element Model?
 - c. What kind of equipment and testing is required?
 - d. What is a representative test setup of real-life applications?
 - e. How to correlate FEM and TMM with test results?
3. In what applications the heat switch can be used?
 - a. What is the temperature range?
 - b. On what type of components can it be used?
 - c. Is the switch scalable?
4. What are the affected subsystems?
 - a. What is the effect on mass?
 - b. What is the effect on the mechanical design?
 - c. What is the effect on power?

5. What are the differences, advantages/disadvantages between the suggested gas-gap heat switch and other similar thermal control means?

1.3 Hypothesis and methodology

The hypothesis to be tested is: “The developed gas-gap heat switch is beneficial to a spacecraft in Earth-Observation missions for its thermal control.”

The initial step for the validation or not of this hypothesis is to determine the evaluation criteria of the gas-gap heat switch. These criteria have been established by performing a literature study on other similar heat switches.

The use of a Systems Engineering approach is necessary in order to determine the changes in the thermal subsystem architecture and its interrelation with other subsystems. A straw-man concept analysis based on typical Earth-Observation mission parameters will be implemented in order to obtain some initial quantitative results, so as to determine the affected subsystems and the extent of these effects, either positive or negative. The main expected effects concern the mass and the power consumption.

For the thermal characterization of the switch, a FEM of the switch is required so as to have an initial estimate of the anticipated results. This model will make use of the basic thermodynamic and heat transfer concepts. Additionally, a FEM of the experimental setup, including the vacuum chamber, test equipment and the switch is required in order to have initial estimations for the results. This is a standard procedure followed by ESA before testing.

Extensive “elegant breadboard” testing is required to evaluate the performance of the heat switch. Elegant Breadboard is an equipment between Breadboard Model and Engineering Model. It is built using commercial grade components and a configuration close to that of the Flight Model. The purpose of the testing is to perform breadboard validation in laboratory environment to achieve concept-enabling levels of performance. The validations is relatively “low-fidelity” compared to the eventual system [4].

Thermal balance tests are conducted under steady state or dynamic conditions to correlate and adjust the FEM and TMM and verify the thermal design [5]. Due to the nature of the tested component, simple manual correlation techniques will be used instead of more complicated methods, such as Monte Carlo simulations, Genetic Algorithms or Adaptive Particle Swarm Optimization.

1.4 Structure of the report

This thesis report begins by providing essential information about the fundamentals of heat transfer and the thermal environment encountered by a spacecraft. It also outlines the methods used to build a thermal model of a spacecraft within its environment by applying these heat transfer fundamentals. In Chapter 3, an overview of the heat switches technology is provided, along with the measures of effectiveness of the technology and its potential applications. In the same chapter, the design concept of the developed gas-gap heat switch is given, as well as

the switch's performance requirements. Additionally, a brief comparison with other similar heat switches is provided. Chapter 4 describes a preliminary straw-man concept systems study that evaluates the impact of the suggested gas-gap heat switch in the Sentinel-2 Earth Observation mission. Chapter 5 provides a detailed analysis of the active heat transfer concepts in preparation of the thermal model of the switch. Chapter 6 provides the findings of the necessary inspections of the second and third prototype of the heat switch, including emissivity measurements, CT scan etc. Chapter 7 defines the test objective, the test setup and its contact interfaces, the test procedure and the stabilization criteria. Additionally, it shows the results of the necessary structural analysis in order to ensure the safety of the test configuration and the integrity of the switch. It also outlines the thermal simulation model and provides an analysis on the dependence of the switch performance with respect to the variation of the effective area of the switch. In Chapter 8, the experimental results and their correlation with the thermal models are provided. Chapter 9 is dedicated to the uncertainty analysis of the experiment. An updated and more detailed straw-man analysis is provided in Chapter 10, based on the correlated data. Chapter 11 provides some manufacturing and design improvements for the switch. Finally, Chapter 12 provides conclusions about the current prototypes, as well as remarks & recommendations for the future iterations.

2 Fundamentals of Heat Transfer

There are 3 modes of heat transfer; conduction, convection and radiation. This chapter briefly explains the fundamentals behind the three heat transfer modes, it defines what is steady-state and transient analysis and provides the basic understanding of a spacecraft thermal environment. In its last section it briefly introduces the methods used to generate mathematical models for thermal analysis.

2.1 Modes of heat transfer

2.1.1 Conduction

Conduction is the transfer of heat energy by collision of particles with different energy levels. Conduction occurs through a body and at the point of contact of different bodies. It is the dominant mode of heat transfer inside the spacecraft.

Conduction can be represented using Fourier's Law as follows [6]:

$$\dot{Q} = -\frac{k \cdot A}{l} \cdot \Delta T [W] \quad (2.1-1)$$

Where k represents the thermal conductivity, A is the cross-sectional area, l is the length of the conductive path and ΔT is the temperature difference between two nodes. The linear conductive conductance is represented by $GL = \frac{k \cdot A}{l} \left[\frac{W}{^\circ C} = \frac{W}{K} \right]$, while the conductive thermal resistance is its inverse $R_{conductive} = \frac{l}{k \cdot A} \left[\frac{^\circ C}{W} \right]$

For the interface between two parts, it is really important to take into account the contact thermal conductance or its inverse, the contact thermal resistance. The contact conductance can only be determined accurately through experimentation and depends on parameters such as the surface and thermal properties of the materials in contact, the applied contact pressure etc. For more details, you can refer to section 7.4.

2.1.2 Convection

Convection refers to heat transfer occurring from a solid surface to the adjacent fluid or vice versa. Even though convection is typically absent in space due to vacuum, it is sometimes present inside the spacecraft.

Convective heat transfer is represented with the following equation [6]:

$$\dot{Q} = h \cdot A \cdot \Delta T [W] \quad (2.1-2)$$

Where h represents the convective heat transfer coefficient in $[W/m^2 \cdot K]$. The convective heat transfer coefficient can be determined experimentally or approximated using correlations that take into account the system geometry and the effects of buoyancy, kinematic viscosity, thermal diffusivity and inertial forces. Such correlations can be obtained from literature, such as reference [6], depending on whether forced or free convection occurs. In the case of the latter, different correlations exist for internal and external flows. Similarly to conduction,

because convection exhibits a linear behavior, the convective coupling can be represented using $GL = h \cdot A$.

2.1.3 Radiation

Radiation is the energy emitted by a body in the form of electromagnetic waves and thus, it does not require the presence of an intervening medium [6]. Radiation is the only way to dissipate the energy outside the spacecraft, since the radiative environment serves as a heat sink that absorbs the heat.

The radiative heat transfer between two surfaces i and j is represented using the Stefan-Boltzmann Law [7]:

$$\dot{Q} = \varepsilon_i \cdot A_i \cdot \sigma \cdot F_{ij} \cdot (T_i^4 - T_j^4) [W] \quad (2.1-3)$$

Where ε_i is the emissivity of surface i , A_i is the area of surface i , $\sigma = 5.67 \cdot 10^{-8} [W/m^2 \cdot K^4]$ is the Stefan-Boltzmann constant, F_{ij} is the view factor of surface j as seen from surface i . The view factor is dependent on the area of the two surfaces and their geometry with respect to each other. It can be calculated using mathematical formulas from literature, such as references [8], [7] or using a GMM developed with computer software, such as NX Unigraphics or ESATAN-TMS. In order to obtain more accurate results, the reflections off the surfaces shall be taken into account. To correct for reflections, the Gebhart factor is introduced [9], [10]:

$$B_{ij} = F_{ij} \cdot \varepsilon_j + \sum_{k=1}^n (1 - \varepsilon_k) \cdot F_{ik} \cdot B_{ik} \quad (2.1-4)$$

For complicated geometries, where more than 3 nodes are taken into account, software such as Therm XL, can calculate the Gebhart factors if provided with the view factors and the optical properties of the surfaces. The eventual radiative thermal conductance is [9]:

$$GR_{ij} = \varepsilon_i \cdot A_i \cdot B_{ij} = \varepsilon_j \cdot A_j \cdot B_{ji} [m^2] \quad (2.1-5)$$

Equation (2.1-4) is iterative and can be simplified to a matrix equation [11]:

$$[B] = \{[I] - [F] + [F][E]\}^{-1}[F][E] \quad (2.1-6)$$

where $[B]$ is the Gebhart factor matrix, $[E]$ is the surface emissivity matrix, $[F]$ is the view factor matrix and $[I]$ is the identity matrix. Eventually, the radiative heat transfer equation can be written as:

$$\dot{Q}_{ij} = GR_{ij} \cdot (\sigma T_i^4 - \sigma T_j^4) [W] \quad (2.1-7)$$

2.2 Steady-state and Transient Analysis

2.2.1 Steady-state Analysis

Steady-state analysis is independent of time and expresses the temperature when heat balance has been achieved throughout the system. The general steady-state differential equation is given by [12]:

$$0 = Q_i^{external} + Q_i^{internal} - \sum_j GL_{ij}(T_i - T_j) - \sum_j GR_{ij}(\sigma T_i^4 - \sigma T_j^4) \quad (2.2-1)$$

where $Q_i^{external}$ and $Q_i^{internal}$ represent the external heat power and internal power dissipation.

2.2.2 Transient Analysis

Transient analysis is dependent on time and expresses the temperatures at every time-step Δt used in the calculations. The general differential equation for the transient analysis is:

$$C_i \frac{\partial T_i}{\partial t} = Q_i^{external} + Q_i^{internal} - \sum_j GL_{ij}(T_i - T_j) - \sum_j GR_{ij}(\sigma T_i^4 - \sigma T_j^4) \quad (2.2-2)$$

where $C_i = \rho_i \cdot Cp_i \cdot V_i$ [J/K] is the thermal capacitance of body i , ρ_i is its density [kg/m³], Cp_i is the specific heat [J/kg · K] and V_i [m³] is the body's volume. The heat capacity expresses the amount of heat required to change the temperature of a body by 1°C.

Under the same conditions, if a transient analysis is given adequate time, it always results in a plateau temperature that is equal to the steady-state solution. Mathematically, this equation exhibits an asymptotic behavior. Transient analysis is necessary in order to obtain the thermal behavior of a spacecraft during illumination and eclipse. Transient analysis is also used for thermal fatigue and thermal cycling calculations.

2.3 Spacecraft thermal environment

2.3.1 Solar Radiation

Solar radiation is the result of the Sun acting as an almost perfect black-body, emitting radiation according to Planck's Black-body Radiation Law. A black-body is an ideal body that allows all the incident radiation to pass into it (no reflected energy) and internally absorbs all the incident radiation (no transmitted energy) for all wavelengths and angles of incidence [7]. Same conditions apply for the emitted energy from a black-body. The received solar radiation on Earth and on orbits around Earth varies because of the elliptical orbit of Earth around the Sun. The minimum solar flux is 1322 W/m² at the summer solstice and the maximum solar flux is at 1414 W/m² at the winter solstice [13]. Using Wien's displacement Law for an average sun temperature of 5770 K, we observe that most of the solar radiation is emitted at 0.5 μm and in the range of visible spectrum [14].

$$\lambda_{max}[\mu m] = \frac{2900}{T} = \frac{2900}{5770} = 0.5 \mu m \quad (2.3-1)$$

2.3.2 Albedo

Some of the incoming sunlight is reflected off a planet. Albedo (or Bond Albedo) is the ratio of the reflected/scattered radiation and the total incoming radiation integrated over frequency. On Earth, albedo varies over areas with land or oceans and generally increases with increasing cloud coverage and increasing latitude. Consequently, the orbit inclination affects the Albedo. Thus, it is always a great challenge for a thermal engineer to decide the albedo parameters of the analysis. Albedo can vary from 0.1 to 0.5 over different orbits and a value of 0.2 and 0.4 can be typically used for the worst cold and worst hot scenario respectively. Albedo, has the same spectral distribution as sunlight, but is not completely diffusive. The absorbed albedo flux on a surface is calculated as [13]:

$$\Phi_{albedo} = \alpha \cdot A_b \cdot F_{planet} \cdot \Phi_{solar} \cdot \cos \theta \quad (2.3-2)$$

α is the absorptivity of the surface, A_b is the bond albedo, F_{planet} is the view factor of the surface to the planet and Φ_{solar} is the solar flux. $\cos \theta$ is the solar zenith angle that the sun rays form with sub-satellite point and the satellite, as shown in Figure 1.

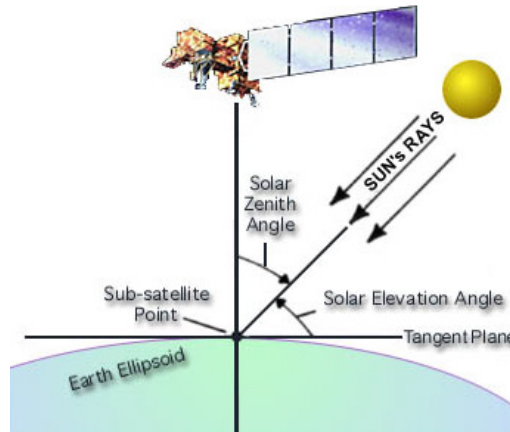


Figure 1: Solar zenith angle¹

The solar zenith angle is given by:

$$\cos \theta = \sin \Phi \sin \delta + \cos \Phi \cos \delta \cos h \quad (2.3-3)$$

Φ, δ, h are the local latitude, the current declination of the sun and the hour angle in local solar time respectively.

2.3.3 Planetary Radiation

A planet absorbs the solar radiation that is not scattered or reflected due to albedo. This energy is re-emitted by the planet according to the Black-body Radiation Law. Earth has an average equilibrium temperature of -18°C (255 K), which can in general vary from 240 K to 260 K, depending on the solar constant and the Albedo assumptions. Using Wien's

¹ Picture obtained from Landsat 7 Handbook

Displacement Law, we observe that Earth emits most of its radiation at 11.4 μm , i.e. in the infra-red spectrum. According to Kirchhoff's Law in its diffuse form, a good emitter is a good absorber at a particular wavelength or at a specific range of wavelengths, i.e. $\alpha_\lambda = \varepsilon_\lambda$ [15]. Because of the temperature variations on the Earth's surface, the emitted infra-red radiation fluxes fluctuate. IR fluxes typically range from 150 to 350 W/m^2 . The absorbed IR flux on a surface is calculated [13]:

$$\Phi_{IR} = \varepsilon_{surface} \cdot \varepsilon_{planet} \cdot F_{planet} \cdot \sigma \cdot T_{planet}^4 \quad (2.3-4)$$

$\varepsilon_{surface}$ is the emissivity of the surface, ε_{planet} is the emissivity of the planet and is equal to 1 since Earth is treated as a black body, F_{planet} is the view factor of the surface to the planet, $\sigma = 5.67 \cdot 10^{-8} [\text{W}/\text{m}^2 \cdot \text{K}^4]$ is the Stefan-Boltzmann constant and T_{planet} is the temperature of the planet.

2.3.4 Low-Earth Orbit Environment

LEO are typical of Earth-Observation missions, as most instruments require close proximity to the target for better resolution and measurements. Altitudes vary from 200 km to 2000 km, but most of the LEO satellites are in the range of 400 km to 800 km. Due to their proximity to Earth, such missions are strongly affected by Earth's albedo and IR. LEO are circular orbits and their orbital period can be found as [14]:

$$T_{orbit} = 2\pi \sqrt{\frac{(R_{earth} + h)^3}{\mu_{earth}}} [\text{sec}] \quad (2.3-5)$$

Where $R_{earth} = 6371 \text{ km}$ is the radius of the Earth, $h [\text{km}]$ is the altitude and $\mu_{earth} = 398600.4 \text{ km}^3/\text{s}^2$ is the Earth's gravitational parameter.

The eclipse time for a circular orbit can be calculated as [13]:

$$T_{eclipse} = T_{orbit} \cdot \frac{1}{180^\circ} \cdot \cos^{-1} \left[\frac{\sqrt{h^2 + 2 \cdot R_{earth} \cdot h}}{(R_{earth} + h) \cos \beta} \right] \quad (2.3-6)$$

β is the orbit beta angle defined as [13]:

$$\beta = \sin^{-1}(\cos \delta_s \sin RI \sin(\Omega - \Omega_s) + \sin \delta_s \cos RI) \quad (2.3-7)$$

where δ_s is the declination of the sun, RI is the orbit inclination, Ω is the right ascension of the ascending node (RAAN) and Ω_s is the right ascension of the sun.

2.4 Geometrical and Thermal Mathematical Model

The Geometrical Mathematical Model (GMM) is generated in order to calculate the radiative links between surfaces [16]. The Thermal Mathematical Model (TMM) is a simplification of the thermal structure of a spacecraft or part of it so as to generate an approximated

representation of their thermal behavior. According to ECSS-E-ST-31C standards, TMM is a “numerical representation of an item and its surroundings represented by concentrated thermal capacitance nodes or elements, coupled by a network made of thermal conductors (radiative, conductive and convective)”. The thermal structure is discretized into isothermal nodes with assigned thermal and optical properties, as well as boundary conditions, such as loads, temperatures and heat fluxes.

2.5 Summary

In nature, there are 3 modes of heat transfer; conduction, convection and radiation, which can be represented with mathematical formulations. These formulations are used in order to determine the thermal behavior of a system with respect to time in a transient analysis or its final state once it has reached thermal balance in a steady-state analysis. The analysis can be performed by taking into account all the environmental conditions, including boundary conditions, such as radiation to space or controlled temperatures, and heat fluxes, such as solar and infrared radiation in the case of an orbiting spacecraft. Then, the thermal behavior of the system can be determined using a Geometrical and Thermal Mathematical Model for either a time-dependent or independent analysis.

3 Heat switches technology

This chapter defines the purpose of a heat switch as a means of satellite thermal control, the measures of its effectiveness and its potential applications. Subsequently, it describes the suggested gas-gap heat switch design and defines its performance requirements as provided by ESA. A brief explanation of the used manufacturing method (Selective Laser Melting) and material selection is also given. The chapter concludes by briefly introducing similar types of heat switches and comparing them with the suggested gas-gap heat switch.

3.1 Heat switches purpose and measures of effectiveness

A heat switch is a device that adjusts its conductance in order to act as a good thermal conductor or a good thermal insulator, depending on the actual temperature of a component or a unit. Heat switches can be used in a wide variety of applications, depending on their size and geometry. For example, they can be used for the passive thermal control of electronics and sensors, minimizing or even eliminating power consumption that would otherwise be required if thermostats or heaters were used. Furthermore, due to their capacity to act as both a thermal insulator and conductor, the heat switches assume the role of two different thermal control means. Heat switches differ from thermostats, as the former controls the temperature of a component by opening/closing a heat path, while the latter by opening or closing an electrical circuit [13]. An important feature of a heat switch is that it is typically self-regulated using its own temperature sensors, a PCM or a sorber material and does not require any control from a computer or human intervention.

The measure of the effectiveness of a heat switch is quantified by taking the ratio of the thermal conductance in the ON-state and the OFF-state. The greater the ratio, the greater the performance of the heat switch. Depending on the application, a high ON-conductance can be more important than a low OFF-conductance or vice versa. Another important parameter is the “time constant” of the switch, which measures its responsiveness in controlling the temperature of the warm component.

3.2 Heat switches applications

Heat switches can be used on two different levels; component and system applications. A heat switch can be used for the temperature control of a specific electronics component or an entire instrument or electronics box, as shown in Figure 2. For the case of the electronics box, when its temperature rises, the heat switch is activated and increases its thermal conductance to allow for efficient heat flow from the box to the radiator.

On a system level, heat switches could be implemented as the main thermal control method for an entire spacecraft. Such approach could revolutionize the design of the thermal control subsystem by replacing currently popular methods, such as the insulated concept. Currently, heat-dissipating components are constantly thermally connected with bulky structures to radiators that are sized according to the worst case hot scenario. Consequently, the radiators are oversized and heaters are required to provide the necessary heat to compensate for the

heat losses due to this oversizing. Heat switches could be implemented between spacecraft structures and radiators as shown in Figure 3. Additionally, heat switches could be placed between dissipating units or modules and spacecraft main structures. This way, the heat switches could control the thermal fluxes to the main structure that are required to maintain the entire spacecraft in the requisite temperatures. Though, such approach would be very challenging in terms of mechanical design and would require meticulous analysis for its optimization.

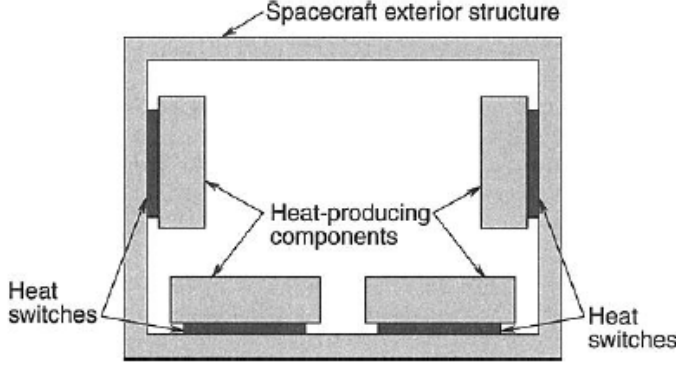


Figure 2: Heat switches between components and spacecraft structure [13]

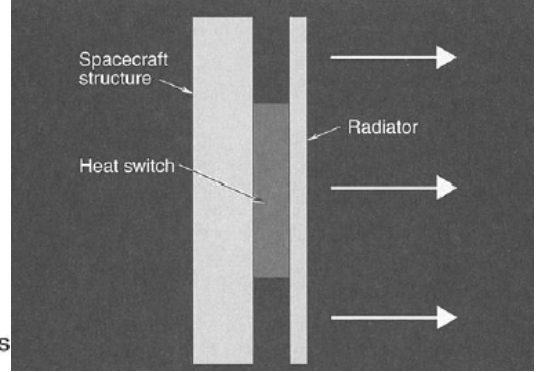


Figure 3: Heat switch between spacecraft structure and radiator [13]

Overall, heat switch technology has the potential to provide more efficient spacecraft temperature control by reducing power consumption and replacing heavy thermal control components. Moreover, thanks to the reduced heating power consumption during the dormant state of the spacecraft, batteries could be resized and hence reduce the launch mass.

3.3 Gas-gap heat switch

University of Twente has developed a gas-gap heat switch. A gas-gap heat switch has an internal cavity (gap) that is pressurized with a gas in the ON-state to allow for conduction through the gas and maximize the thermal conductance. In the OFF-state, the gap is depressurized to near vacuum, minimizing the thermal conductance, which is eventually the result of the conduction through the fine walls of the structure and the support pillars and radiation from the hot to the cold side.

The designed switch can be either passive or active. A sorber material that adsorbs the gas can be used as a thermal actuator. As the temperature increases, the capacity of the sorber material to adsorb the gas decreases, thus releasing gas and pressurizing the gap. Consequently, by selecting the appropriate sorber material based on the desired activation temperature, the effective temperature of the controlled component can be used to activate and deactivate the heat switch without consuming any power. Alternatively, a closed or an open-loop feed system can supply the gas to the switch. However, such a system would require tanks, valves, pumps, injectors and tubing, increasing the mass and complexity of the design and increasing its points of failure. Additionally, the responsiveness of the switch would decrease.

As mentioned earlier, the suggested gas-gap heat switch is currently in its third design iteration. The first prototype was significantly heavier and its performance was significantly far from the performance requirements indicated in Table 1. The vertical and horizontal cross-section of the first prototype are shown in Figure 4 and Figure 5 respectively.

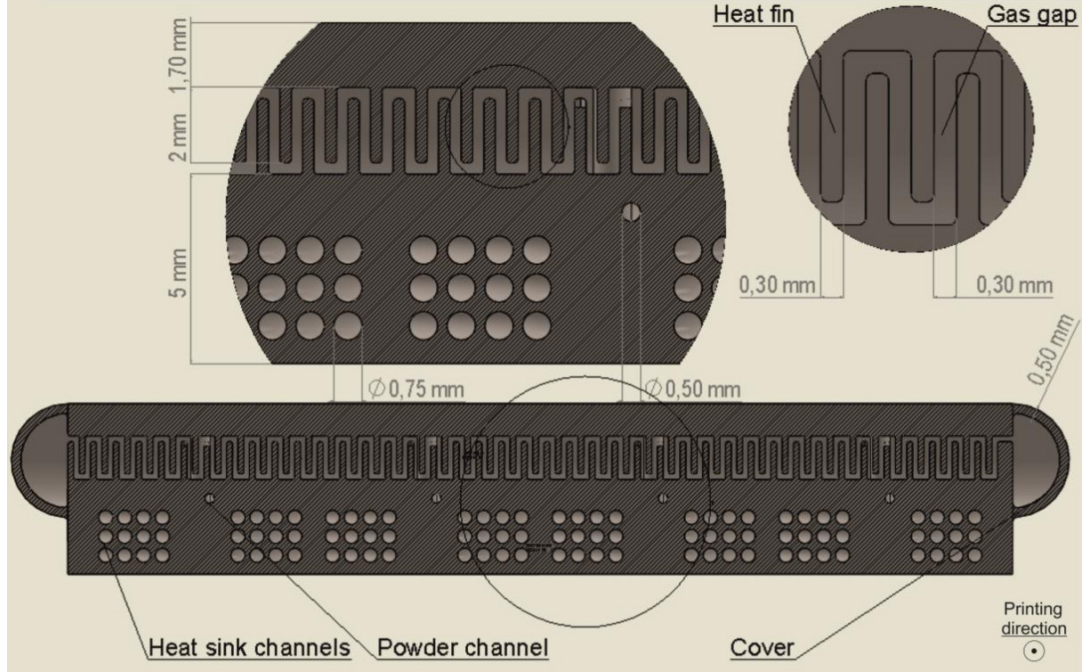


Figure 4: First prototype vertical cross-section

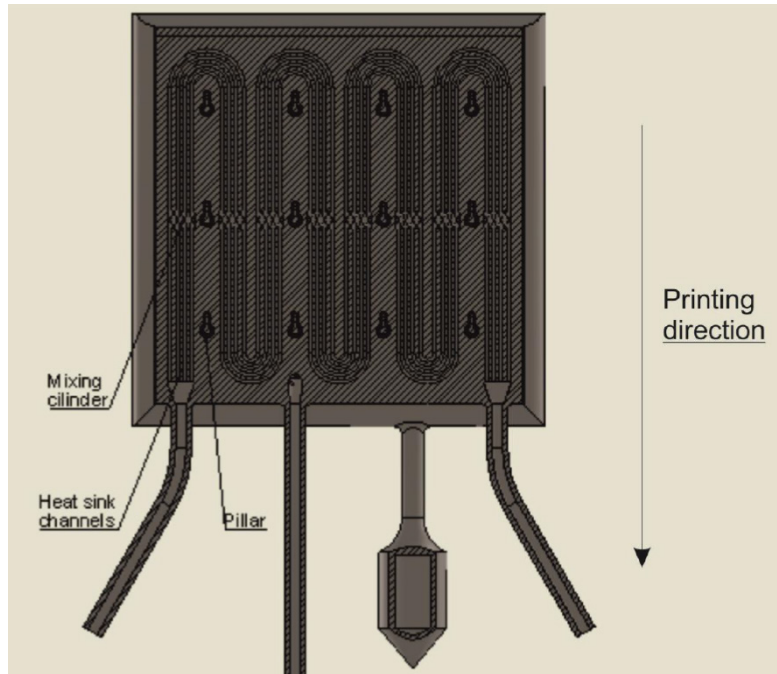


Figure 5: First prototype horizontal cross-section

The second prototype is significantly lighter by reducing the thickness of the switch and its theoretical performance has substantially improved thanks to the change in the shape of the internal gap from the 4-channel serpentine shape to a multiple parallel channel configuration

as shown in Figure 6. Finally, the only difference between the second and third prototype is the change in the length of the fins from 1.6 mm to 0.6 mm as indicated in the fin profile views in Appendix E. This change is the result of an optimization process, since it provides a desired decrease in the OFF-conductance at the expense of the undesired decrease in the ON-conductance. Both are the result of the reduction in the effective area of the fins.

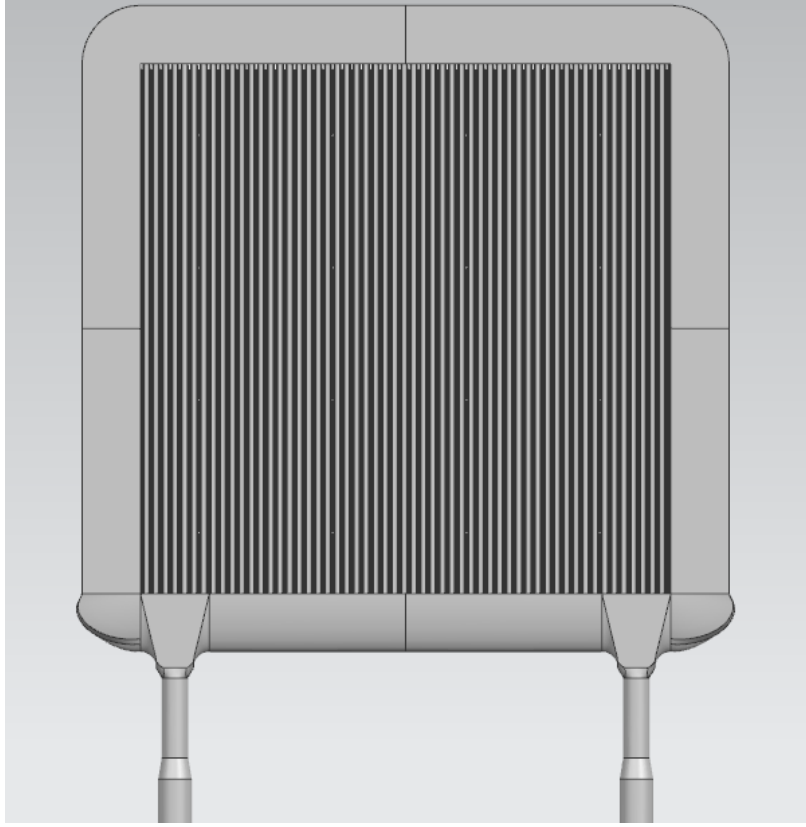


Figure 6: Second prototype horizontal cross-section

3.3.1 Heat switch requirements

As a first approach, the switch is expected to be used in Earth-Observation missions at room temperature, with a nominal component temperature range from -20°C to $+40^{\circ}\text{C}$. However, its application in other space missions with different temperature requirements could be investigated. Table 1 summarizes the performance requirements set by ESA.

Table 1: Heat switch performance requirements

Requirement	Value
OFF conductance [$\text{W}/\text{m}^2 \cdot \text{K}$]	<5
ON conductance [$\text{W}/\text{m}^2 \cdot \text{K}$]	>500
ON/OFF ratio	>100
Temperature range [$^{\circ}\text{C}$]	$-20 < T < +40$
Area density [kg/m^2]	<8

Figure 7 shows the design of the latest iteration, which is the third prototype. It measures 200 mm x 200 mm, with a thickness of 2.2 mm. For the internal gap geometry, please refer to

Figure 132 in Appendix E. Of course, the area of the switch can be adjusted accordingly to provide a good interface with the mating unit.

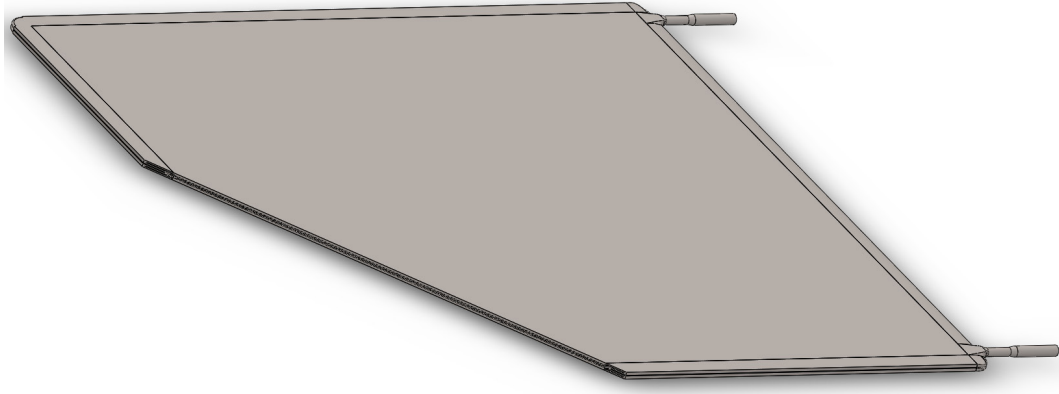


Figure 7: Third prototype design

3.3.2 Manufacturing method

The switch is manufactured using Selective Laser Melting (SLM). SLM is an additive manufacturing technique that uses the geometry information from CAD files to slice the part into multiple thin layers of several microns and uses laser beams to fuse fine metal powder into solid parts. The currently available technology of SLM is a limiting factor for the design of the heat switch. The smaller the gap, the higher is the ON-conductance of the switch. However, test samples have shown that a minimum gap of 200 microns can be currently achieved, as shown in Figure 8. Currently, the typical size of the powder used in SLM is 50 microns, which is one quarter of the feature size. Consequently, it is possible that imperfections occur for such small features.

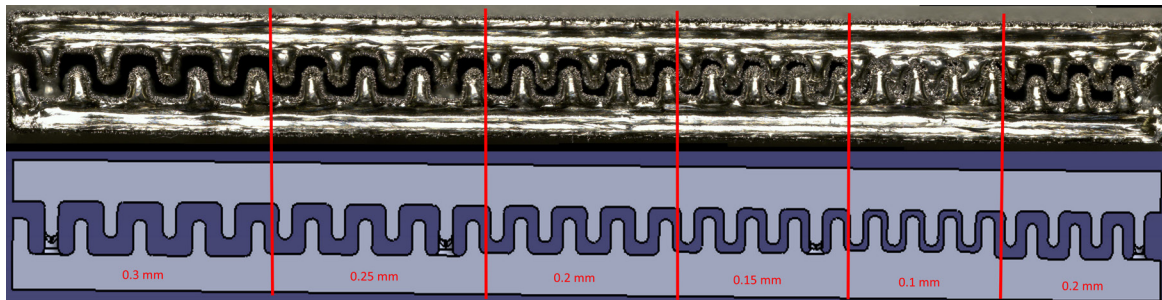


Figure 8: Test sample for gap size

3.3.3 Material selection

Before the procurement of the third prototype there was a debate on the material selection for the switch. The first two prototypes were manufactured with Ti-6Al-4V. However, Inconel 718®, a nickel alloy, was also considered as a potential candidate after recommendation from University of Twente and the manufacturer of the third prototype.

According to the manufacturer's experience, titanium alloys are more susceptible to cracking and residual stresses because of high temperatures compared to Inconel. Additionally, if Hydrogen is to be used as the operating gas in the heat switch, special care shall be given to

titanium alloys due to their degradation when exposed to hydrogen containing environments. At elevated temperatures, titanium alloys tend to accumulate high concentrations of hydrogen, as hydrogen solubility increases. Hydrogen remains in the titanium lattice, reducing the mechanical properties of the alloy and it can diffuse through the metal leading to embrittlement [17]. Figure 133 in Appendix F shows the diffusivity of Hydrogen in Ti-6Al-4V. Extrapolating for the maximum operating temperature of 40°C, the hydrogen permeability/cm³ is $2.5 \cdot 10^{-8}$ (STP)/m·s·kPa^{0.5}, which is negligible. In case diffusion and embrittlement are observed, a TiN (Titanium Nitride) coating could be applied. This coating considerably reduces hydrogen diffusion into the substrate and the effects of the hydrogen content to tensile properties [18].

In terms of mass, Inconel has almost double the density of Ti-6Al-4V, thus making it not suitable for space applications. More specifically, an Inconel heat switch has a surface density of 15.5 kg/m² based on the third prototype design, which is almost double the maximum requirement from Table 1. A Ti-6Al-4V heat switch has a surface density of 8.35 kg/m². Ti-6Al-4V has a specific strength (Yield Strength over density) 35.3% greater than Inconel.

Preliminary investigations showed that the thermal conductivity of the heat switch material is more critical for the OFF-conductance rather than the ON-conductance. Consequently, Ti-6Al-4V would outperform Inconel due to its lower thermal conductivity. This was confirmed using a FEM, which showed that the overall ON/OFF ratio (including 2 thermal fillers) of a titanium switch is 20% higher than an Inconel one. The straw-man concept analysis showed that a unit placed on top of an Inconel heat switch would require 16.76% more heating power than if placed on top of a Ti-6Al-4V heat switch. For details about the methods used for the straw-man concept analysis and the thermal simulations, please refer to chapters 4 and 5 respectively.

3.4 Currently available heat switches

At the moment, since the general heat switch technology is at its infancy, there is not an extensive variety of available heat switches. Furthermore, the already developed heat switches have not yet reached a high TRL in order to be used in future missions in the short-term. The most popular technologies are paraffin and gas-gap heat switches. Though, most of the developed heat switches are designed for cryogenic applications and are typically dedicated to specific instruments and small components rather than electronics units, which is the intended use of the heat switch in question.

With respect to heat switches in the same size range as the suggested heat switch, there is limited available literature. One of the most interesting cases is a partnership between JAXA and the University of Tsukuba that has led to the design of a paraffin-actuated heat switch. The breadboard model of the switch measures 62 mm in diameter and 38 mm in height as shown in Figure 9. Testing of the breadboard model resulted in an ON/OFF ratio of 127, with an ON-conductance of 1.6 W/K and an OFF-conductance of 0.0126 W/K. The performance of the switch with respect to temperature is shown in Figure 10. Dividing with the surface area leads to an ON heat transfer coefficient of 530 W/m²·K and an OFF heat transfer coefficient of 4.17 W/m²·K. The total mass of the breadboard model is 320 g equivalent to a

surface density of 106 Kg/m^2 [19]. Even though this particular switch satisfies the aforementioned conductance requirements set by ESA, it is more than 10 times thicker than the suggested gas-gap heat switch and it exceeds the surface density requirement by more than 13 times. Additionally, it is a rather complex device, which is against the principle behind the manufacturing suggested heat switch.

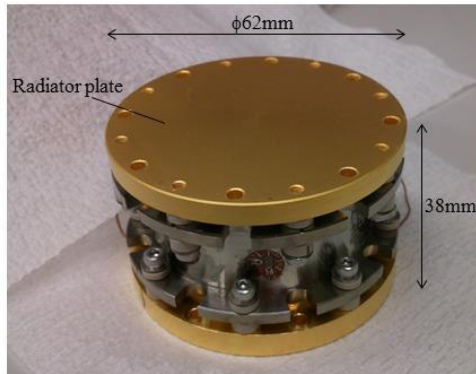


Figure 9: Paraffin heat switch dimensions

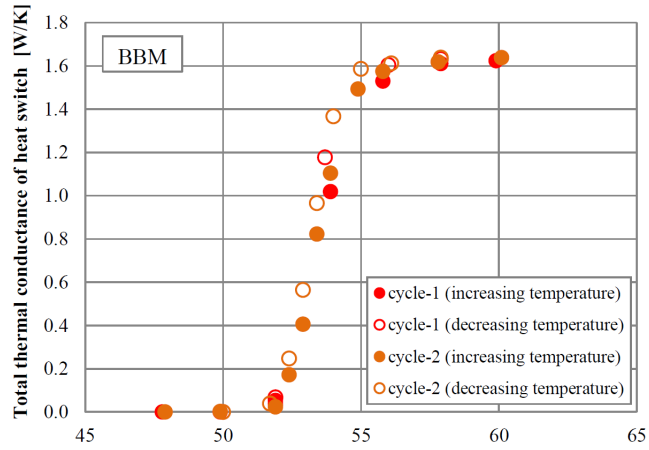


Figure 10: Total thermal conductance with temperature

Starsys technologies has developed one of the first and most efficient paraffin heat switches. The configuration and the performance characteristics of the Starsys pedestal heat switch are provided in Figure 11. Normalizing based on the area, the ON-case heat transfer coefficient is $640 \text{ W/m}^2 \cdot \text{K}$ and the OFF-case heat transfer coefficient is $6.6 \text{ W/m}^2 \cdot \text{K}$. Similarly, the surface density is 87.7 Kg/m^2 . Even though the switch satisfies all the thermal performance requirements but the OFF-conductance, its bulky and heavy structure is a prohibitive factor for the desired application.

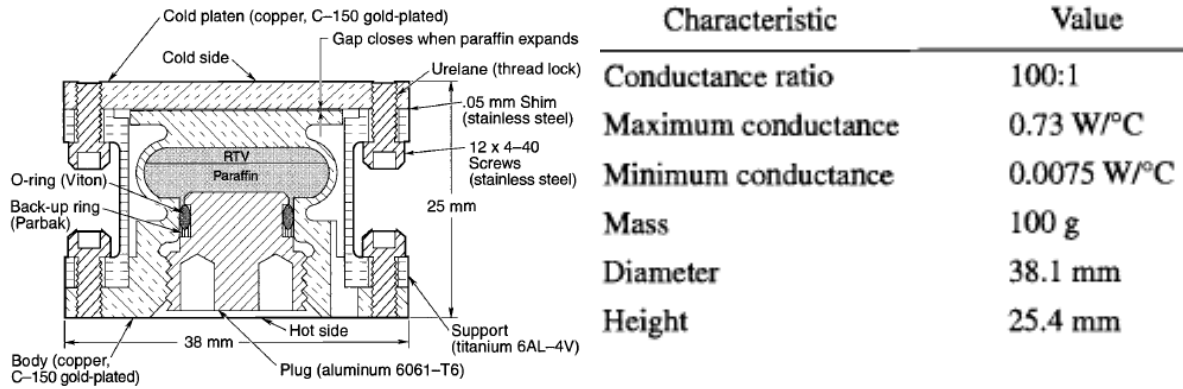


Figure 11: Starsys pedestal heat switch [13]

IberEspacio has developed a heat switch based on variable conductance loop heat pipes (LHP) with Ammonia as the working fluid. The device is independent of the gravity field. The configuration of this switch is shown in Figure 12. Table 2 outlines the components of the heat switch along with their main characteristics. The ON-conductance is 3.5 W/K and the OFF-conductance 0.006 W/K for a heat transfer coefficient of 683 and $1.17 \text{ W/m}^2 \cdot \text{K}$ respectively. The ON/OFF ratio is 580. The surface density is 28.6 Kg/m^2 [20]. This switch is the most promising case compared to the ones above, as it offers the best ON/OFF ratio and has the

smallest surface density. Furthermore, it appears to be easily scalable. The only concerns are the size of the switch and the fact that the surface density requirement is not respected.

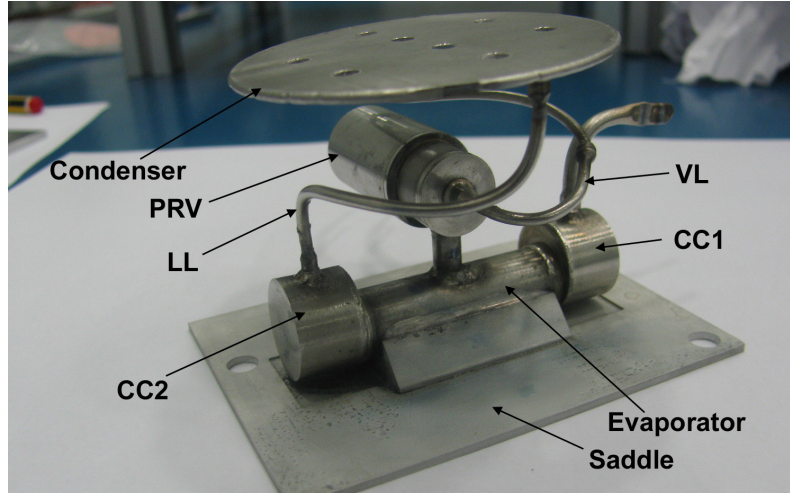


Figure 12: IberEspacio heat switch

Table 2: IberEspacio heat switch characteristics

Component	Material	Length [mm]	OD [mm]	Mass [g]
Evaporator	SS	40	12	31.6
Condenser	SS	h=1.5	60	30.3
Double Compensation Chamber (CC)	SS	10.8	17	17.7
Vapor Line (VL)	SS	111.4	2	2
Saddle	Aluminium	34 (interface with EV)	84x61	27.6
Pressure Regulated Valve (PRV)	SS	48.4	17	32.5
Working Fluid	NH ₃	-	-	3
Total mass [g]	-	-	-	146.5

Another interesting case is the paraffin-actuated heat switch developed for the thermal control of the batteries onboard the 2003 Mars Explorations Rovers. The achieved ON-conductance is 0.6 W/K and the OFF-conductance is 0.019 W/K for an ON/OFF ratio 31.6 [21]. However, no information is provide about the size and the weight of the device. Consequently, it is difficult to compare it with the suggested heat switch.

3.5 Summary

A heat switch constitutes a variable thermal conductance satellite thermal control technology. The ratio between the ON/OFF-state of the switch is the most important measure of its performance. The designed gas-gap heat switch adjusts the thermal conductance by varying the pressure of the active gas inside the gap. The currently available manufacturing technology imposes limits on the design of the switch and its performance. The suggested heat switch is an innovative idea because of its intended application in large units and at room temperature, rather than in small components at cryogenic temperatures.

4 Systems Engineering Study

In this chapter, a preliminary investigation is conducted in order to determine the effects of the use of the suggested gas-gap heat switch. This investigation is performed using the straw-man concept. The environment encountered by the spacecraft is described, along with the attitude of the spacecraft and the thermal modeling assumptions. A key element in this study is the process of sizing the bus's radiators, which is described in section 4.3.5. Finally, the on-orbit temperature profiles are provided and some preliminary conclusions about the implementation of the gas-gap heat switch in the Sentinel-2 mission.

4.1 Straw-man concept

A preliminary systems engineering analysis is required in order to determine the effects of the implementation of the gas-gap heat switch in the system architecture of an Earth-Observation satellite. This is achieved by performing a straw-man concept analysis. The straw-man concept refers to a preliminary, simplified model intended to determine the advantages and disadvantages of a proposal and it provides initial estimations of variables and parameters. Such variables include the temperatures of electronics and payload units, as well as the unit heating power that is consumed. Parameters among others can refer to radiators size, orbital heat fluxes and surface coatings. The depth of the details in a straw-man proposal is such that it is representative of real life cases.

4.2 Sentinel-2

In this case, ESA's Sentinel-2 is used as a reference point for the study. Sentinel-2 is a constellation mission of two satellites that provide high resolution optical imagery, using a filter based push-broom scanner. The mission offers global coverage and a temporal resolution of 10 days with one satellite and 5 days with two satellites. Each satellite has a total launch mass of 1200 kg and overall dimensions of 3.4 m x 1.8 m x 2.35 m in stowed position. The power consumption at nominal mode is 1.4 kW. The thermal control is achieved mainly with passive means, using radiators [22]. The lifetime of the mission is 7 years with consumables for 12 years. The orbit profile of the mission is given in Table 3.

Table 3: Sentinel-2 orbital parameters [22]

Orbit Type	Sun-Synchronous
Altitude h [km]	786.13
Inclination i [deg]	98.6206°
Local Time Ascending Node	22:30
Eccentricity e	~0
Argument of Periapsis ω [deg]	~90°

From these values we can obtain the orbital period and the eclipse time, using the mean Earth radius of 6371 km and Earth's gravitational constant $\mu = 398600.4 \text{ km}^3/\text{s}^2$ [14].

$$T_{orbit} = 2\pi \sqrt{\frac{(R_{earth} + h)^3}{\mu_{earth}}} = 2\pi \sqrt{\frac{(6371 + 786.13)^3}{398600.4}} = 6025.9 \text{ sec} = 100.43 \text{ min}$$

$$T_{eclipse} = 100.43 \cdot \frac{1}{180^\circ} \cdot \cos^{-1} \left[\frac{\sqrt{786.13^2 + 2 \cdot 6371 \cdot 786.13}}{6371 + 786.13} \right] = 35.09 \text{ min}$$

ESA's documentation indicate a mean orbital period of 100.58 min and a mean eclipse duration of 33.9 min.

4.3 Thermal environment simulation model

4.3.1 Orbit, Attitude and Layout

The straw-man concept thermal environment simulation model uses the same orbital parameters and power budget with the Sentinel-2 mission. The satellite bus has the shape of a parallelepiped with dimensions of 1300 mm x 1300 mm x 1930 mm. This geometry represents only the platform of the spacecraft and does not include the payload, which is considered to be isolated from the platform (adiabatic top panel). An illustration of the spacecraft is given in Figure 13.



Figure 13: Artist's rendition of Sentinel-2

Figure 14 indicates the dimensions and the layout of the power dissipating units. The velocity vector is in the +X direction and the nadir pointing in the +Z direction.

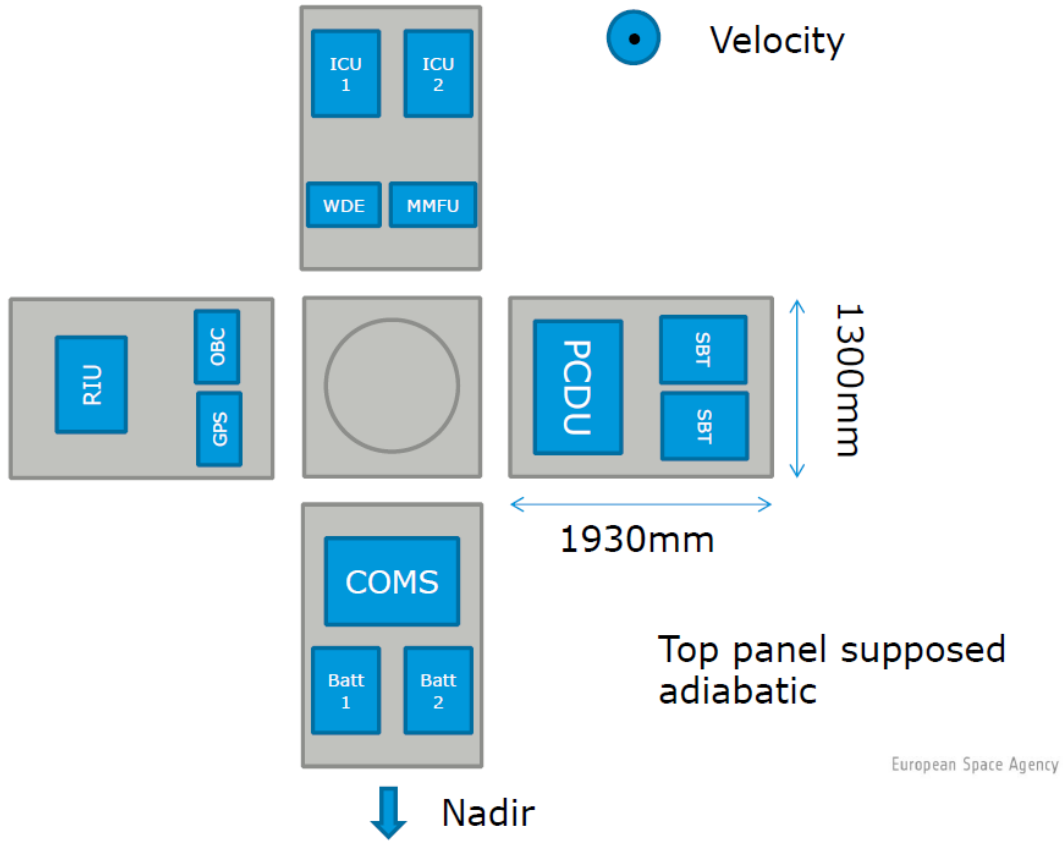


Figure 14: Unit layout of simulation model

Table 25 in Appendix A provides the minimum and maximum power dissipation of the units during sun illumination and eclipse, as well as their respective operational temperature range. Table 26 provides the acronyms, dimensions and thermal capacitance of the Sentinel-2 units. The thermal capacitance indicates the ability of a body to store energy and its inertia to temperature fluctuations [6].

4.3.2 Investigated Scenarios

This analysis investigates two different main scenarios, each with two subcases. The first main case assumes there is no heat switch in between the dissipating units and the walls, while the second main case uses the heat switch. Both cases, have two subcases; worst case hot and worst case cold. The worst case hot and worst case cold assumptions are listed in Table 4.

Table 4: Sizing cases

Assumptions	Worst Case Hot	Worst Case Cold
Surface Properties	EOL	BOL
Solar Declination [deg]	-23.45° (Winter Solstice)	23.45° (Summer Solstice)
Earth Temperature [K]	260.26	240.28
Albedo Factor	0.4	0.2
Dissipations	Max	Min

4.3.3 Orbit modeling

The satellite structure was modeled in NX Space Systems Thermal. A Finite Element Model with 6 two-dimensional elements was generated. Each element represents one panel of the spacecraft. The NX Space Systems Thermal solver can account for orbital heating. With the orbital parameters mentioned in Table 25, the software determines the incident infrared, albedo and solar fluxes on each of the six panels of the satellite at 36 equidistant positions throughout the orbit for the winter and summer solstice.

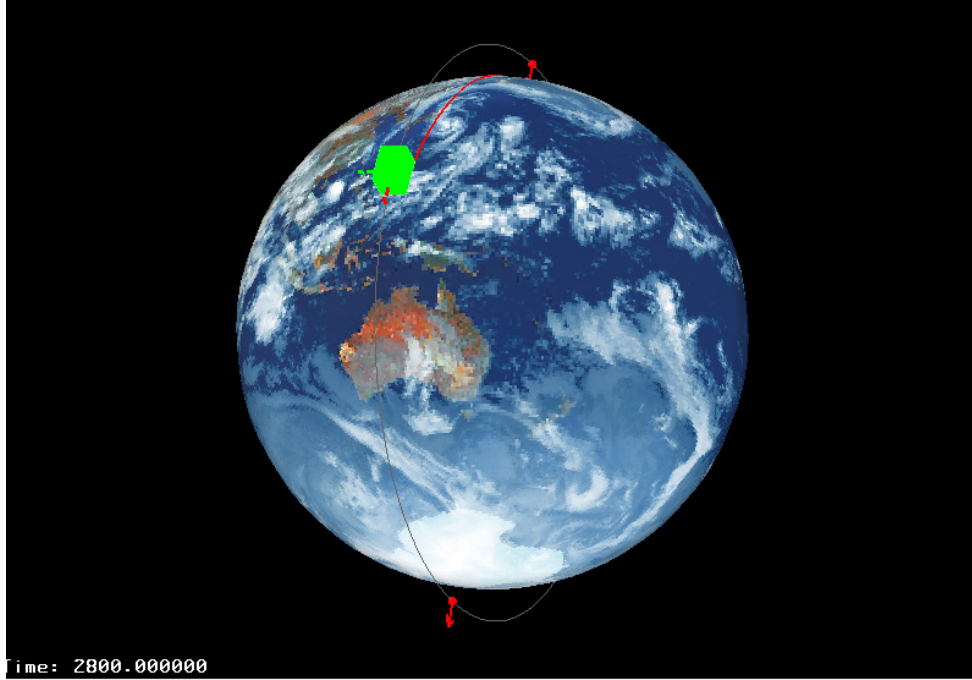


Figure 15: Visualization of the orbit as seen from the sun at 2800 sec

Throughout the orbit, there is no spacecraft rotation and thus the view factor of all panels to the Earth is constant. Consequently, since a constant Earth temperature is assumed, all panels receive a constant infrared flux from Earth in the hot and cold cases. Table 5 provides the incident infrared fluxes on all 6 panels in $[W/m^2]$. Figure 123 and Figure 124 in Appendix A provide the incident albedo flux profile for the worst hot and worst cold scenarios. Figure 125 and Figure 126 provide the incident solar flux profile for the worst hot and worst cold scenarios respectively.

Table 5: Average external fluxes on spacecraft

Panel	Earth IR Flux $[W/m^2]$	
	Worst Hot	Worst Cold
+X	57.490	41.639
+Y	57.490	41.639
+Z	206.784	149.769
-Z	0	0
-Y	57.490	41.639
-X	57.490	41.639

4.3.4 Modeling assumptions

For the thermal model, values for the thermal coupling between the elements were given by ESA. A contact conductance of $750 \text{ W/m}^2 \cdot \text{K}$ was used for the interface between Unit/Panel and $500 \text{ W/m}^2 \cdot \text{K}$ for the Panel/Panel interface (thickness 44 mm). These values are based on legacy from testing and the thermal report of the Sentinel-2 mission.

The conductivity through the honeycomb panels is $3.5 \text{ W/m} \cdot \text{K}$ in plane and $1.5 \text{ W/m} \cdot \text{K}$ out of plane (thickness 44 mm). The panels have a total thermal capacitance per unit area of $5940 \text{ J/m}^2 \cdot \text{K}$.

As shown in Figure 14, the +X panel is considered adiabatic. The areas of the panels that are used as a radiator are covered with a white paint coating, while the rest is assumed to be covered with Kapton (MLI outer layer). The End-Of-Life (EOL) and Beginning-Of-Life (BOL) optical properties for both surfaces are given in Table 6.

Table 6: Model optical properties

Optical Property	White Paint		MLI	
	EOL	BOL	EOL	BOL
Absorptivity (α)	0.19	0.35	0.44	0.52
Emissivity (ϵ)	0.91	0.91	0.75	0.75

Apart from its emission to space, the MLI blanket is assumed to have an effective radiative and a conductive coupling to the panel. The conductive conductance is $0.019 \text{ W/m}^2 \cdot \text{K}$, and the radiative conductance $0.014 \text{ m}^2/\text{m}^2$. The MLI blankets are assumed to have a total thermal capacitance per unit area of $390 \text{ J/m}^2 \cdot \text{K}$.

For this stage of the analysis, the theoretical values provided by the University of Twente were used. More specifically, a heat transfer coefficient of $950.71 \text{ W/m}^2 \cdot \text{K}$ for the ON-state and $11.16 \text{ W/m}^2 \cdot \text{K}$ for the OFF-state were used. The mass per unit area of the switch is 9.04 Kg/m^2 . These values were provided for the intermediate design of the heat switch between the first and second prototype.

Internal radiation between the panels was also taken into account. A black coating with emissivity $\epsilon = 0.9$ was assumed for the surface of the panels. The view factors were calculated using the MAYA Thermal Wizard and were confirmed using hand calculations from references [6], [7]. The view factors are summarized in Table 7. Table 8 provides the Gebhart Factors that account for the reflections off the surfaces.

Due to the significantly different operating temperature ranges, the internal surface of the panel containing the batteries (+Z) is considered to be covered with MLI blankets. This is to radiatively decouple the panel from the rest of the spacecraft.

Table 7: View Factors for internal radiation

Panel	+X	+Y	+Z	-X	-Y	-Z
+X	0	0.222	0.222	0.113	0.222	0.222
+Y	0.149	0	0.225	0.149	0.251	0.225
+Z	0.149	0.225	0	0.149	0.225	0.251
-X	0.113	0.222	0.222	0	0.222	0.222
-Y	0.149	0.251	0.225	0.149	0	0.225
-Z	0.149	0.225	0.251	0.149	0.225	0

Table 8: Gebhart Factors for internal radiation

Panel	+X	+Y	+Z	-X	-Y	-Z
+X	0.014	0.218	0.218	0.114	0.218	0.218
+Y	0.147	0.023	0.221	0.147	0.243	0.221
+Z	0.147	0.221	0.023	0.147	0.221	0.243
-X	0.114	0.218	0.218	0.014	0.212	0.218
-Y	0.147	0.243	0.221	0.147	0.023	0.221
-Z	0.147	0.221	0.243	0.147	0.221	0.023

4.3.5 Sizing cases

The flux profiles were imported into ThermXL, which is an add-in for Microsoft Excel developed by ITP Engines UK. ThermXL was used to perform a transient analysis in order to size the radiator of each face so as to keep the units within their temperature range. The worst case hot was run first in order to size the radiator area using an iterative process. For optimization, the radiators are sized in such way that the units reach their maximum allowable temperature. The worst case cold uses the radiator area to calculate the required power to keep the units above their minimum allowable temperature. These calculations were performed for both with and without the heat switch in between the units and the panel. For the temperature limits, a safety margin was used for the operating temperature of the units, as dictated by ESA. More specifically, the maximum allowable operating temperature is reduced by 15°C, while the minimum operating temperature is increased by 5°C. Due to the high heat transfer coefficient of the ON-state of the heat switch, the radiators have the same size in both main cases, i.e. with and without the heat switch.

4.3.6 Results

From preliminary estimations, only the batteries require the heat switch due to their tight operating temperature range. Thus, the additional mass to the spacecraft is 1.822 kg or 0.15% of the Sentinel-2 total mass. Figure 16 shows the units temperature profiles over 10 orbits for the worst hot scenario in the absence of the heat switch. All units are operating at almost their maximum allowable temperature. The maximum allowable temperature cannot be reached for all units because there is no dedicated radiators for each unit and due to the assumption of isothermal panels for the spacecraft.

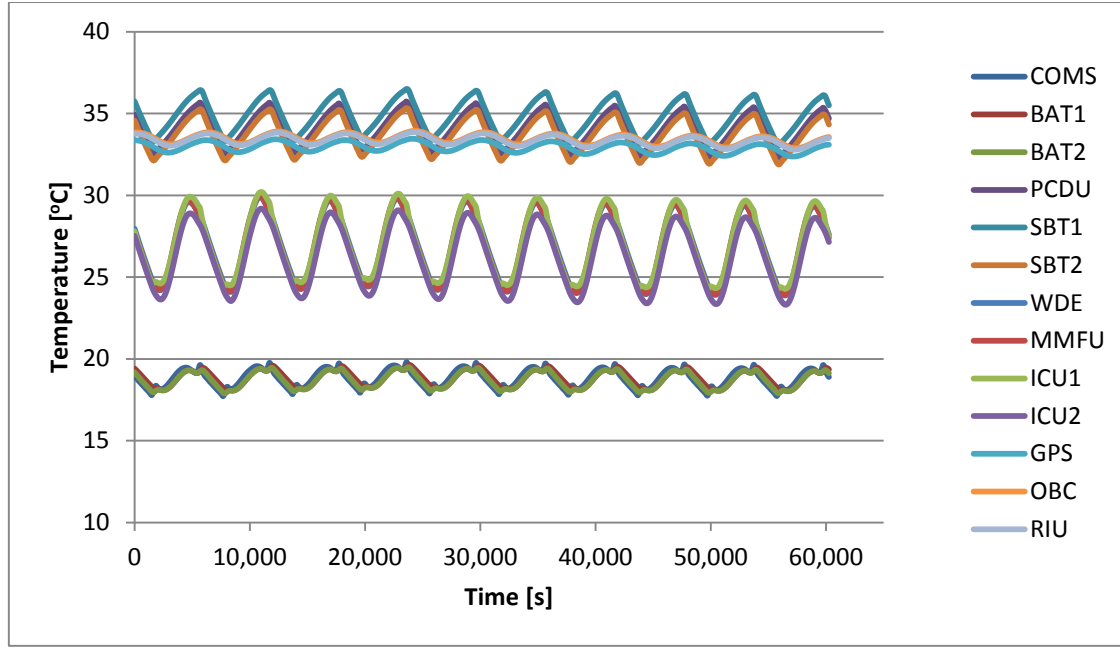


Figure 16: Units temperature profile (worst hot, no switch)

Figure 17 shows the temperature profile of the +Z panel, which accommodates the batteries, for the worst cold case in the absence of the heat switch. In order to maintain the temperature of the batteries above the minimum temperature of 14°C, an average heating power of 30.19 W and 34.07 W needs to be supplied to Battery 1 and Battery 2 respectively, for a total of 64.26 W. This is achieved by supplying a power of 50 W to Battery 1 and 60 W to Battery 2 if their individual temperature drops below 14.5°C. The difference in the power is due to the fact that only one battery is operating and thus dissipating power, while the second one exists for redundancy purposes.

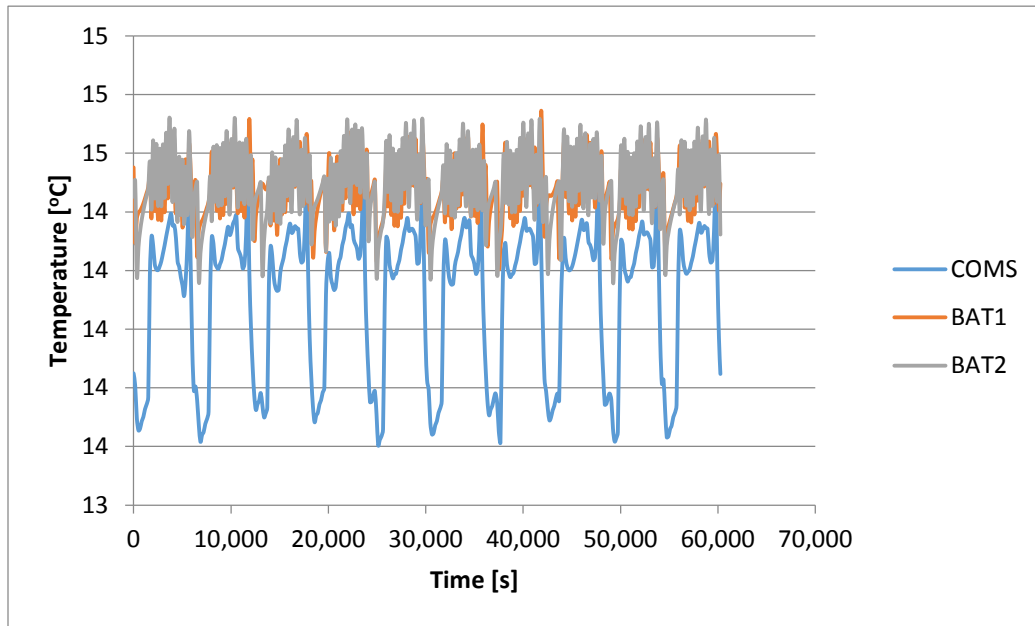


Figure 17: +Z panel temperature profile (Worst cold, no switch)

The implementation of the heat switch in the model did not alter the results for the worst hot case thanks to its high ON-conductance. Consequently, the radiators did not need any resizing. The switch activation temperature was set at 15°C. Figure 18 shows the temperature profile of the +Z panel units in the presence of the heat switch for the worst cold case. In order to maintain the temperature of the batteries above their minimum temperature of 14°C, an average heating power of 9.54 W and 13.00 W needs to be supplied to Battery 1 and Battery 2 respectively, for a total of 22.54 W. This is achieved by providing a power of 10.8 W to Battery 1 and 14.4 W to Battery 2 if their individual temperature drops below 14.1°C. In the case where the heat switch is applied, a lower temperature is observed for the COMS unit. This is the result of the reduced heating power on the batteries.

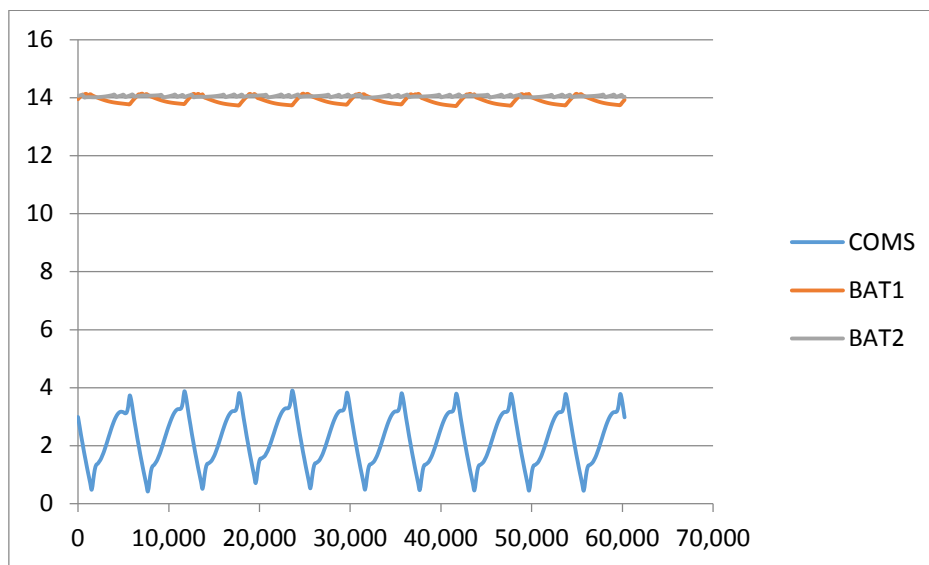


Figure 18: +Z panel temperature profile (Worst cold, with switch)

4.4 Summary

A preliminary straw-man concept analysis was performed to determine the advantages and disadvantages of the suggested gas-gap heat switch technology. From the obtained results, it is observed that there is a significant reduction of the worst case heating power required by almost a factor of 3. In total, a maximum of 41.72 W could be saved from the power budget of the Sentinel-2 mission if the suggested heat switch were implemented. This gain in power comes at the expense of only 1.822 kg addition in mass. For a more detailed analysis, please refer to Chapter 10.

5 Heat switch thermal modeling

This chapter begins by providing a simplified thermal network of the heat switch in order to obtain some preliminary estimations of the performance of the switch. Subsequently, it deepens into the conductive and gaseous heat transfer. Section 5.3 that is dedicated to gaseous heat transfer is essential as it determines the best candidate gases for the operation of the heat switch and it establishes their behavior with respect to temperature and pressure. Further in this chapter, the effect of convective and radiative heat transfer is investigated, as well as methods to reduce the necessary computational time for the radiative couplings.

5.1 Heat switch thermal network

As a first analysis, the heat switch can be represented using a lumped mass thermal network. Two separate networks can be generated; one for the ON-case and one for the OFF-case.

5.1.1 OFF-state

As a first approximation, the heat switch in the OFF-state can be described using the thermal network depicted in Figure 19.

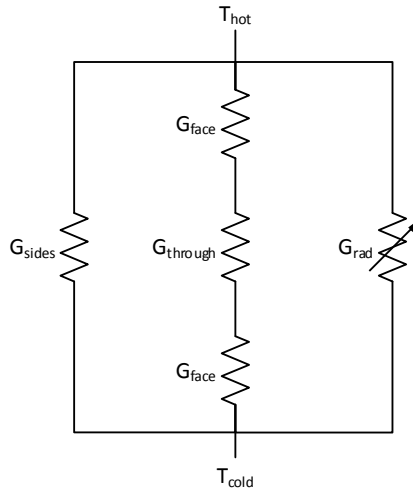


Figure 19: OFF-state thermal network

G_{sides} represents the heat flow through the sides of the switch. G_{rad} is the radiative conductance, which varies with temperature. G_{face} is the conductance through the faces of the switch. $G_{through}$ represents the combined conductance of the support pillars with the fins they are located on according to:

$$G_{through} = N_f \left(\frac{1}{N_p \cdot G_{pillar}} + \frac{1}{G_{fin}} \right)^{-1}$$

G_{pillar} is the conductance through a pillar, N_p is the number of pillars per fin, G_{fin} is the conductance through the fin and N_f is the number of fins with pillars on them.

Table 9: 10x10 cm² OFF-case thermal conductances

Label	l [mm]	A [mm ²]	Quantity	Conductance [W/K]
G_{sides_1}	11.14	50	1	0.0301
G_{sides_2}	21.24	50	3	0.0158
G_{face}	0.7	10,000	2	95.7143
G_{pillar}	0.2	0.0491	$N_p = 8$	0.00164
G_{fin}	1.6	25	$N_f = 8$	0.1047
G_{cond}	-	-	-	0.1919

For small temperature differences between two radiating surfaces the non-linear radiative conductance can be transformed into a linear conductance using the Taylor-series expansion [23].

$$G_R' = 4\sigma\bar{T}^3 G_R \quad (5.1-1)$$

Assuming an average temperature of 288 K between the hot and cold side and linearizing the radiative conductance, $G_{rad,linearized} = 0.0758 \text{ W/K}$. Thus, the total OFF-conductance is $G_{OFF,total} = 0.268 \text{ W/K}$. For the estimation of the radiative conductance, refer to section 5.5.1.

Table 10: 20x20 cm² OFF-case thermal conductances

Label	l [mm]	A [mm ²]	Quantity	Conductance [W/K]
G_{sides_1}	9.94	80	1	0.0539
G_{sides_2}	19.29	80	3	0.0278
G_{face}	0.7	40,000	2	382.8571
G_{pillar}	0.2	0.0866	$N_p = 16$	0.00290
G_{fin}	0.6	50	$N_f = 16$	0.5583
G_{cond}	-	-	-	0.6854

Assuming an average temperature of 288 K between the hot and cold side and linearizing the radiative conductance, $G_{rad,linearized} = 0.1325 \text{ W/K}$. Thus, the total OFF-conductance is $G_{OFF,total} = 0.818 \text{ W/K}$.

Eventually, in the OFF-state the switch can be represented with two isothermal nodes that are coupled together with one radiative and one conductive conductance (combination of all other conductive conductances) in parallel. The equation to describe this heat exchange is:

$$Q = G_{cond}(T_h - T_c) + G_{rad}(\sigma T_h^4 - \sigma T_c^4) \quad (5.1-2)$$

5.1.2 ON-state

As a first approximation, the heat switch in the ON-state can be described using the thermal network in Figure 20.

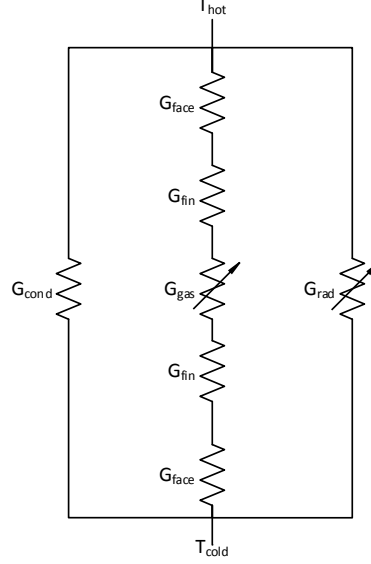


Figure 20: ON-state thermal network

G_{gas} is the conductance through the gas. Because this is a variable conductance that is dependent on the gas temperature, the average of the top and bottom faces temperature is used. Eventually, the total conductance is equal to:

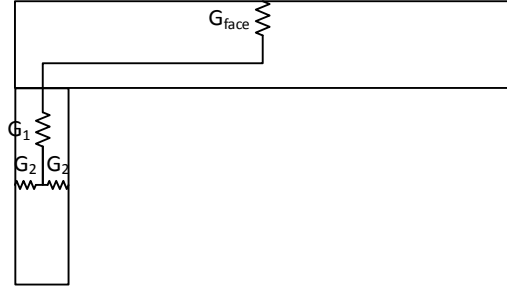
$$G_{ON,total} = G_{cond} + G_{rad} + \left(\frac{2}{G_{face}} + \frac{2}{N_{fin} \cdot G_{fin}} + \frac{1}{G_{gas}} \right)^{-1} \quad (5.1-3)$$

where N_{fin} is the number of fins per side. Using the geometry of Figure 131 and Figure 132 from Appendix E, we can obtain the following approximation for the gas conductance.

$$G_{gas} = \frac{k_{gas} \cdot (2 \cdot N_{fin} \cdot w \cdot L + 2 \cdot N_{fin} \cdot L \cdot (L_{fin} - L_{gap}))}{L_{gap}}$$

Where k_{gas} is the gas thermal conductivity, w is the width of the fin (dimension 1), L is the length of the fin, L_{fin} is the height of the fin (dimension 3) and L_{gap} is the gap distance (dimension 8). The comparison of this approximation with the Finite Element Analysis performed later on shows that the approximation over-estimates the gas conductance by less than 10%. Consequently, it is a good initial approximation.

It should be noted that G_{fin} in the ON-case is different than the one in the OFF-case. G_{fin} can be found as follows:



$$G_{fin} = \left(\frac{1}{G_1} + \frac{1}{2 \cdot G_2} \right)^{-1} \quad (5.1-4)$$

$$G_1 = \frac{k_{Ti} \cdot w \cdot L}{L_{fin}/2}$$

$$G_2 = \frac{k_{Ti} \cdot L_{fin} \cdot L}{w/2}$$

Combining G_{face} and G_{fin} gives the effective thermal conductance G_{eff} from the switch face to the fins. This approximation under-estimates the effective thermal conductance by 13% in comparison to a detailed FEM.

$$G_{eff} = \left(\frac{1}{G_{face}} + \frac{1}{N_{fin} \cdot G_{fin}} \right)^{-1} \quad (5.1-5)$$

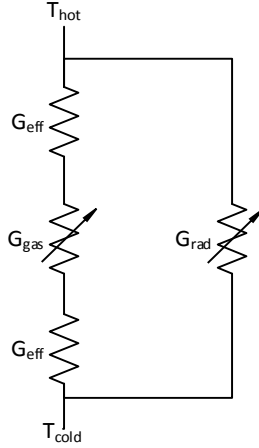


Figure 21: Simplified ON-case thermal network

Because the temperature difference between the top and the bottom face is expected to be very small in the ON-state, radiation exchange is eventually neglected in both the thermal network and the simulation. The reduced thermal network results in a difference of less than 5% with the detailed FEM.

5.2 Conductive heat transfer

The conductive heat transfer (G_{cond}) through the heat switch material can be estimated using a 3D FEM. The final values of G_{cond} for the different prototypes and materials were found

through an iterative process that involved the improvement of the FEM building up to the test setup. Eventually, in the thermal simulation, the baseplate of the vacuum chamber is held at a constant temperature $T_{baseplate} = 20^{\circ}\text{C}$, while a constant heat load is applied on the top face of an aluminium plate. For more information on the test setup, please refer to Chapter 7. In the absence of other thermal couplings, radiative or conductive, G_{cond} can be calculated using the temperature difference between the hot and cold side of the switch as:

$$G_{cond} = \frac{Q}{T_h - T_c} \quad (5.2-1)$$

Table 11 summarizes the obtained results for the conductive conductances for the second and third prototype of the heat switch.

Table 11: Conductive conductances of different prototypes

Prototype	Area	Material	# of pillars	Conductive Conductance [W/°C]	Conductive heat transfer coefficient [W/m²K]
Second	10 cm x 10 cm	Ti-6Al-4V	64	0.1465	14.65
Second	10 cm x 10 cm	Inconel 718®	64	0.2345	23.45
Third	20 cm x 20 cm	Ti-6Al-4V	256	0.4084	10.21

5.3 Gaseous heat transfer

Knudsen number is a dimensionless number used particularly in the microscale in order to determine whether the continuum assumption is respected. Knudsen number expresses the ratio of the mean free path to the characteristic length of the system. The mean free path expresses the probability distance a fluid particle travels before undergoing collision with another fluid particle [24]. Assuming the molecules to be rigid and spherical, the mean free path for a single component ideal-gas can be approximated as [15]:

$$\lambda = \frac{k_B T}{\pi d^2 \sqrt{2} p} \quad (5.3-1)$$

$k_B = 1.38065 \cdot 10^{-23} [\frac{J}{K}]$ is the Boltzmann constant, T is the gas temperature in Kelvin, d is the effective molecular diameter and p is the gas pressure in Pascals.

The Knudsen number is expressed as [25]:

$$Kn = \frac{\text{mean free path}}{\text{characteristic length}} = \frac{\lambda}{L} \quad (5.3-2)$$

If $Kn < 0.01$, the interfluid particle collisions dominate and the system is in the continuum regime. In the continuum regime, the gas particles collide with each other and the heat is

transferred in the most efficient way through the gas. Further increase in pressure does not affect the thermal conductivity of the gas.

If $Kn > 10$, the continuum assumption breaks down and the system is in the molecular regime. In this case, the probability of the fluid particles colliding with the surrounding walls is significantly higher than colliding with each other.

For the intermediate range $0.01 < Kn < 10$, heat conduction takes place in the transition regime. The temperature jump approximation, which is an averaging of the two extreme regimes, can be used in order to estimate the thermal conductivity of the gas.

It should be noted that these limits are approximate and can vary depending on the gas and the solid it comes in contact with. For more information, please refer to section 5.3.4.

The profile of the thermal conductivity of a gas across the three different regimes is similar to the one in Figure 22. The figure shows the variation of thermal conductivity of Argon gas occupying spacing between two Tungsten plates separated by 1 μm , at 300 K.

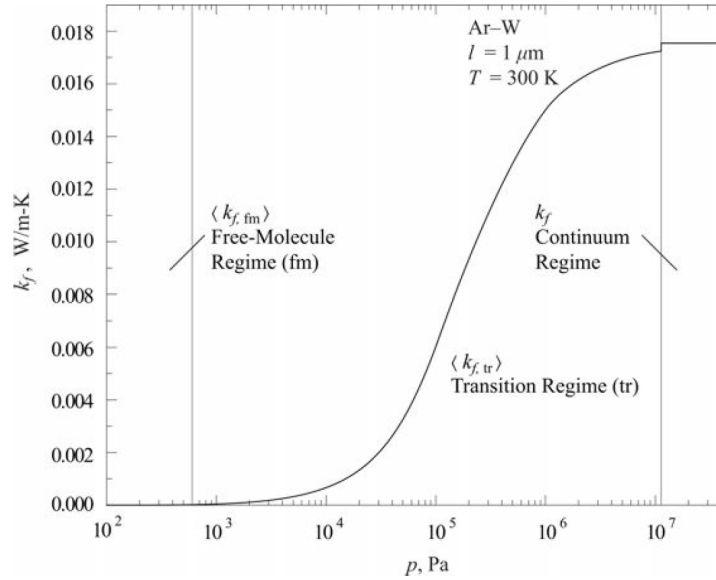


Figure 22: Variation of thermal conductivity of Argon [24]

5.3.1 Continuum regime thermal conductivity

In the continuum regime, the thermal conductivity of a gas can be estimated using the Prandtl number. The Prandtl number is dimensionless and expresses the ratio of the viscous to the thermal diffusion rate [6].

$$Pr = \frac{c_p \mu}{k} = \frac{9\gamma - 5}{4\gamma} \quad (5.3-3)$$

$c_p [\frac{J}{kg \cdot K}]$ is the specific heat, $\mu [Pa \cdot s]$ is the dynamic viscosity and $k [\frac{W}{m \cdot K}]$ is the thermal conductivity of the gas.

The dynamic viscosity can be estimated using the average molecular speed [15]:

$$\mu = \frac{1}{2} \rho \bar{C} \lambda \quad (5.3-4)$$

The average molecular speed is given by Maxwell's equilibrium formula [15]:

$$\bar{C} = \sqrt{\frac{8N_A k_B T}{\pi M}} \quad (5.3-5)$$

$N_A = 6.022 \cdot 10^{23} [mol^{-1}]$ is the Avogadro number and M is the gram molecular mass.

From thermodynamics we know:

$$C_p = \gamma C_v = \gamma \frac{fR}{2} \quad (5.3-6)$$

Where, $R = 8.314 [\frac{J}{mol \cdot K}]$ is the universal gas constant and f expresses the number of degrees of freedom of the gas. For a monoatomic gas $f = 3$, and for a diatomic gas $f = 5$.

The number of degrees of freedom for linear and non-linear molecules are given by equations (5.3-7) and (5.3-8) respectively, where is n the number of atoms in the molecules:

$$f = 3n - 5 \quad (5.3-7)$$

$$f = 3n - 6 \quad (5.3-8)$$

Combining equations (5.3-1) to (5.3-6), the thermal conductivity of a gas in the continuum regime can be approximated with equation (5.3-9). From this equation, it is clear that the thermal conductivity is independent of the gas pressure. The only environmental condition affecting the thermal conductivity is the gas temperature.

$$k = \frac{9\gamma - 5}{8} \frac{fR}{N_A \pi d^2} \sqrt{\frac{RT}{\pi M}} \quad (5.3-9)$$

For the ON-state of the heat switch, the thermal conductivity of the gas shall be as high as possible. Thus, this equation can be used in order to determine the best candidates for the working fluid inside the heat switch gap. From equation (5.3-9), it is clear that a gas with a minimal molecular mass and diameter along with a high number of degrees of freedom and specific heat ratio is required.

Summarizes the approximated thermal conductivities in descending order for several of the gases that were taken into account at 300 K. All properties except for k were obtained from references [15] and [24].

Table 12: Gas thermal conductivities at 300 K

Gas	d [Å]	f	γ	M [kg/kmol]	k [W/mK]
H ₂ (Hydrogen)	2.74	5	1.408	2.016	0.1761
He (Helium)	2.18	3	1.667	4.003	0.1545
Ne (Neon)	2.59	3	1.667	20.18	0.0487
N ₂ (Nitrogen)	3.75	5	1.401	28.01	0.0250
Air	3.64	5	1.401	28.96	0.0250
CH ₄ (Methane)	4.14	5	1.320	16.04	0.0246
CO ₂ (Carbon dioxide)	3.91	4	1.288	44.01	0.0157

Consequently, the best candidates are by far Hydrogen and Helium with Neon as another option. However, because of ESTEC safety constraints, experiments with Hydrogen are not allowed in the facilities. Consequently, Hydrogen can be used only as a reference for future testing at a different facility. Only Helium and Neon will be used throughout the experiments.

After the best candidates are identified, more accurate formulations can be used in order to determine the thermal conductivity of the three gases within a certain temperature range. For monoatomic gases, such as Helium and Neon, the thermal conductivity can be estimated as [15]:

$$k = \frac{0.083228}{d^2 \Omega_k} \sqrt{\frac{T}{M}} \quad (5.3-10)$$

For polyatomic gases, such as Hydrogen, a variation of equation (5.3-3) can be used to estimate the thermal conductivity:

$$k = \frac{9\gamma - 5}{4\gamma} \mu C_p \quad (5.3-11)$$

The dynamic viscosity is predicted as follows [15]:

$$\mu = 2.6693 \cdot 10^{-6} \frac{\sqrt{M \cdot T}}{\sigma^2 \Omega_\mu} \quad (5.3-12)$$

The dynamic viscosity is in Pa·s, the thermal conductivity in W/m·K, the molecular diameter in Å. Ω_μ and Ω_k are collision integrals for the viscosity and thermal conductivity obtained from Table 27 and Table 28 in Appendix A. The equations are derived using the Lennard-Jones intermolecular potential. The obtained results at 300 K were almost identical with tabulated data for Helium and Neon, with a deviation of less than 1%. In the case of Hydrogen, the thermal conductivity was under-predicted by 5%, which was expected according to reference [26]. Appendix D includes graphical data of the experimental values for the thermal conductivity, density and heat capacity of the gases with respect to temperature.

5.3.2 Free molecular regime thermal conductivity

In the free molecular regime, the thermal conductivity of a gas can be estimated using equation (5.3-13) [24].

$$k_{FM} = \frac{P \left(C_{v,m} + \frac{R}{2} \right)}{\frac{1}{\beta_1} + \frac{1}{\beta_2} - 1} \frac{1}{\sqrt{2\pi MRT'}} \quad (5.3-13)$$

$C_{v,m}$ is the molar heat capacity of the gas at constant volume, β_1, β_2 are the accommodation coefficients of the surfaces. T' is defined as [27]:

$$\frac{1}{\sqrt{T'}} = \frac{1}{2} \left(\frac{1}{\sqrt{T_1'}} + \frac{1}{\sqrt{T_2'}} \right) \quad (5.3-14)$$

$$T_1' = \frac{\beta_1 T_1 + \beta_2 (1 - \beta_1) T_2}{\beta_1 + \beta_2 - \beta_1 \beta_2} \quad (5.3-15)$$

$$T_2' = \frac{\beta_2 T_2 + \beta_1 (1 - \beta_2) T_1}{\beta_1 + \beta_2 - \beta_1 \beta_2} \quad (5.3-16)$$

The accommodation coefficient is a physical quantity that varies between 0 and 1 and characterizes the behavior of gas molecules colliding with a solid body. It is dependent on the surface and the composition of the gas [28]. The accommodation coefficient for the gases can be estimated using the following experimental correlation [29]:

$$\beta = \left\{ \left(\frac{M_g^*}{C_1 + M_g^*} \right) e \left[c_0 \left(\frac{T_s - T_0}{T_0} \right) \right] \right\} + \left\{ \frac{2.4\mu}{(1 + \mu)^2} \cdot \left[1 - e \left[c_0 \left(\frac{T_s - T_0}{T_0} \right) \right] \right] \right\} \quad (5.3-17)$$

$C_0 = -0.57$, $C_1 = 6.8$, $T_0 = 273 \text{ K}$, T_s is the surface temperature, $M_g^* = M_g$ for monoatomic gases and $M_g^* = 1.4M_g$ for diatomic or polyatomic gases, where M_g is the gas molecular mass. $\mu = \frac{M_g}{M_s}$ is the ratio of the molecular mass of the gas to the molecular mass of the solid.

In this case we could assume $T_s = T'$ from equation (5.3-14). Additionally, because Ti-6Al-4V and Inconel 718® are alloys, a weighted average of their molecular masses of the constituent molecules was used. For their chemical composition, please refer to Appendix F. Table 13 summarizes the obtained results for the accommodation coefficient of three gases with the two alloys, when $T_1 = 293 \text{ K}$ and $T_2 = 318 \text{ K}$. This gradient is an initial estimation for the OFF-case at a baseplate temperature of 20°C .

Table 13: Gases accommodation coefficients

Gas	Ti-6Al-4V	Inconel 718®
Hydrogen	0.280	0.279
Helium	0.358	0.237
Neon	0.732	0.349

5.3.3 Transition regime thermal conductivity

The thermal conductivity of a monoatomic gas in the transition regime can be modeled using the temperature jump approximation according to [28]:

$$k_{Tr} = k_{FM} \left(1 + \frac{4}{15} \frac{B}{Kn} \frac{\beta_1 \beta_2}{\beta_1 + \beta_2 - \beta_1 \beta_2} \right)^{-1} \quad (5.3-18)$$

$B = 1.0$ for monoatomic gases, $B = 45/38$ for polyatomic gases.

Figure 23 provides a plot of the thermal conductivity of Helium, Neon and Hydrogen across the transition regime. Below 0.1 mbar, the thermal conductivity is in the order of 10^{-4} W/m·K and consequently the conduction through the gas is insignificant. Helium reaches a plateau at a pressure of around 1000 mbar, Neon around 200 mbar and Hydrogen around 700 mbar.

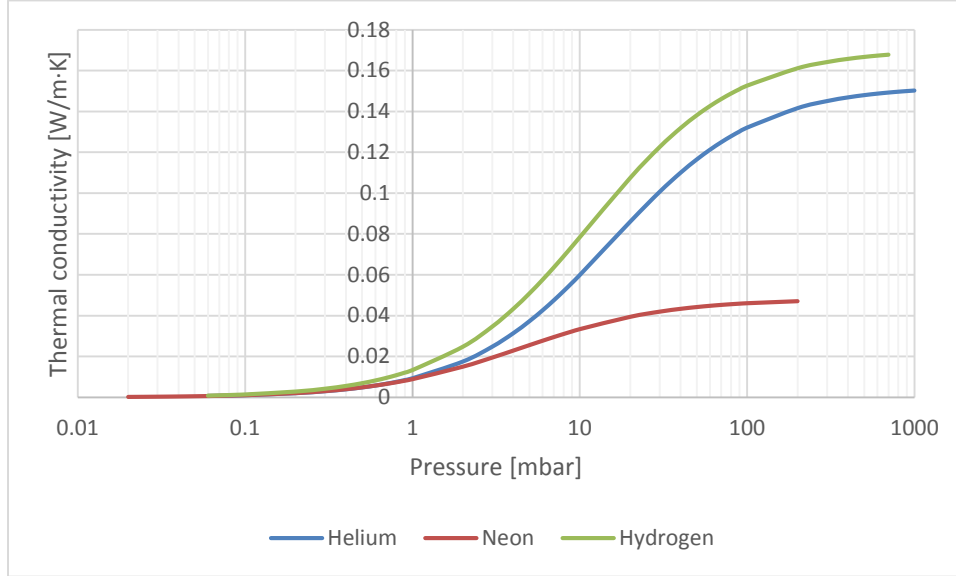


Figure 23: Gas thermal conductivity in the transition regime

Normally, a slight jump in the thermal conductivity of a gas is observed at the continuum regime boundary. Such a jump can be seen in Figure 22. This jump explains the slightly smaller value of the estimated thermal conductivity at the continuum regime boundary compared to the experimental values in the continuum regime.

5.3.4 Regime pressure limits

The pressure that corresponds to the entry in the continuum regime and the free molecular regime had to be determined for all the gases in preparation of the test procedure. Combining

equations (5.3-2) and (5.3-1) and applying the nominal regime limits, the respective pressure can be obtained. For pairs of fluid particle and solid surface with small accommodation coefficients, such as Helium with Titanium, the transition to the continuum regime occurs at a smaller Knudsen number, i.e. at a higher pressure [24]. Figure 24 provides a correlation between the accommodation coefficient and the Knudsen number for the different regimes.

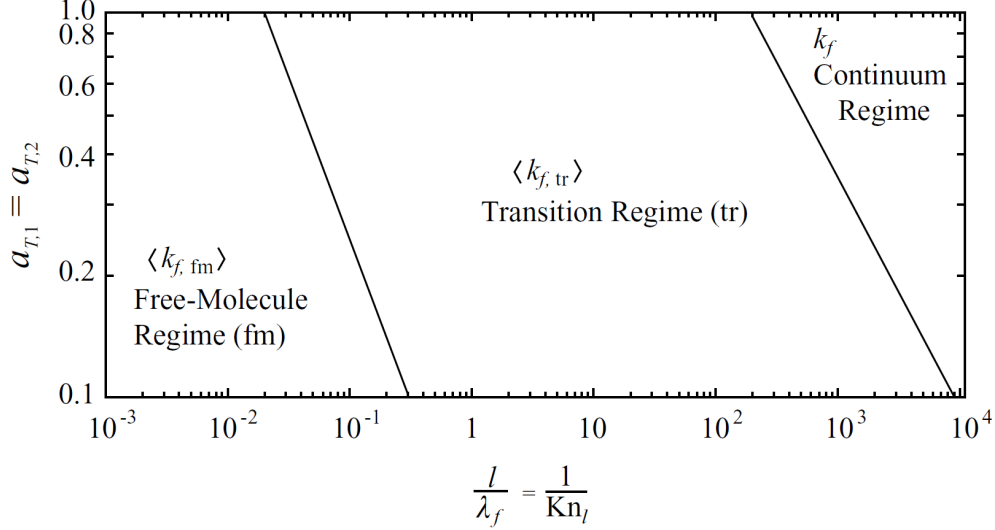


Figure 24: Classification of free-molecular, transition, and continuum regimes for heat conduction across a gas confined between parallel plates [24]

Table 14 summarizes the estimated pressure limits for Hydrogen, Helium and Neon at 20°C for the characteristic length of 0.2 mm.

Table 14: Regime pressure limits

Regime	H ₂		He		Ne	
	Kn	P [mbar]	Kn	P [mbar]	Kn	P [mbar]
Molecular	>12.50	<0.0485	>16.67	<0.0575	>50	<0.0136
Continuum	<9.091E-04	>667	<1.0E-03	>958	<5.0E-03	>136

5.4 Convective heat transfer

In addition to the conduction through the gas, the free convection effects needed to be evaluated. The natural convection heat transfer mechanism relies on buoyancy forces. Consequently, in the absence of gravity no convection occurs. However, since this is a ground test, the extent of the convection effects have to be determined.

The natural convection coefficient h is estimated using Rayleigh and Nusselt numbers. Rayleigh number is the product of the Prandtl number and the Grashof number. Grashof number expresses the relationship between buoyancy and viscosity within a fluid. For free convection inside enclosures, the Rayleigh number is determined as [6]:

$$Ra_L = \frac{g\beta(T_1 - T_2)L_c^3}{\nu^2} Pr \quad (5.4-1)$$

g is the gravitational acceleration, β is the coefficient of volume expansion ($1/T$ for ideal gases), L_c is the distance between the hot and cold surfaces and ν is the kinematic viscosity of the fluid. All the fluid properties are evaluated at the average surface temperature $\bar{T} = \frac{T_1 + T_2}{2}$.

In an enclosure, a fluid behaves like a fluid whose thermal conductivity is $k \cdot Nu$ as a results of convection currents. This value is defined as the effective thermal conductivity [6]:

$$k_{eff} = k \cdot Nu \quad (5.4-2)$$

$$Nu = \frac{hL}{k} \quad (5.4-3)$$

When the hotter plate is at the top, as shown in Figure 25a, no convection currents develop in the enclosure, since the lighter fluid is always on top of the heavier fluid. Consequently, the heat transfer occurs only by conduction and $Nu = 1$. Thus, the effective thermal conductivity becomes the thermal conductivity of the fluid [6]. This is the case for the heat transfer between faces 1-2 and 5-6 in Figure 131 and Figure 132 of Appendix E.

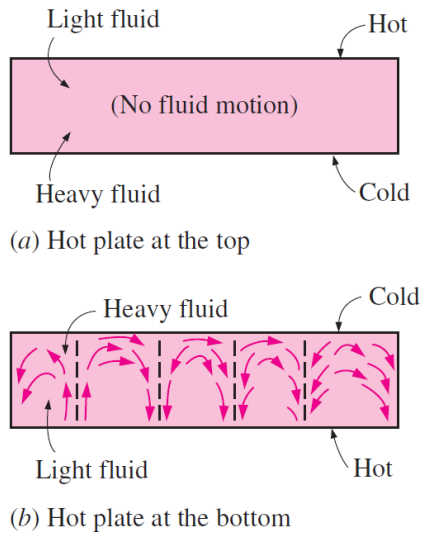


Figure 25: Convective currents in a horizontal enclosure [6]

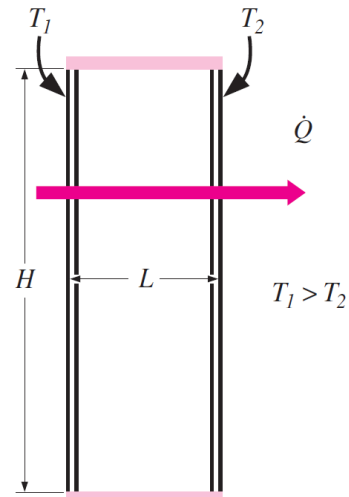


Figure 26: A vertical rectangular enclosure with isothermal surfaces [6]

However, this is not the case for the vertical plate configuration of faces 3-4. In this case the natural convection coefficient can be approximated using correlations of the Nusselt number with the Rayleigh number for vertical rectangular enclosures [6].

$$Nu = 0.22 \left(\frac{Pr}{0.2 + Pr} Ra_L \right)^{0.28} \left(\frac{H}{L} \right)^{-0.25} \quad (5.4-4)$$

This correlation is valid for any Prandtl number, $2 < \frac{H}{L} < 10$, and $Ra_L < 10^{10}$. Assuming $T_1 = 295 \text{ K}$ and $T_2 = 285 \text{ K}$ and taking the Helium properties at $\bar{T} = 290 \text{ K}$ and a pressure of 2 bar, $k = 0.1524 \text{ W/m} \cdot \text{K}$, $\nu = 5.872 \cdot 10^{-5} \text{ m}^2/\text{s}$, $C_p = 5193 \text{ J/kg} \cdot \text{K}$, $Pr = 0.6635$. For the given characteristic length of 0.2 mm, this results in $Ra_L = 5.2 \cdot 10^{-4}$. For the second and third prototype $\left(\frac{H}{L}\right)_{2nd} = 8$ and $\left(\frac{H}{L}\right)_{3rd} = 3$ respectively, we obtain $(Nu)_{2nd} = 0.015$ and $(Nu)_{3rd} = 0.019$. These values are below the minimum value of 1 for the Nusselt number. Consequently, no convection occurs in this case either. The order of magnitude does not change with

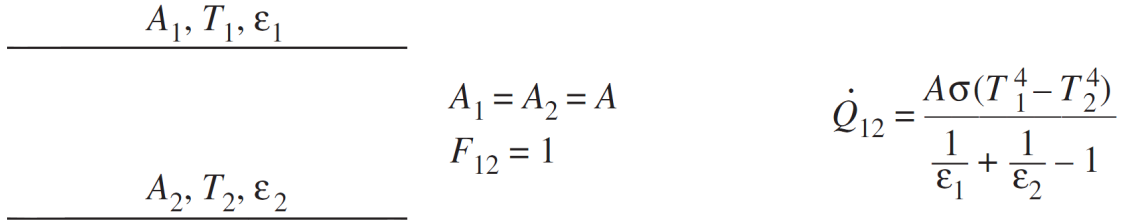
temperature, pressure and gas. Therefore, it is safe to assume that convection does not occur in any case.

5.5 Radiative heat transfer

The effects of radiative heat transfer through the gap needed to be evaluated. In the thermal model, a hemispherical emissivity of 0.57 and 0.48 was used for the second and third prototype respectively. For more information on the origin of these values, please refer to section 6.1.

5.5.1 Radiative coupling through gap

A simplification of the system would be to consider the gap to consist of infinitely long parallel plates. This is because the length of the fins is two to three orders of magnitude larger than the gap. In this case the view factor between the plates is 1 and the radiative heat transfer can be estimated according to the configuration shown in Figure 27.



$$\begin{array}{c} \text{---} A_1, T_1, \varepsilon_1 \text{---} \\ \\ A_2, T_2, \varepsilon_2 \text{---} \end{array} \quad \begin{array}{l} A_1 = A_2 = A \\ F_{12} = 1 \end{array} \quad \dot{Q}_{12} = \frac{A\sigma(T_1^4 - T_2^4)}{\frac{1}{\varepsilon_1} + \frac{1}{\varepsilon_2} - 1}$$

Figure 27: Infinitely large parallel plates radiation heat exchange [6]

The effective emissivity is expressed by the equation:

$$\varepsilon_{eff} = \frac{1}{\frac{1}{\varepsilon_1} + \frac{1}{\varepsilon_2} - 1} \quad (5.5-1)$$

The effective emissivity for the second prototype is 0.3986. The second prototype has a total internal gap area of 0.044 m². With an emissivity of 0.57, the radiative conductance is:

$$G_{rad} = \varepsilon_{eff} \cdot A = 0.01754 \text{ m}^2$$

For a more detailed analysis, the two parallel strip configuration from Appendix E can be used in order to calculate the view factors for one fin. The resulting radiative conductance per fin is $1.1522 \cdot 10^{-4} \text{ m}^2$. When multiplied with the total number of fins, the total radiative conductance of the switch is 0.01279 m². This results in a difference of 37.1%.

Using the infinitely long parallel plates assumption, the third prototype has an effective emissivity of 0.3158 and a total internal gap area of 0.0930 m². In this case, the radiative conductance is:

$$G_{rad} = \varepsilon_{eff} \cdot A = 0.02937 \text{ m}^2$$

The analytical view factor approach, similar to the second prototype results in a radiative conductance per fin of $1.0090 \cdot 10^{-4} \text{ m}^2$. When multiplied with the total number of fins, the total

radiative resistance of the switch is 0.02230 m^2 , which represents a 31.7% difference with the infinitely large parallel plate configuration.

Because of the large number of elements in the FEM, calculating the actual view factors for all fins would be computationally very expensive. Consequently, the effective emissivity can be adjusted in order to obtain the same radiative conductance. A dummy case was generated using only two fins per side to reduce the computational time. A detailed radiation enclosure was generated, using the Monte Carlo method by firing 5000 rays per element. The results of this simulation were used to derive a simplified radiative model. Through an iterative process the effective emissivity of the gap radiation was adjusted. Eventually, an effective emissivity of 0.318 for the second prototype and 0.263 for the third prototype resulted in deviations of temperature and radiative heat fluxes of less than 1% when compared to the Monte Carlo method. The resulting total radiative conductance is 0.01399 m^2 and 0.02446 m^2 for the second and third prototype respectively. The difference with the analytical view factor approach can be attributed to the reflections on the surfaces, which were not taken into account in the latter. Additionally, in the GMM the fins are discretized into smaller surfaces providing higher accuracy.

5.5.2 Gas radiation

For transparent media, the radiation that propagates through them remains unchanged. Though, certain gases absorb and emit radiation in various wavelength spectra, the absorption bands. This concept is used in spectroscopy in order to identify the gases present in a planet's atmosphere. The emissivity of the gases is a function of the temperature, the partial and total pressure, as well as the thickness of the gas. Gases that exhibit such behavior are CO, NO, CO₂, SO₂ and water [7]. Among these gases, only CO₂ had been taken into account as a potential candidate for the heat switch, but it was discarded due to its low thermal conductivity. Hydrogen and noble gases do not exhibit gas radiation properties and therefore no further analysis was required on this topic.

5.6 Summary

The main thermal concepts behind the function of the heat switch are the conductive heat transfer through the solid material, the gaseous heat transfer with respect to pressure and temperature and the radiative heat transfer between the hot and cold side of the heat switch. Reduced thermal models and FEM were produced to simulate the behavior of the switch based on these concepts. Convective heat transfer and gas radiation were also investigated. Though their effect on the behavior of the heat switch was proved to be of no importance and thus, no further attention is paid to them.

6 Part inspection

Before proceeding with testing, an inspection of the second and third prototype was necessary. It should be reminded that the first prototype was not of interest in this thesis work, since the second and third prototype were of significantly superior performance and offered an improved design.

6.1 Emissivity measurements

A TEMP 2000A emissometer was used to measure the normal emissivity of the external surface of the second and the third prototype. Because of the heat switch geometry it is impossible to directly measure the emissivity of the internal surfaces. It should be noted that the external surfaces had been subjected to wire EDM and grinding, processes that have an impact on the surface emissivity. The emissometer measured a normal emittance of 0.57 and 0.32 for the second and third prototype respectively. The difference in the emissivity between the two prototypes is attributed to the fact that different manufacturers produced the prototypes. The measurements were performed by taking multiple samples on several locations on both sides of the prototypes. The measurements were consistent and deviated only in the third decimal. The margin of error for the measurement is ± 0.05 for the normal emittance. Figure 129 in Appendix E provides conversion curves from normal to hemispherical emissivity. Based on these curves, the hemispherical emissivity is 0.57 and 0.34 for the second and third prototype respectively. It should be noted that the measurements were conducted at room temperature. For metals, emissivity increases with increasing temperature, but significant changes typically occur at temperatures exceeding 100°C. Because of the small temperature range of testing, the emissivity is considered constant. For the third prototype, eventually an emissivity value of 0.48 was used for the internal radiation based on sample testing documentation provided by the manufacturer for samples that have not been subjected to any post-processing.

6.2 Visual inspection

A simple visual inspection was conducted for the manufactured second prototype in order to assess its deviation from the CAD model. This inspection provides essential information for the proper mounting of the prototype. Similarly, the third prototype, which was manufactured during the course of this thesis work, was subjected to visual inspection throughout its different manufacturing iterations. These inspections were necessary in order to take the requisite actions so as to be able to produce a part that respects the needed manufacturing tolerances.

6.2.1 Second prototype visual inspection

The second prototype had been manufactured prior to the start of this thesis. It exhibited some manufacturing problems, which in turn led to assembly and performance issues. More specifically, the second prototype had buckled leading to an arc shape. In principal, the switch needs to be as flat as possible in order to optimize the thermal contact. The deformity of the second prototype can be seen in Figure 28.

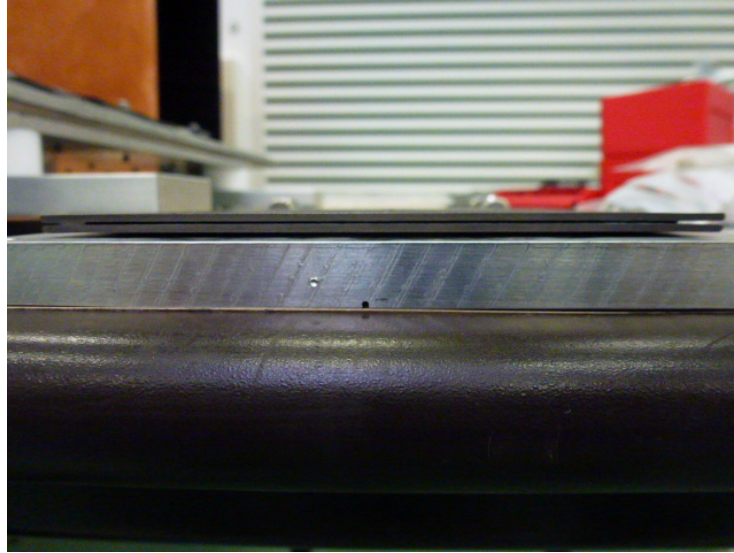


Figure 28: Front view of second prototype

From the picture it is clear that the heat switch is not flush with aluminium plates as required and consequently a significant torque is necessary to flatten it. High torques can damage the part. The main concern is that some support pillars can crack if they are not already cracked due to the buckling and that the fins can deform. Figure 29 and Figure 30 show the gap profile before and after applying a $1 \text{ N}\cdot\text{m}$ torque on another specimen. This specimen has a more severe deformity than the actual second prototype and was cut in half for inspection. As can be seen from the pictures, after applying a relatively small torque, the fins deform, reducing the gap distance. It is also possible that the fins are touching. Thus, the performance of the switch can be gravely degraded especially in the OFF-case.

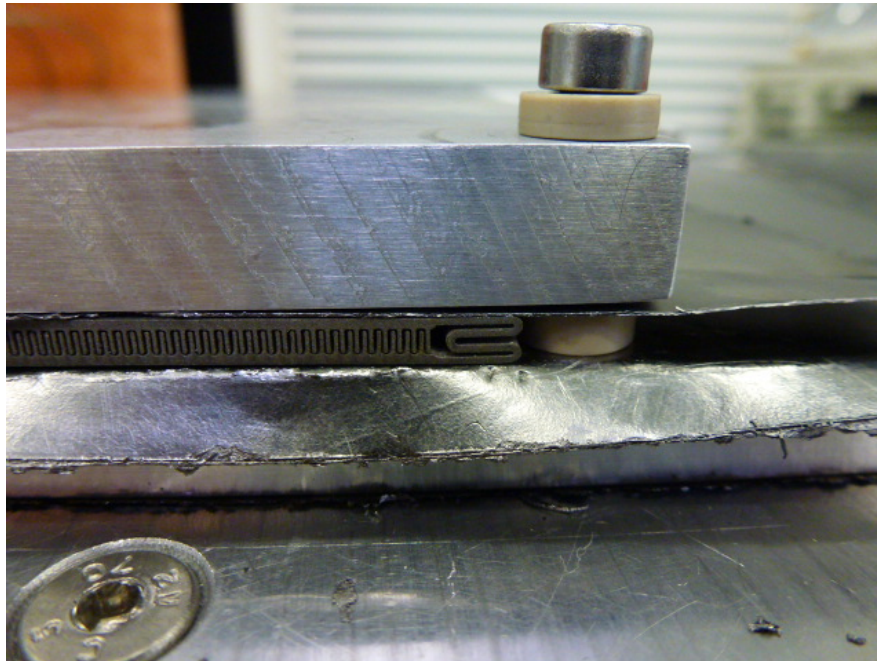


Figure 29: Test assembly with no applied torque

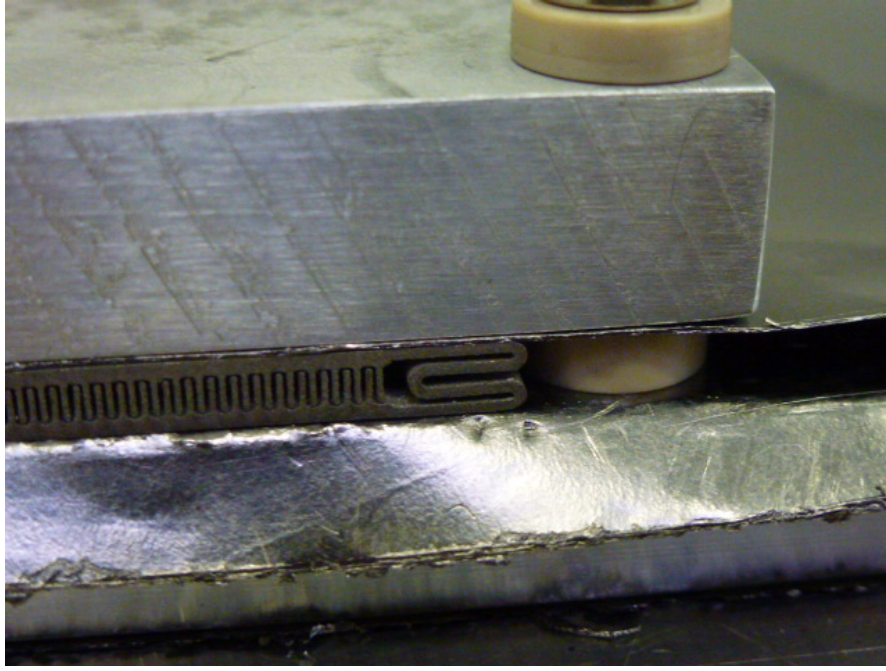


Figure 30: Test assembly with a $1\text{ N}\cdot\text{m}$ torque

6.2.2 Third prototype visual inspection

The third prototype was manufactured during the course of this thesis. During manufacturing of the third prototype, several problems and challenges arose due to its intricate geometry. Four iterations were required in order to manufacture the part. The first iteration experienced buckling of the large top and bottom plates as can be seen in Figure 31. To prevent buckling, extra vertical stiffeners were added (Figure 32). These stiffeners, as well as the build-plate are eventually removed from the part.

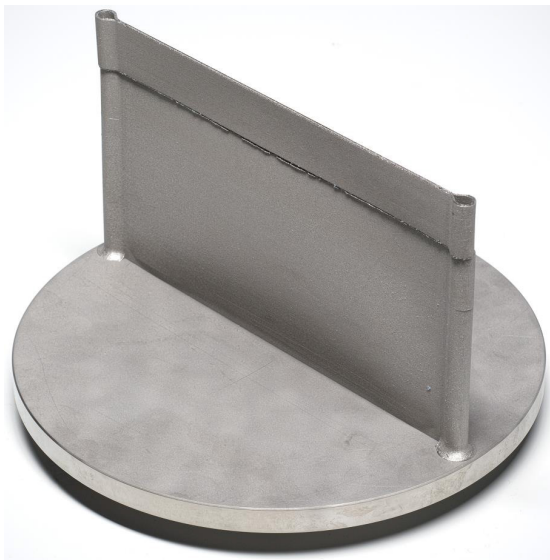


Figure 31: Buckling of iteration 1

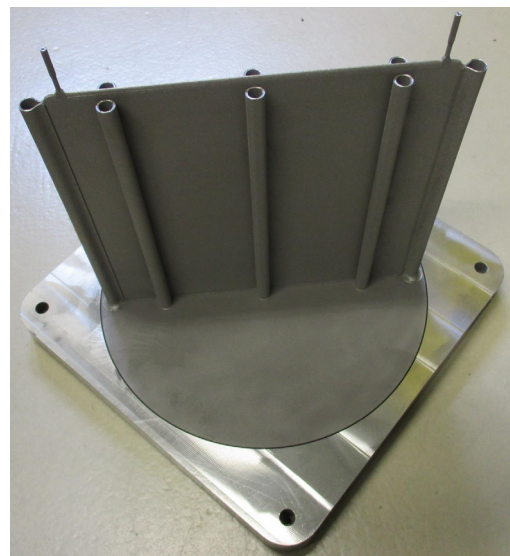


Figure 32: Added stiffeners to prevent buckling

Though, the second iteration also failed, as the build plate was detached due to significantly high residual stresses and bad connection to the substrate plate. Proceeding to the third iteration, the manufacturer raised concerns over the integrity of the support pillars, since they

are thin, overhanging structures. The pillars are critical because they provide structural support so that the switch does not fail in compression or over-pressurization. Eventually, the third iteration was successfully printed and the powder was removed without problems. However, the heat switch buckled during the stress relief process as can be seen below.

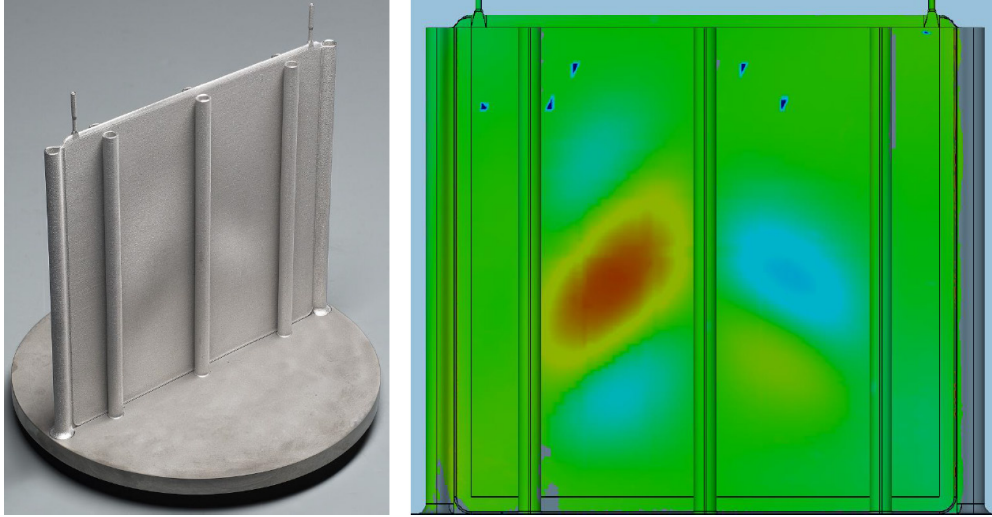


Figure 33: Buckling of iteration 3

This failure can be attributed to the high bending moments in the center of the plate. Following the failure of the third iteration it was certain that the local stiffness at the locations of failure should be enhanced. To do so, a lattice structure was eventually preferred, as illustrated in Figure 34. For the same reasons, it was also mutually agreed between ESA and the manufacturer to enlarge the cross-sectional area of the support pillars before proceeding with the manufacturing of the fourth iteration. It is possible that some of the pillars have cracked in the third iteration, reducing the stiffness. It should be noted that an increase in the pillars cross-sectional area leads to an undesired increase in the OFF-conductance. Eventually, a negotiated increase of 76.35% was agreed for the cross-sectional area. Updating the FEM of the switch resulted in an increase of the OFF-conductance by 16.0%. This increase reduces the performance of the switch. Though, according to the early straw-man concept model, this leads to an increase of the heating power by only 8.1%, which is deemed acceptable.

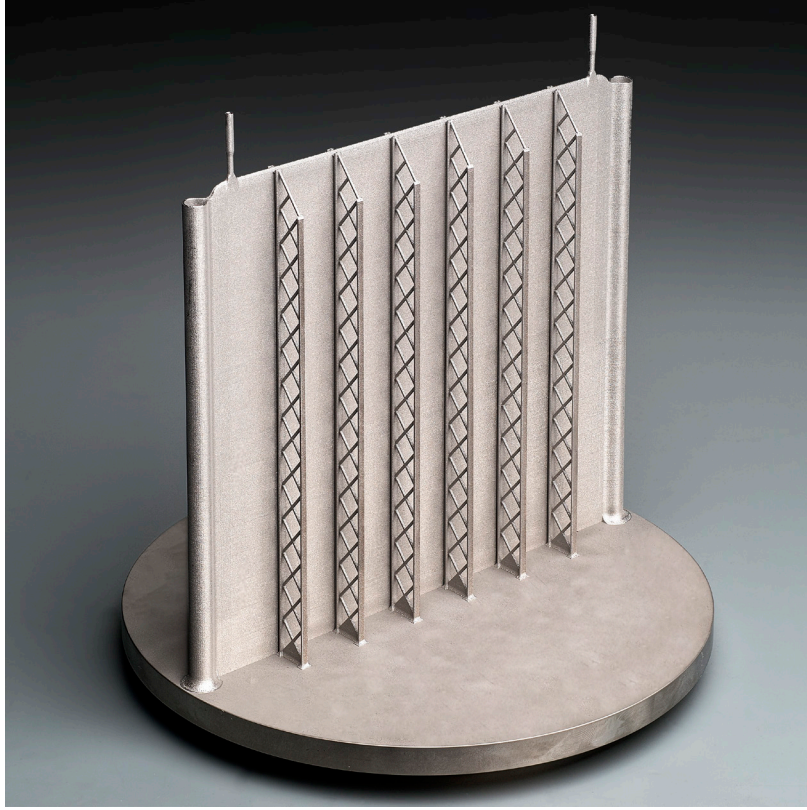


Figure 34: Iteration 4 - lattice structure for additional stiffness

6.3 CT scan inspection

Both the second and the third prototype were inspected using a CT scan prior to testing. The results were very interesting and provided essential information for the proper mounting of the test setup and for the interpretation of the experimental results.

6.3.1 Second prototype CT scan

The second prototype has a nominal effective area of $100 \times 100 \text{ mm}^2$ and a thickness of 3.2 mm. The CT scan showed significant inconsistencies for the thickness and flatness of the switch as can be seen in Figure 35. Comparison of Figure 36 and Figure 37 shows a substantial disparity of the size of the gaps from 0.27 mm to 0.54 mm. The nominal size of the gap is 0.2 mm.

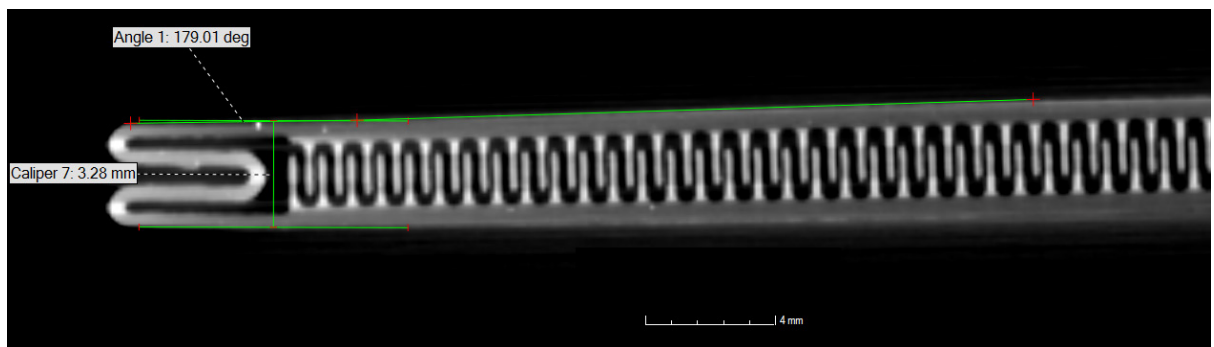


Figure 35: Second prototype thickness and flatness deviation

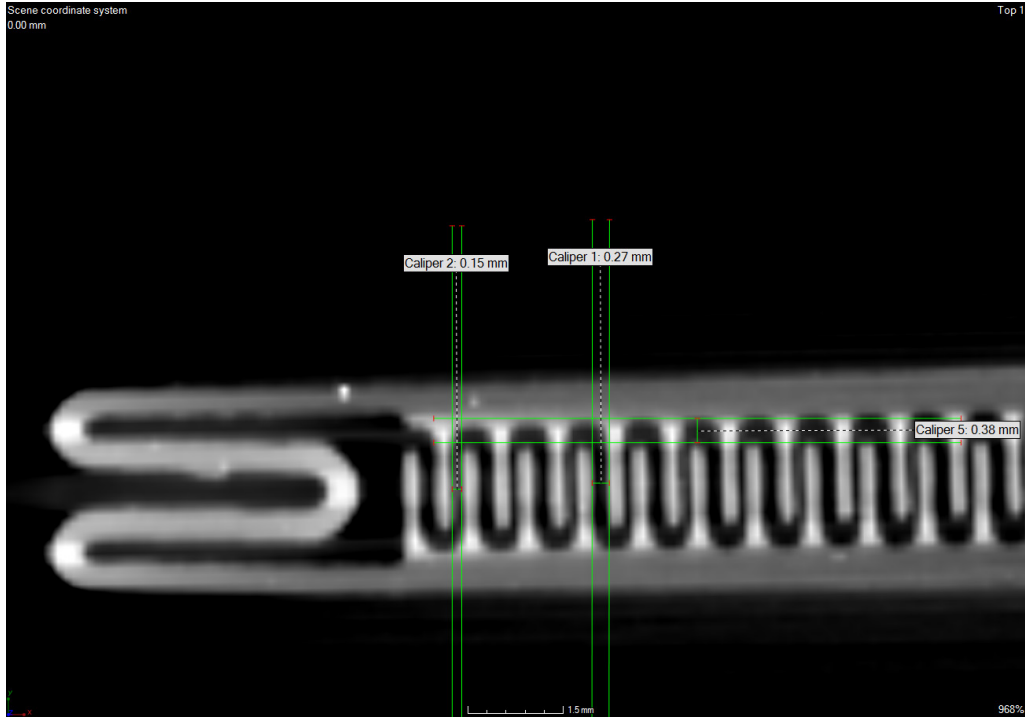


Figure 36: Second prototype gap size (edge)

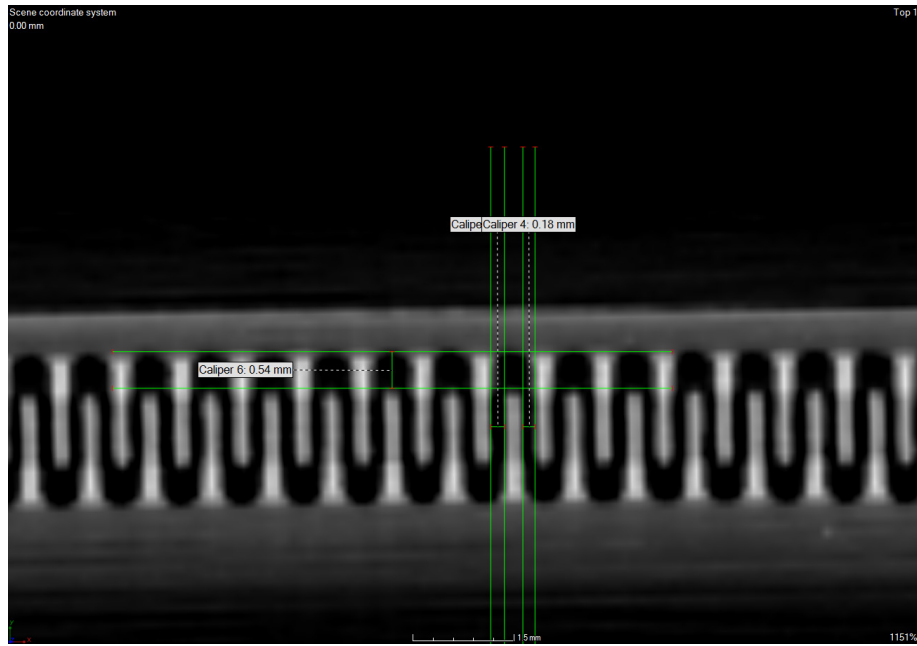


Figure 37: Second prototype gap size (middle)

In Figure 38, the top view of the support pillars of the second prototype can be seen. The side views of a pillar in Figure 39 show that it has cracked. The crack appears to be at a 45 degree angle, which is typical of brittle materials. One-by-one inspection of the pillars showed that all of them have cracked. The most plausible explanation for the cracks is the residual thermal stresses that eventually led to the buckling of the switch. The increased gap distance between the two sides resulted in tensile stresses exceeding the ultimate tensile strength of the material. For a gap of 0.54 mm as shown above, the strain is:

$$\varepsilon = \frac{0.54 - 0.2}{0.2} = 1.7 \frac{mm}{mm}$$

Which, assuming elastic deformation, leads to a tensile stress of:

$$\sigma = \varepsilon \cdot E = 1.7 \cdot 121 = 205.7 \text{ GPa}$$

The UTS of Ti-6Al-4V is 860 MPa and consequently it is certain that this large deformity of the gap distance has led to the pillar cracking.

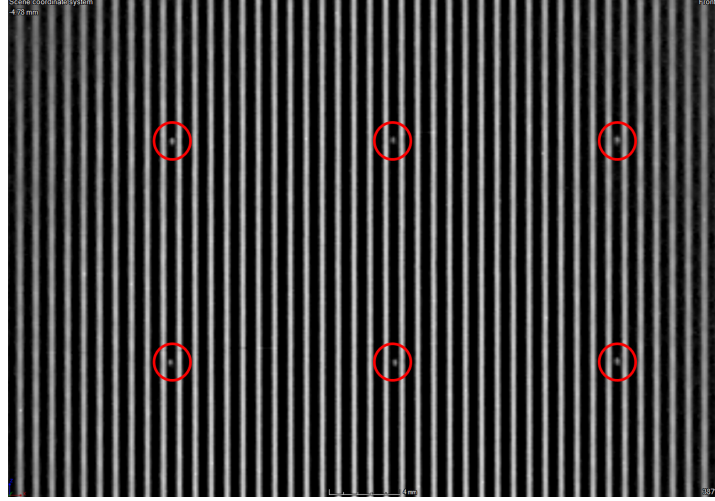


Figure 38: Second prototype support pillars

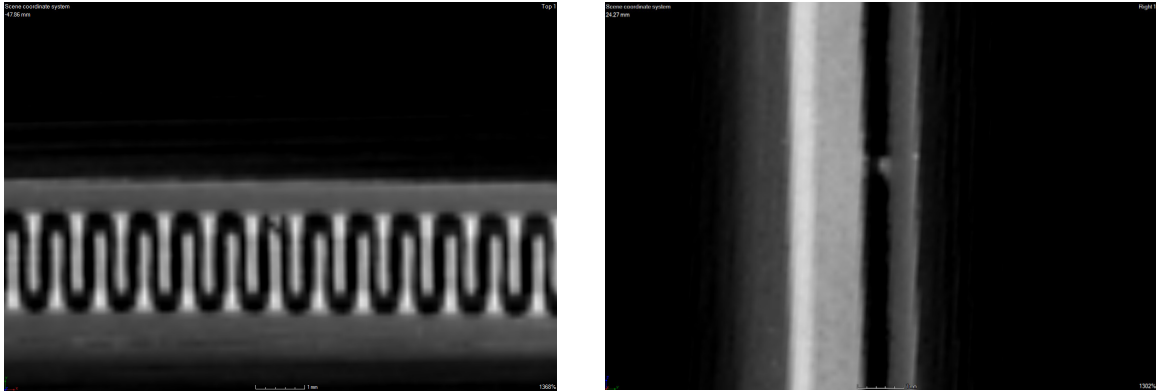


Figure 39: Side views of a cracked support pillar

Because the heat switch is manufactured using Selective Laser Melting, powder removal from the internal cavity is very critical. The CT scan did not show any clogging of the channels of the second prototype. Some powder remains near the tubes of the switch as seen in Figure 40, which should not affect the performance.

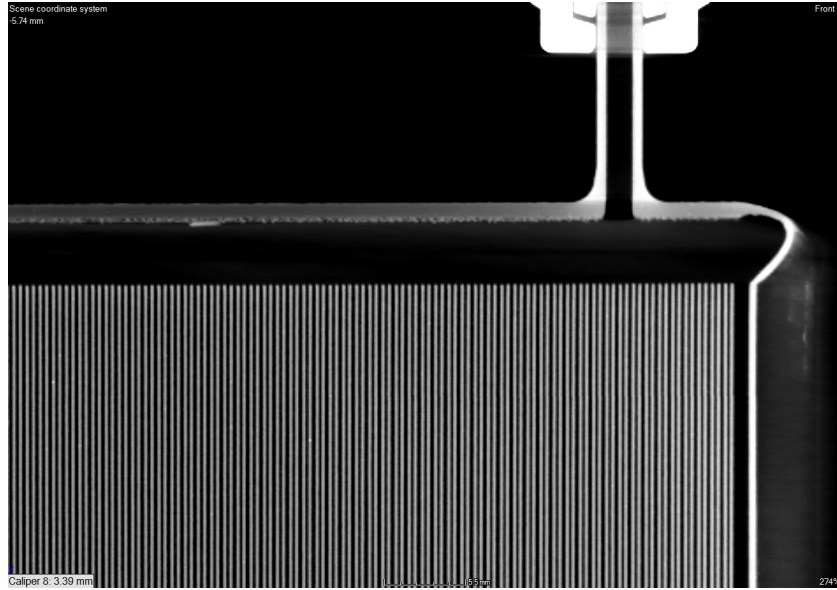


Figure 40: Remaining powder inside second prototype

6.3.2 Third prototype CT scan

Due to the larger size of the third prototype, the resolution of the scan is two times lower than the second prototype. This is because, the X-Ray gun cannot further approach the part, as seen in Figure 41. Consequently, the images are blurry and cannot be always conclusive, unless a higher resolution is used over a specific area.

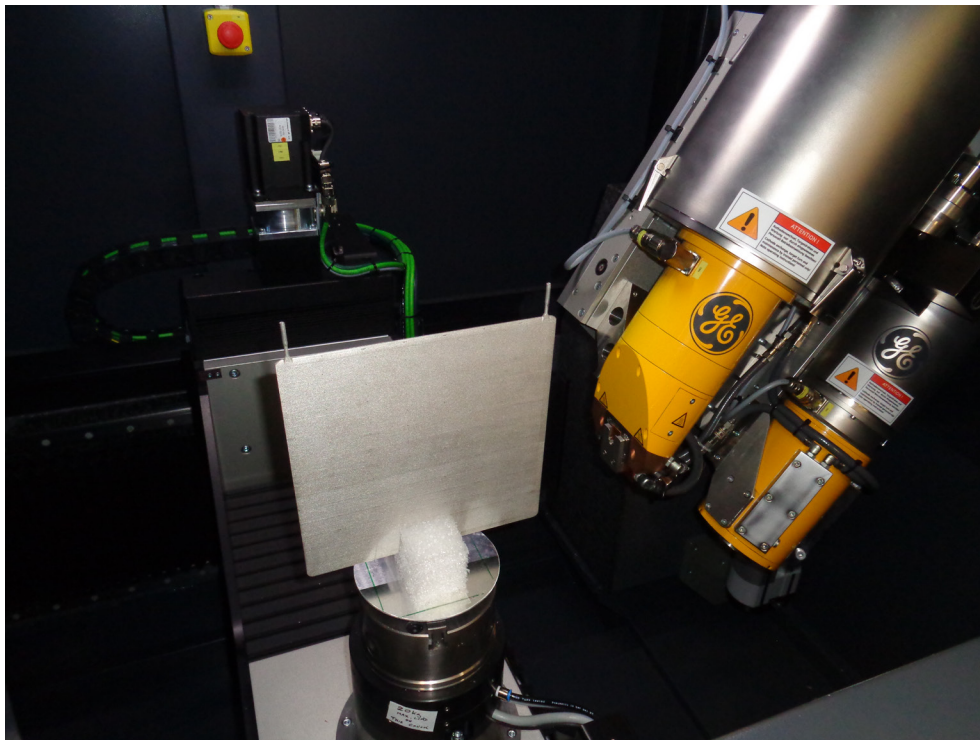


Figure 41: CT scan setup

The third prototype has a nominal effective area of $200 \times 200 \text{ mm}^2$ and a thickness of 2.2 mm. Similarly to the second prototype, the CT scan showed significant inconsistencies with respect

to thickness and flatness of the switch. The thickness from one side to the other was measured to be between 2.40 mm and as high as 2.65 mm. This significant deviation generates problems for the mounting of the switch on the test setup and is expected to create severe inconsistencies on the contact heat transfer coefficient at the interfaces.

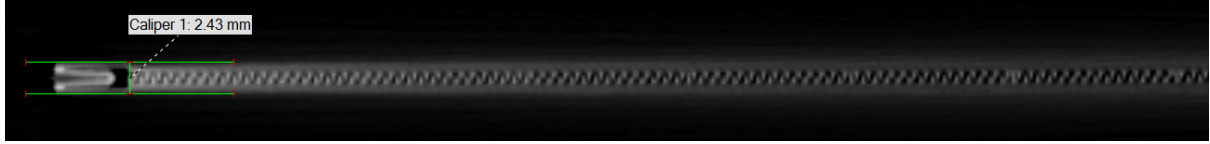


Figure 42: Third prototype cross-section

The nominal gap size of the third prototype is still 0.2 mm. However, the CT scan showed gap sizes as large as around 0.50 mm in the middle of the switch.

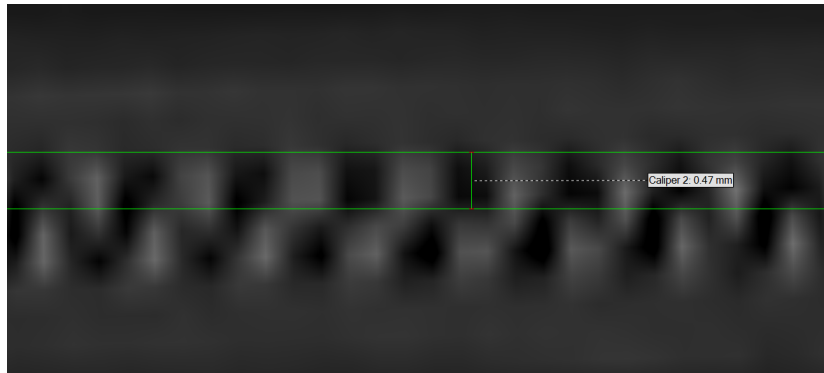


Figure 43: Third prototype gap size

With respect to the pillars, the CT scan was inconclusive, due to the low resolution. Though, with a gap size as large as 0.50 mm, the pillars are expected to have failed as well. Figure 44 shows a cross section view of the switch.

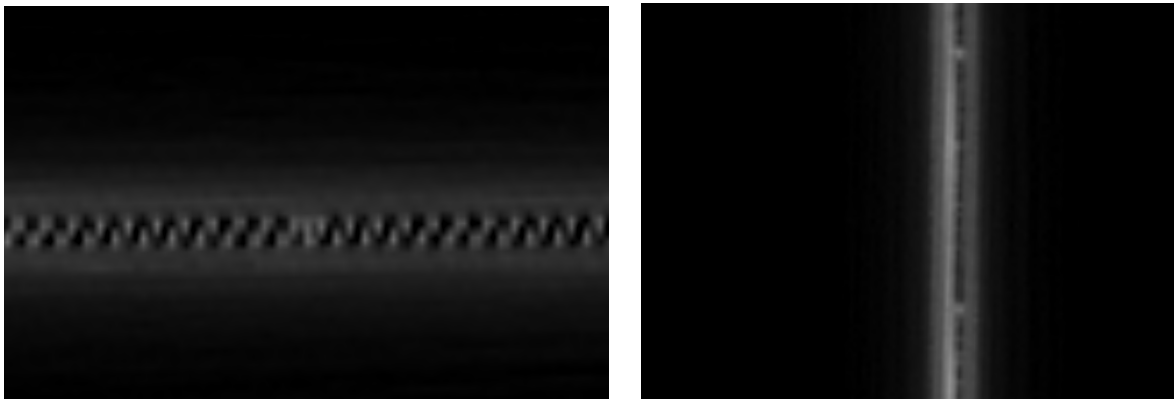


Figure 44: Third prototype pillars side views

The CT scan showed some shadows, which could be trapped water after the manufacturing post-processing or powder that could not be entirely removed from the channels.

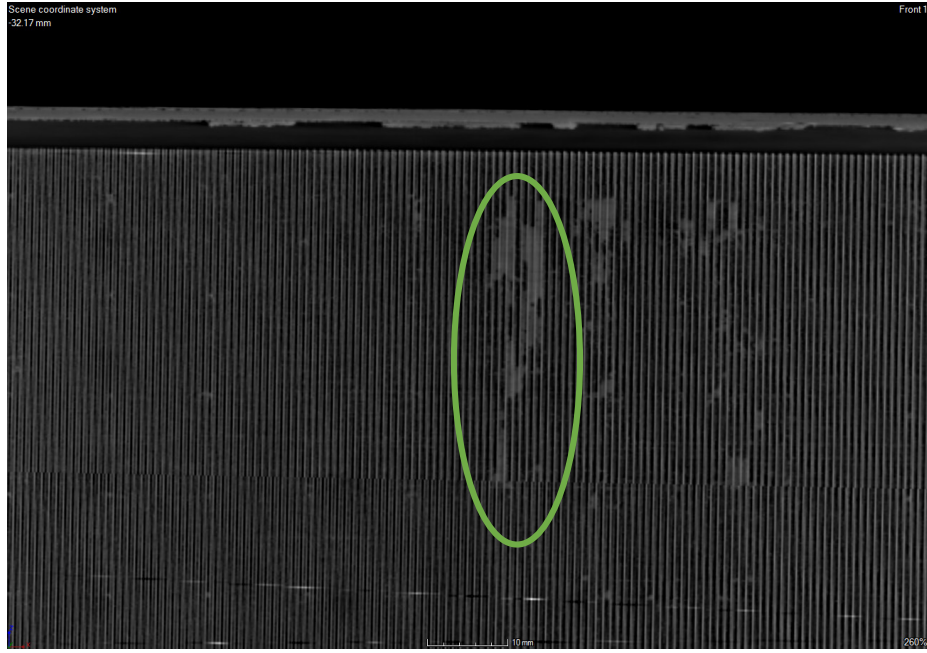


Figure 45: Third prototype channel clog



Figure 46: Third prototype channel clog cross-section

6.4 Summary

The received second and third prototypes have been subjected to thorough testing to provide essential information that could affect the experimental results and to ensure the safe conduct of the experiment. Uncertainties in the emissivity of the surfaces lead to modeling problems in the radiative heat transfer. Eventually an emissivity of 0.57 and 0.48 is assumed for the second and third prototype respectively. Furthermore, significant deviations of the produced parts were found in comparison with their CAD models, mainly due to the complexity of the geometry and the limitations of the currently available SLM technology. These deviations cannot be integrated into the thermal models, since they would add severe complexity and require immense computer resources.

7 Experimental setup

A major part of this thesis work has been dedicated to designing an experimental setup that would be representative of real-life applications. This chapter provides an overview of the test objective, test configuration, detailed information about thermal/structural modeling of the test configuration and design assumptions. Furthermore, a scale analysis is provided in order to determine the performance of the switch with an increase in size. The chapter concludes with the test procedure and stabilization criteria. The experimental results and their correlation with the thermal simulation model of the experimental configuration are provided in Chapter 8.

7.1 Test objective

The primary objective of the test is to determine the performance of the heat switch, defined by the ON and OFF conductance at different temperatures and the ON/OFF conductance ratio at the respective temperatures. The secondary objective is the verification of the TMM and FEM of the heat switch by comparing test results with test predictions and providing correlations.

7.2 Test configuration

The mounting of the heat switch has proven to be a very challenging task, since the switch does not have any interfaces to allow for efficient mating with a baseplate and a dissipating unit. Similar problems are encountered in the mounting of thermoelectric coolers (TEC). Though, in the case of thermoelectric coolers, holes can be drilled in order to mount them directly on dissipating components, as shown in Figure 47. However, this is not possible for a gas-gap heat switch, since drilling holes would compromise its structural integrity and produce gas leak. Consequently, a sandwich configuration that is clamped using preloaded bolts was considered to be the best option for obtaining both accurate measurements and mimicking real-life applications.

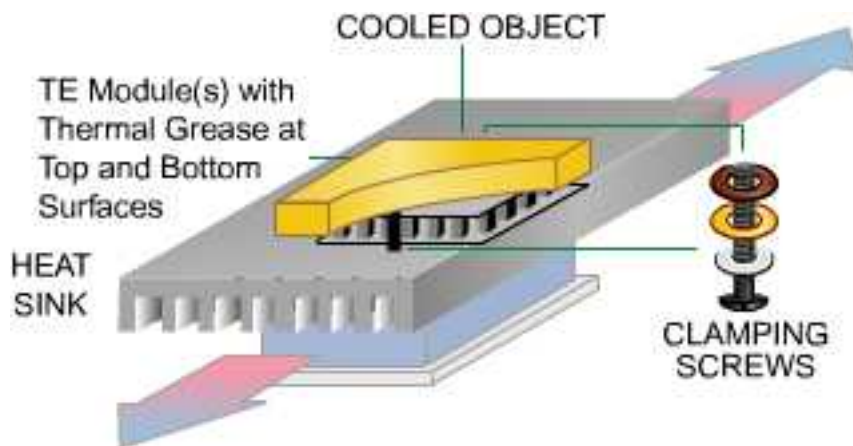


Figure 47: Thermoelectric cooler mounting scheme. (From FerroTec)

The sandwich configuration used for the test setup is illustrated in Figure 48. A cross-section of the setup is shown in Figure 49. A 50 cm x 28.5 cm aluminium baseplate, which is held at a constant temperature using liquid nitrogen, is placed inside the vacuum chamber. An aluminium plate (Plate 2) of 10 mm thickness is placed in the center of the baseplate with a thermal filler in between. The switch is placed on top of Plate 2 with a thermal filler in between. On top of the switch, another aluminium plate (Plate 1) of 10 mm thickness is placed with another thermal filler in between. In order to apply pressure and provide a good thermal contact, Plate 1 is bolted to the baseplate through Plate 2 using class A2-70, M4 bolts. A symmetrical bolt pattern is necessary in order to obtain a more uniform pressure. Because the M4 bolt pattern is perimetric, additional six M5 countersunk bolts are used on Plate 2 so as to obtain a better contact in the center. The technical drawings of the plates are included in Appendix I.

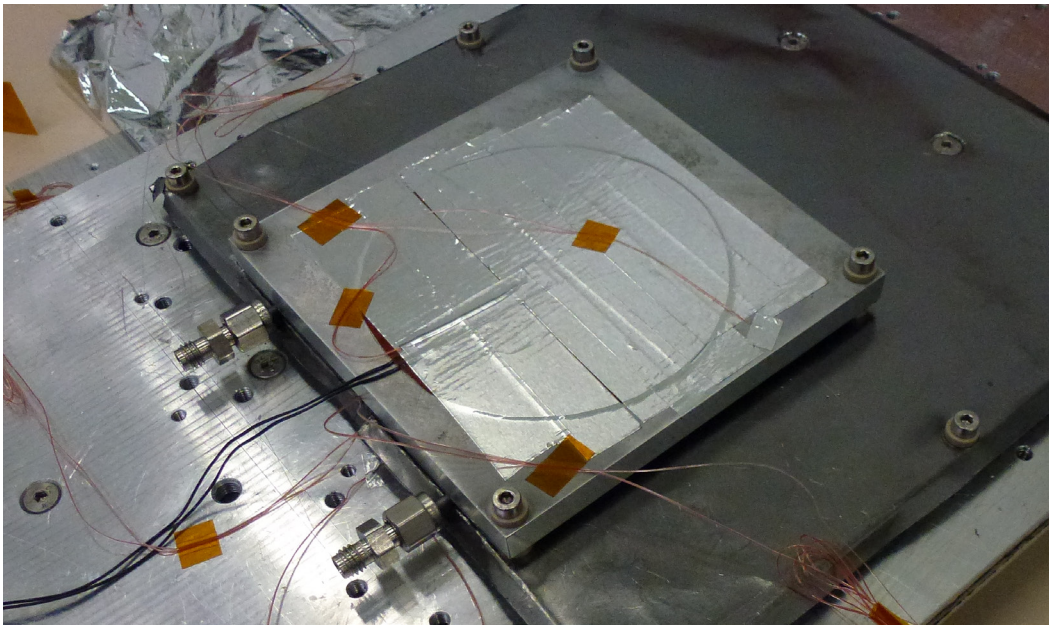


Figure 48: Test setup sandwich configuration

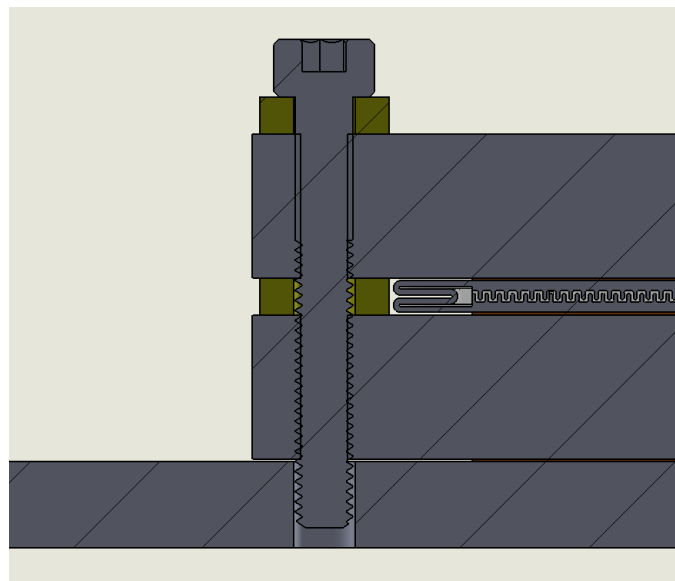


Figure 49: Test setup cross-section

Thermally insulating washers made out of PEEK are placed between the top of Plate 1 and the bolt head in order to thermally isolate the bolts. Consequently, the thermal leak to the baseplate through the bolt is minimized. Additionally, PEEK stand-offs are used for structural support and for minimization of the thermal conductance between the aluminium plates.

A 6x6 in² flexible Kapton heater with a maximum power density of 5 W/in² is placed on top of Plate 1 for the third prototype test, and a round heater with a 4-inch diameter for the second prototype. To ensure good contact and minimize losses to the environment, the heaters are covered with aluminium tape. The heater resistances were measured to be 71.7 Ohm and 226.3 Ohm respectively. The heating power can be controlled by adjusting the applied voltage on the heater according to $P = \frac{V^2}{R}$. To be able to provide sufficient electrical power, three voltage sources are placed in series. The heater is connected to the power supplies using external and internal 24-pin Deutsch connectors through a Deutsch electrical feedthrough. The applied voltage is recorded by the data acquisition system.

Type K thermocouples are used to measure the temperature at different locations. Type K is a Chromel-Alumel thermocouple and it is the most common general purpose thermocouple. Its selection was based on temperature range suitability, cost and availability. For the test setup, the thinnest possible (0.35 mm) thermocouples were required in order to fit in the groove (1 mm x 1 mm) on the aluminium plates that is dedicated to the proper placement of the thermocouples, as shown in Figure 50. Additionally, type K was preferred to Type T, Copper-Constantan thermocouples, due to their smaller internal losses and therefore more accurate measurement. This is important when long thermocouples are required. The thermocouples are connected to a Yokogawa GP20 Data Acquisition Controller via a 37-pin Deutsch connector. Two TRPs are used in the test, one at the top and one at the bottom of the switch, since these are the most critical measurements. All the information about the thermocouples, their location and their channel for the second and third prototype test is summarized in Table 15 and Table 16 respectively.

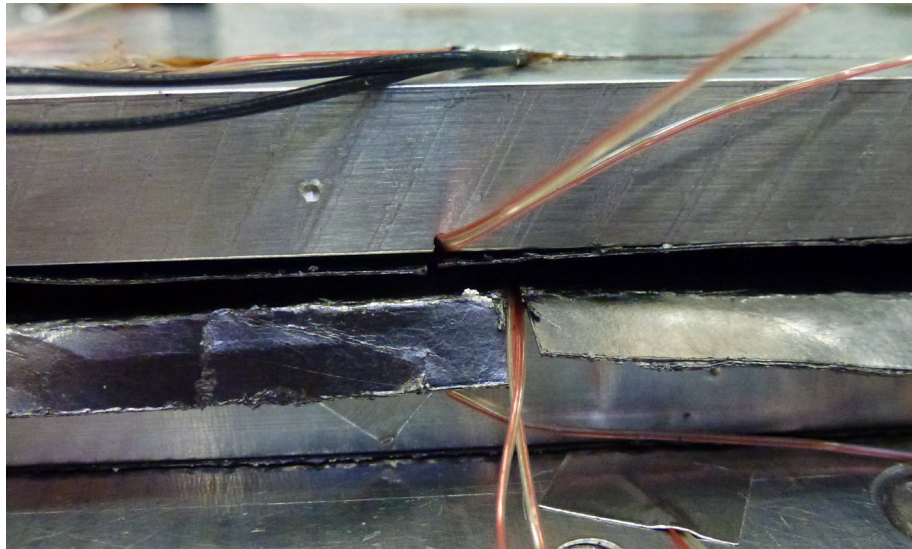


Figure 50: T/C placement through groove

Table 15: Thermocouples channel and location (2nd prototype)

T/C	Te1	Te2	Te3	Te4	Te5	Te6	Te7	Te8
Channel	1	12	3	4	5	6	7	8
Location	Plate 1 – Bottom	Baseplate	Switch – Top (center)	Switch – Bottom (center)	Switch – Bottom (edge)	Heater	Plate 1 - Top	Plate 2

Table 16: Thermocouples channel and location (3rd prototype)

T/C	Ti4	Te2	Te5	Ti2	Ti1	TH1	TH2	Ti5	Ti3	Te4	Ti8
Channel	1	3	4	6	7	8	9	10	11	12	13
Location	Plate 2 - Top	Baseplate	Baseplate	Plate 2 - edge	Switch – Top center	Plate 1 – Bottom	Plate 1 - Top	Switch – Bottom edge	Switch – Top edge	Switch – Bottom center	Heater

An MLI with 10 layers covers the test assembly as shown in Figure 51. This is to radiatively insulate the assembly from its surroundings inside the vacuum chamber. The losses through the MLI are very small because most of the radiation losses to the MLI are reflected back to the assembly. Typically a conservative radiative heat transfer coefficient of $0.014 \text{ m}^2/\text{m}^2$ and a conductive heat transfer coefficient of $0.019 \text{ W}/\text{m}^2\cdot\text{K}$ to the MLI is assumed, similar to the straw-man concept analysis. These heat transfer coefficients are two orders of magnitude smaller than the rest of the thermal couplings in the assembly and consequently have negligible effect in the simulations and testing.

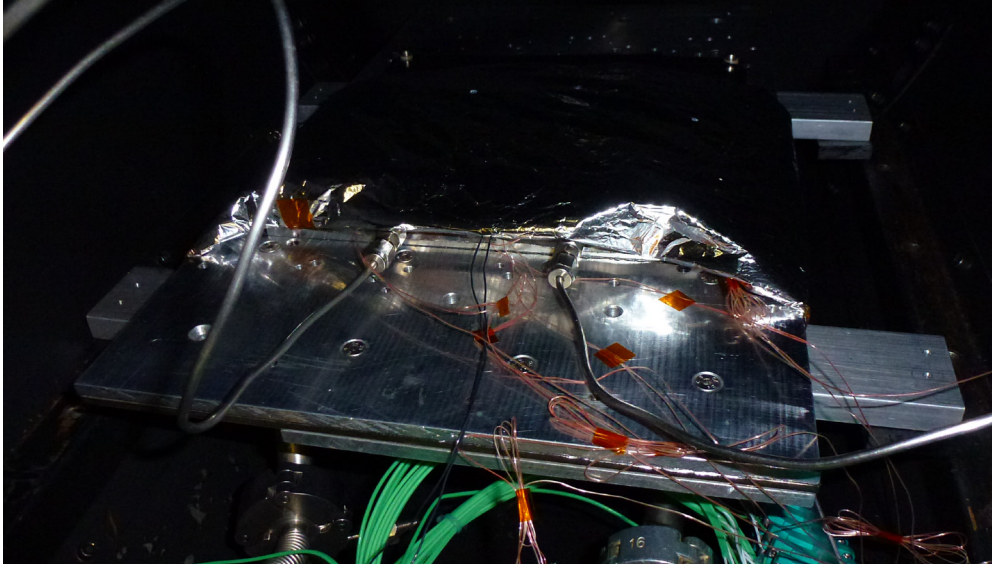


Figure 51: Heat switch covered with MLI

The vacuum chamber used for the experiment is the Little Vacuum Facility (LIVAF) of the Mechanical Systems Laboratory at ESTEC. Thermal cycling and thermal balance tests of space equipment can be performed in LIVAF. The shroud is 0.55 m in diameter and 1 m long.

The cold plate and shroud temperature range is -170°C to $+80^{\circ}\text{C}$. The vacuum limit is less than $5 \cdot 10^{-4}$ mbar.

The inlet and outlet of the switch have an outer diameter of 3.18 mm (1/8 inch) and are connected to stainless steel tubing using straight union Swagelok® fittings made of stainless steel. According to manufacturer's specification, the tubing shall be softer than the fitting. Ti-6Al-4V has a hardness of HRB 71², while SS of HRB 79³, satisfying this requirement. Additionally, in vacuum and hence in the absence of an electrolyte, no galvanic corrosion is expected to occur externally. Internally, Helium and Neon are used, which are inert gases and do not contribute to corrosion. Because of the CTE mismatch between Ti-6Al-4V and SS, extreme care shall be taken not to have significant temperature gradients at the interface. Such gradients induce thermal stresses that can damage the prototype and the test equipment.

The heat switch is pressurized using either Helium or Neon tank depending on the test case. A pressure regulator is attached to the tanks and a precision valve is used to control the inlet flow when pressurizing the switch. The maximum pressure shall not exceed 5.33 bar, which is dictated by the overpressure limit of the pressure transducer used. The pressure transducer that measures the internal pressure of the heat switch is the 722B Baratron® Compact Absolute Capacitance Manometer from MKS. The full scale pressure range is 1 to 2000 Torr with a reading accuracy of $\pm 0.5\%$, including non-linearity, hysteresis and non-repeatability. The pressure reading is provided as a measured voltage from the pressure transducer. The nominal curve is given by $P = 0.2666 \cdot V [\text{bar}]$. The curve of pressure against measured voltage for the calibrated pressure transducer is shown in Figure 52. Because the pressure sensor is impossible to be placed inside the heat switch, it is placed at the outlet tubing just outside of the vacuum chamber. A rotary pump is placed at the end of the outlet tubing. A schematic of the pressure handling system is show in Figure 53.

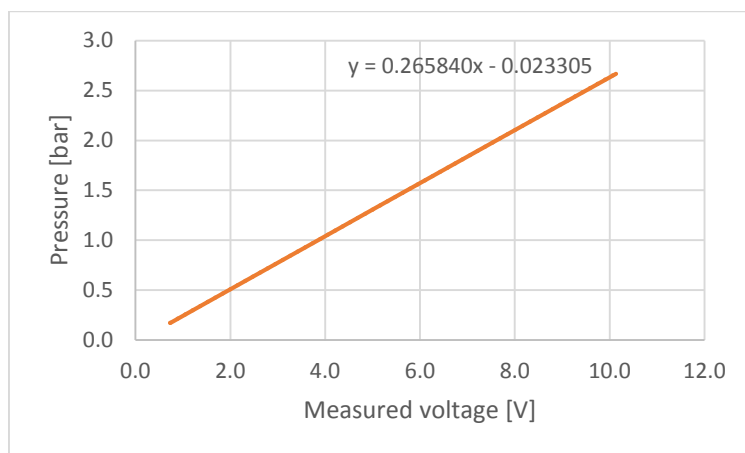


Figure 52: Pressure sensor calibration curve

² From MatWeb: Titanium Ti-6Al-4V (Grade 5), STA

³ From MatWeb: 316 Stainless Steel, annealed sheet

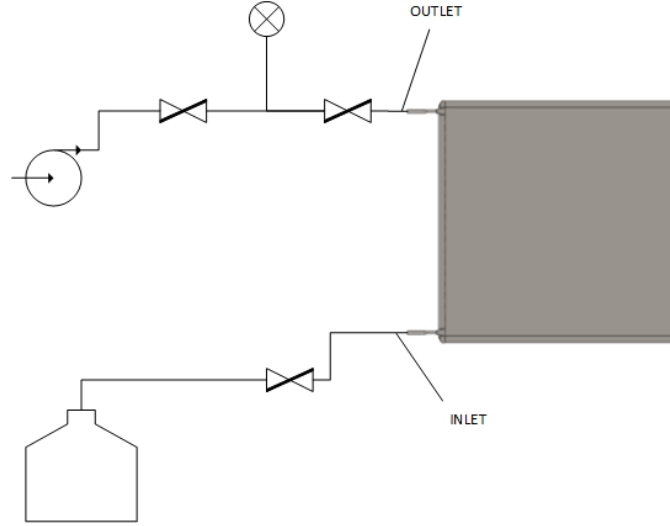


Figure 53: Pressure handling system schematic

7.3 Test configuration leak inspection

A leak inspection was conducted on the heat switch and the test assembly to prevent significant gas losses and contamination. The maximum allowable leakage rate can be determined using equation (7.3-1) [25].

$$Q_L = \frac{\Delta p \cdot V}{\Delta t} \quad (7.3-1)$$

where Δp is the allowable pressure change, Δt is the measurement period and V is the volume. For the given test, it was deemed appropriate to not allow for a pressure drop of more than 10 mbar over 24 hours. This is to ensure the gas remains in the continuum regime over the entire test process that lasts no more than a day for the ON-case. The total internal volume of the test setup, including the heat switch and the tubing is 0.0280 L for the 10x10 cm² and 0.0223 L for the 20x20 cm² heat switch. Consequently, the allowable leakage rate is $3.2 \cdot 10^{-6}$ and $2.6 \cdot 10^{-6}$ mbar·L/s respectively. The helium leak detector (Mass Spectrometer Leak Detector) measured a maximum leakage rate in the order 10^{-7} in the tubing. However, for the second prototype, a significant leakage of $4.0 \cdot 10^{-6}$ mbar·L/s was detected around the sides of the switch. Unfortunately, this leakage cannot be controlled since it stems directly from the solid part. Such leakage could be the result of cracks or of the porosity of the 3D-printed titanium heat switch that could potentially allow the tiny molecules of Helium to penetrate through the solid. For the third prototype, the maximum leakage rate was measured at $3.7 \cdot 10^{-6}$ mbar·L/s. It should be noted that the leak test was conducted at room temperature. The effects of the materials contraction and expansion due to temperature variation are not known. Since stainless steel tube fittings are placed on Ti-6Al-4V parts, it is possible to experience leakage, especially when exposed to a cold environment due to the difference in the material CTE.

7.4 Thermal interface resistance

When two or more components come in contact, heat is not conducted as efficiently as within a continuous body. The heat transfer between bodies is characterized by the contact heat transfer coefficient. The contact heat transfer coefficient is dependent on various parameters, including but not limited to a) the surface roughness and flatness of the geometries, b) the thermal conductivity, hardness and elastic modulus of the mating materials, and c) the applied pressure. In the application of the heat switch, the contact resistance shall be as low as possible in order to facilitate the heat flow from the unit to the baseplate through the switch in the ON-case.

7.4.1 Thermal filler

A thin thermal interface is the ideal solution for such setup. An important parameter that should be taken into account is the electrical resistivity of the thermal interface. The switch is to be used under electrical units. Typically, a material with high-electrical resistivity is used in such cases in order to isolate the unit. This is essential especially in the case of batteries that are very sensitive equipment. In addition, when multiple units are mounted on the same baseplate, the risk of short-circuiting increases, since the neighboring units can discharge current on the baseplate. On the other hand, different configurations can be used based on the satellite and the mission.

The thermal interface material can be either a thin foil or a thermal paste. Permanent adhesives are not taken into account, since the components shall be removable. In the past, extensive experiments have been conducted for the determination of the thermal behavior of the most common space-qualified fillers. Cho-therm® 1671, TPLI™ 220 and eGRAF® HITHERM™ 1210 (graphite) have been determined to be the best interface materials based on their thermal performance, cost and ease of use. Though, TPLI™ has exhibited silicone leaking and is under investigation by ESA for spaceflight qualification. On the other hand, Cho-therm® 1671 has been extensively used by ESA under batteries for electrical insulation. Additionally, it is more deformable than graphite and therefore can compensate better for the non-flatness of the switches. However, because of the limited availability of Cho-therm, Sigraflex was preferred in the end.

Table 17 shows the experimental resistance measurements for the three interface materials (fillers). A significant difference is observed between the experimental resistances and the vendor specified resistances. The difference can be attributed to different experimental setups and applied pressure. For example, the thermal resistance for Cho-therm® 1671 is provided at 300 psi by the vendor, whereas the experimental values were measured at 44 and 110 psi for the 10 lb-in and 25 lb-in torque respectively. The experiment was conducted on a 6 in x 6 in aluminium plate with six #10 bolts (equivalent to M5). This corresponds roughly to 38.8 cm²/bolt. Additionally, the experimental resistance was measured in vacuum conditions, whereas the vendor thermal resistance measurement is not clarified under what pressure conditions it was conducted.

Table 17: Fillers thermal resistance⁴

Thermal Filler	Electrically conductive	Thickness [mm]	Vendor thermal resistance [cm ² ·K/W]	Experimental resistance [cm ² ·K/W]	
				10 lb-in	25 lb-in
Cho-therm® 1671	No	0.381	1.484	14.323	11.355
TPLI™ 220	No	0.508	1.355	2.624	2.108
eGRAF® HITHERM™ 1210	Yes	0.254	0.194	5.139	4.573

For unit installations, M4 fasteners are typically used and therefore were selected for the experiment. According to ECSS⁵ standards, the initial recommended torque value for Class A2-70 Stainless Steel M4 fasteners is 1.7 N·m. However, given the thin geometry of the switch, a lower torque is preferable in order to avoid any damage. Additionally, the thermal contact resistance does not show significant decrease when increasing the torque from 10 lb-in (1.13 N·m) to 25 lb-in (2.82 N·m). The applied contact pressure can be estimated as follows [30]:

$$P = \frac{\tau \cdot N}{f \cdot d \cdot A_c} \quad (7.4-1)$$

Where τ is the applied torque, N is the number of bolts, f is the friction factor (typically 0.2 for unlubricated bolts), d is the bolt diameter and A_c is the total contact area. The obtained pressure can be interpolated with the experimental values from Table 17 to obtain an initial estimate for the contact heat transfer coefficient.

7.4.2 Bolted connection

Lockheed Martin has provided recommendations for bolt maximum thermal resistance, shown in Table 18, with respect to the plate thickness.

⁴ NASA/TM-2003-212500: Performance Testing of Thermal Interface Filler Materials in a Bolted Aluminum Interface Under Thermal-Vacuum Conditions

⁵ ECSS-E-HB-32-23A: Space engineering – Threaded fasteners handbook

Table 18: Bolt Thermal Resistance estimate [13]

Maximum Resistance versus Bolt Size and Plate Thickness (°C/W bolt)					
Steel Bolt		1.57 mm Aluminum	3.18 mm Aluminum	6.35 mm Aluminum	9.53 mm Aluminum
Size	Shaft Diam [mm]				
NC 4-40	2.84	12.6	-	-	-
NC 6-32	3.51	6.61	2.2	-	-
NC 8-32	4.17	4.5	1.5	0.75	-
NF 10-32	4.83	3.0	1.0	0.50	0.333
NF ¼-28	6.35	2.1	0.7	0.35	0.233
NF 5/16 -24	7.92	1.5	0.5	0.25	0.167
NF 3/8-24	9.5	-	0.39	0.194	0.128
NF 7/16-20	11.1	-	-	0.16	0.106
NF ½-20	12.7	-	-	-	0.089

Initially, Lagrange interpolation was used in order to determine the bolt thermal resistances of all bolt sizes for a plate of 10 mm in thickness.

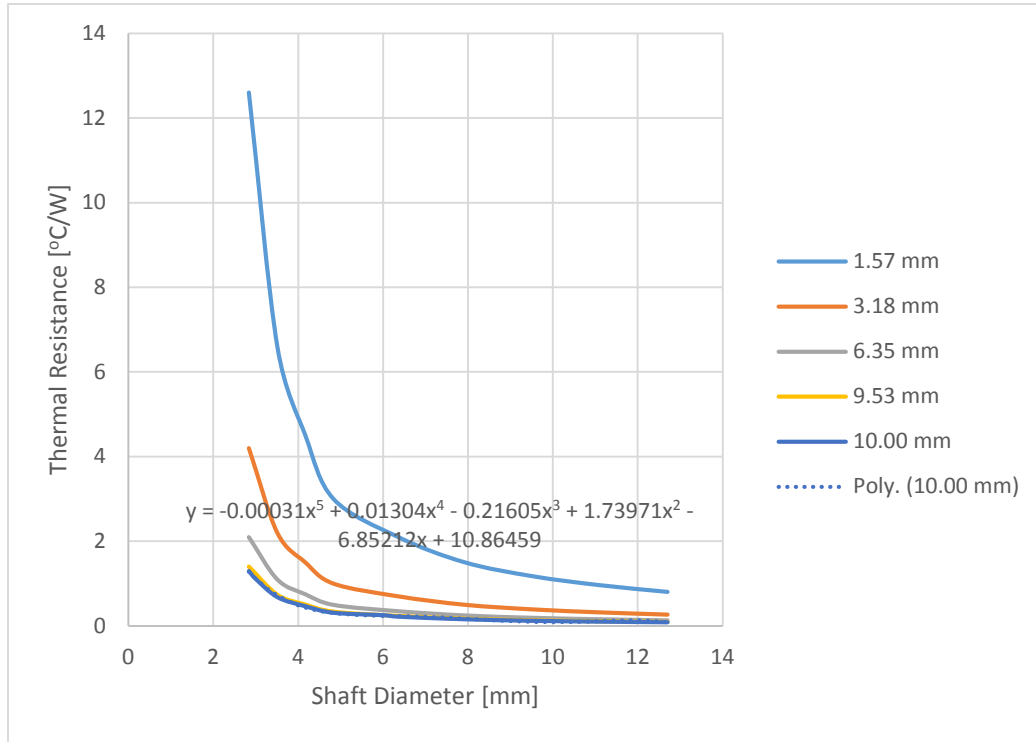


Figure 54: Bolt thermal resistance against bolt shaft diameter

Subsequently, Lagrange interpolation was used in order to determine the bolt thermal resistance of M4 for the given plate thickness of 10 mm. This resulted in an estimated bolt resistance of 0.518 °C/W.

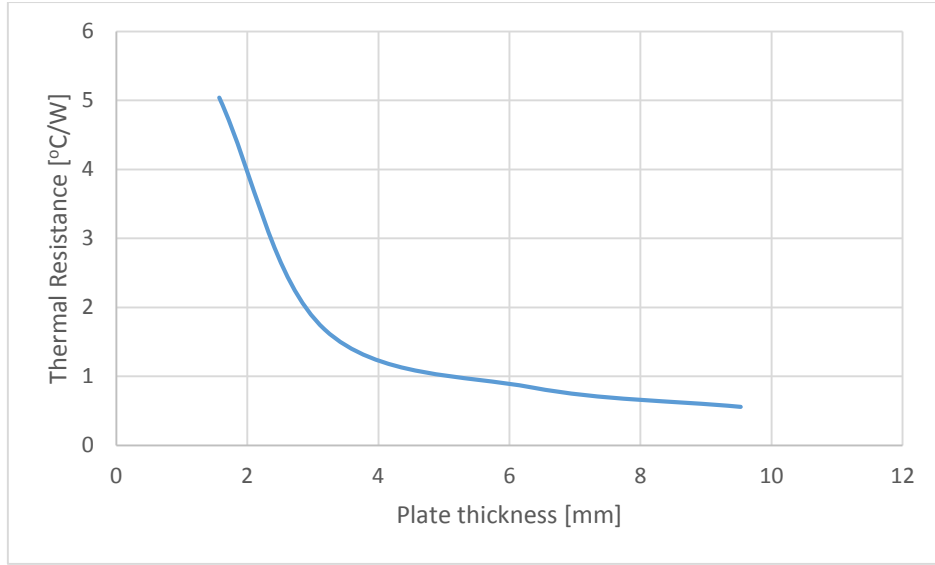


Figure 55: M4 bolt thermal resistance against plate thickness

An additional correlation with a corrected torque parameter in $N \cdot m$ was used in order to approximate the bolted-joint conductance.

$$C_b = 503[\tau(\alpha_{al} - \alpha_{ss})(T_p - 200)]^{0.775} \quad (7.4-2)$$

where α_{al} and α_{ss} are the coefficients of thermal expansion (CTE) of aluminium and stainless-steel, T_p is the plate temperature in K and τ is the applied torque on the bolt. For the material properties, please refer to Appendix F.

There are specific guidelines for the applied torque for the aforementioned fasteners based on their material. The values for the suggested tightening torque for initial calculations for class A2-70 stainless steel bolts can be obtained from ANNEX A in ECSS-E-HB-32-23A⁶.

The thermal resistance is the inverse of the thermal conductance. For the M4 screw, applying a torque of 1.7 $N \cdot m$, with a plate temperature of 273 K, the estimated bolt resistance is 0.601 $^{\circ}C/W$, which is similar to the recommended maximum resistance above.

⁶ ECSS-E-HB-32-23A: Space engineering – Threaded fasteners handbook

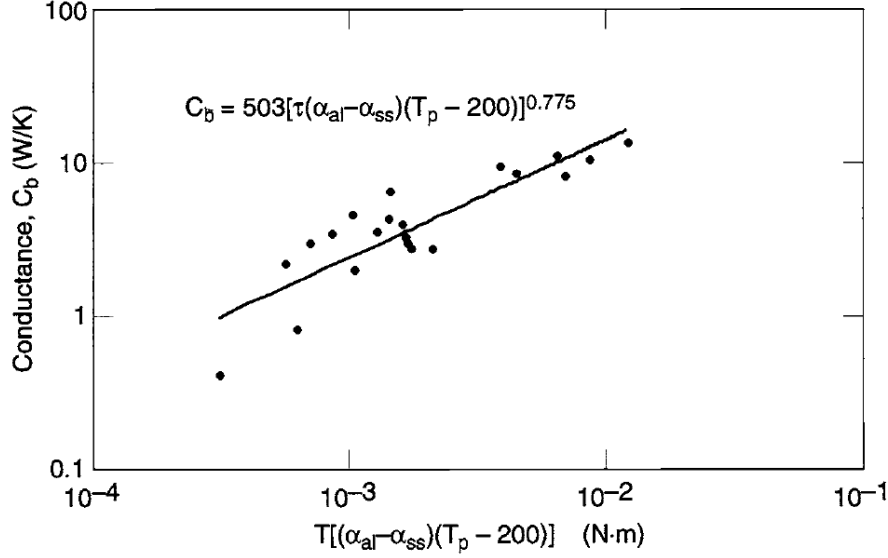


Figure 56: Dimensional correlation of bolted-joint conductance [13]

The average of the two methods yields a thermal resistance of $0.56 \text{ }^\circ\text{C/W}$. When 8 bolts are placed in parallel, a conductance of $14.29 \text{ W/}^\circ\text{C}$ is obtained. It should be noted that this conductance includes the contact conductance with a bear surface. This is a significant leak conductance that would affect the test results, especially in the OFF-case. For this reason PEEK washers and standoffs are used in the test setup. Alternatively, PEEK bushings could be used to thermally insulate both the bolt shank from the holes' surface and the bolt head from Plate 1. However, through holes of 4.20 mm provide sufficient clearance from the bolt shank and no additional insulation is required.

The thermal conductance of the PEEK washer/standoff can be found as [6]:

$$G_{PEEK} = \frac{k_{PEEK} \cdot \frac{\pi}{4} (d_{out}^2 - d_{in}^2)}{t}$$

$t = 2.6 \text{ mm}$ is the washer thickness, $k_{PEEK} = 0.25 \text{ W/m} \cdot \text{K}$ is the thermal conductivity of PEEK, $d_{out} = 9 \text{ mm}$ and $d_{in} = 4.3 \text{ mm}$ are the outer and inner diameter of the washer.

The thermal conductance through the bolt is:

$$G_{bolt} = \frac{k_{SS} A_{bolt}}{L_{bolt}}$$

$k_{SS} = 16.2 \text{ W/m} \cdot \text{K}$ is the thermal conductivity for a class A2-70 stainless steel bolt, $L_{bolt} = 30 \text{ mm}$ is the bolt length and $A_{bolt} = 12.57 \text{ mm}^2$ is the cross sectional area of the bolt.

As a first approximation, perfect contact can be assumed between the washers and the plates. Assuming perfect contact and combining the washer and the bolt conductances in series, a total conductance of $G_{bolt,tot} = 0.00285 \frac{\text{W}}{^\circ\text{C}}$ per bolt is obtained.

Several models for the thermal contact conductance have been suggested by independent researchers over the last decades. The most prominent models are discussed below. All of the

models use the surface microhardness (H_c) of the softer of the two materials that are in contact. It should be noted that the surface microhardness is different than the macro-scale hardness.

Some useful equations are:

$$\sigma_s = \sqrt{\sigma_1^2 + \sigma_2^2} \quad (7.4-3)$$

$$m_s = \sqrt{m_1^2 + m_2^2} \quad (7.4-4)$$

$$k_s = \frac{2k_1k_2}{k_1 + k_2} \quad (7.4-5)$$

Where σ_s is the average surface roughness, m_s is the average asperity slope and k_s is the harmonic mean thermal conductivity. The indices 1, 2 indicate the properties of the two mating surfaces. Because the asperity slope is not a geometrical property that is typically measured, researchers have developed and implemented different correlations between the surface roughness and the asperity slope in their models.

Mikic Elastic/Plastic model

In 1974, Mikic and colleagues developed an elastic/plastic model for the estimation of the contact thermal conductance for rough flat surfaces in vacuum based on whether elastic or plastic deformation occurs. The deformation is characterized based on the parameter [13]:

$$\gamma = \frac{H_c}{E'm_s} \quad (7.4-6)$$

where

$$E' = \left(\frac{1 - \nu_1^2}{E_1} + \frac{1 - \nu_2^2}{E_2} \right)^{-1} \quad (7.4-7)$$

If $\gamma < 0.33$, the deformation is predominantly plastic. If $\gamma > 3.0$, the deformation is predominantly elastic.

For the elastic case ($\gamma > 3.0$):

$$h_c = 1.55 \left(\frac{k_s m_s}{\sigma_s} \right) \left(\frac{\sqrt{2}P}{E'm_s} \right)^{0.94} \quad (7.4-8)$$

Where P is the applied pressure.

For the plastic case ($\gamma < 0.33$):

$$h_c = 1.13 \left(\frac{k_s m_s}{\sigma_s} \right) \left(\frac{P}{H_c} \right)^{0.94} \quad (7.4-9)$$

The asperity slope is corrected to the roughness using equation (7.4-10).

$$m = 0.076(\sigma \cdot 10^6)^{0.52} \quad (7.4-10)$$

Tien plastic model

In 1968, Tien developed a purely plastic model for the estimation of the thermal contact conductance as follows [31]:

$$h_c = 0.55 \frac{k_s m_s}{\sigma_s} \left(\frac{P}{H_c} \right)^{0.85} \quad (7.4-11)$$

This model is very similar to the plastic case of the Mikic model with simply different constants.

Antonetti plastic model

In 1993, Antonetti and colleagues simplified the plastic model developed in 1982 by Yovanovich, eliminating the parameter average asperity slope from the model. The contact heat transfer coefficient is expressed with the relation [32]:

$$h_c = 4,200 k_s \sigma_s^{-0.257} \left(\frac{P}{H_c} \right)^{0.95} \quad (7.4-12)$$

For all models, the equations are expressed in metric units and are valid for $\sigma \leq 2.6 \mu m$.

Aluminium 6061-T6 is softer than PEEK and consequently, the surface microhardness of aluminium is used for the calculations. The reported surface microhardness of aluminium is estimated at 135,000 psi or 931 MPa [33]. The surface roughness of the aluminium plates and PEEK spacers are about 1 and 2 micrometers respectively.

The Mikic model cannot be conclusive, as for the given values, $\gamma = 1.76$. Consequently, the deformation cannot be determined whether it is elastic or plastic. Summarizes the results for the contact heat transfer coefficient for the different models.

Table 19: Aluminium-PEEK contact heat transfer coefficient

Model	Estimated h [W/m ² K]
Mikic Elastic	5,300
Mikic Plastic	2,834
Tien	1,851
Antonetti	2,670
Average	3,164

When the contact conductance is placed in series with the thermal conductances of the washer and the bolt a total thermal conductance of 0.0028 W/°C per bolt is obtained.

Additionally, a conductance equal to $G_{PEEK} = 0.00491 \frac{W}{^{\circ}C}$ is obtained for the interface between Plate 1 and Plate 2 at the spacers locations.

7.5 Test configuration structural analysis

Before conducting the actual experiment, a structural analysis of the test setup was necessary. This was to ensure the integrity of switch in two scenarios; a) maximum applied bolt preload because of the bolt connections, and b) after maximum pressurization of the internal gap, when placed in the vacuum chamber. A structural FEM was created using the “SOL 101 Linear Statics” solver of NASTRAN.

7.5.1 FEM mesh

The heat switch was defeatured in order to simplify the model for better quality and easier meshing. 2D shell meshing (CQUAD4 and TRIA3) was used by extracting the midsurfaces of the solid body and by applying shell offset conditions. A 2D mesh was preferred due to the significantly less computational time required. Additionally, a 3D meshing of a thin wall could potentially lead to low quality elements with high aspect ratios (>10) and would require at least 3-5 elements through thickness to properly estimate the stresses.

The aluminium baseplate of 6 mm thickness was meshed with CQUAD4 elements, whereas 3D meshing with CTETRA4 elements was used for the aluminium plates with a thickness of 10 mm. CTETRA4 elements were also used for the PEEK spacers. 3D meshing was used only for the parts with rather large thickness relative to their size, where a 2D mesh would not be representative.

The bolt connections were modeled using PBAR and a spider of Rigid Body Elements (RBE3). This is a common practice in the aerospace industry that is rather conservative, since all the stresses are applied on the bolt shank. Through the RBE3 spider connection, the mean translations and rotations of the holes’ edges are transferred to the central node of the spider connection.

7.5.2 Preload calculations

ECSS-E-HB-32-23A, the “Threaded Fasteners Handbook”, provides a detailed procedure for the estimation of the bolt preload. The preload is dependent on the applied torque, as well as

the geometry and material of the fasteners. For Metric thread screws, the minimum and maximum tensile load on each bolt can be determined as:

$$F_{max/min} = \frac{\tau(1 \pm \varepsilon)}{0.16p + 0.58\mu_{th}d_2 + \frac{0.5\mu_{uh}}{\sin(\lambda/2)}d_{uh}} \quad (7.5-1)$$

Table 20 summarizes all the necessary data for the estimation of the bolt preload for M4 socket head cap screws and M5 countersunk head cap screws of class A2-70 according to ECSS-E-HB-32-23A.

Table 20: Unlubricated M4 class A2-70 socket head cap screw bolt preload parameters

Variable	Notation	Equation	M4 (flat)	M5 (countersunk)
Under-head bearing angle	λ	-	180°	90°
Nominal diameter	d	-	4 mm	5 mm
Pitch thread	p	-	0.7 mm	0.8 mm
Minor diameter of female thread	d_1	-	3.242 mm	4.134 mm
Pitch diameter	d_2	$d_2 = d - 0.64952p$	3.545 mm	4.480 mm
Head diameter	D_{head}	-	7 mm	10 mm
Hole diameter	D_h	-	4.5 mm	5.5 mm
Under-head diameter	d_{uh}	$d_{uh} = 0.5(D_{head} + D_h)$	5.75 mm	7.75 mm
Thread interface friction coefficient	μ_{th}	-	0.15	0.15
Under-head friction coefficient	μ_{uh}	-	0.15	0.15
Torque uncertainty measurement	ε	-	0.05	0.05

The required tightening torque is applied using a torque wrench properly calibrated to an accuracy of $\pm 5\%$. A torque of 1.35 N·m yields a nominal bolt preload of 1,585 N and a maximum bolt preload of 1,665 N for the M4 flat heat screws. However, the initial analysis showed that the switch might experience significant stresses and a more conservative torque value of 0.85 N·m was preferred. The nominal bolt preload in this case is 1000 N and the maximum 1,050 N. For the M5 countersunk screws, a torque of 3.2 N·m yields a nominal bolt preload of 2,390 N and a maximum bolt preload of 2,510 N. For the structural analysis, the maximum bolt preload was taken into account as the worst case scenario.

On the aluminium baseplate, SS 304 inserts are used instead of tapped holes for the M4 screws. This is to enhance the strength of the fastened joint and to allow for removal of the fasteners without damaging the threads. Due to its high ductility and relatively low modulus of

elasticity, aluminium requires at least 1.5 times the nominal diameter of the fasteners in thread engagement. The minimum acceptable thread engagement for high strength steel, such as SS 304, is only 0.8 times the nominal diameter. In the test setup, an engagement of $L_{eng} = 4.60 \text{ mm}$ is achieved, which corresponds to 1.15 times the nominal diameter. In real life, the thread engagement is greater due to the actual deformation of the very soft Sigraflex. Tests with the torque of $0.85 \text{ N} \cdot \text{m}$ were conducted to determine the deformability of Sigraflex. The tests showed that Sigraflex thickness was reduced from 0.20 mm to 0.15 mm . In addition, the aluminium plates were milled in order to obtain a surface flatness of 0.01 mm/m and a surface roughness of 1 microns. This resulted in a plate thickness of 9.82 mm . Consequently, the actual thread engagement can exceed 5 mm , corresponding to more than 1.25 times the nominal screw diameter, which is safe.

The maximum axial load transmitted by the thread shall be estimated in order to ensure no pull-out failure occurs for either the male or female fastener. The ultimate load for the female and male fastener can be calculated as:

$$F_{ult,f/m} = \tau_{ult,f/m} A_{th,f/m} c_1 c_2 \quad (7.5-2)$$

Where, the indices f/m indicate female and male respectively. $\tau_{ult} = 420 \text{ MPa}$, is the ultimate shear strength of the fastener, A_{th} is the failure area of the thread and c_1, c_2 are coefficients. The thread failure area for the female fastener is given by:

$$A_{th,f} = \pi d \left(\frac{L_{eng,eff}}{p} \right) \left[\frac{p}{2} + (d - d_2) \tan \theta \right] \quad (7.5-3)$$

Where $L_{eng,eff} = L_{eng} - 0.8p$ is the effective length of engaged thread and $\theta = 30^\circ$ is the half angle of the thread groove. Similarly, the thread failure are for the male fastener is:

$$A_{th,m} = \pi d_1 \left(\frac{L_{eng,eff}}{p} \right) \left[\frac{p}{2} + (d_2 - d_1) \tan \theta \right] \quad (7.5-4)$$

The shear strength ratio of the female and male threads is expressed as:

$$R_s = \frac{\tau_{ult,f} A_{th,f}}{\tau_{ult,m} A_{th,m}} = 1.44 \quad (7.5-5)$$

$c_1 = 1.0$ for threaded holes or holes with inserts. $c_2 = 0.897$ for $R_s \geq 1.0$.

The maximum axial load transmitted by the thread for pull-out failure is 16.7 kN and 11.6 kN for the female and male fastener respectively. These values are much larger than the applied load and consequently the fastened joint is safe.

The equations of this section are drawn from ECSS-E-HB-32-23A. The handbook uses the VDI 2230 standards for “Systematic Calculations of High Duty Bolted Joints” and the peer-reviewed references [34], [35].

7.5.3 Structural simulation modeling

The structural model of the test setup is sophisticated as it involves rather complicated non-linear conditions, such as surface contacts and bolt preloads. Surface contact is usually treated using PGAP elements. PGAP are gap elements that open or close a gap. They are assigned an axial and a transverse stiffness, as well as a coefficient of friction. Their stiffness can be obtained using Hooke's law:

$$F = kx \quad (7.5-6)$$

Where x is the maximum allowable penetration (typically 10^{-5} m) and F is the estimated force acting on the surfaces. Overall, the use of PGAP elements is very demanding in terms of the mesh. More specifically, it is ideal that there is a one-to-one connection between the nodes of the mating surfaces. This means that the two surfaces should have an identical mesh in order to have perfectly normal PGAP elements. This fact significantly complicates the generation of the FEM. Furthermore, if the Linear Statics solver were to be used, the PGAP elements should have been treated as linear contact elements, which reduces the accuracy of the results. The Non-linear solver would yield more accurate results, but at the expense of computational time.

The Linear Statics solver offers the "Surface-to-Surface Contact" algorithm. This algorithm was used to simulate the contact between the spacers and the aluminium plates, the switch and the aluminium plates, and the baseplate and aluminium plate 2. The algorithm automatically forms contact elements between the mating surfaces and computes their stiffness. Subsequently, this contact algorithm iterates in two nested loops: an inner and an outer loop. The inner loop imposes a zero penetration between the contacting bodies and it is satisfied when the contact force convergence ratio is less than 0.01. The outer loop determines which contact elements are active and it is satisfied when the amount of contact changes is less than 2% of the active contact elements. These are the default settings of the solver. Of course more stringent requirements can be implemented, but for complicated models, such as this one, convergence can be very difficult. In order to reach convergence, the two loops need to be satisfied at the same time. A coefficient of friction of 0.1^7 was used for the contact between the switch and the aluminium plates due to the presence of Sigraflex.

Regarding the bolt preload, the linear solver imposes some limitations, as each bolt needs to be modeled with a single 1D element. In this case, the load is applied at the two ends of the bolt in the axial direction. The solver then calculates the strains of the bolt strains using:

$$\varepsilon = -\frac{(x_2 - x_1)}{L} - \frac{F_{preload}}{AE}$$

x_1, x_2 are the displacements of the end nodes, L is the bolt initial length, $F_{preload}$ is the bolt preload, A is the cross-sectional area of the 1D element and E is the modulus of elasticity.

Apart from the bolt preloads, gravitational forces were also taken into account in the model.

⁷ SIGRAFLEX® Graphite Foil Type TF datasheet

7.5.4 Structural analysis results

The structural integrity of the titanium alloy heat switch is determined using the classical rule-of-thumb safety factor. This simple approach takes into account the various parameters that can affect the safety of the product and combines them to derive the overall product safety factor given by [36]:

$$FS = FS_{material} \cdot FS_{stress} \cdot FS_{geometry} \cdot FS_{failure\ analysis} \cdot FS_{reliability} \quad (7.5-7)$$

Table 35 in Appendix G provides the values of the respective safety factors and their criteria. Eventually, the total safety factor is 1.8876. The yield tensile strength of $\sigma_{YT} = 805\text{ MPa}$ and the yield compressive strength of $\sigma_{YT} = 860\text{ MPa}$ result in a maximum allowable applied stress of 426 MPa and 456 MPa respectively.

7.5.4.1 Maximum bolt preload

As a first iteration, the simulation was run without the PEEK spacers. In this case, the analysis showed that the switch experiences very high stresses in the corners near the tubes. Due to their profile, the corners act as stress concentrators and are subjected to Von-Mises stresses up to 1,650 MPa, which is almost double the material compressive yield strength of $\sigma_y = 860\text{ MPa}$. Thus, the spacers are necessary for structural support in order to not damage the switch. The second iteration that includes the spacers yielded significantly better results. The maximum local Von-Mises stresses were reduced to just 300 MPa, resulting in a safety factor of 2.87. Figure 57 provides a stress map of the corners. However, the pillars at the four corners are subjected to a compressive stress of 760 MPa that corresponds to a safety factor of 1.13. This happens because of their proximity to the corners. The rest of the pillars are subjected to stresses less than 400 MPa. Consequently, the heat switch is considered to be able to survive even in case of failure of those four pillars. For the contact pressure and the displacement of the test setup, please refer to the figures in Appendix G. The contact pressure results were used to validate the assumptions for the thermal contact conductances.

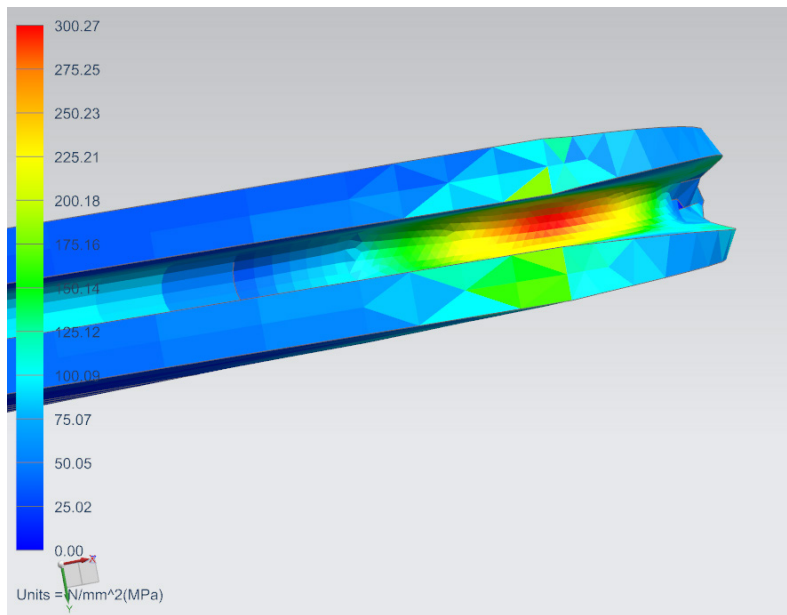


Figure 57: Maximum Von-Mises stresses location

7.5.4.2 Overpressurization

For the case of overpressurization during testing, the maximum overpressure limit of the pressure sensor was used, which corresponds to 5.33 bar. All the other parameters that were set for the maximum bolt preload case remained unchanged. This simulation resulted in axial tensile stresses of 990 MPa at the pillars, which exceeds the Ti-6Al-4V yield tensile strength. Consequently, assuming the axial stress behavior to be linear, the maximum gap pressure shall be reduced by a factor of 2.32. This internal gap pressure can be controlled with the pressure regulator mounted on the gas tank and using the precision valve at the inlet. Figure 58 and Figure 59 show the stresses experienced by the pillars at 5.33 and 2.3 bar respectively.

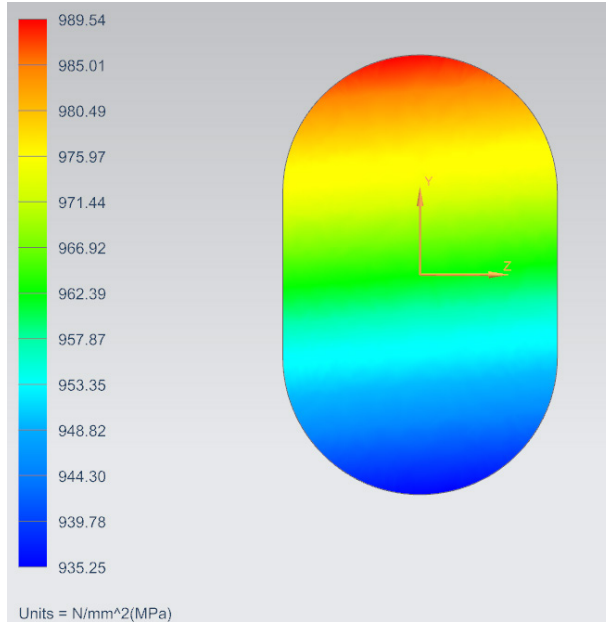


Figure 58: Pillar cross-section stresses [5.33 bar]

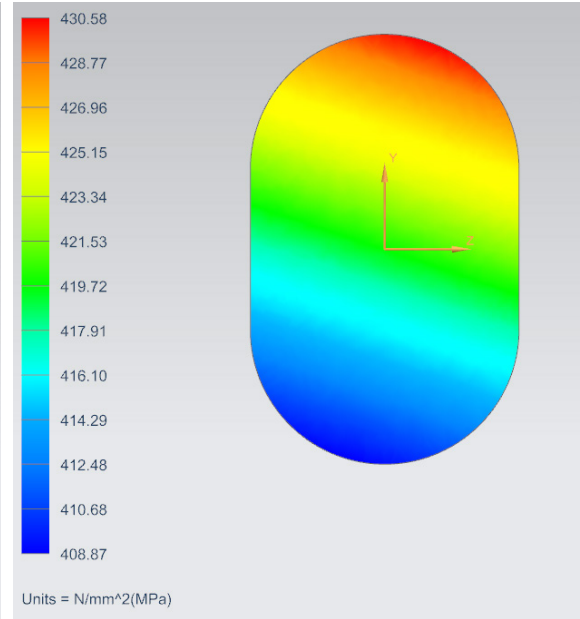


Figure 59: Pillar cross-section stresses [2.3 bar]

Thus, the absolute internal pressure of the heat switch shall not exceed 2.3 bar. For the displacement of the heat switch, please refer to Figure 136 in Appendix G.

7.6 Test configuration thermal simulation

A thermal simulation model of the test setup was created based on the assumptions mentioned in sections 7.2 and 7.4. The FEM uses 3D tetrahedral meshes for the heat switch and the aluminium plates and baseplate. For the OFF-case the radiative coupling between the two sides of the switch was simulated using the effective emissivities estimated in section 5.5.1. A more complicated model that uses the Monte Carlo method with 1,000 rays showed minimal differences between the two models, validating the dummy case generated earlier.

For the ON-case, an additional 3D solid mesh is used to simulate the gas. Perfect conduction occurs between the mesh of the gas and the mesh of the heat switch by making the two meshes to share the nodes at the interface. The gas mesh is given temperature dependent thermal properties obtained from the National Institute of Standards and Technology (NIST) Chemistry WebBook.

The contact conductance was adjusted through the various iterations according to the experimental values. The heat load is applied on an area identical to the size of the heater,

directly on the top of plate 1. The bottom face of the baseplate is set at constant temperature as the system's boundary condition. The heat leak through the bolts is simulated using linear conductive couplings to reduce the number of elements and the complexity of the model.

Figure 60 and Figure 61 show the temperature profile of the cross section of the heat switch in the ON-state, when the baseplate is held at a temperature of 20°C, with a power of 180 W.

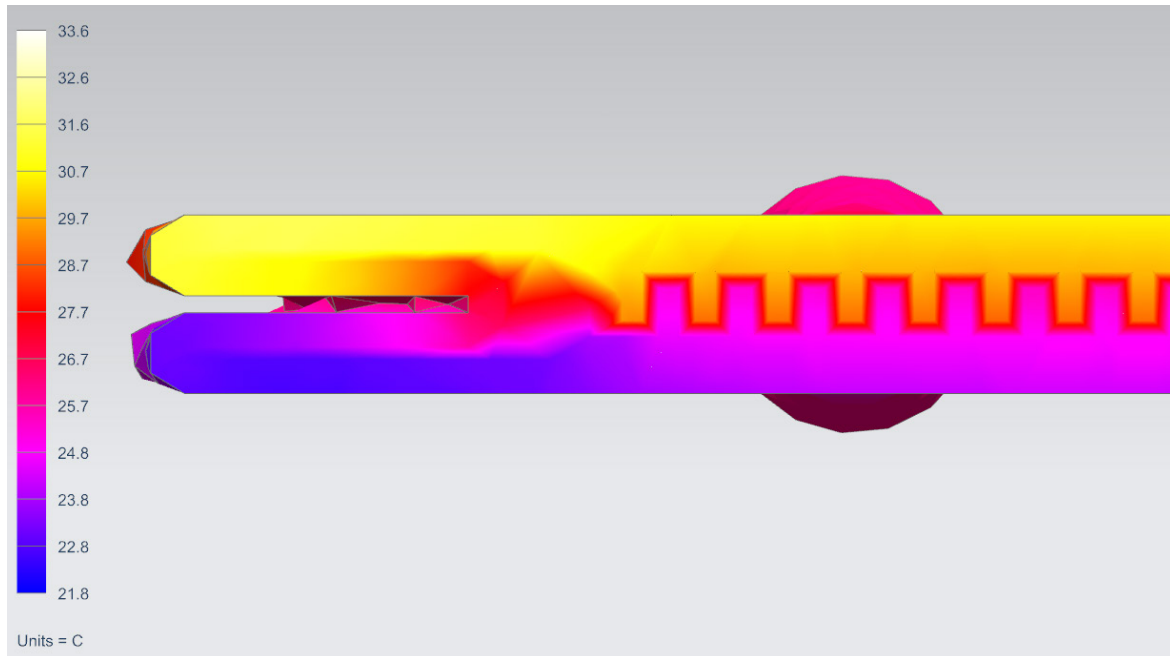


Figure 60: Switch cross-section near edges (baseplate at 20°C)



Figure 61: Switch cross-section middle (baseplate at 20°C)

The thermal simulations result in a theoretical $h_{\text{ON}}/h_{\text{OFF}}$ ratio of 656.4/27.7 W/m²·K and 677.9/14.0 W/m²·K at a baseplate temperature of 20°C for the second and third prototype respectively, when only the conductance through the switch is considered. Accounting for the contact heat transfer coefficient at the top and bottom of the switch, these values translate into 228.3/25.7 W/m²·K and 230.8/13.5 W/m²·K. The third prototype appears to have both a larger ON-conductance and a lower OFF-conductance leading to a ratio that is 2.04 times better than the second prototype. This is the result of the larger effective area, whose effects are discussed in the following section. For detailed graphs of the theoretical performance of the two prototypes, please refer to Chapter 8.

7.7 Scale analysis

A scale analysis is performed in order to determine the thermal performance of the heat switch with respect to its surface area. This is because the heat switch is expected to behave differently with an increasing size of its effective area until convergence is reached. This happens because different modes of heat transfer dominate with increasing size, especially in the OFF-case, where radiation is expected to dominate. In the models, the applied power increases proportionally with the effective area in order to generate a significant gradient. This way round-off and accuracy errors are minimized. It should be noted that the analysis was based on the latest design iteration, identical to the third prototype, i.e. the fin length is 0.6 mm. For more information about the fin profile, please refer to Figure 132 in Appendix E.

The finite element thermal model consists of a 3D mesh of the heat switch and two 0D (lumped mass) elements that simulate the dissipating unit and the heat sink. The lumped masses are thermally coupled to the heat switch using a contact heat transfer coefficient of 700 W/m²·K (yellow arrows), an average value that has been drawn from the experimental data of section 8.1. The heat load (red arrow) is applied on the lumped mass representing the dissipating unit, while the other lumped mass is set at a constant temperature of 20°C as a boundary condition (blue arrow). An illustration of the thermal model is shown in Figure 62. In the ON-case, an additional 3D mesh is used to simulate the conduction through the gas. This mesh shares nodes with the mesh of the heat switch, assuming perfect contact between the gas and the heat switch surfaces.

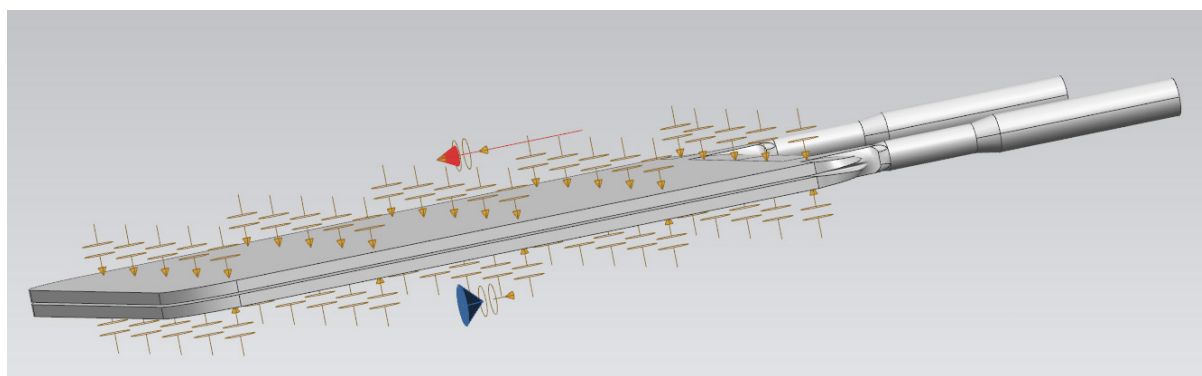


Figure 62: Thermal model couplings and BCs

It should be reminded that Hydrogen was not used as the operating gas during testing because of the safety constraints at ESTEC as mentioned in section 5.3.1. However, it is the best

candidate for the gas-gap heat switch, since it is the gas with the highest thermal conductivity. Consequently, in this chapter, the simulations were run for both Helium and Hydrogen to provide an indication of the improvement in performance. Figure 63 shows the overall ON-conductance (including contact conductance) of the heat switch with respect to the effective area. The effective area is defined as the flat surface in contact with the unit and the heat sink. The figure shows that the ON-case heat transfer coefficient reaches a plateau around 0.06 m^2 , with a value of $232 \text{ W/m}^2\cdot\text{K}$ for Helium and $241 \text{ W/m}^2\cdot\text{K}$ for Hydrogen. This represents an improvement of the overall ON-conductance by 3.9%. For the smaller sizes, the heat transfer coefficient is higher since the in-plane heat spread is more efficient and heat can be conducted more efficiently through the sidewalls.

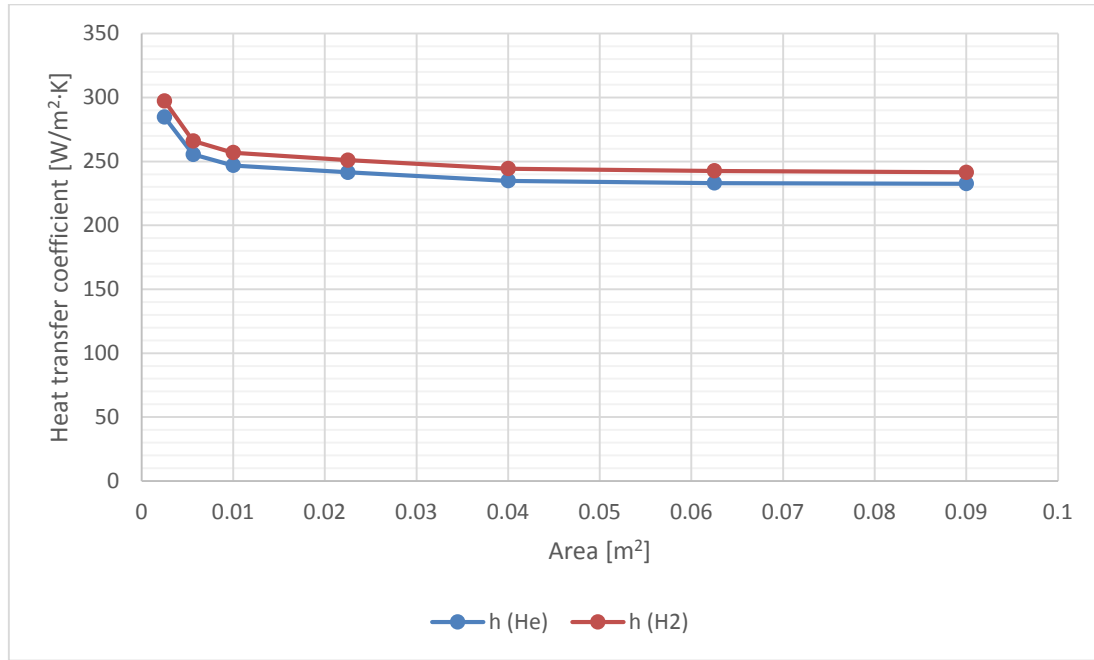


Figure 63: ON-conductance scale analysis

In the OFF-case, an effective emissivity of 0.263 is applied for the radiative coupling from one side of the switch to the other, an approximation explained in detail in section 5.5.1. The solid mesh representing the gas is deactivated, assuming zero conduction through the gas. Figure 64 shows the overall heat transfer coefficient (including contact conductance) for the OFF-case with respect to the effective area. Similarly to the ON-case, the heat transfer coefficient is significantly higher at smaller sizes of the heat switch, since conduction through the sidewalls dominates. With increasing size, the heat is conducted less efficiently in-plane through the thin faces (0.7 mm) as the conductive thermal resistance increases. As a result, the radiation across the gap starts dominating as the main heat transfer mode. From the graph, it can be seen that the curve has not yet reached a convergence as good as in the ON-case. For a $30 \times 30 \text{ cm}^2$ switch, the OFF-case heat transfer coefficient is $9.28 \text{ W/m}^2\cdot\text{K}$, whereas for a $35 \times 35 \text{ cm}^2$ switch it is $8.83 \text{ W/m}^2\cdot\text{K}$. This yields an overall ON/OFF ratio of 27.3 for Hydrogen and 26.3 for Helium. Further simulations were impossible to be carried out because of computational resources limitations. Tens of millions of elements are necessary for larger sizes of the heat switch.

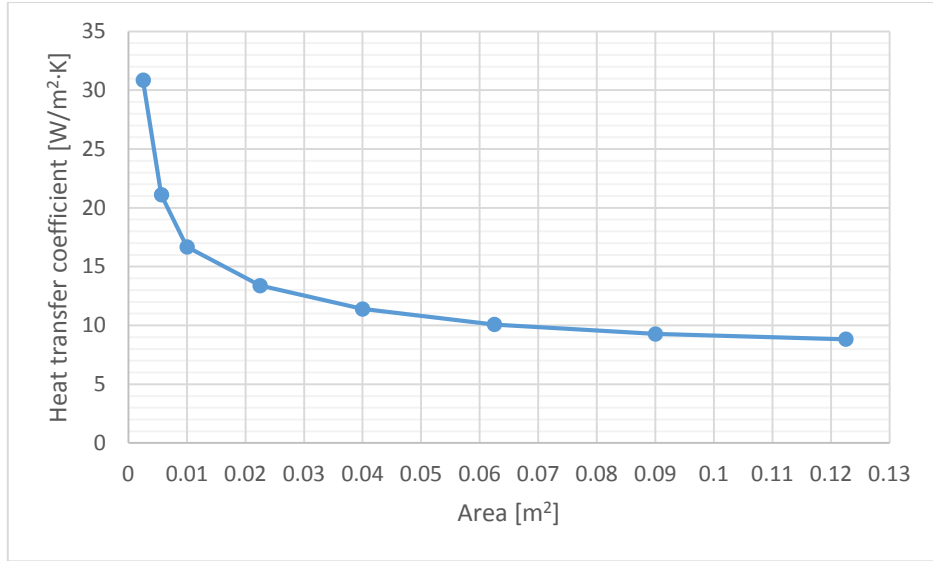


Figure 64: OFF-conductance scale analysis

For the ON and OFF-case, we have a good indication of the ideal performance of the heat switch, by making a plausible assumption for the contact heat transfer coefficient that is based on the experimental results of Chapter 8. According to the information provided for the units of Sentinel-2, a heat switch of 0.1 m^2 is required under the batteries. For this size, both the ON and OFF heat transfer coefficient have reached significant convergence. In order to confirm these models, further testing is necessary with parts manufactured with good tolerances and in vacuum facilities that can accommodate such sizes. Though, it should be noted that the ON and OFF heat transfer coefficients are still far from the requirement values of 500 and 5 $\text{W/m}^2\cdot\text{K}$ respectively and therefore far from the ratio of 100. For the performance requirements, please refer to Table 1 in section 3.3.1.

Figure 65 shows the area density of the heat switch with respect to the effective area. The area density converges to a value of 8.16 kg/m^2 , when the effective area is larger than 0.1 m^2 . This value violates the minimum requirement of 8.0 kg/m^2 established in Table 1.

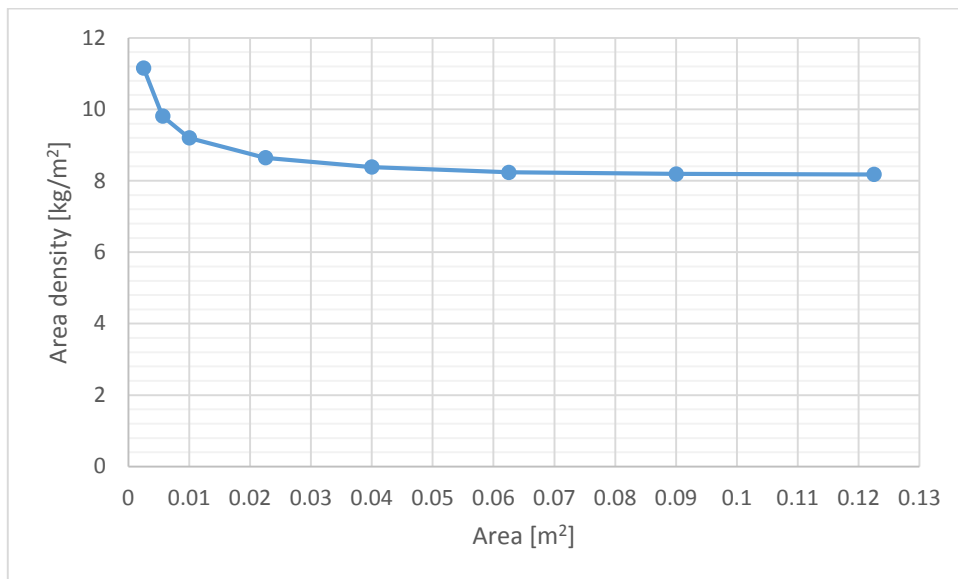


Figure 65: Heat switch area density

7.8 Test procedure

The test procedure for the third prototype is outlined with the following steps:

1. Set tank pressure regulator to 2 bar
2. Open all valves to purge the switch
3. Pump the gas (Helium) out
4. Perform bake-out at 80°C
5. Pressurize gas to 1.7 bar (exceed the continuum regime limit) using the pressure regulator
6. Set the baseplate temperature at -40°C
7. Set the heater power at 180 W
8. Wait for system stabilization. For the stabilization criteria, see section 7.9
9. Increase baseplate temperatures by increments of 20°C until +40°C
10. Turn OFF the heater
11. Depressurize the switch using the rotary pump below molecular regime pressure limit
12. Repeat steps 6 to 9. Instead of 180 W, apply 15 W respectively
13. Switch Helium tank with Neon tank
14. Repeat steps 1 to 14

Ultimately, the performance of the switch should be dependent only on its temperature. More specifically, in the ON-state, the switch conductance increases with increasing temperature due to the increasing thermal conductivity of the gases. In the OFF-state, the switch conductance increases with increasing temperature, since the radiative heat transfer inside the gap increases. For the second prototype, the test procedure is identical with the only differences being that the applied power in the ON-case is 40 W and in the OFF-case 5 W and that no testing with Neon is necessary. It should be reminded that only Helium and Neon were eventually considered for conducting the test because of the safety constraints at ESTEC that prohibit the use of Hydrogen.

7.9 Test stabilization criteria

The stabilization criterion is critical when performing a thermal balance test, since it defines whether the tested system has reached thermal equilibrium. The stabilization criterion can be specified as a maximum rate of change of the temperature (dT/dt), as a specified temperature difference ΔT_{target} from the steady-state or a combination of both. However, a temperature difference requirement is problematic, since the true steady-state temperature is not accurately known prior to testing, especially for powered test setups, and can only be approximated with simulations [37].

A full finite element model takes several hours to solve for both the ON and OFF case because of the large number of elements and the complicated couplings between them. For this reason, a simplified thermal network was generated in ThermXL, using lumped masses. This network is very useful in the correlation process between the simulation and experimental data as it provides results that are comparable to the finite element model, within a few seconds. Consequently, this network can be adjusted iteratively in order to provide an initial correlation

between tests and simulations, and before implementing the changes in the time-consuming FEM. The code of this model was exported to an ESATAN-TMS data file, written in FORTRAN 77 and is attached in Appendix G. Once correlated, this parametric model can be used to predict the behavior of the test setup under any thermal vacuum boundary conditions (baseplate/shroud temperatures, power dissipation), part dimensions and thermo-optical properties. It can also be integrated into a complicated thermal network, as it is done in Chapter 10. The model can be adjusted either directly using ThermXL or altering the code. This reduced model is also used in order to determine the terminal time constant of the test setup.

The test setup was discretized into isothermal nodes that were connected according to the thermal network provided in Figure 66. The aluminium plates and the baseplate were simulated using a node at the top and bottom face, but for simplicity they are merged into a single node in the schematic. The heat load is applied on the node representing the top of Plate 1. The shroud and the bottom of the baseplate are set as the boundary nodes.

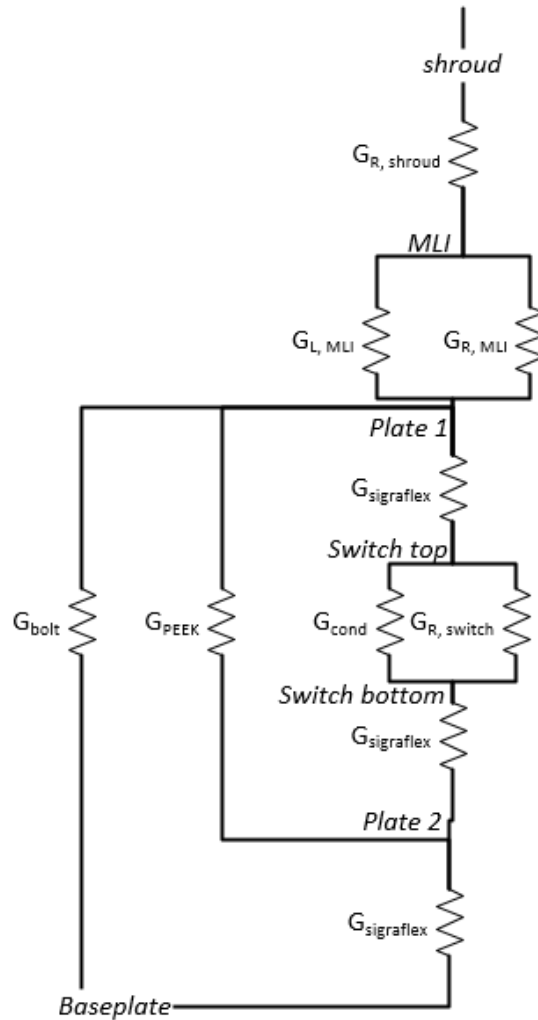


Figure 66: Test setup reduced thermal network

The lumped-mass model and the FEM for the ON-case are well correlated as can be seen from Figure 67 and Figure 68. Using second order exponential curve fitting for the two models, the individual time constant for the top of the switch is 3.13 minutes and 3.64 minutes respectively.

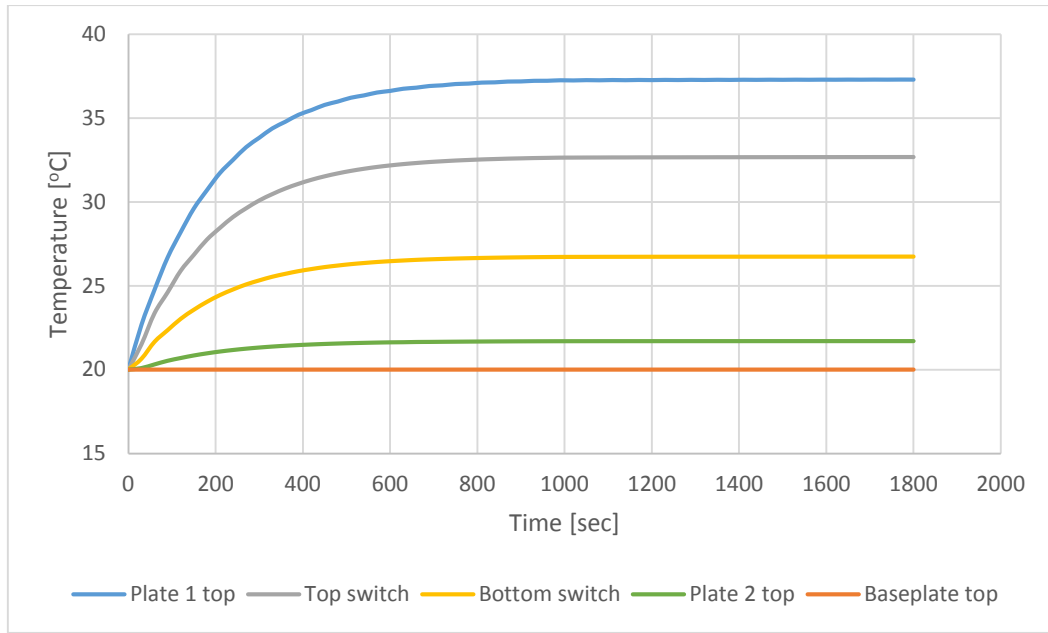


Figure 67: Lumped mass test setup transient response at 20°C (ON-case)

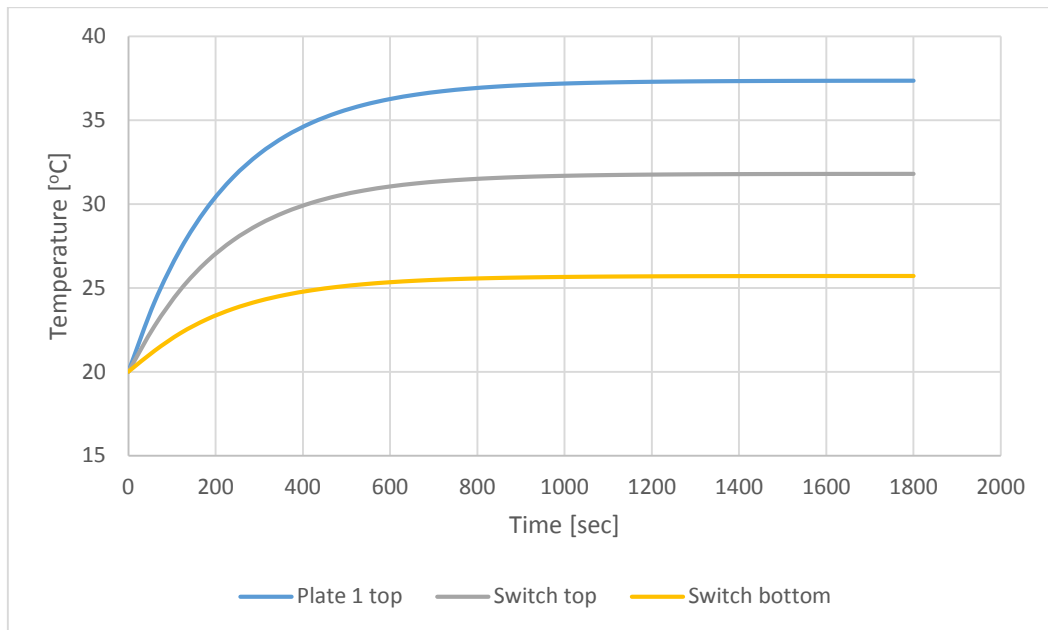


Figure 68: FEM test setup transient response at 20°C (ON-case)

The lumped-mass model and the FEM for the OFF-case are very well correlated too. Using second order exponential curve fitting for the two models, the individual time constant for the top of the switch is 27.7 minutes and 30.8 minutes respectively.

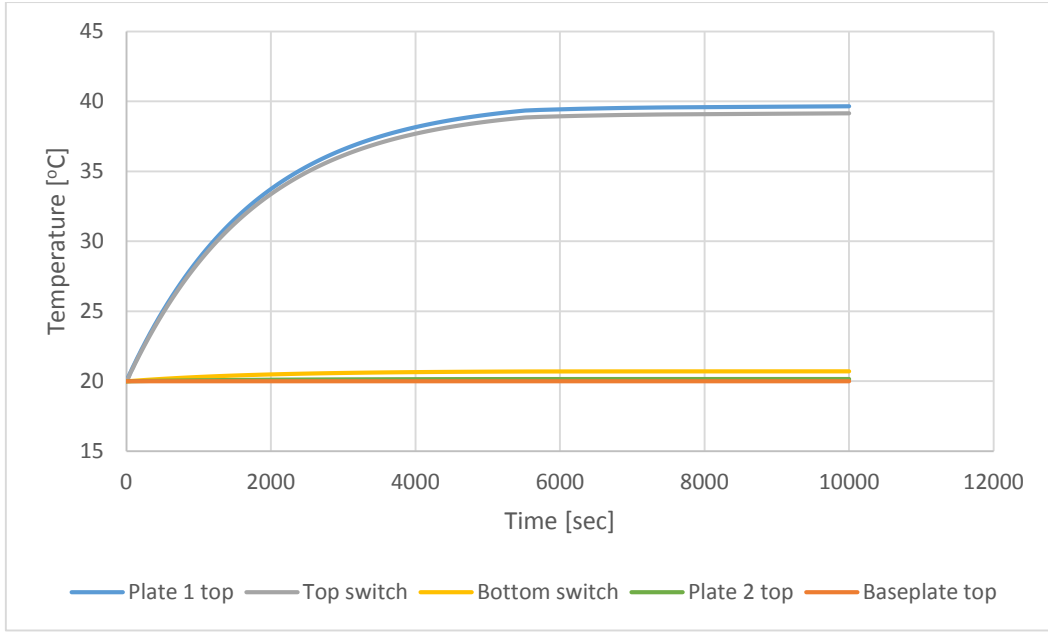


Figure 69: Lumped mass test setup transient response at 20°C (OFF-case)

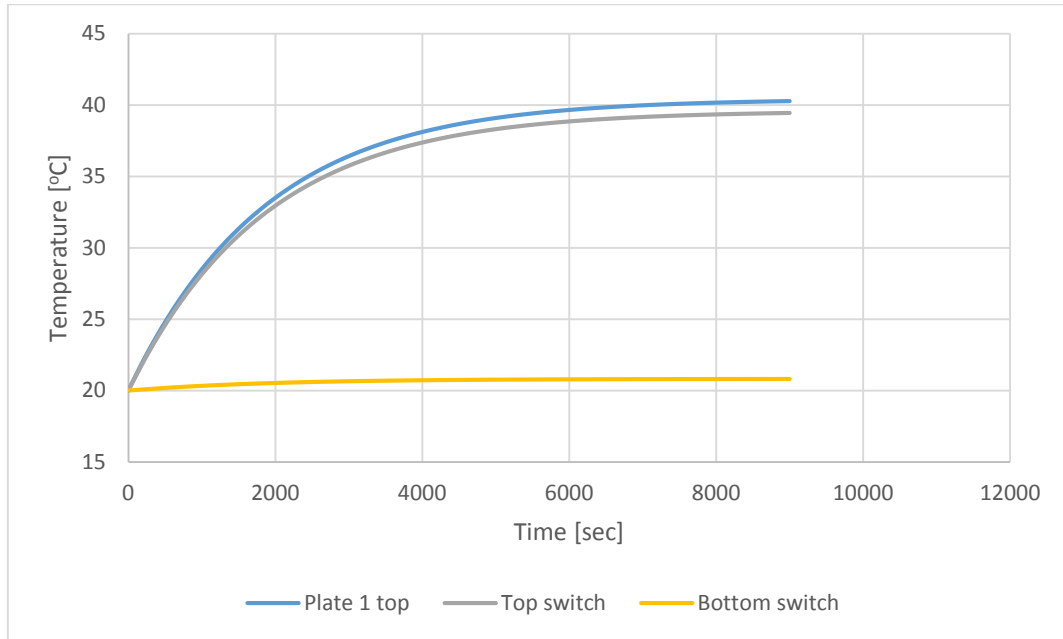


Figure 70: FEM test setup transient response at 20°C (OFF-case)

In preparation for the test, a preliminary stabilization criterion can be determined using the concept of the “terminal time constant”. In this method, the thermal network is described by a system of N simultaneous first-order differential equations that follow the energy balance equation [38]:

$$c_n \frac{dT_n}{dt} = p_n - \sum_{q=1}^N G_{n,q}(T_n - T_q) - \sum_{b=1}^{N_b} G_{n,b}(T_n - T_b) \quad (n = 1, 2, \dots, N) \quad (7.9-1)$$

Where N is the number of nodes, c_n is the heat capacity of node n and p_n is the power dissipation. $G_{n,q}$ represents the internal conductances of the system (conductive, convective or radiative) and $G_{n,b}$ the external conductances, i.e. conductances to the boundaries. For this equation to hold true, the radiative conductances need to be linearized according to equation (5.1-1). This linearization is very accurate when relatively small temperature differences occur, such as the ones expected in the case of the heat switch. Eventually, the equations are reduced to [38]:

$$T_n(t) = v_n + \sum_{q=1}^N b_k u_{k,n} e^{\lambda_k t} \quad (7.9-2)$$

Where λ_k represents the eigenvalue. The eigenvalue is negative so that the nodes can converge to a steady state temperature. The v_n coefficient is determined from the boundary conditions. The eigenvalue and $u_{k,n}$ are determined by the characteristics of the network and b_k from the initial conditions of the network. Eventually, the terminal constant is defined as [38]:

$$\tau_\infty = -\frac{1}{\lambda_m} \quad (7.9-3)$$

Where λ_m is the minimum absolute eigenvalue. The terminal time constant differs from the individual time constant, as it represents the limit value of the time constant common to all the diffusive nodes of the network.

For the second prototype, for the ON-case, $\lambda_m = |-0.0054294|$, which corresponds to a terminal constant of 184 seconds or 3.1 minutes. For the OFF-case, $\lambda_m = |-0.00060453|$, which corresponds to a terminal constant of 1,654 seconds or 27.6 minutes.

For the third prototype, for the ON-case, $\lambda_m = |-0.0025581|$, which corresponds to a terminal constant of 6.5 minutes. For the OFF-case, $\lambda_m = |-0.00038792|$, which corresponds to a terminal constant of 43.0 minutes.

The allowable rate of rate of change of the temperature is dictated by the accuracy of the thermocouples and the time constant. As explained later in section 9.4, thermocouples have usually an overall accuracy of about $\pm 0.2^\circ\text{C}$. Thus, a rate of change less than $\Delta T_j = 1 \text{ K}$ over a period $\Delta t = \tau_\infty$ is a typically set as a criterion for every node j . More relaxed duration criteria can be used when the previous requirement is impossible to be satisfied. Though, to preserve minimum significance of a thermal balance test, a temperature change of 1 K over a minimum $\Delta t = \frac{\tau_\infty}{3}$ is the limit. The maximum deviation with respect to the ideal stabilization temperature can be determined as:

$$\varepsilon_{j,max} = \frac{|\Delta T_j|}{e^{\frac{\Delta t}{\tau_\infty}} - 1} \quad (7.9-4)$$

For Δt equal to $\tau_\infty, \frac{\tau_\infty}{2}$ and $\frac{\tau_\infty}{3}$, the maximum deviation is 0.58 K, 1.54 K and 2.52 K respectively.

It should be reminded that this approach is only useful to provide an initial indication of the test duration and test stability. The time constant depends highly on the boundary conductances of the system. Consequently, the real time constant could differ significantly from the estimated one, especially when assumptions have been made or inaccurate approximations have been used to estimate contact and bolt conductances. For better accuracy, the real-time time constant can be obtained by performing an exponential curve fitting of $|dT/dt|$ versus time. This methodology is implemented in section 8.2.

7.10 Summary

A simplified test setup with a sandwich configuration consisting of two aluminium plates and the heat switch was considered to be the most appropriate method to evaluate the performance of the heat switch. Several critical parameters have been taken into account in order to minimize the uncertainty of the results. Conductive and radiative insulation is used to minimize heat leaks during the experiment. Bolt conductances and contact heat transfer coefficients, calculated using mathematical correlations, have been integrated into the thermal models for more accurate results.

A structural analysis was necessary to ensure the integrity of the test setup. The results showed that special care shall be taken with the support pillars and the corners of the switch, since they can be subjected to excessive stresses due to over-torquing and overpressurization.

A reduced Thermal Mathematical Model correlated with a FEM has been produced to obtain an initial estimation of the steady-state temperatures and of the responsiveness of the heat switch in the ON and OFF-case. This responsiveness provides essential information for establishing the stabilization criteria of the system during testing. Moreover, a scale analysis showed that the latest design of the heat switch reaches sufficient convergence at a size of 0.1 m², achieving an ON/OFF ratio as high as 27.4.

8 Experimental results & correlation

This chapter provides an analysis of the experimental results for the second and the third prototype and a correlation with the developed thermal models. An iterative process was followed for the thermal models, which have been updated with experimental data to improve modeling assumptions and provide a better correlation with experimental results.

8.1 Contact heat transfer coefficient

The experimental results are used in order to improve the thermal model by adjusting the contact heat transfer coefficient assumptions between the aluminium plates and the heat switch through the Sigraflex foils.

8.1.1 Second prototype

Figure 71 provides a relation of the contact heat transfer coefficient with respect to baseplate temperature for the second prototype experiment. The data points exhibit some scattering, which is attributed to the accuracy of the thermocouples and the relatively small temperature gradient that increases the uncertainty. The dependence of the contact heat transfer coefficient with respect to temperature can be explained by the linear thermal expansion of the materials. The fact that the top side heat transfer coefficient decreases with temperature, while the bottom side increases could be explained by the arc-shape of the second prototype and the location of the thermocouples. The thermocouples are placed in the center of the top and bottom faces of the switch, the location that exhibits the largest deformation. Consequently, with increasing temperature and expansion, one side is getting better pressed against the aluminium plate at the location of the thermocouples, while the opposite side is experiencing the exact opposite effect. In order to reduce the complexity of the thermal model, temperature dependencies of the contact heat transfer coefficients were not taken into account and the average values in the temperature range were used. Overall, there is an uncertainty in the values of the contact heat transfer coefficient, since the measurements are conducted at a single location. Because the pressure is not uniformly distributed, this impacts the local values of the contact heat transfer coefficient, especially on non-flat surfaces such as in this case. For this reason, a better estimation of the contact heat transfer coefficient can be established by assuming the average contact heat transfer coefficient on both sides to be the same and making use of the heat transfer through the heat switch. This method is elaborated in section 8.3.2.

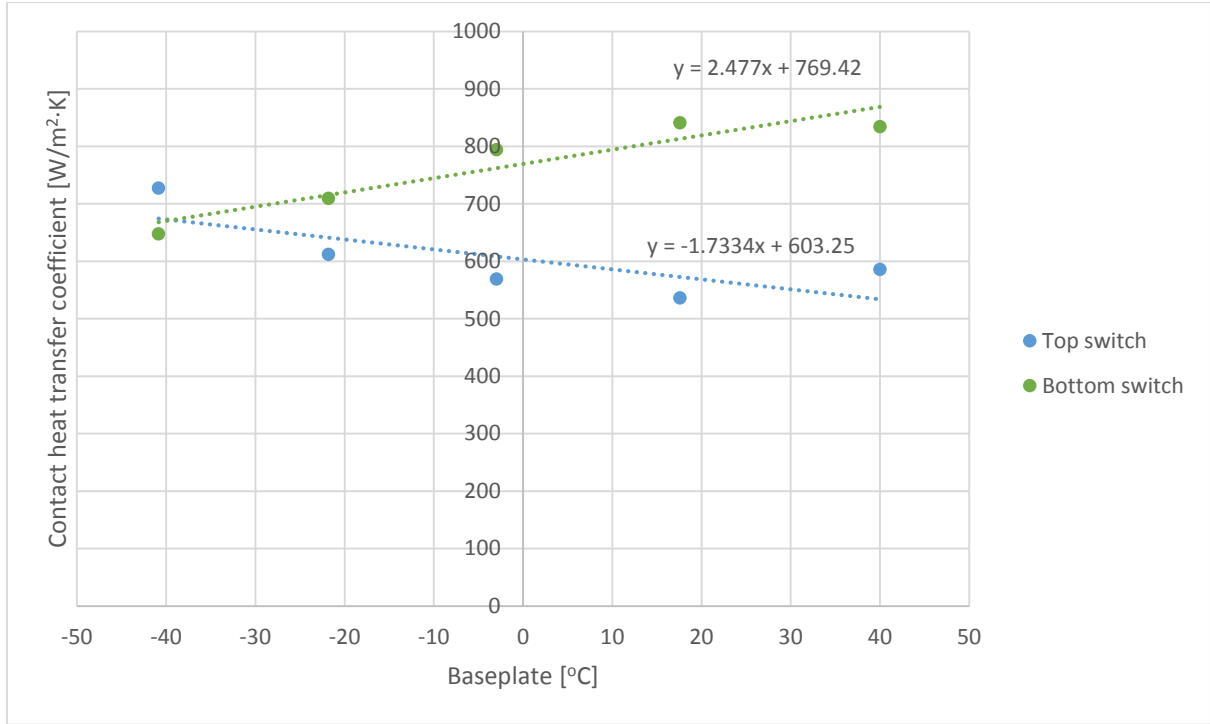


Figure 71: Sigraflex contact heat transfer coefficient for second prototype

8.1.2 Third prototype

Figure 72 and Figure 73 show the contact heat transfer coefficients with respect to temperature for the third prototype for the OFF and ON-case respectively. Because in the third prototype, the setup is experiencing more severe deviations in the contact heat transfer coefficient with temperature variations, a temperature dependent heat transfer coefficient has been implemented in the thermal model.

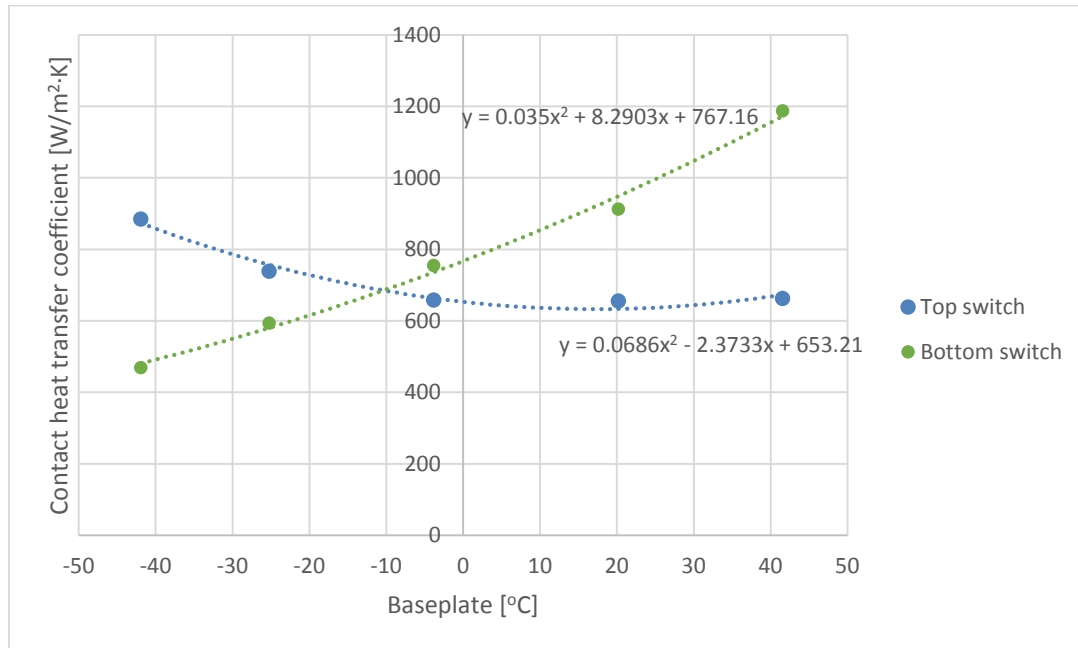


Figure 72: Sigraflex contact heat transfer coefficient for third prototype (OFF-case)

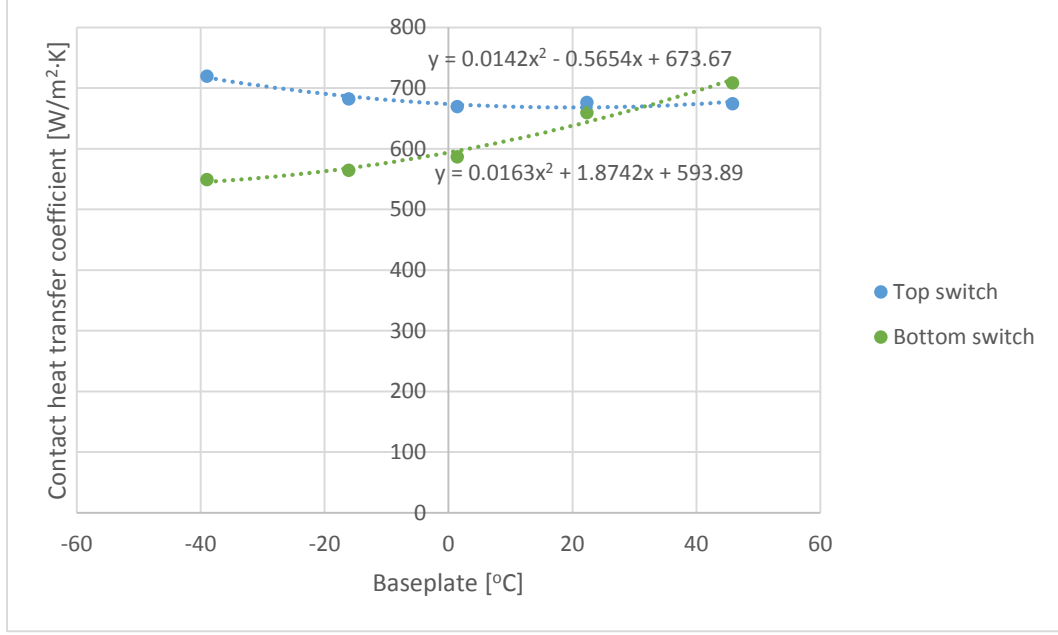


Figure 73: Sigraflex contact heat transfer coefficient for third prototype (ON-case)

8.2 Real time constant calculations

The real-time constant methodology is used in order to validate that the system has reached steady-state. In this methodology, the experimental time rate of change of the temperature dT/dt is monitored with respect to time. More precisely, a backwards difference of 3 minutes is used for each time step, which is normalized per minute and then curve-fitted using an exponential function. The inverse of the curve fit exponent yields the time constant. It should be noted that as the system approaches steady-state, an increased scattering is caused due to the increased relative effect of thermocouple measurement instabilities. Consequently, such data points are not included in the curve fitting [37]. Eventually, the stabilization criterion is taken as:

$$\left. \frac{dT}{dt} \right|_{target} = \frac{\Delta T_{target}}{\tau}.$$

ΔT_{target} is selected to be 0.2°C which is defined by the accuracy of the thermocouples.

8.2.1 Second prototype

8.2.1.1 ON-state

For the ON-case, the terminal time constant from section 7.9, which represents a system averaged time constant, was found to be 3.07 minutes. The FEM yields a theoretical time constant of 3.58 minutes for the top of the switch. The real time constant of the top of the switch was experimentally determined to be 4.48 minutes, a 25.1% difference. This difference is the direct result of the performance of the heat switch in its ON-state, when it is pressurized with Helium. The higher the ON-conductance of the heat switch the smaller the time constant. As it can be seen from Figure 82 in section 8.2.1.1, the actual performance of the heat switch at +20°C, when applying a power of 40 W is at 74.2% of the theoretical value and consequently longer dwell time is required for temperature stabilization. Figure 75 provides a comparison

between the experimental and the FEM results for the ON-case transient response at a nominal baseplate temperature of 20°C. It should be noted that due to instability problems controlling the baseplate temperature, there is an inconsistent offset between the experimental and the theoretical baseplate temperature.

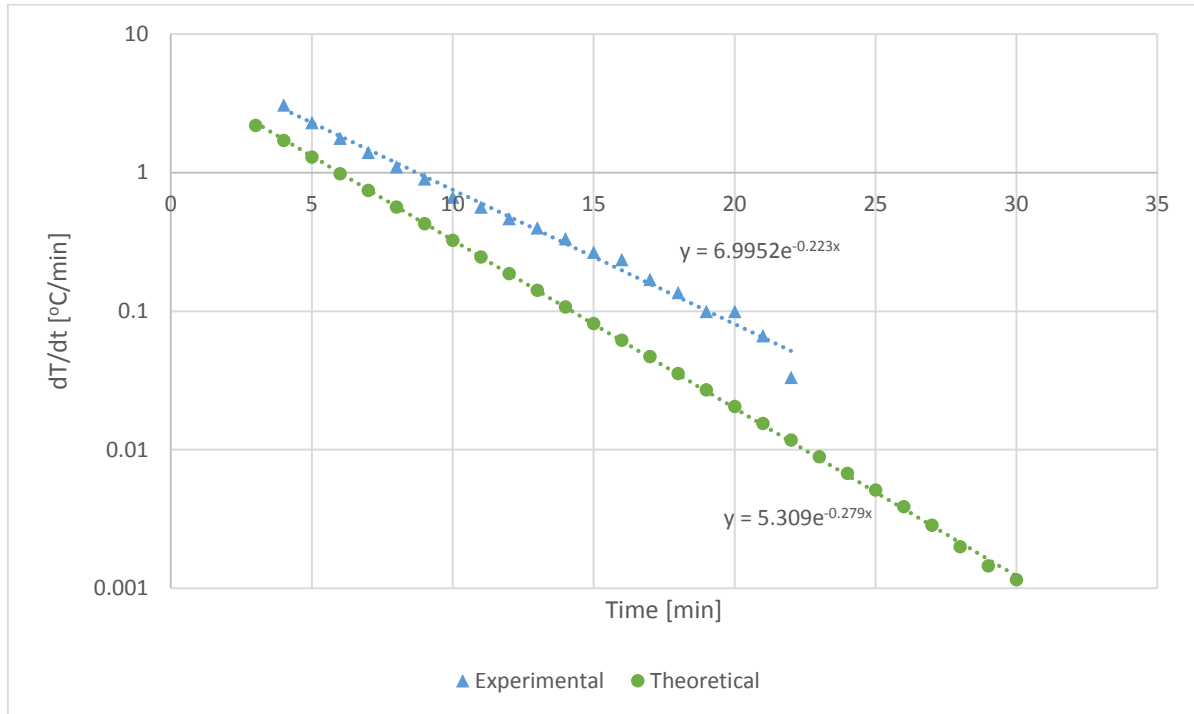


Figure 74: Second prototype real time constant - ON-state (20°C)

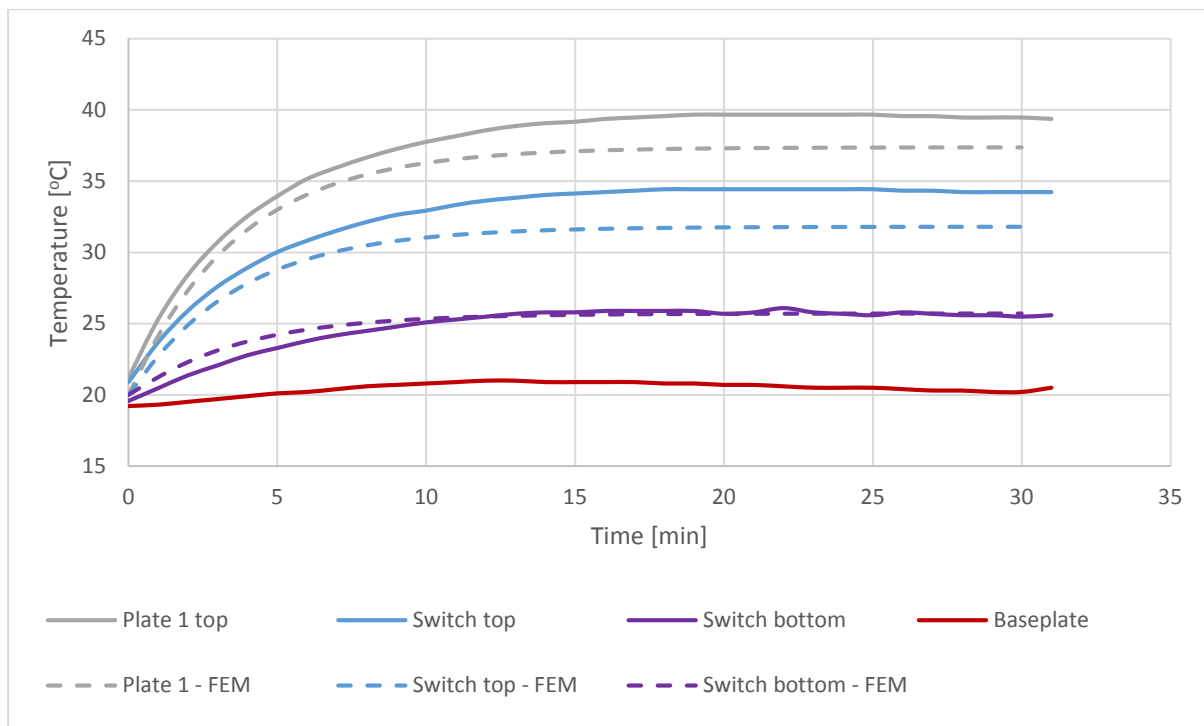


Figure 75: Second prototype ON-case transient response (20°C)

8.2.1.2 OFF-state

For the OFF-case, the terminal time constant from section 7.9 was found to be 27.56 minutes. For the OFF-case, the FEM yields a theoretical time constant of 30.6 minutes for the top of the switch. The same real time constant was experimentally determined to be 21.1 minutes, a -31.0% difference. This difference is the direct result of the performance of the heat switch in its OFF-state. The higher the OFF-conductance of the heat switch the smaller the time constant. As it can be seen from Figure 91 in section 8.2.1.2, the heat transfer coefficient of the heat switch at +20°C, when applying a power of 5 W is 26.6% higher than the theoretical value. However, it should be noted that the baseplate exhibited significant instability during the test for the evaluation of the time constant. This can be seen from Figure 77, where the baseplate, the switch and plate 1 exhibit periodic fluctuations with a period of 66 minutes. Based on the temperature profile, the top and the bottom of the switch are out of phase by about 15 minutes. Throughout a mission lifetime, the baseplate of a unit experiences periodic temperature variations. Consequently, the phase difference provides an indication of the responsiveness of the switch.

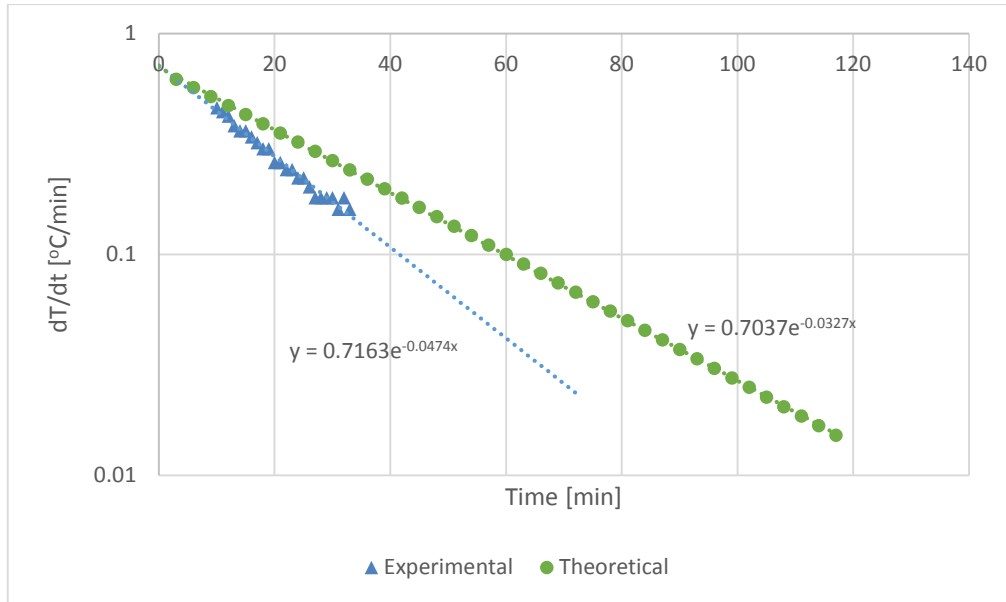


Figure 76: Second prototype real time constant - OFF-state (20°C)

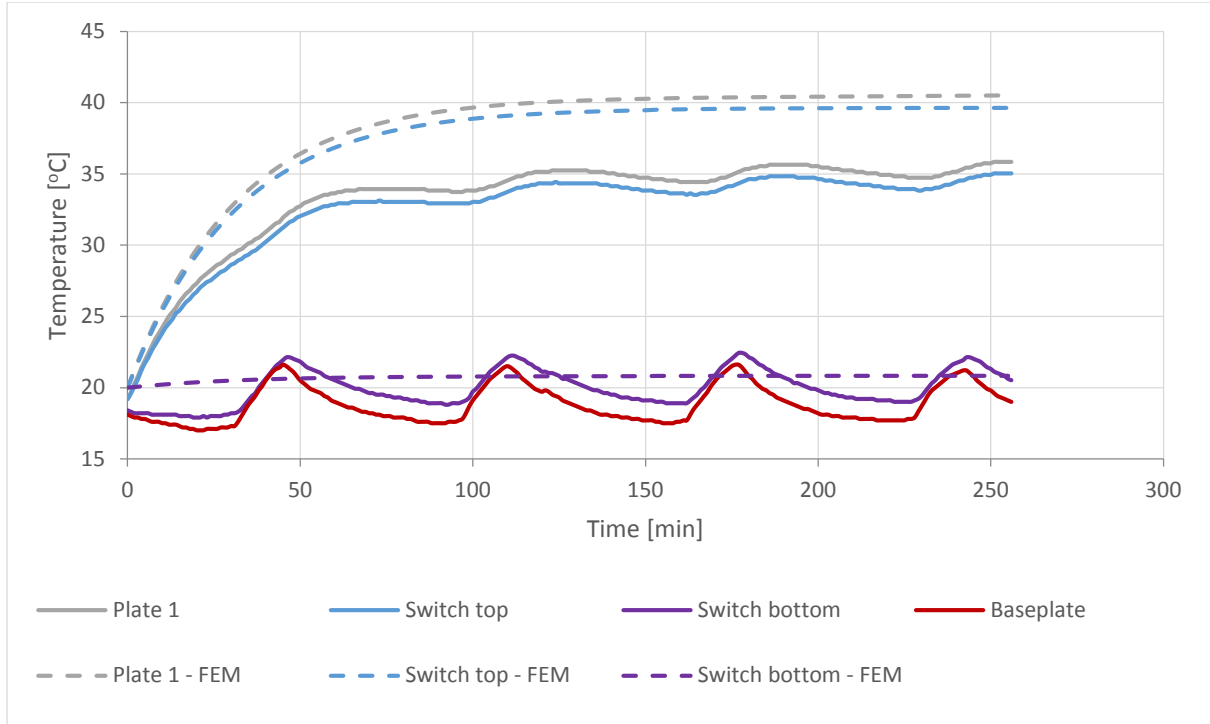


Figure 77: Second prototype OFF-case transient response (20°C)

8.2.2 Third prototype

8.2.2.1 ON-state

For the ON-case, the terminal time constant from section 7.9 was found to be 6.52 minutes. The FEM yields a theoretical time constant of 6.45 minutes for the top of the switch. The real time constant of the top of the switch was experimentally determined to be 12.44 minutes, a 92.8% increase. This difference is the direct result of the performance of the heat switch in its ON-state, when pressurized with Helium. As it can be seen from Figure 90 in section 8.3.1.2, the actual performance of the heat switch at +20°C, when applying a power of 50 W is at only 14.8% of the theoretical value and consequently longer dwell time is required for temperature stabilization. Because of this significant deviation in performance, a heating power of 50 W is used instead of 180 W as mentioned in section 7.8. Figure 78 provides a comparison between the experimental and the FEM results for the ON-case transient response at a nominal baseplate temperature of 20°C. As can be seen from Figure 79, the baseplate temperature could not be maintained stable during the heating process of the system and increased from 16.5°C to 23°C, when the rest of the system reached stability, indicated by the plateau of the temperatures.

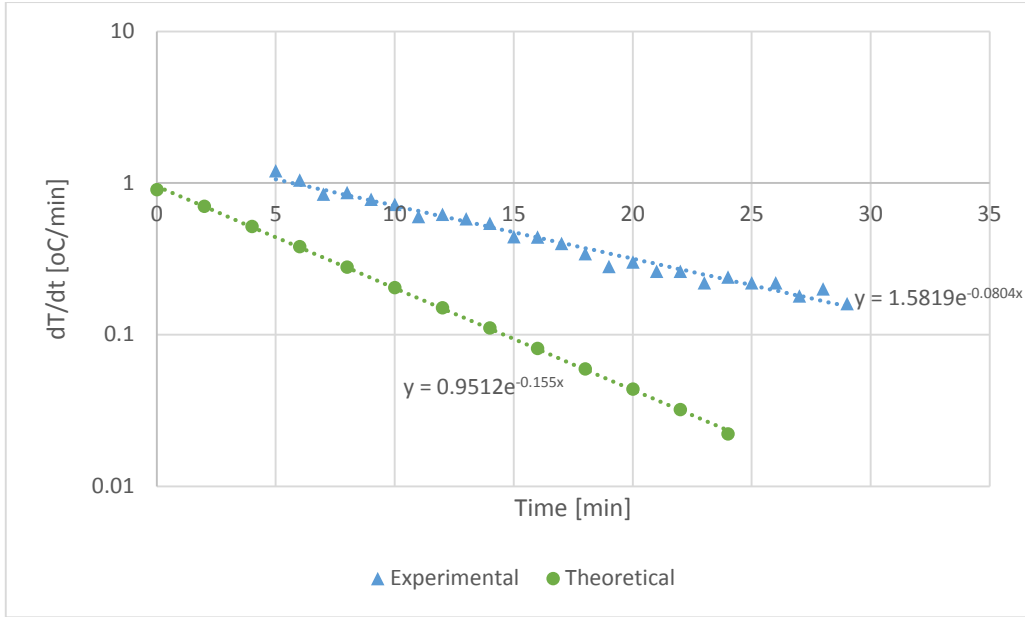


Figure 78: Third prototype real time constant - ON-state (20°C)

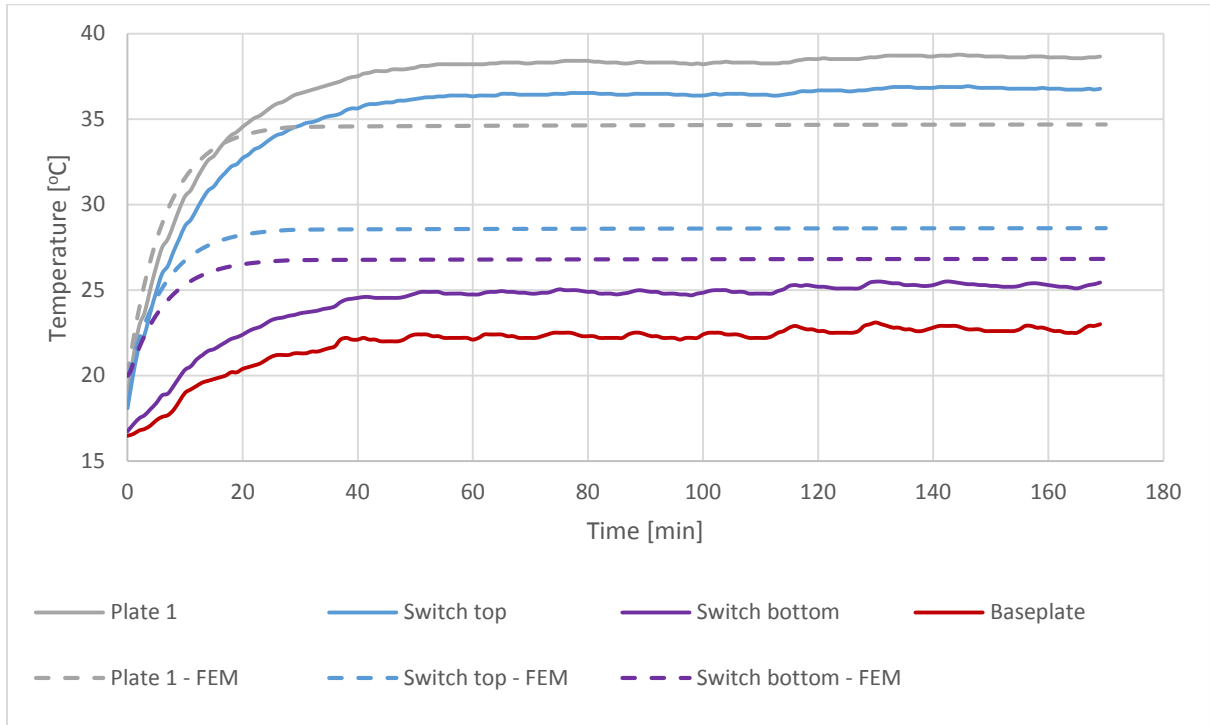


Figure 79: Third prototype ON-case transient response (20°C)

8.2.2.2 OFF-state

For the OFF-case, the terminal time constant from section 7.9 was found to be 43.0 minutes. For the OFF-case, the FEM yields a theoretical time constant of 44.9 minutes for the top of the switch. The real time constant of the top of the heat switch was experimentally determined to be 23.9 minutes, a -46.8% difference. Similarly to the second prototype, the difference is the direct result of the performance of the heat switch in its OFF-state. As it can be seen from Figure 94 in section 8.3.2.2, the heat transfer coefficient of the heat switch at +20°C, when applying a power of 15 W is 89.8% higher than the theoretical value, which entails a significant

decrease in the time constant. It should be noted that in this case, the baseplate exhibited a much better stability compared to Figure 77, providing better accuracy in the estimation of the real time constant.

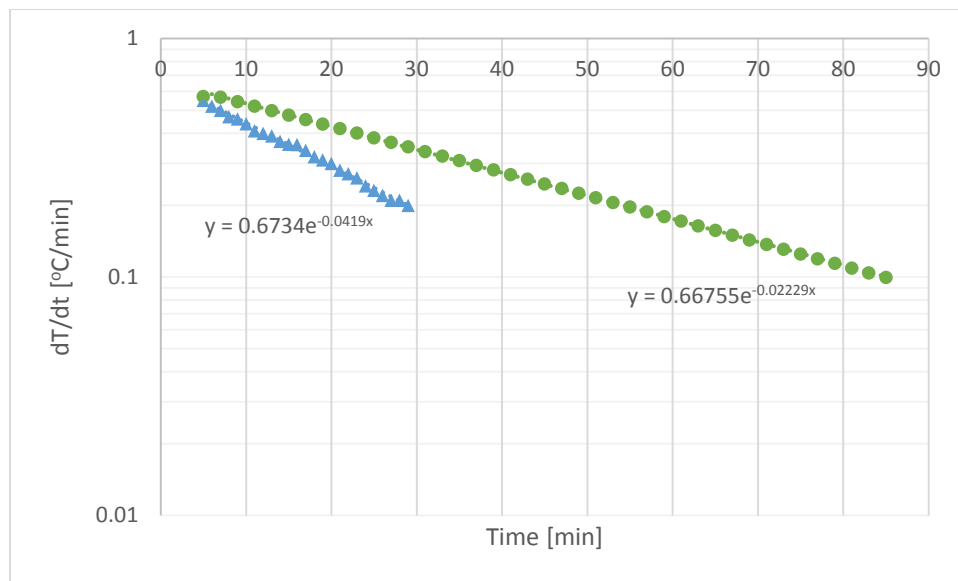


Figure 80: Third prototype real time constant - OFF-state (20°C)

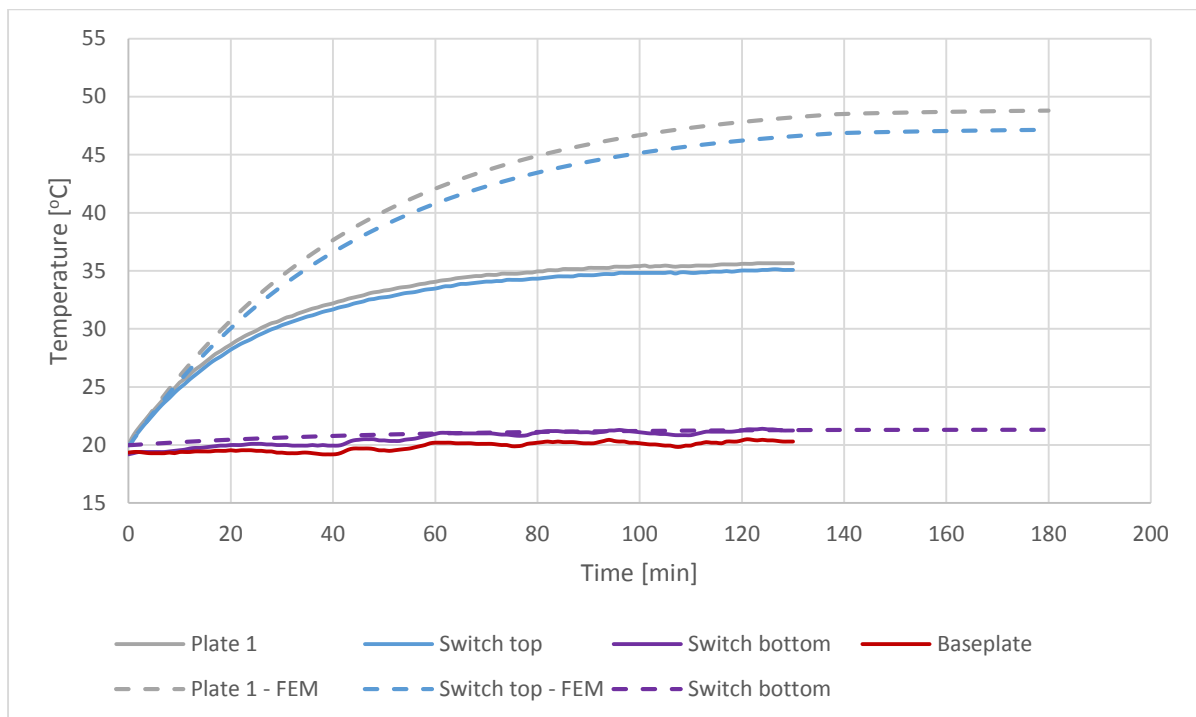


Figure 81: Third prototype OFF-case transient response (20°C)

8.3 ON/OFF conductances

8.3.1 ON-conductance

8.3.1.1 Second prototype

Figure 82 shows the experimental and theoretical values of the heat transfer coefficient across the heat switch in its ON-state with respect to the baseplate temperature, when a power of 40 W is applied on Plate 1. All measurements were performed at a controlled pressure of 1.7 bar, thus exceeding the theoretical continuum regime pressure limit of ≈ 1 bar for Helium. The experimental measurements show a degraded performance when compared to the theoretical values of the FEM. Additionally, the curve of the experimental data has a steeper slope than the theoretical curve. The gas thermal conductivity values were obtained from the NIST Chemistry WebBook, which states “The uncertainty in thermal conductivity is 5%, except at low temperatures where it increases to 10%”. Such uncertainty cannot fully justify this deviation. The differences can be attributed to impurities in the operating gas and the geometry of the heat switch. The impurities in the operating gas can stem from a) the gas tank, b) mixing of helium with ambient air due to tubing leakage, c) trapped air in the switch. The switch is 3D-printed and consequently cavities with trapped air can be created during manufacturing. To minimize the effect of trapped air in the switch, a thermal bake-out was performed at a temperature of $+80^{\circ}\text{C}$ prior to testing. Furthermore, as shown in section 6.3, there is a significant deviation of the actual gap distance from the nominal. The gap distance is critical for the performance of the switch, since a larger gap filled with a gas that has low thermal conductivity leads to a significantly degraded performance. Unfortunately, the actual gap distance after mounting of the test setup cannot be measured and consequently cannot be taken into account for the theoretical results. Moreover, because of the inaccessibility between the aluminium plates and the switch, only one thermocouple per surface is used and consequently heat spread is not taken into account in this measurement. This can explain the deviation from the theoretical values.

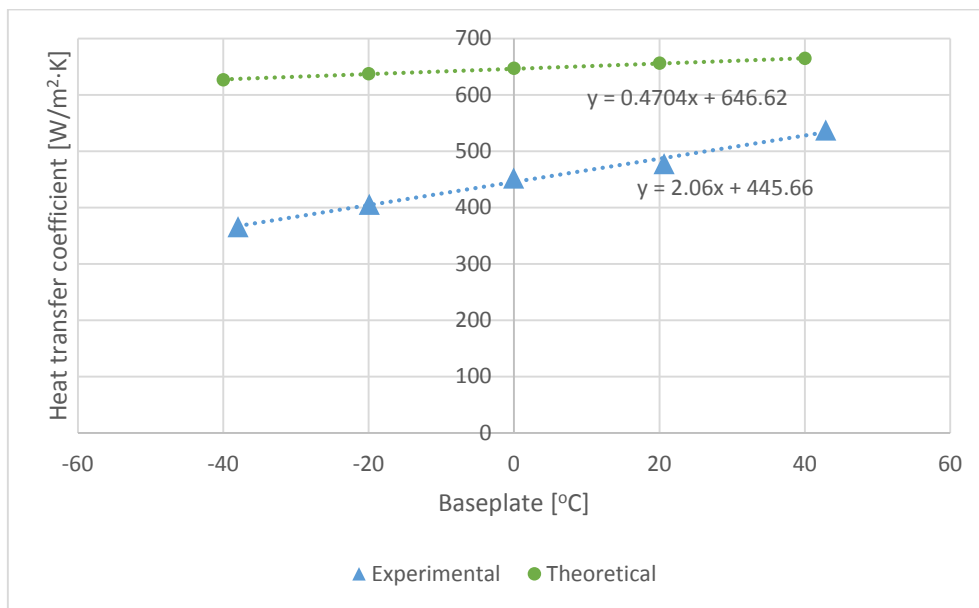


Figure 82: Second prototype ON-state heat transfer coefficient ($P = 40$ W)

A major consideration for the ON-case is the contact heat transfer coefficient. Because of the non-uniform heat transfer coefficient, there is a preferable heat path, where the thermal conductance is higher. In this case, because of the arc-shape of the switch, it is possible that most of the heat flows through the edges of the top side and outflows through the middle of the bottom side, as shown below. Consequently, since the thermocouples are placed in the middle, a larger temperature gradient is measured across the switch. Additionally, in the ON-case a significant in-plane temperature gradient is expected compared to the OFF-case, as shown in Figure 84. The straight line in the middle is the result of the groove on Plate 1.

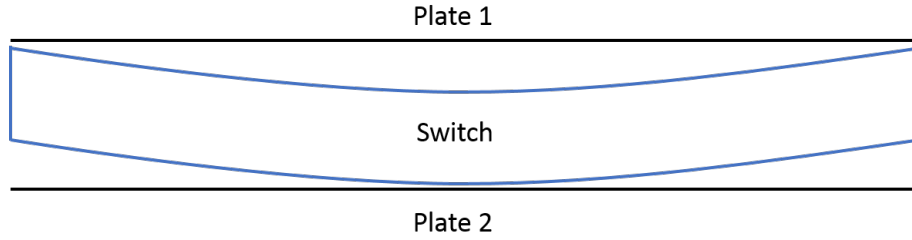


Figure 83: Exaggerated arc-shape deformation of second prototype

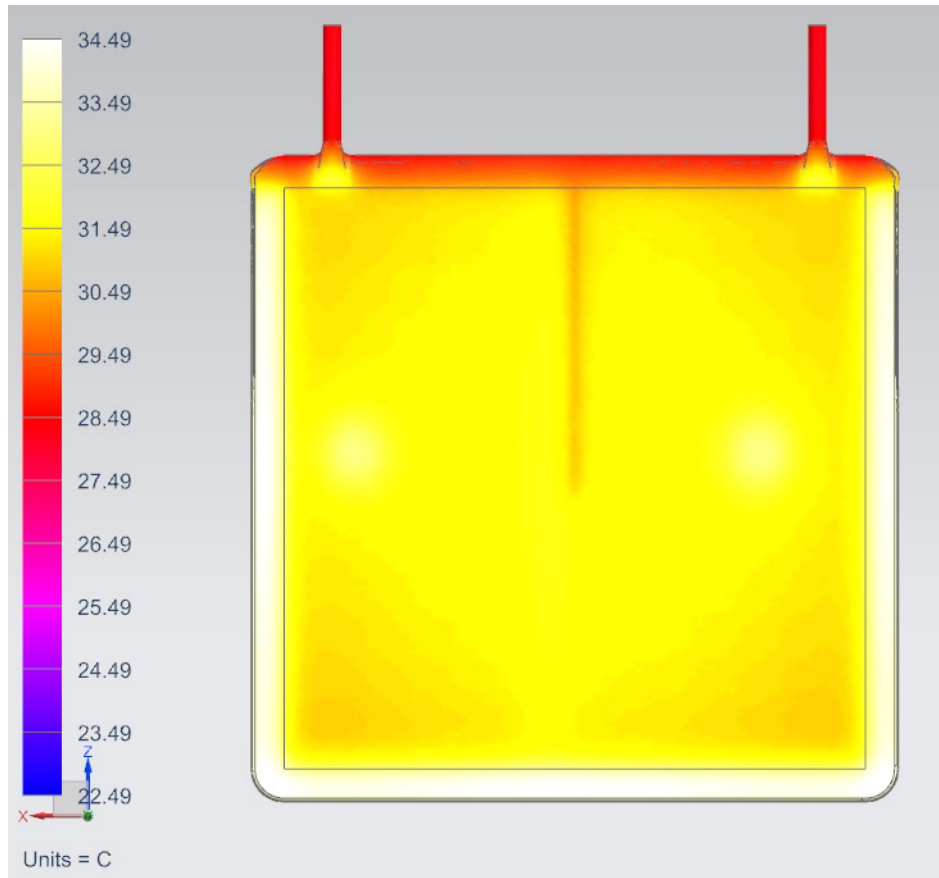


Figure 84: Second prototype in-plane temperature distribution (ON-case)

Consequently, in order to obtain a more accurate measurement of the conductance, the temperature gradient from Plate 1 all the way to Plate 2 can be used. Because of the high thermal conductivity of aluminium, both plates exhibit significant temperature uniformity,

with temperature variations of only 0.2°C. Therefore, the location of the thermocouples is not critical and there is an essential reduction in the uncertainty.

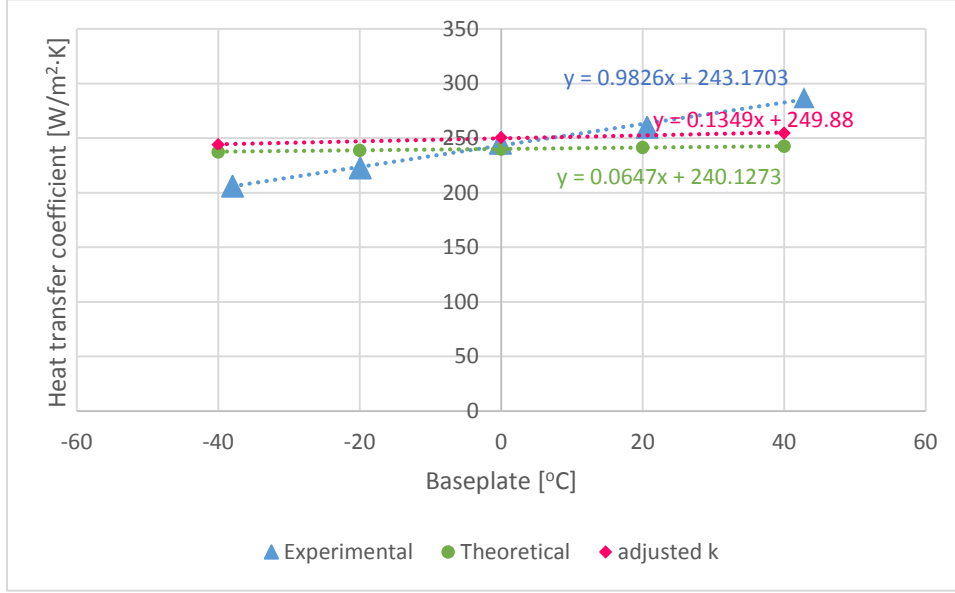


Figure 85: Second prototype ON-state overall heat transfer coefficient (Plate 1 to Plate 2)

As can be seen from Figure 85, the FEM is much better correlated with the experimental values when compared to Figure 82. The pink curve in Figure 85 indicates the overall heat transfer coefficient when a temperature-dependent thermal conductivity for Ti-6Al-4V is used. This dependency is more critical in the OFF-case. For more information, please see section 8.3.2. The experimental data still exhibits a higher sensitivity on temperature. This sensitivity is most likely the result of the uncertainty in the contact heat transfer coefficient. Additionally, because of the thermal expansion and contraction with varying temperatures, the gap size changes, a factor that has not been taken into account in the theoretical model. Moreover, the applied torque on the fasteners changes with changes in temperature, thus affecting the contact heat transfer coefficient. Eventually, the model exhibits maximum deviation of +19.9% at -40°C and -9.6% at +40°C. At 20°C, the deviation is only 3.9%.

8.3.1.2 Third prototype

Initially, it was intended to apply a heat load of 180 W for the ON-case of the third prototype as mentioned in section 7.8. However, because of the low ON-conductance, a lower power was applied in order to not generate an excessive gradient that could harm the equipment. Figure 86 shows the experimental and theoretical values of the heat transfer coefficient across the heat switch in its ON-state (Helium) with respect to the baseplate temperature, when a power of 50 W is applied on Plate 1. All measurements were performed at a controlled pressure of 1.7 bar, thus exceeding the theoretical continuum regime pressure limit of ≈ 1 bar for Helium. Similarly to the second prototype, the overall heat transfer coefficient from Plate 1 to Plate 2 is provided in Figure 87.

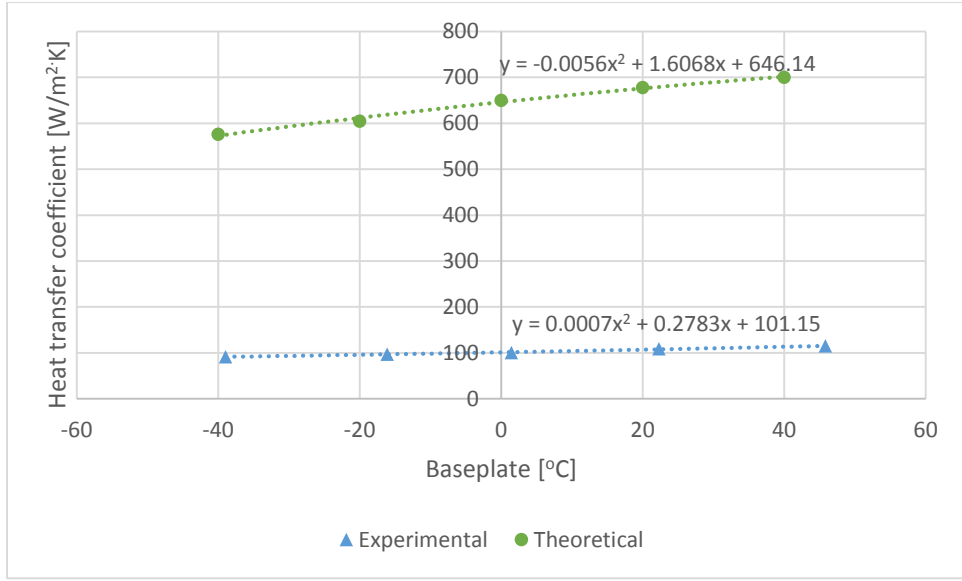


Figure 86: Third prototype ON-state heat transfer coefficient ($P = 50 \text{ W}$)

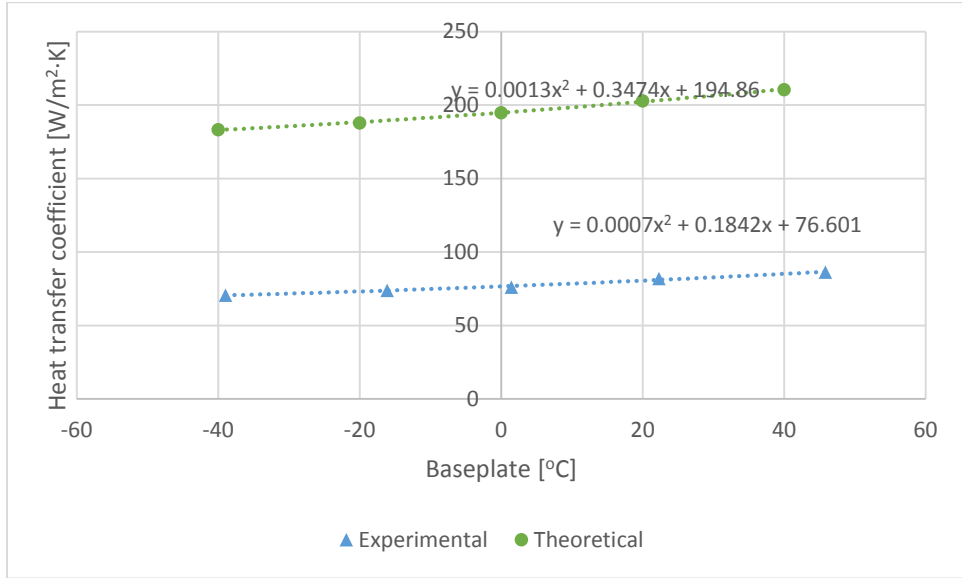


Figure 87: Third prototype ON-state overall heat transfer coefficient (Plate 1 to Plate 2)

The experimental measurements show a significantly degraded performance when compared to the theoretical values of the FEM. This degradation stems from the severe deviation of the manufactured third prototype from the CAD model as explained in section 6.3.2. Due to its larger area compared to the second prototype, the third prototype cannot be flattened easily, even when applying a high bolt torque. This is because the bolt pattern is perimeteric and the pressure in the middle is not greatly affected. Consequently, the gaps in the middle of the switch cannot be reduced significantly and reach a value closer to the nominal as happened with the second prototype. Unfortunately, the actual gap distance after mounting of the test setup cannot be measured directly. However, the effective gap distance can be estimated by repeating the test under similar conditions with another gas. More specifically, another round of testing was repeated for the third prototype using Neon as the active gas. At a baseplate temperature of 20°C, the total thermal resistance from plate 1 to plate 2 was measured at 0.36925 °C/W and 0.30500 °C/W for Neon and Helium respectively. For simplification of the

calculations, all the leak conductive and radiative conductances from Figure 66 can be neglected, since the leak power is estimated at only 2% according to section 9.2. G_{cond} is the total conductance represented in Figure 21. The two experiments showed insignificant differences in the contact conductances through the Sigraflex and consequently we can assume they are equal. In this case, the thermal networks consists of multiple thermal resistances in series that are identical, except for the gas resistance. The difference between the two experimental total resistances provides the difference between the resistances of the two gases.

$$\Delta R_{\text{total}} = R_{\text{Ne}} - R_{\text{He}} = \frac{L_{\text{eff}}}{A} \left(\frac{1}{k_{\text{Ne}}} - \frac{1}{k_{\text{He}}} \right) \quad (8.3-1)$$

With $k_{\text{Ne}} = 0.0476 \text{ W/m} \cdot \text{K}$ and $k_{\text{He}} = 0.1535 \text{ W/m} \cdot \text{K}$ at 20°C , the ratio of the area to the effective gap is $\frac{A}{L_{\text{eff}}} = 226$. Using the nominal dimensions, the ratio is:

$$\left(\frac{A}{L} \right)_{\text{nom}} = \frac{0.0930}{0.2 \cdot 10^{-3}} = 465 \quad (8.3-2)$$

Comparing the two results and using the nominal area of 0.0930 m^2 , we see that the effective gap is 2.06 times the nominal, which translates into 0.412 mm . Section 8.4.2 provides an estimation of the effective gap size of the third prototype by measuring the pressure of the transition into the continuum regime for Helium. The two methods are in very good agreement and result in an effective gap that is twice as large as the nominal one.

Figure 88 and Figure 89 provide the experimental and theoretical values of the heat transfer coefficient of switch and the overall heat transfer coefficient respectively, for the ON-case using Neon. A heating power of 25 W is applied. A smaller power is applied, when compared to Helium in order to avoid overheating due to the smaller thermal conductivity of Neon, which entails a worse ON-conductance.

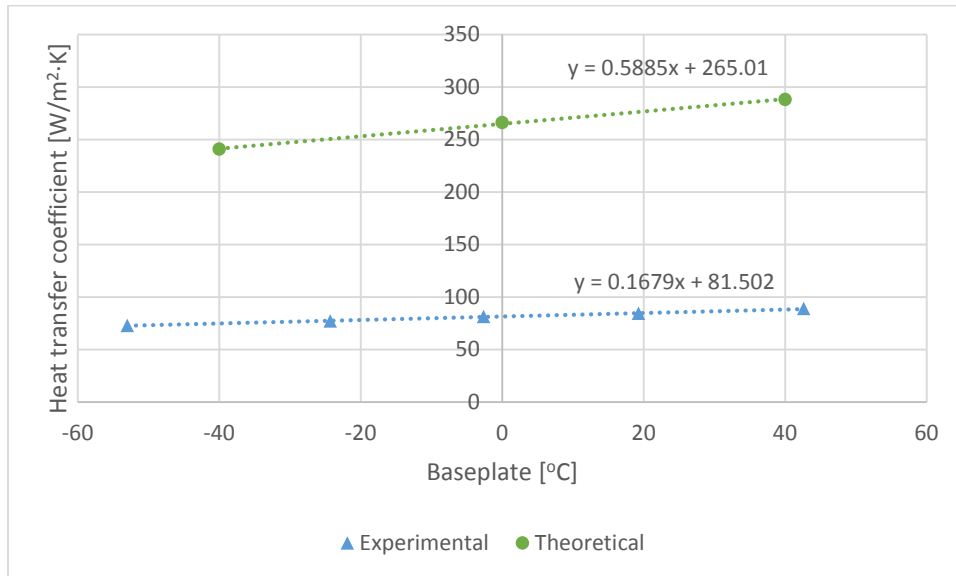


Figure 88: Switch heat transfer coefficient (Neon)

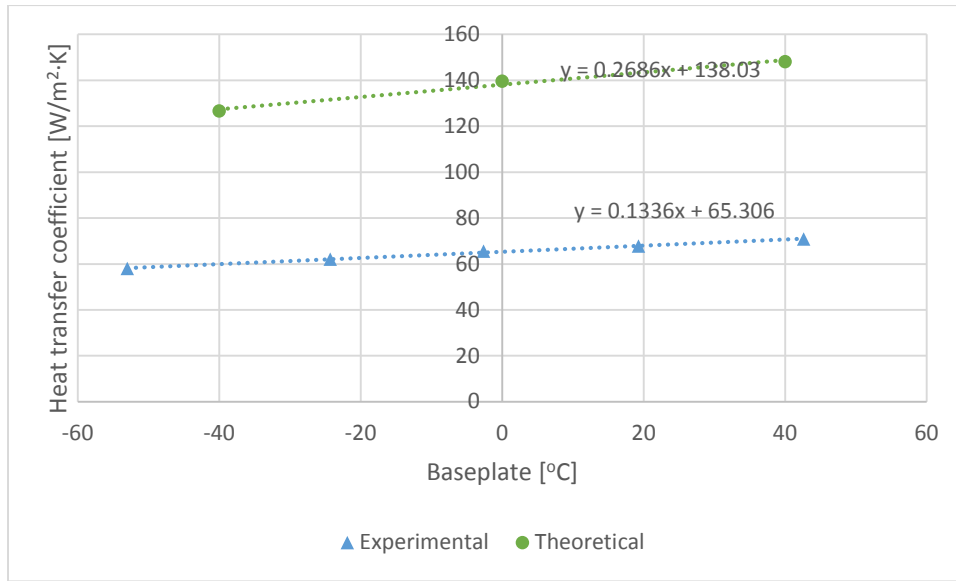


Figure 89: Overall heat transfer coefficient (Neon)

8.3.2 OFF-conductance

8.3.2.1 Second prototype

Figure 91 shows the experimental and theoretical values of the heat transfer coefficient across the heat switch in its OFF-state with respect to the baseplate temperature, when a power of 5 W is applied on Plate 1. The initial predictions indicated by the green curve exhibited a deviation of -13.0% to -20.2% from the experimental values. An important parameter that adds some uncertainty in the simulations is the thermal conductivity of the material. Initially, in the simulations, the thermal conductivity of Ti-6Al-4V was considered to be independent of the temperature, with a constant value of 6.7 W/m · K. Figure 90, obtained from the Military Handbook for “Metallic Materials and Elements for Aerospace Vehicle Structures” (MIL-HDBK-5H), shows the dependence of the thermal conductivity of some titanium alloys with respect to temperature. In the temperature range of -40°C to +60°C, the thermal conductivity of the alloy changes from 6.4 to 7.5 W/m · K, a 17.2% increase, which is significant for the OFF-case. The pink curve on Figure 91 shows the heat transfer coefficient of the heat switch with the adjusted thermal conductivity. This led to a better correlation between the experimental and theoretical data, with a deviation from -11.8% at -40°C to -16.2% at +40°C baseplate temperature.

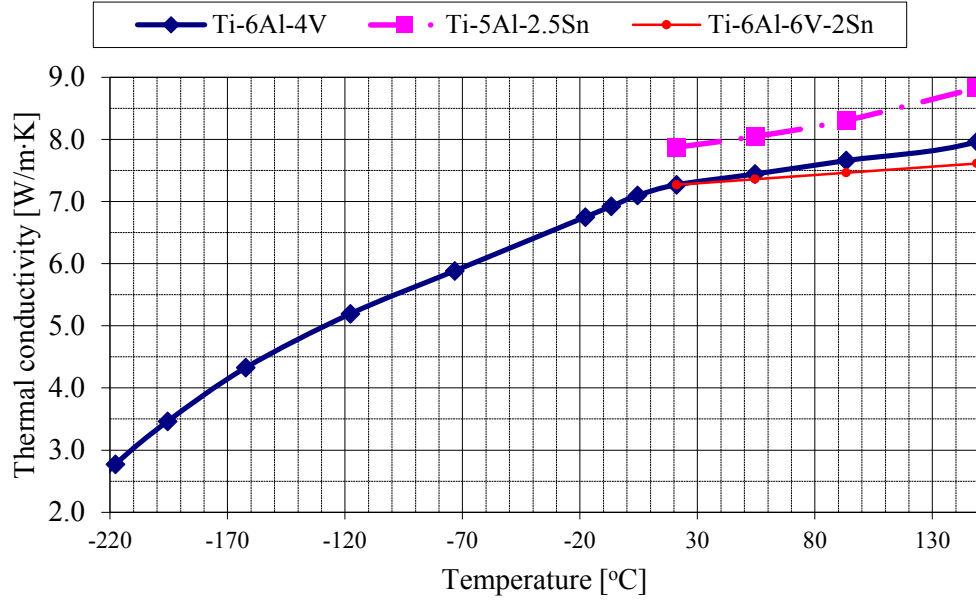


Figure 90: Effect of temperature on titanium alloys thermal conductivity

Another important consideration is the uncertainty on the emissivity of the internal surfaces of the heat switch. As mentioned in section 6.1, the emissivity measurement was conducted on the smoother external surface. Increasing roughness leads to an increase in the emissivity and consequently a larger heat transfer coefficient. An increase of the emissivity from 0.57 to 0.62, combined with the adjustment for the thermal conductivity closed the gap between the experimental and theoretical values (-10.3% to -12.6%). However, this emissivity value is simply an assumption and cannot be measured exactly.

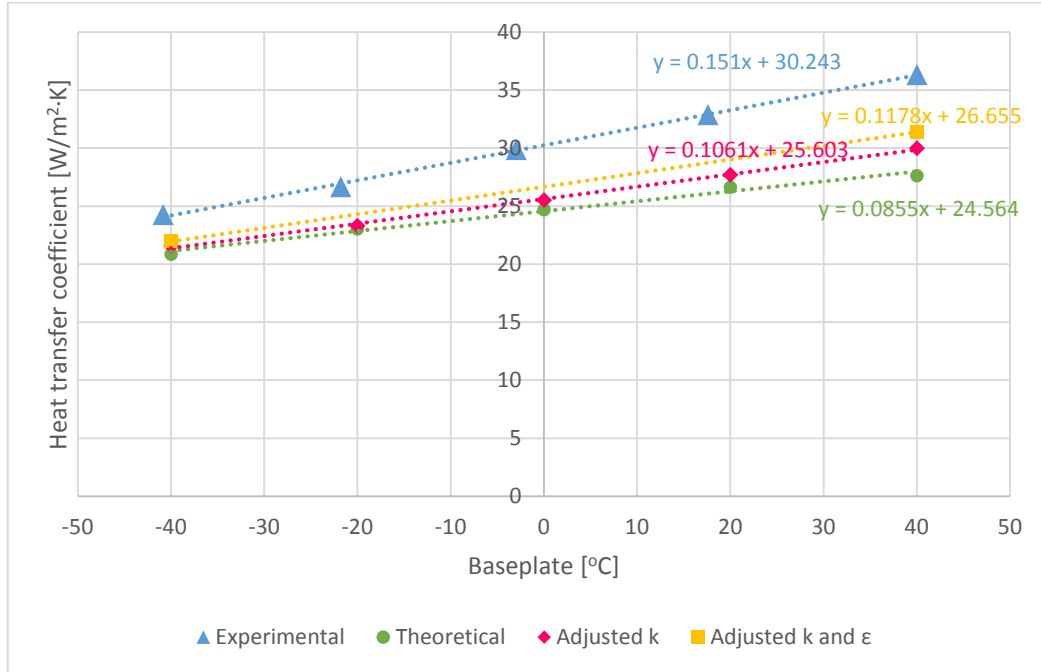


Figure 91: Second prototype OFF-state heat transfer coefficient ($P = 5 \text{ W}$)

The remaining deviations can be attributed to other factors that cannot be controlled or quantitatively be taken into account, such as the deviation of the manufactured heat switch from the CAD model. The internal features of the heat switch have an impact on the performance. This is true especially when the applied bolt torque is taken into account. The applied torque deforms the heat switch, reducing the gaps between the fins, especially since the support pillars have cracked. A reduction in the gap distance is translated into an increase in the view factors between the fin surfaces, which leads to an increased radiative conductance. It is possible that some of the fins are so deformed that they come in contact, providing an additional parasitic heat path.

In order to minimize the internal pressure, the rotary pump kept running continuously throughout testing of the OFF-case to provide a vacuum of less than 10^{-4} mbar. Such low pressure is measured by an additional pressure sensor placed at the outlet of the pressure line. Since it is impossible to place a pressure sensor inside the heat switch, there is an uncertainty about the pressure in the cavity of the switch. It is possible that some gas molecules remain trapped inside the miniscule channels of the switch and with increasing temperature these molecules conduct more heat.

Similarly to the ON-case, to the overall gradient from Plate 1 to Plate 2 can be found. In this case the deviation of the theoretical from the experimental value is from -11.8% to -16.2%.

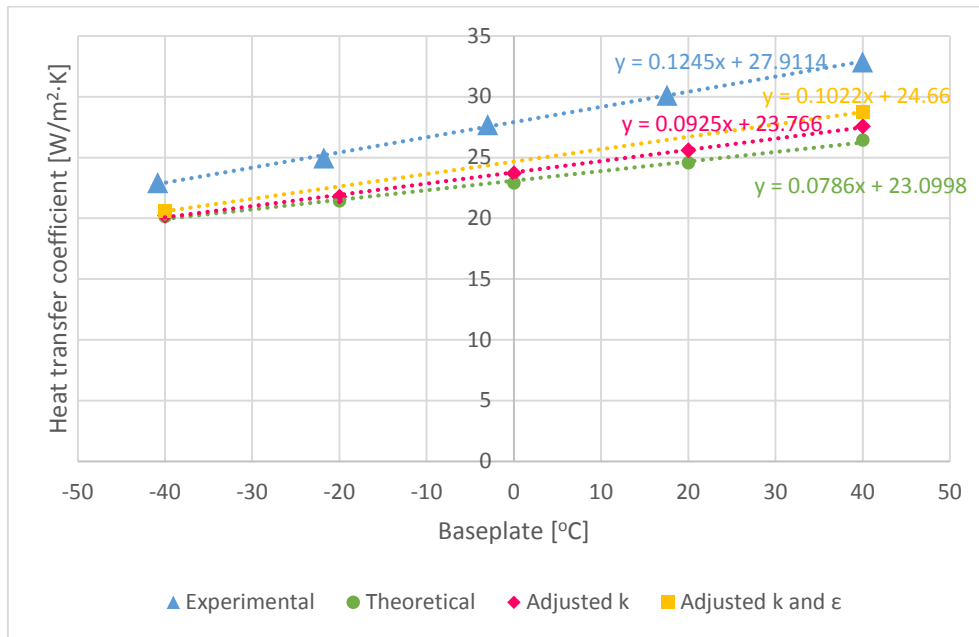


Figure 92: Second prototype OFF-state overall heat transfer coefficient (Plate 1 to Plate 2)

In the OFF-case, the temperature of the two faces is more uniform and only small in-plane gradients occur. This can be proved by comparing Figure 93 with Figure 84. Therefore, the temperature measurements are more representative in the OFF-case and are independent of the thermocouple location.

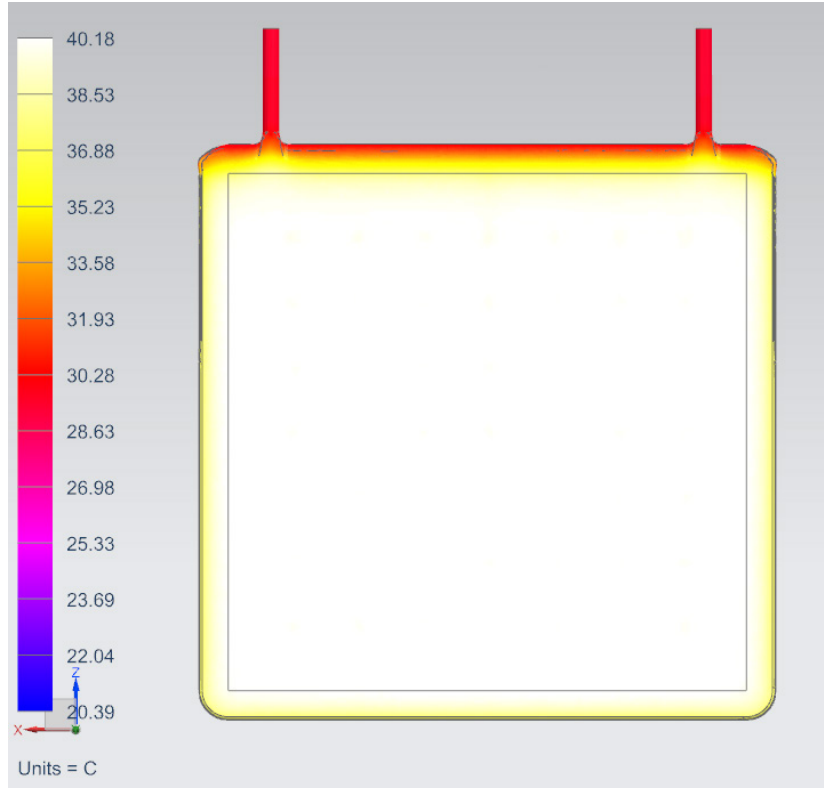


Figure 93: Second prototype in-plane temperature distribution (OFF-case)

For this reason, the heat transfer coefficient of the OFF-state can be used to determine the average effective contact heat transfer coefficient between the aluminum plates and the heat switch. Assuming the contact heat transfer coefficient to be equal on both sides of the switch, the total heat transfer coefficient can be found as:

$$\frac{1}{h_{total}} = \frac{1}{h_{switch}} + \frac{2}{h_{contact}}$$

This equation results in average of $h_{contact} = 755 \text{ W/m}^2 \cdot K$, with a standard deviation $\sigma = 48.6 \text{ W/m}^2 \cdot K$. This value was used iteratively in the simulations to correlate the theoretical with the experimental data.

8.3.2.2 Third prototype

Figure 94 shows the experimental and theoretical values of the heat transfer coefficient across the heat switch in its OFF-state with respect to the baseplate temperature, when a power of 15 W is applied on Plate 1. The experimental values of the OFF-conductance are almost double of the theoretical values.

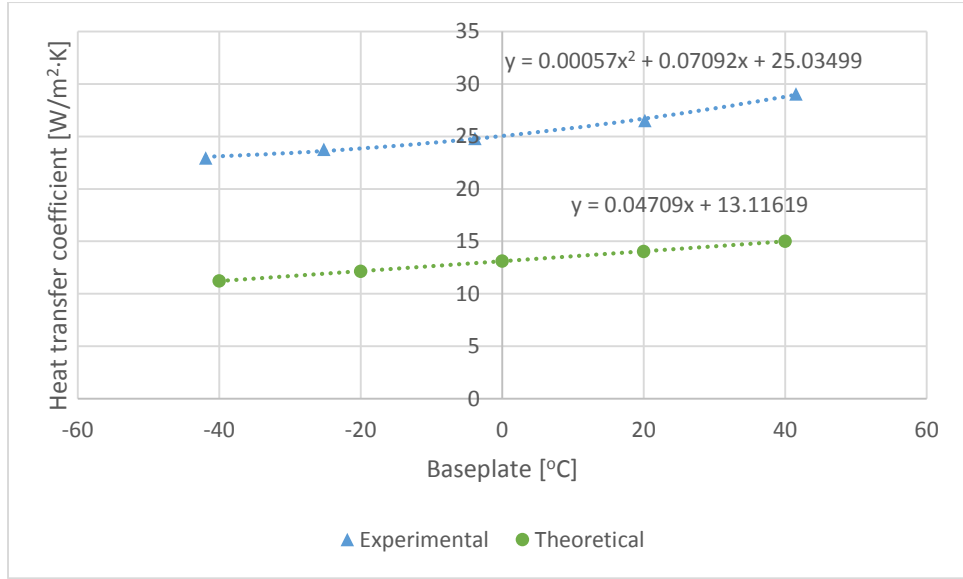


Figure 94: Third prototype OFF-state heat transfer coefficient ($P = 15 \text{ W}$)

This significant difference can be explained by the deviation of the manufactured third prototype from the original CAD model, such as the increased thickness, which leads to a smaller thermal resistance. The theoretical mass of the third prototype is 335.3 g. However, the measurements showed a mass of 354.6 g, a 5.8% increase, which could partially explain the deviation in the OFF-conductance. It is also possible that at some locations the fins are touching the other side of the switch similarly to Figure 30. Additionally, the uncertainty about the pressure inside the cavity of the switch remains. Consequently, it is possible that trapped gas molecules conduct heat across the channels.

Figure 95 shows the overall gradient from Plate 1 to Plate 2. This graph removes any uncertainties stemming from the thermocouples placement, since the overall experimental heat transfer coefficient remains almost double the theoretical one and it proves that the third prototype does not operate in its ideal performance.

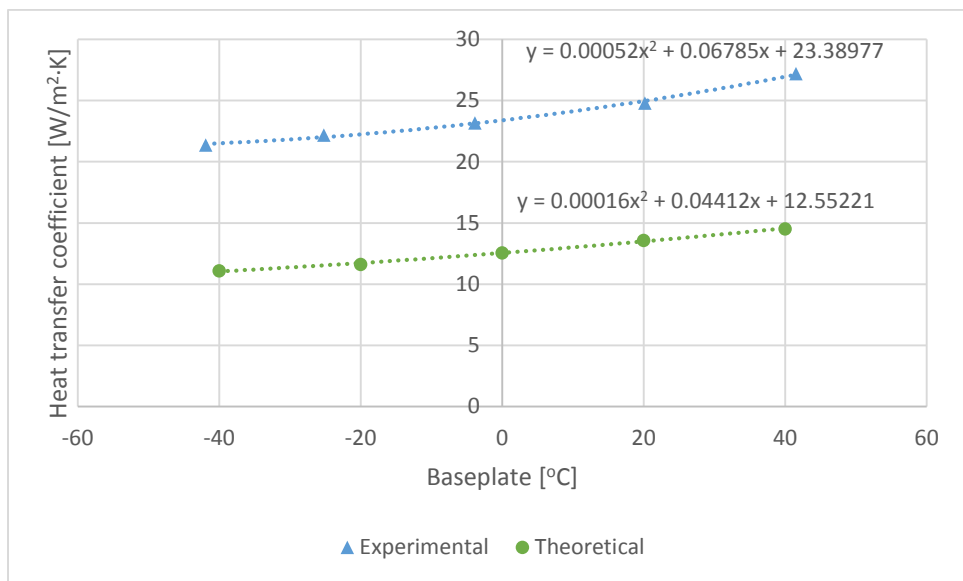


Figure 95: Third prototype OFF-state overall heat transfer coefficient (Plate 1 to Plate 2)

8.4 Conductance dependence on pressure

As mentioned in section 5.3, the pressure inside the switch is very critical for its performance, as it dictates the thermal conductivity of the gas. Even though the test setup passed the initial inspections for the leak rate, both prototypes showed a significant pressure drop throughout the experiment. The leak test was conducted at room temperature, while the test temperature range was between -40°C and $+40^{\circ}\text{C}$ for the baseplate. Due to the mismatch of the CTE between stainless steel and Ti-6Al-4V, the materials contract and expand differently. Thus, when the baseplate temperature is reduced to its minimum value of -40°C , there is some loosening of the tubing connection, which in turn leads to a leak. Typically, this loosening is permanent, even if the temperature is increased, as the nuts need to be retorqued. It should be noted that controlling the pressure below 1 bar is very difficult. Consequently, this leak provided an opportunity to measure the performance of the heat switch with respect to pressure in a controlled manner.

8.4.1 Second prototype

The pressure drop for the second prototype is shown in Figure 96. The scatter after 1500 minutes is the result of the resolution of the data acquisition system and the sensor. However, the exponential trendline appears to fit accurately the obtained data with a constant exponent coefficient.

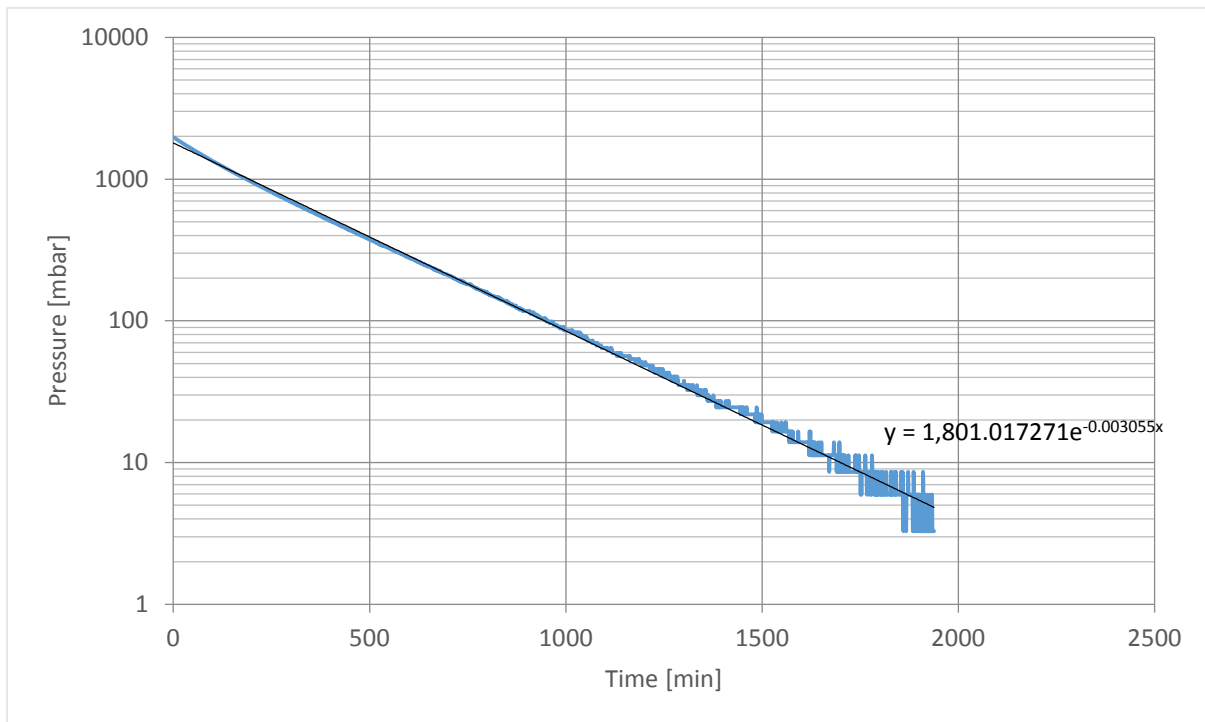


Figure 96: Second prototype pressure drop

Problems with the PID controller of the vacuum facility resulted in instabilities of the baseplate temperature, which exhibited periodic fluctuations of up to 5°C peak-to-valley with a sharp change rate similar to Figure 77. These instabilities produced spikes in the estimation of the heat transfer coefficient. To smooth the spikes, the moving average method was used.

The heat transfer coefficient of the heat switch with respect to pressure is shown in Figure 97. The lower limit of the measurements is dictated by the resolution of the data acquisition system and the lower limit of the pressure sensor (1.33 mbar).

In Figure 97, the heat transfer coefficient has an S-shape as expected, similar to Figure 22 and Figure 23. Figure 98 is a magnification of the 200 to 1800 mbar range that shows the shift from the transition to the continuum regime. The plateau value is around $450 \text{ W/m}^2 \cdot \text{K}$ at a pressure just above 1 bar. This value is in good agreement with the estimated value of 958 mbar from section 5.3.4. At the lower limit, the heat transfer coefficient keeps decreasing with decreasing pressure, which confirms that the gas remains in the transition regime and has not yet shifted to the molecular regime. Unfortunately, because of the baseplate instabilities, it is not possible to distinguish the expected transition jump as explained in section 5.3.

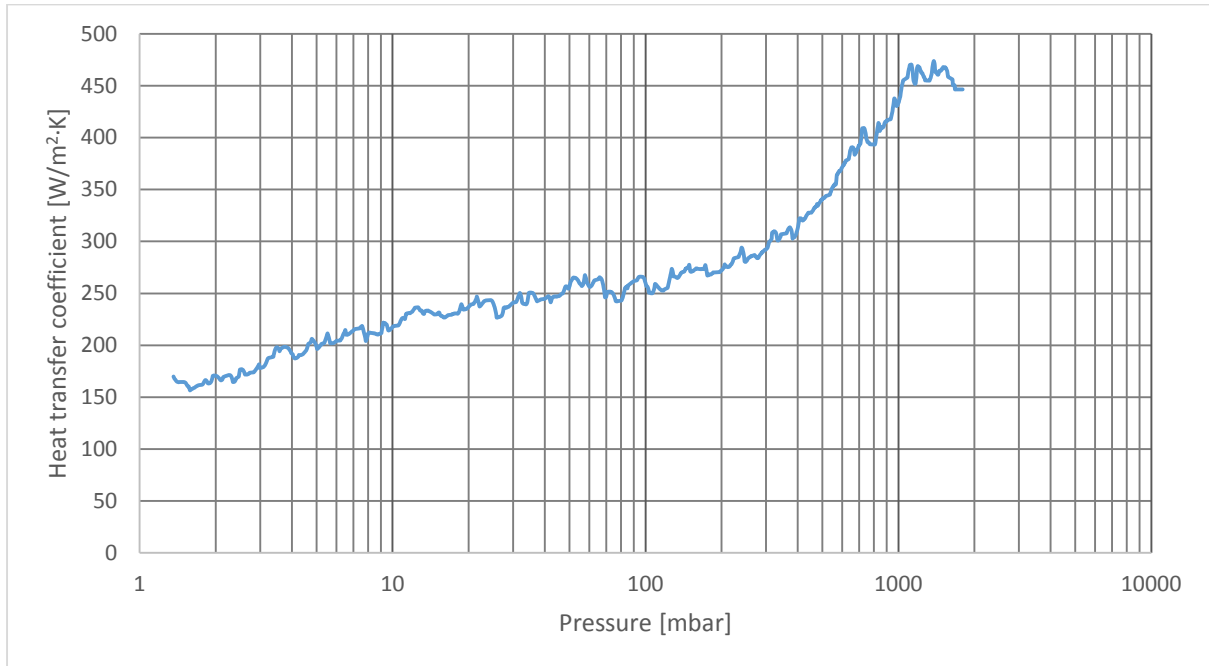


Figure 97: Heat transfer coefficient against pressure (second prototype)

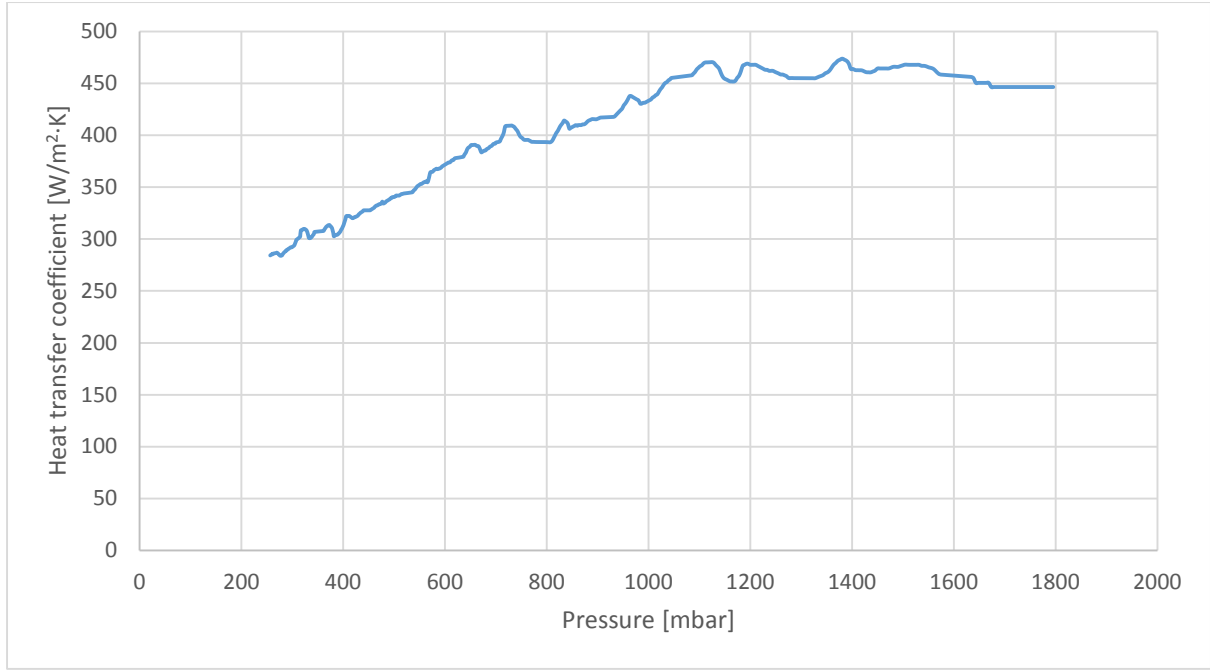


Figure 98: Transition to continuum regime heat transfer coefficient (second prototype)

8.4.2 Third prototype

The third prototype eventually exhibited a leak, despite passing the initial leakage rate inspection. Figure 99 shows the Helium pressure drop over time. Due to scattering because of the sensitivity of the sensor close to its lower limit, points below a pressure of 40 mbar are removed from the graph to allow for a better exponential curve fitting.

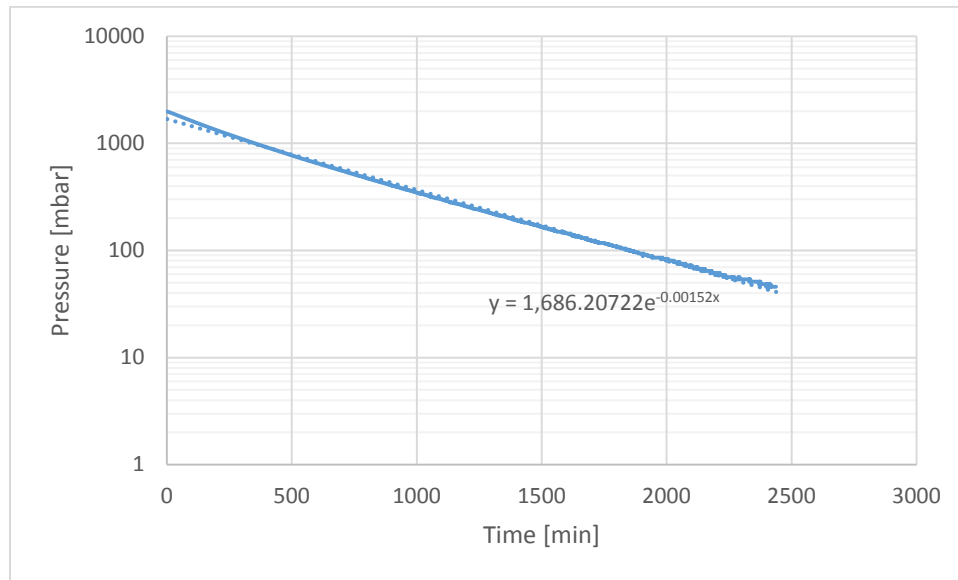


Figure 99: Third prototype pressure drop

Figure 100 shows the performance of the heat switch with respect to pressure, when the baseplate is maintained at an average temperature of 17.86°C. Problems with the baseplate instability remained during testing of the third prototype as well. However, the baseplate exhibited improved behavior with a maximum deviation of 2°C and a standard deviation of

0.338°C. Because of the temperature fluctuations of the baseplate, the moving average approach has been used. Figure 100 shows that the third prototype reaches a plateau for the heat transfer coefficient at around 500 mbar. This plateau corresponds to the transition to the continuum regime. The reduced value of this transition pressure compared to the value of 1000 mbar for the second prototype confirms that even after torquing the bolts with 0.85 N·m, the effective gap between the two sides of the switch is about double according to equations (5.3-1) and (5.3-2). This result is in very good agreement with the result obtained using a different method in section 8.3.1.2. Consequently, because of this excessive gap, the performance of the third prototype in its ON-state is severely degraded compared to its theoretical value as is shown in section 8.3.1.2. At the lower limit, of the graph, the heat transfer coefficient keeps decreasing with decreasing pressure, and therefore, the molecular regime limit has not yet been reached.

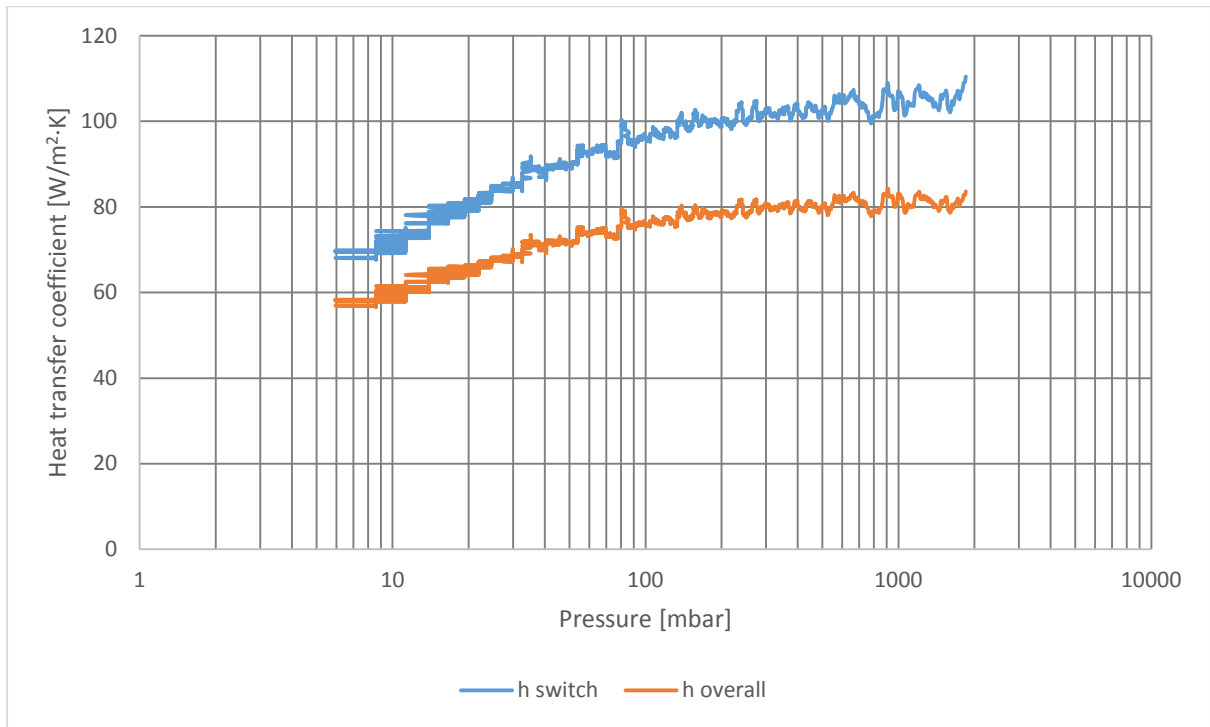


Figure 100: Heat transfer coefficient against pressure (third prototype)

8.5 ON/OFF ratio

The ON/OFF ratio is the most important indicator of the performance of a heat switch. The function of the ON/OFF ratio with respect to temperature can be found by taking the ratio of the two experimental trendlines for the overall heat transfer coefficient.

Thus, for the second prototype:

$$R_{ON/OFF} = \frac{0.9826 \cdot T + 243.1703}{0.1245 \cdot T + 27.9114}$$

For the third prototype:

$$R_{ON/OFF} = \frac{0.0013 \cdot T^2 + 0.3474 \cdot T + 194.86}{0.00052 \cdot T^2 + 0.0679 \cdot T + 23.39}$$

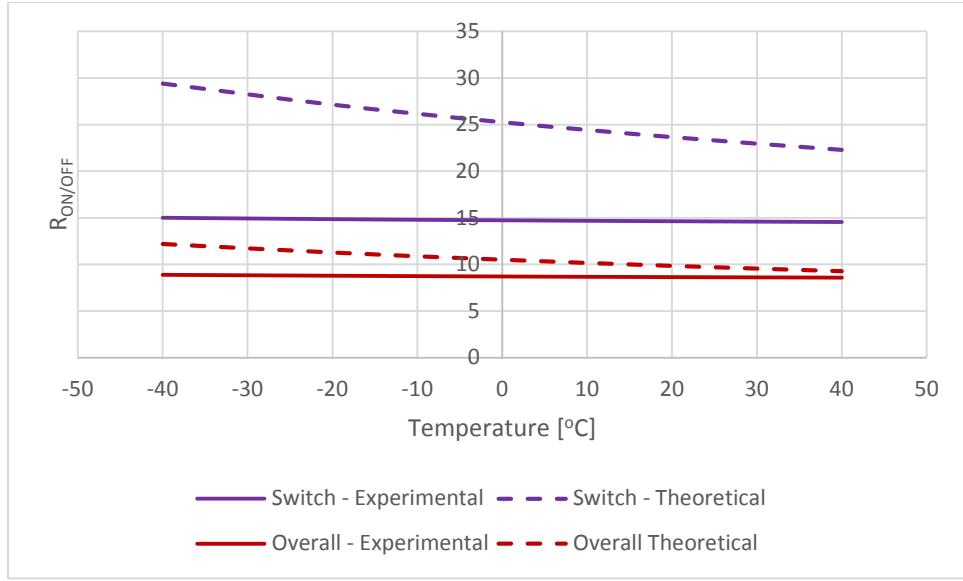


Figure 101: Third prototype ON/OFF ratio

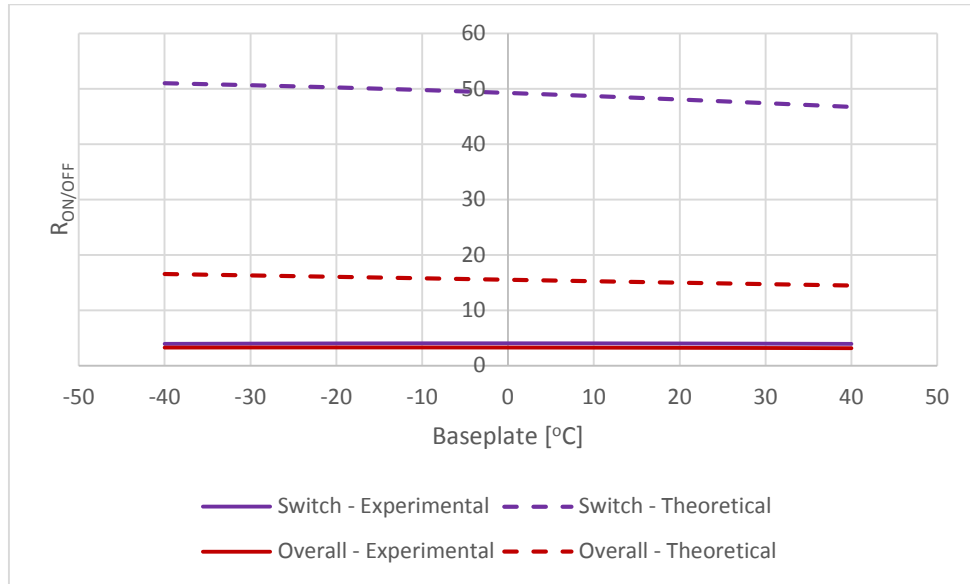


Figure 102: Third prototype ON/OFF ratio

8.6 Summary

Detailed Finite Element Models and reduced Thermal Mathematical Models have been created for the prediction of the behavior of the developed gas-gap heat switch. The conducted experiments have shown that these models are within 11.8% to 16.2% accurate for the OFF-case and -19.9% to 9.6% for the ON-case for the second prototype. Such differences are deemed satisfactory, especially given the deviation of the manufactured prototype from the CAD model used in the Finite Element Analysis and the uncertainties in the thermal contact conductances. For the third prototype, the FEM is off by a factor of 2 for the OFF-case and a factor of 6 for

the ON-case. This is because the FEM is based on an ideal CAD model, which is not representative of the manufactured prototype and its dimensions. Obtaining an accurate mesh, representative of the real case prototype while fully mounted on the test setup is impossible. This is because a high accuracy CT scan is required for the entire test setup and the generated mesh of the heat switch would require extreme computational resources to solve. Overall, the FEM of the second prototype is reliable and can offer good predictions, while no conclusion can be drawn about the FEM of the third prototype. The experiments have shown that when the manufacturing tolerances are respected, the developed thermal models are quite accurate. Consequently, these models can be used in the future for the analysis of the new design iterations.

9 Uncertainty analysis

“Uncertainty is a quantification of the doubt about the measurement results” [39]. For proper interpretation of the results, a measurement uncertainty analysis was performed. This is because, even for the most careful measurements there is always a margin of uncertainty that can be attributed to the measurement process, the measuring instrument or even uncontrolled factors, such as environmental ones.

In the case of the heat switch experiment, the measurement in question is the heat transfer coefficient in the ON and OFF state. The governing equation for the measurement is thus:

$$h_{ON,OFF} = \frac{P_{heater} - P_{leak}}{A(T_h - T_c)} \quad (8.6-1)$$

P_{heater} is the power generated by the heater, P_{leak} is the power that leaks through the system, A is the cross-section area, T_h is the temperature measured on the hot side and T_c on the cold side. Because the temperatures and the heating power are measured by separate instruments, they are independent of each other. In this case, the relative uncertainty of the heat conductance can be expressed using the root sum of squares:

$$\frac{dh_{ON,OFF}}{h_{ON,OFF}} = k \cdot \sqrt{\left(\frac{dP_{heater} + dP_{leak}}{P_{heater} - P_{leak}}\right)^2 + \left(\frac{dP_{leak}}{P_{leak}}\right)^2 + \left(\frac{dA}{A}\right)^2 + \left(\frac{dT_h + dT_c}{T_h - T_c}\right)^2} \quad (8.6-2)$$

The numerator of each component indicates their respective standard uncertainty and the denominator their nominal value.

This combined uncertainty was multiplied by a coverage factor $k = 2$, for a confidence level of 95%, assuming the combined standard uncertainty follows a normal distribution.

9.1 Heating power uncertainty

The heating power supplied to the test setup is determined by measuring the voltage across the power supply terminals using the multimeter of the data acquisition unit. In this case, the power can be calculated using $P = \frac{V^2}{R}$. However, because long wires are used to connect the heater to the electrical feedthrough of the chamber and from the feedthrough to the power supply, wire resistances are introduced. Typically, a four-point measurement can be implemented for more accurate results, where two separate pairs of electrodes measure the current and the voltage across the heater resistance. The measurement of the electrical resistances of the heater and of the heater with the wires showed an increase of the resistance by less than 0.1%. Consequently, these losses can be neglected. However, these measurements were conducted at room temperature. The electrical resistance of the wires changes with temperature. Consequently, for more accurate measurements the current through the circuit was measured using the ammeter of the power supply. The heating power can then be established simply using $P = V \cdot I$. The accuracy of the measurement of the DC voltage is

$\pm 0.05\%$ +2 digits with a resolution of two decimals. Thus, for a measured voltage of 95.31 Volts, the accuracy is $0.05\% \cdot 95.31 + 0.02 \cong 0.07 \text{ Volts}$. The accuracy of the current measurement is $\pm 0.5\%$ +3 digits with a resolution of 3 decimals. For a current measurement of 0.419 Amps, the accuracy is $0.5\% \cdot 0.419 + 0.003 \cong 0.005 \text{ Amps}$. The combined uncertainty for the supplied power is:

$$\frac{dP_{heater}}{P_{heater}} = \sqrt{\left(\frac{dV}{V}\right)^2 + \left(\frac{dI}{I}\right)^2} = \sqrt{\left(\frac{0.07}{95.31}\right)^2 + \left(\frac{0.005}{0.419}\right)^2} = 0.012$$

Where $P_{heater} = 95.31 \cdot 0.419 = 39.935 \text{ W}$. So $dP_{heater} = 0.486 \text{ W}$. This is the power uncertainty for the ON-case of the second prototype at 20°C.

Similarly, for a DC voltage reading of 33.64 Volts and current of 0.149 Amps, the power uncertainty for the OFF-case of the second prototype at 20°C is $dP_{heater} = 0.126 \text{ W}$, for a nominal power of $P_{heater} = 33.64 \cdot 0.149 = 5.012 \text{ W}$.

The voltage and current measurements throughout testing were rather stable even within the wide baseplate temperature range of -40°C to +40°C. The voltage in the ON-case ranged from 95.26 to 95.46 Volts, while in the OFF-case only from 33.64 to 33.65 Volts. The current in the ON-case varied from 0.419 to 0.420 Amps and for the OFF-case from 0.148 to 0.149 Amps. Such variations do not exhibit significant changes in the calculations of the uncertainty and therefore the uncertainty of the heating power can be considered independent of temperature.

9.2 Leaking power uncertainty

A significant source of uncertainty for the test stems from the leak conductances in the setup and especially for the OFF-case. The losses can be deduced from the reduced TMM by measuring the heat flow through the nodes. The estimations include the radiative losses through the MLI and the leak conductances through the bolts, spacers and washers. Table 21 summarizes the estimated percentage of heat leak through the entire system for the ON and OFF-case of both prototypes at a baseplate temperature of 20°C. The exact losses are very difficult to be determined and an uncertainty margin of $\pm 20\%$ is implemented in the calculations.

Table 21: Heating power leak

Prototype	Second (10x10 cm ²)	Third (20x20 cm ²)
Losses in ON-case	1.1%	2.0%
Losses in OFF-case	11.6%	12.0%

Therefore, the power losses for the ON-case of the second prototype at 20°C are:

$$P_{leak} = 1.1\% \cdot 39.935 = 0.439 \text{ W}$$

$$dP_{leak} = 0.2 \cdot 0.439 = 0.088 \text{ W}$$

The power losses for the OFF-case of the second prototype at 20°C are:

$$P_{leak} = 11.6\% \cdot 5.012 = 0.581 \text{ W}$$

$$dP_{leak} = 0.2 \cdot 0.581 = 0.116 \text{ W}$$

9.3 Area uncertainty

The external dimensions of the heat switch were measured with a Vernier caliper with an uncertainty of 0.01 mm. Consequently, for a nominal contact area of 210 mm x 210 mm, the uncertainty is less than 0.007%. This value is insignificant relative to the other uncertainties and can therefore be neglected in the combined uncertainty budget.

9.4 Thermocouples uncertainty

For the test, Type K thermocouples were used. The thermocouples were calibrated in accordance with the requirements of ISO/IEC 17025 “General requirements for the competence of testing and calibration laboratories” and following the instructions of ESA’s TEC-MTV-MSL/D001 document for “Calibration of Thermocouple Sensors”. Four calibration points were used; -195.8°C (boiling point of LN₂), -100°C, 0°C and +75°C. Figure 103 shows the curve of the temperature difference between each thermocouple and the calibration points. As expected, the deviation from the calibration point is minimized at room temperature. Third order polynomial curve fitting was used to establish the calibration equations that were implemented in the Data Acquisition Controller to obtain accurate temperature measurements.

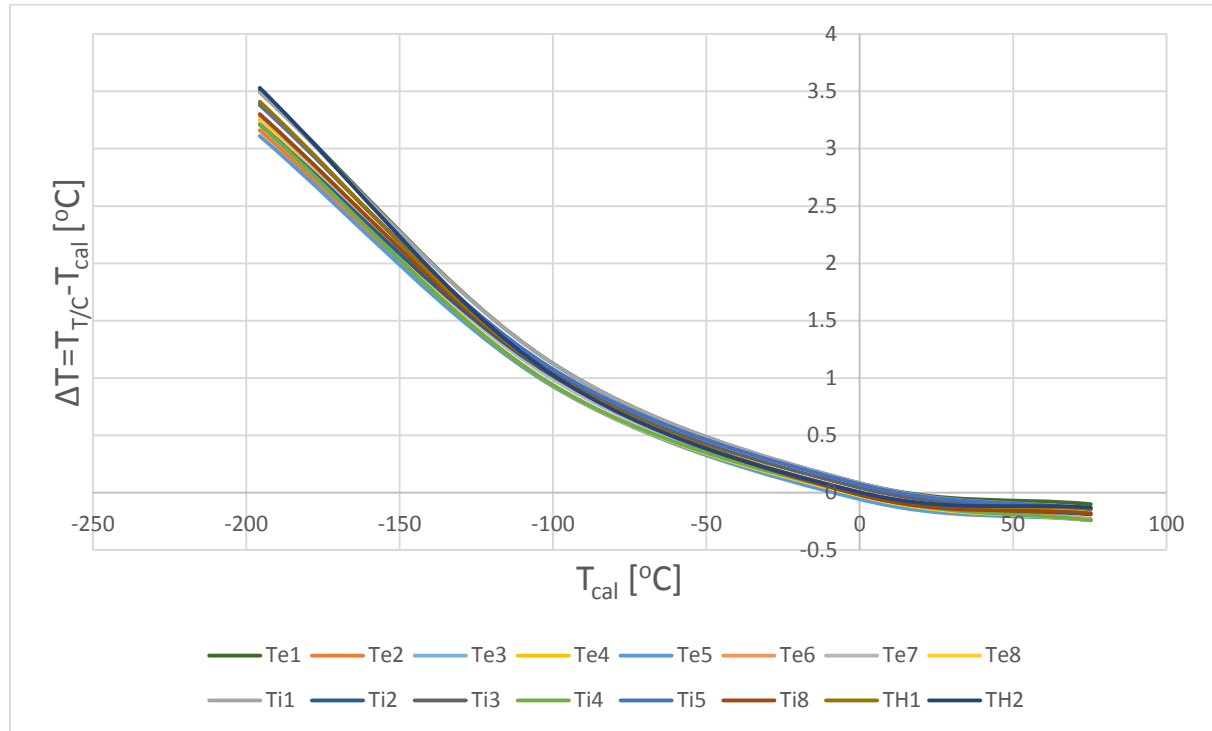


Figure 103: T/C temperature difference with calibration points (second prototype)

The combined uncertainty budget of the thermocouples includes uncertainties of the working standard calibration and uncertainties of the measurements during calibration. Eventually, the combined uncertainty budget with a coverage factor of 2 is less than 0.16°C within the test temperature range of -40°C to +40°C. The uncertainty of the thermocouples with respect to temperature is plotted in Figure 104.

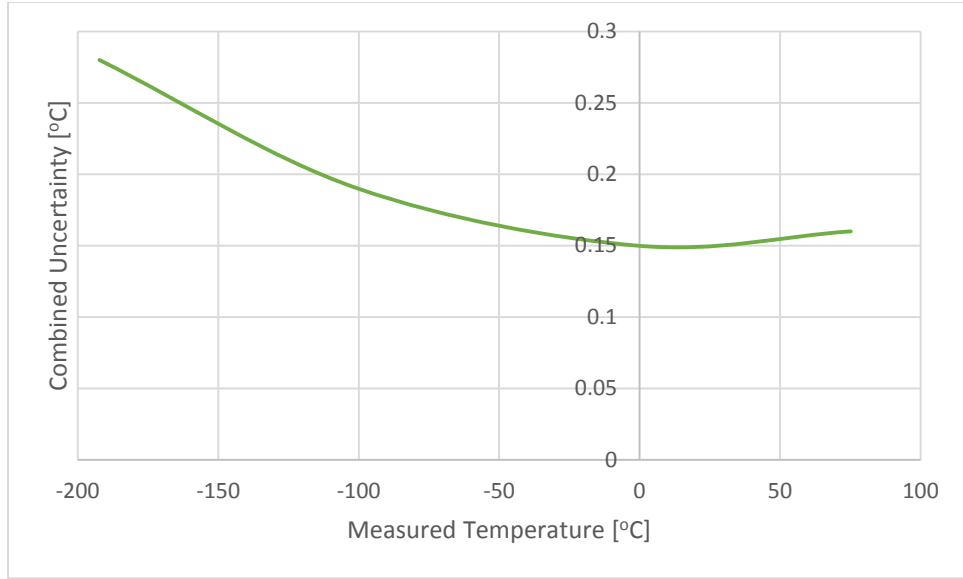


Figure 104: Combined T/C uncertainty budget

9.5 Sample uncertainty calculations

Below a sample calculation for the uncertainty of the overall ON and OFF heat transfer coefficient of the second prototype at a baseplate temperature of 20°C is given. The overall heat transfer coefficient refers to the gradient from Plate 1 to Plate 2.

$$\frac{dh_{ON}}{h_{ON}} = 2 \cdot \sqrt{\left(\frac{0.486 + 0.088}{39.935 - 0.439}\right)^2 + \left(\frac{0.16 + 0.16}{(39.53 - 24.10)}\right)^2} = 5.1\%$$

$$\frac{dh_{OFF}}{h_{OFF}} = 2 \cdot \sqrt{\left(\frac{0.126 + 0.116}{5.012 - 0.581}\right)^2 + \left(\frac{0.16 + 0.16}{(34.75 - 18.15)}\right)^2} = 11.6\%$$

9.6 Summary

An uncertainty analysis for the obtained values of the heat transfer coefficient was performed. The uncertainty parameters are considered to be independent of each other and the combined uncertainty can be obtained using the root sum of squares. The estimated uncertainties are provided with a confidence level of 95%. The uncertainty for the OFF-case is more than double the uncertainty of the ON-case, which is attributed mainly to the higher heat leak relative to the supplied power.

10 Correlated straw-man analysis

After the completion of the tests, the correlated measured values of the ON and OFF conductance of the second prototype were implemented into a more detailed straw-man analysis model using ESATAN-TMS. The experimental data from the testing of the third prototype were not used because of its severely deviating performance from the theoretical values.

10.1 Detailed Geometrical Mathematical Model

A Geometrical Mathematical Model (GMM) consisting of 974 shell elements was generated in order to calculate the orbital fluxes and the radiative links among spacecraft surfaces and the space environment. ESATAN-TMS radiative module (previously known as ESARAD) implements an enhanced Monte-Carlo ray-tracing algorithm to accurately calculate the view factors and the radiative exchange factors. This GMM is more accurate in comparison to the GMM in section 4.3, since multiple shell elements were used to discretize the spacecraft surfaces. Furthermore, the unit boxes were also represented using shell elements instead of lumped masses. A black paint coating was assigned to the units. Though, because of the significant difference in maximum operating temperature between the batteries and the rest of the units, the batteries are covered with MLI. Additionally, the solar array geometry of the Sentinel-2 spacecraft was integrated into the model. The array was allowed to rotate around the Y-axis of the spacecraft to face the true sun at all times. The solar array produces some shadowing on the $-Y$ panel affecting the sizing of the radiators. In its deployed state, the array has dimensions of 3.768 m x 1.884 m, for a total area of 7.1 m². An illustration of the solar array and the S/C is provided in Figure 13 in section 4.2. Table 22 shows the assigned thermo-optical properties of the solar array for BOL and EOL. All other optical properties remain the same as in section 4.3. Figure 105 and Figure 106 show the incident orbital fluxes for the worst hot and worst cold case respectively with an angle step of 10 degrees from a near sun position.

Table 22: Solar array thermo-optical properties

Optical Property	Solar Cell (illuminated side)		Kapton (rear side)	
	EOL	BOL	EOL	BOL
Absorptivity (α)	0.68	0.64	0.44	0.52
Emissivity (ϵ)	0.84	0.84	0.75	0.75

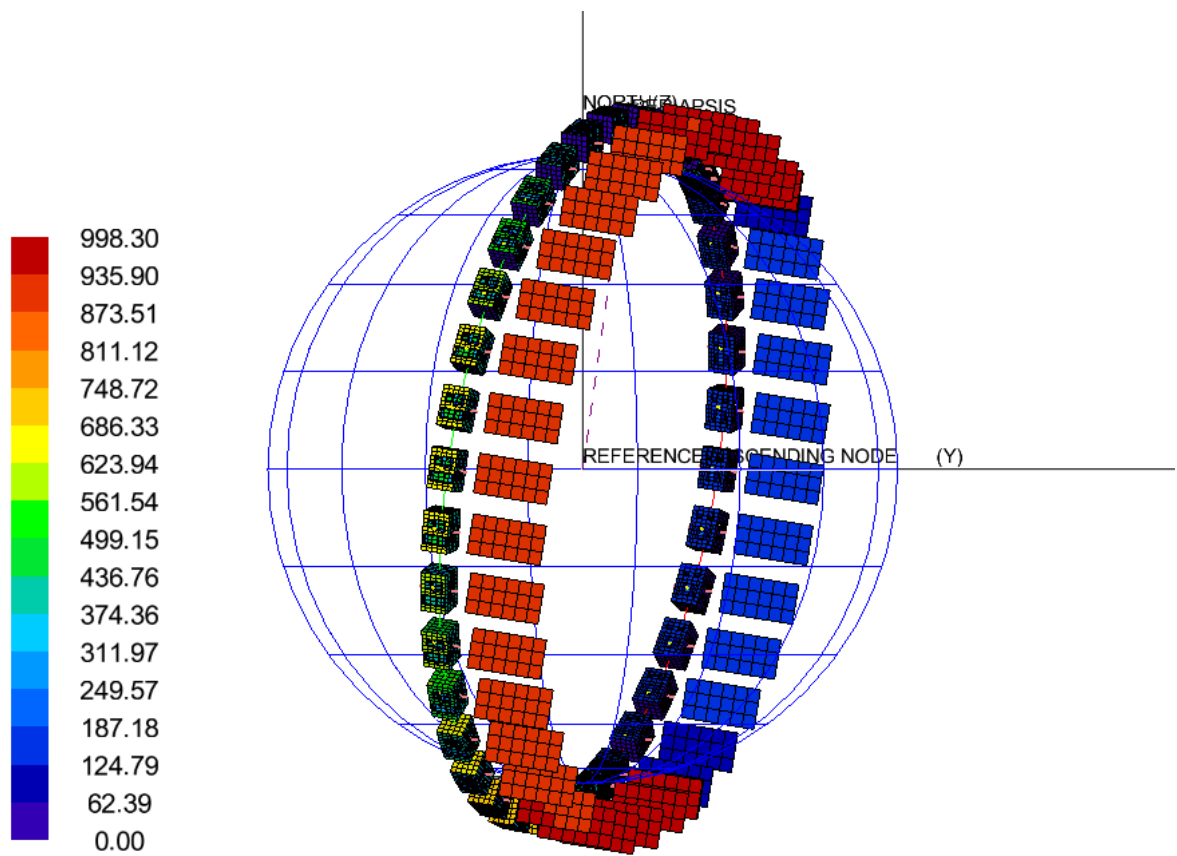


Figure 105: Worst hot incident solar fluxes

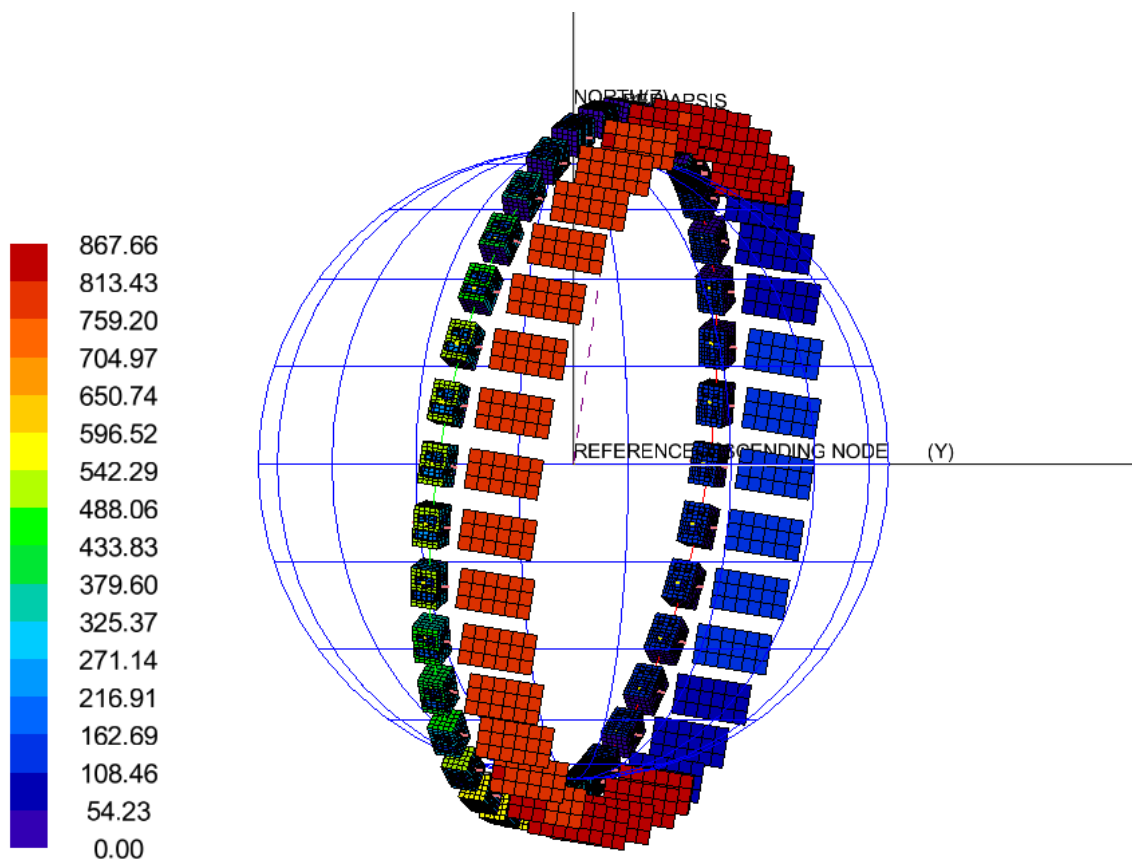


Figure 106: Worst cold incident solar fluxes

10.2 Detailed Thermal Mathematical Model

The Thermal Mathematical Model (TMM) uses the calculated radiative fluxes and couplings from the GMM to estimate the temperatures of the isothermal nodes. Compared to the ThermXL TMM, the ESATAN model is more representative, as the panels of the spacecraft are represented by multiple isothermal nodes instead of a single node. Consequently, in-plane and out-of-plane gradients exist. The solar array was assigned Aluminium 6061 thermal properties (see Appendix F) and a through conductance of 50 W/m²K from the cell to the rear side of the panel. Table 23 indicates the node label assigned in the ESATAN model for each unit.

Table 23: Units node label

Unit	Node
RIU	10000
GPS	11000
OBC	12000
COMS	13000
Battery 1	14000
Battery 2	15000
PCDU	16000
SBT1	17000
SBT2	18000
ICU1	19000
ICU2	20000
WDE	21000
MMFU	22000

10.2.1 Results without switch implementation

Figure 107 shows the temperature profile of all units for the worst hot scenario, when no switch is applied. When compared to Figure 16, the obtained results for most units are very close. The main difference is observed in the COMS and Battery units. This is attributed to the fact that the ESATAN model is more detailed and the units are coupled to multiple and separate isothermal nodes instead of a single isothermal node, which represents the spacecraft +Z panel in the ThermXL model. Additionally, each unit has a dedicated radiator, which was not the case for the ThermXL analysis.

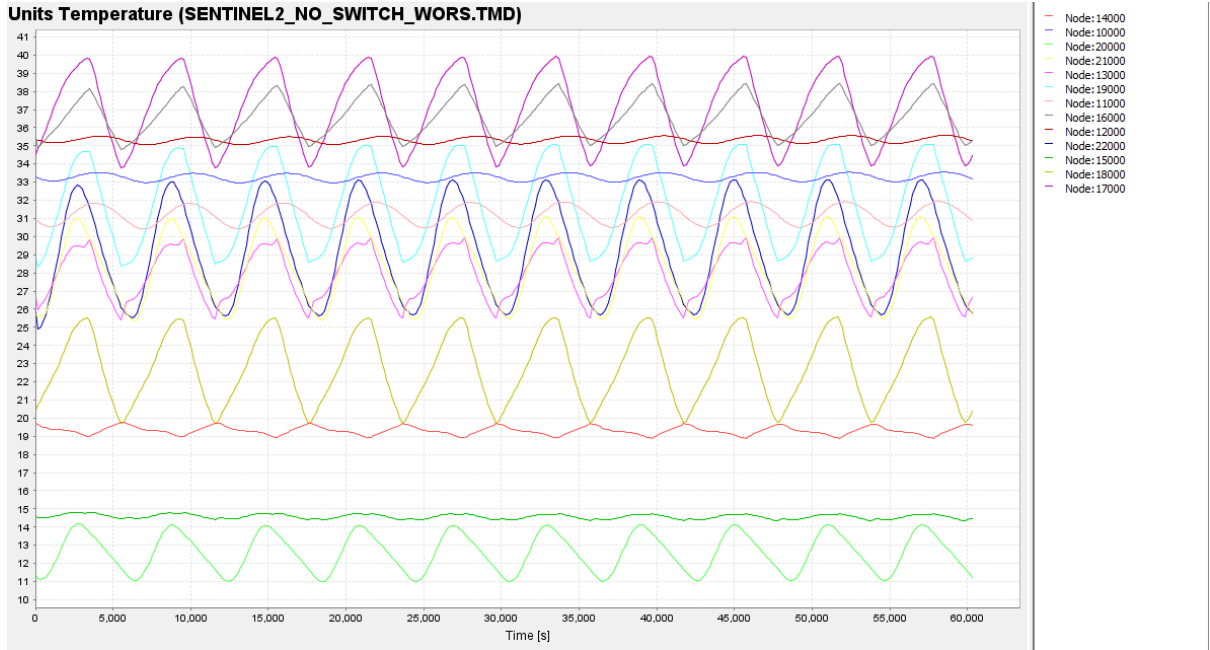


Figure 107: Units temperature profile (worst hot, no switch)

Figure 108 and Figure 109 show the temperature profile of all units and the +Z panel units respectively for the worst cold scenario, when no switch is applied. For the heating power, same conditions as the ones mentioned in section 4.3.6 were used. Ultimately, Battery 1 requires an average heating power of 20.27 W and Battery 2 of 21.08 W.

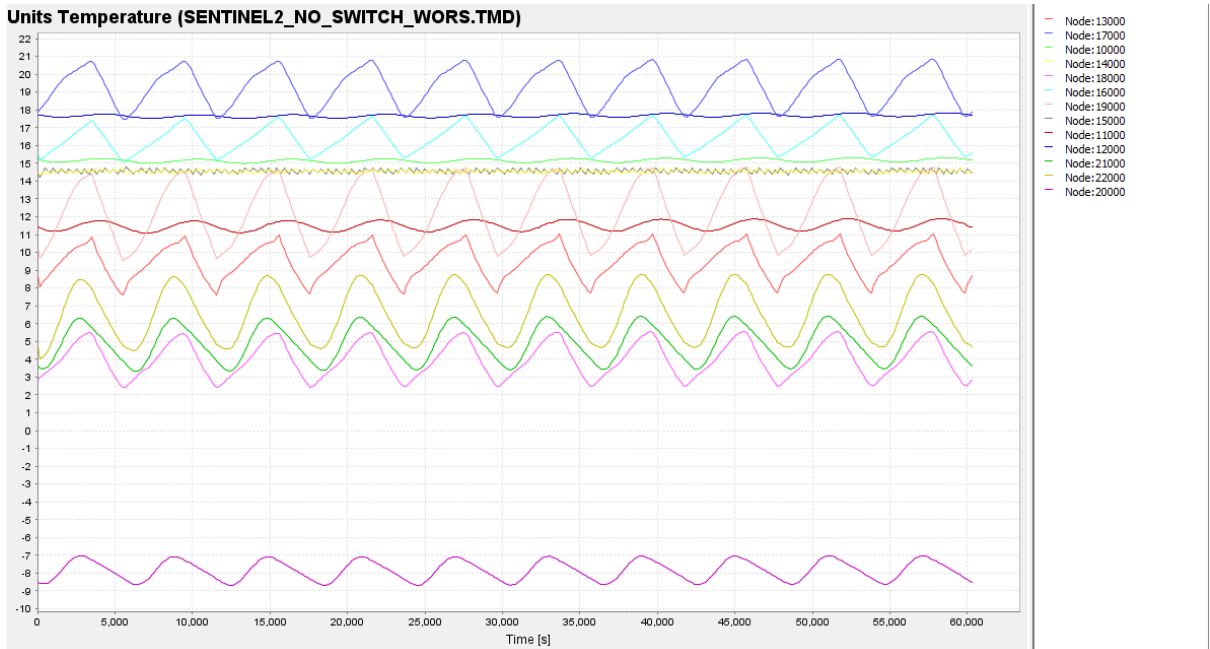


Figure 108: Units temperature profile (worst cold, no switch)

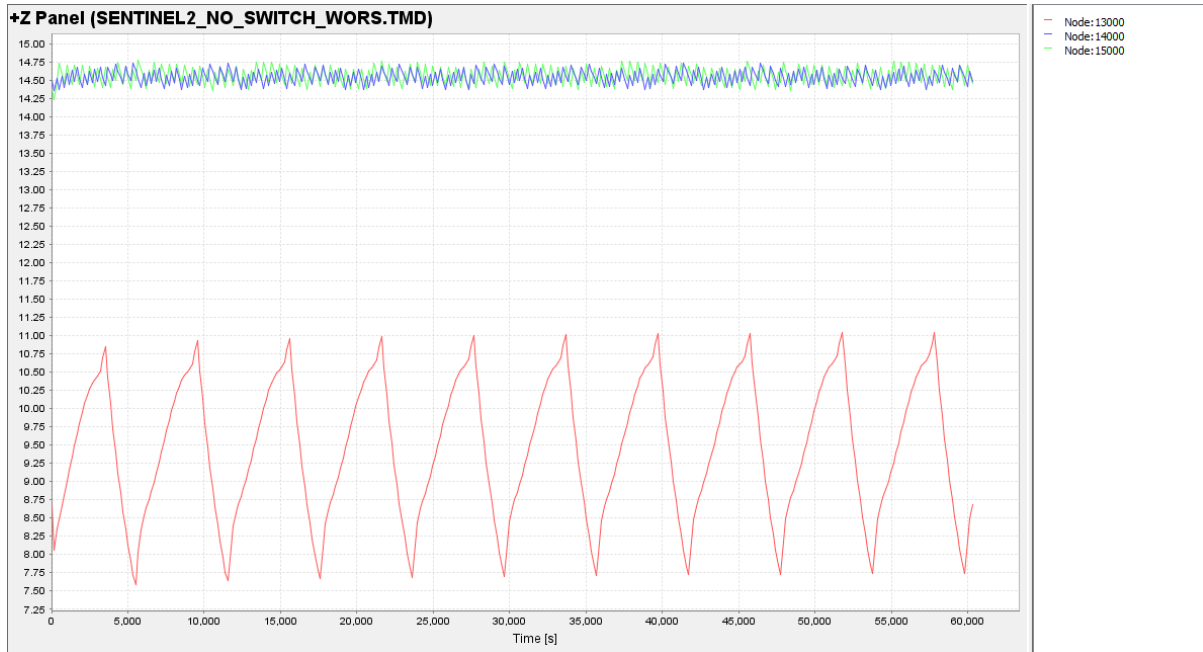


Figure 109: +Z Panel unit temperature profile (worst cold, no switch)

10.2.2 Results using second prototype data

Figure 110 shows the temperature profile of all units for the worst hot scenario, when the experimental overall ON and OFF-conductance of the second prototype is implemented in the model at a temperature of 20°C for the ON and 14°C for the OFF case respectively. Temperature profiles are almost identical to the ones from Figure 107. This means that for at least this mission, the ON-conductance is not critical. More specifically, a decrease of the ON-conductance by 2.80 times resulted in virtually no difference in temperature and also sizing of the radiator.

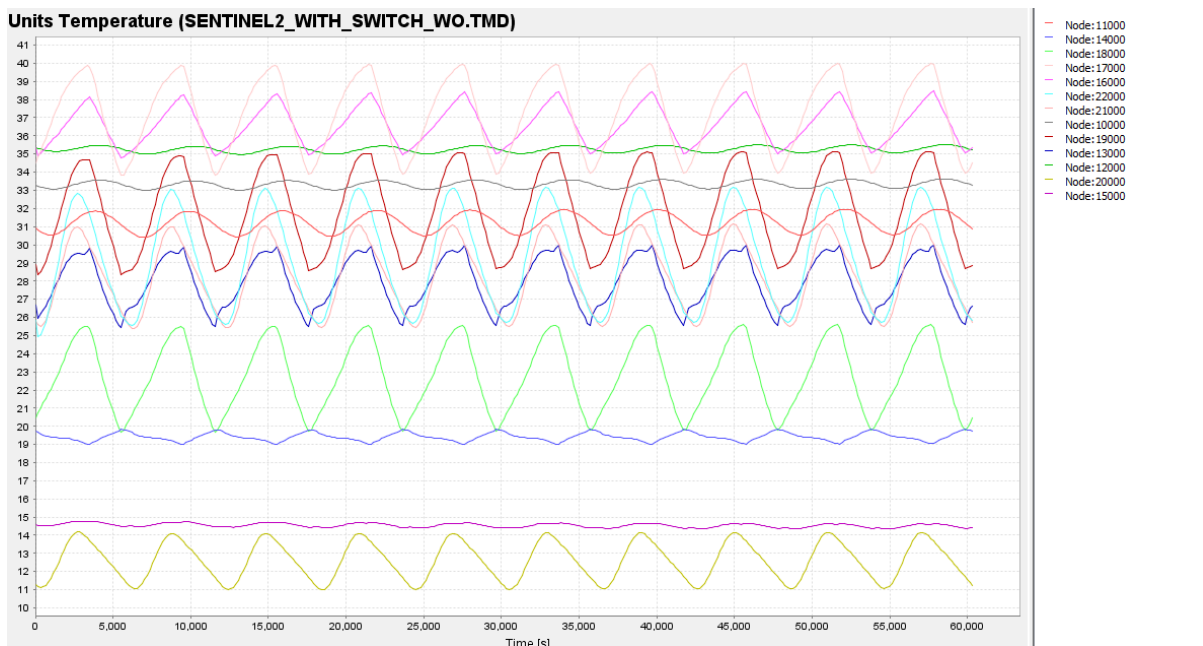


Figure 110: Units temperature profile (worst hot, no switch)

Figure 111 and Figure 112 show the temperature profile of all units and the +Z panel units respectively for the worst cold scenario. Ultimately, Battery 1 requires an average heating power of 13.42 W and Battery 2 of 15.76 W. This represents a reduction of 12.17 W in the heating power consumption or equivalently a 29.4% decrease when compared with the values of section 10.2.1.

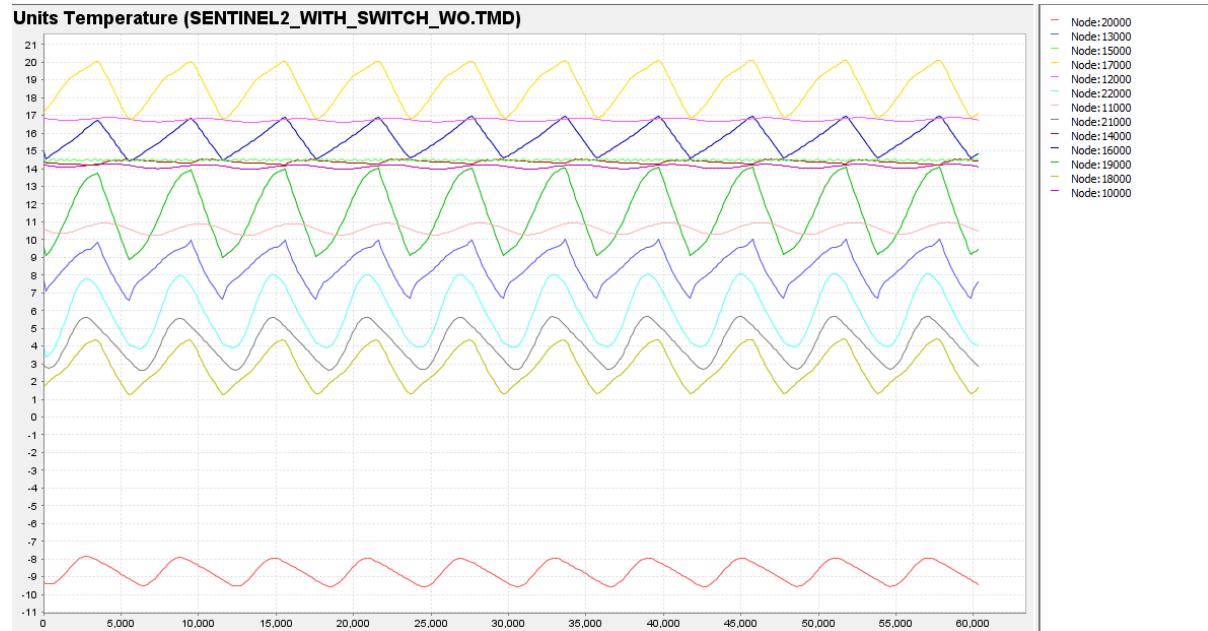


Figure 111: Units temperature profile (worst cold, no switch)

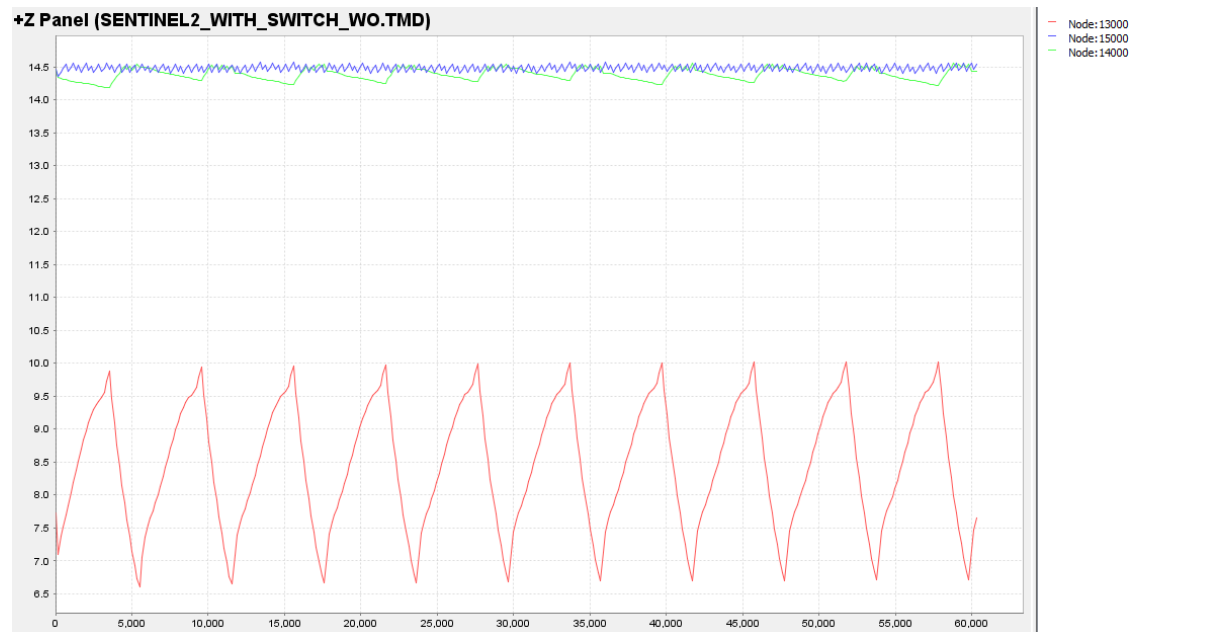


Figure 112: +Z Panel unit temperature profile (worst cold, no switch)

An additional scenario was studied in order to obtain an estimate of the impact of further reducing the OFF-conductance of the switch. The nominal OFF-case heat transfer coefficient from Table 1 was used. In this case the total heating power required is 18.92 W, which corresponds to a decrease of 54.2% when compared to section 10.2.1.

10.3 Heat switch impact on interrelated subsystems

The implementation of the heat switch in the Sentinel-2 mission has a direct impact on the heating power required to maintain the battery units above their minimum allowable temperature. Though, this reduction in power has an induced effect on the design of the power subsystem.

More specifically, the power production capability of the satellite at BOL is 2289 W and at EOL it is 2170 W. A $\pm 10\%$ power system margin is implemented in the design of the spacecraft. Consequently, at EOL, the solar array shall be able to generate $0.9 \cdot 2170 = 1953$ W. Saving 12.17 W, according to the second prototype experimental measurements, represents a reduction of 0.62% in the power budget.

As a first approximation, we can assume the mass reduction of the power subsystem to be linear with the power consumption reduction. Table 24 provides the mass of the mostly affected components of the power subsystem of the spacecraft.

Table 24: Power subsystem components mass

Component	Mass
Solar array	42.6 kg (including yoke)
Batteries	2 x 30.1 kg
PCDU	28.77 kg

A 0.62% reduction in the power budget entails a reduction of 0.816 kg of the power subsystem. For two batteries with an area of 360 mm x 280 mm, the total added mass is 1.690 kg. Eventually, because of the power subsystem mass reduction, the added mass is 0.874 kg. The launch mass of the spacecraft is 1140 kg. Thus, the addition of the heat switch represents an increase of the mass budget by 0.077%.

10.4 Summary

From the results of this analysis it can be concluded that the benefits of the implementation of the tested heat switch in a mission similar to Sentinel-2 would be limited. This is because eventually the nature of the mission is not significantly demanding in terms of thermal control. More specifically, of all the electronics and payload units, only the batteries would require additional measures for remaining within their allowable temperature range. Consequently, further investigation of different Earth Observation missions is required in order to obtain more conclusive results, which is beyond the scope of this thesis.

Additionally, the potential implementation of the heat switch in other types of mission shall be investigated, especially for Geo-stationary, low-thrust trajectory and interplanetary

missions, since they are more demanding and complex in terms of thermal control. During such missions, the spacecraft goes through different phases, where it is exposed to different thermal environments and it operates in different modes. For example JUICE is an ESA interplanetary mission to Jupiter and the Jovian moons. In order to reach Jupiter the spacecraft will execute a slingshot maneuver about Venus, reaching a minimum mission distance of 0.645 AU from the sun. Consequently, the incident solar fluxes throughout the mission vary from 46 to 3342 W/m². Figure 113 provides the mission profile of JUICE.

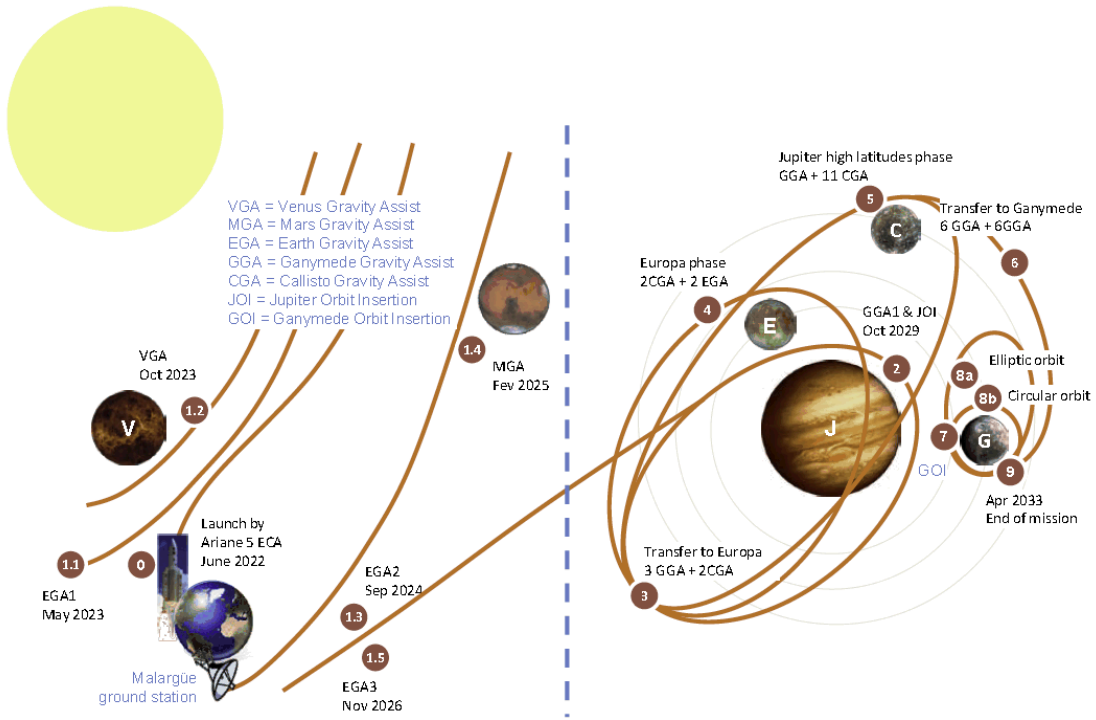


Figure 113: JUICE mission trajectory

11 Improvement recommendations

11.1 Manufacturing improvements

The concept behind the 3D-printed heat switch is that it should be easily and quickly manufactured and it should be reproducible. Consequently, post-processing shall be minimized. As explained in chapter 3, the performance of the heat switch is currently limited by the available manufacturing techniques. Selective Laser Melting or Selective Laser Sintering are two very similar methods that offer the best combination of tolerances and the ability to print overhanging structures, such as the support pillars of the heat switch. For the case of metals, they require relatively low post-processing, including blasting, sanding and annealing. Though, the accuracy and the surface finish are related to the manufacturing process and parameters such as the diameter of the focused laser beam, the scanning speed and the energy input. The accuracy and surface finish are also limited by the size of the particles of the powder. Typically, the mean particle size for Ti-6Al-4V powder is around 50 microns. However, high quality fine powder is available by various suppliers worldwide. Figure 114 shows the particle distribution for some of the finest powder available in the market by Advance Powders & Coatings.

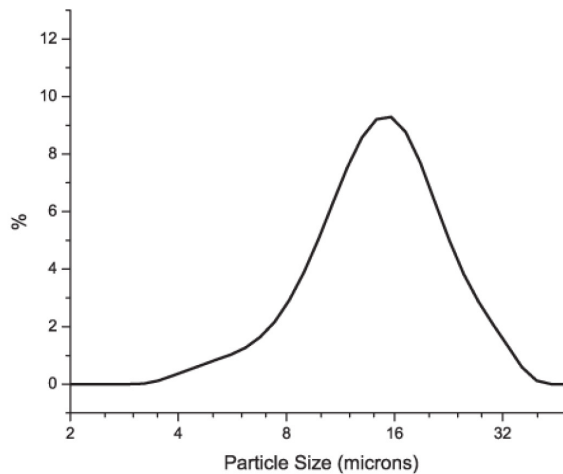


Figure 114: Fine Ti-6Al-4V powder particle size distribution

This distribution has a mean particle size of 15 microns, which is already 3 times better than the typically available powder. Therefore, at this development stage of the heat switch, the manufacturing tolerances may be improved with the use of fine powder. Though, it should be noted that a particle size distribution (from small to large) is necessary in order to have acceptable flow properties. The ideal particle size can be determined only by trial-and-error, conducting multiple iterations. Additionally, special care shall be taken when using very fine powder, since it can be very hazardous for the human body. Especially, particles with diameter smaller than 10 microns can get deep into the lungs and may even enter the bloodstream.

Apart from the powder, the part shall be sliced into thinner layers for printing and a compatible 3D-printing machine that offers adequate tolerances shall be used. These changes can offer improvements for the size of the design features, as for example the size of the gap which could be further reduced from the current design of 0.2 mm.

Apart from the minimum feature size, another important aspect of manufacturing is the flatness and surface roughness of the heat switch. The manufactured prototypes have so far exhibited significant flatness problems due to buckling that stems from residual thermal stresses generated during production. In order to further reduce these residual stresses a combination of the lattice structure from Figure 34 with an increase in the thickness of the top and bottom faces of the heat switch can be used. The increased thickness of the two faces will facilitate the heat spreading and the heat sinking to the build-plate of the structure. Furthermore, it provides additional torsional stiffness that will prevent the buckling effect. Following the annealing process, the extra material will be shaved off using face milling or grinding as shown in Figure 115 to reduce the thickness to its nominal value of 0.7 mm. Grinding is preferable since the dimensions of the heat switch are similar to that of a sheet of metal. Consequently, milling can generate excessive shear stresses, it will last longer and will provide a worse surface roughness.

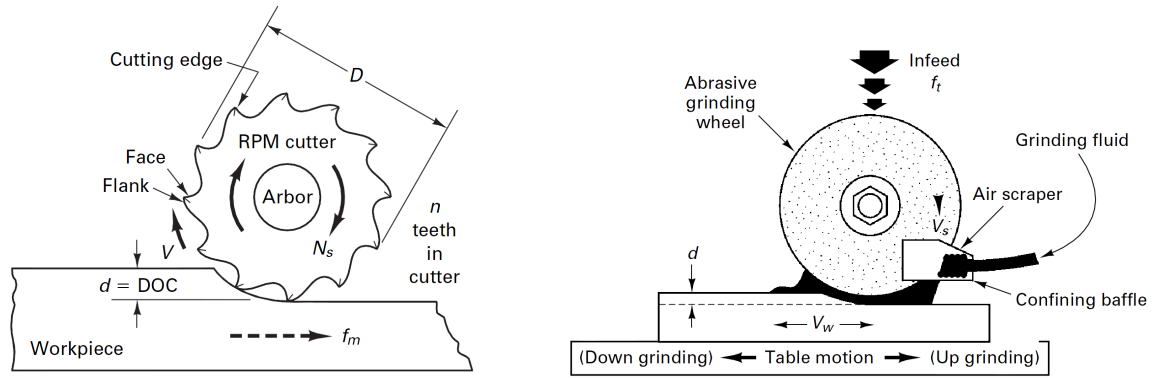


Figure 115: Milling versus grinding process [40]

This material shaving will provide an ideal flatness and surface roughness that are critical for the proper mounting of the switch, especially when taking into account the contact thermal conductance. Additionally, the surface roughness of the tubes is also critical, as it affects the leakage at the interface with the tube fittings. Increased roughness creates voids through which the gas is easier to escape. Consequently, the thickness of the tubes can be locally increased and then reduced to the nominal diameter using face milling to provide an improved surface finish.

A cost analysis is necessary to determine whether the cost of the excessive material is an inhibiting factor. With a simple market research, the cost of Ti-6Al-4V powder is about 250-500 €/kg. Adding a conservative thickness of 5 mm per side corresponds to a surface mass density of 44.3 kg/m². Thus, the excessive material cost per area taking the maximum price of 500 €/kg is 22,150 €/m², which corresponds to 11% of the total cost per area charged for the latest prototype. Through this basic cost analysis, it is confirmed that this is a viable option. A more elaborate cost analysis would be beneficial to determine also the marginal cost, which represents the cost added by producing one extra unit of the product.

11.2 Design improvements

The developed heat switch is currently in its third iteration. There are further design improvements that could enhance the performance of the switch, its mountability and structural integrity.

Currently, there is no dedicated interface for the proper mounting of the heat switch on a baseplate. A simple solution would be to add features, such as through holes to allow for a perimetric bolt pattern for mounting of the units. A material with low thermal conductivity ($<0.5 \text{ W/m} \cdot \text{K}$) can be used as a bushing in order to minimize the leak thermal conductance to the baseplate. Otherwise, a clearance fit between the screw and the hole would be necessary. An example of such configuration is shown in Figure 116.

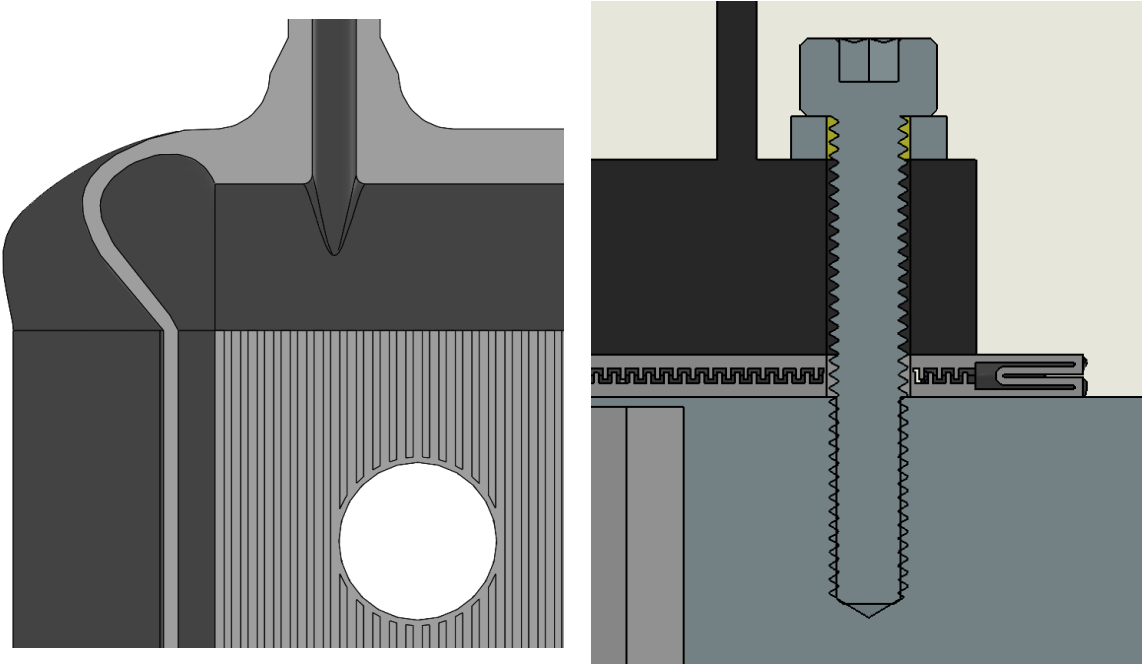


Figure 116: Mounting hole cross-section

Initially, a solid cylinder can be printed and subsequently the holes can be drilled using a drill press or a milling machine. This way, better tolerances can be achieved compared to when the holes are printed from the beginning. Furthermore, this way an added stiffness will reduce potential deformation due thermal residual stresses during manufacturing. After drilling the hole, this design leads to an increased stiffness in the vertical direction. A feature with an outer diameter of 4.75 mm and inner diameter of 4.3 mm has a stiffness of:

$$k = \frac{E \cdot A}{L} = \frac{120 \cdot 10^9 \cdot \frac{\pi}{4} (4.75^2 - 4.3^2) \cdot 10^{-6}}{2.2 \cdot 10^{-3}} = 174.5 \text{ MN/m}$$

If we assume a nominal torque of 1 N·m, which corresponds to a maximum bolt preload of 1,200 N, the compression is only 0.0069 mm and the compressive stress is 375 MPa, which is 0.44 the compressive yield strength of the material. Additionally, it is possible that the fragile and difficult to 3D-print support pillars are now redundant and therefore can be removed from the design.

A preliminary analysis of the suggested design, including all the pillars shows that the support pillars close to the mounting holes are subjected to stresses slightly exceeding the compressive yield strength of the material, as shown in Figure 117. Only the closest pillars to the mounting hole experience such high stresses of around 1,000 MPa. The pillars that are second in row experience a stress of only 330 MPa.

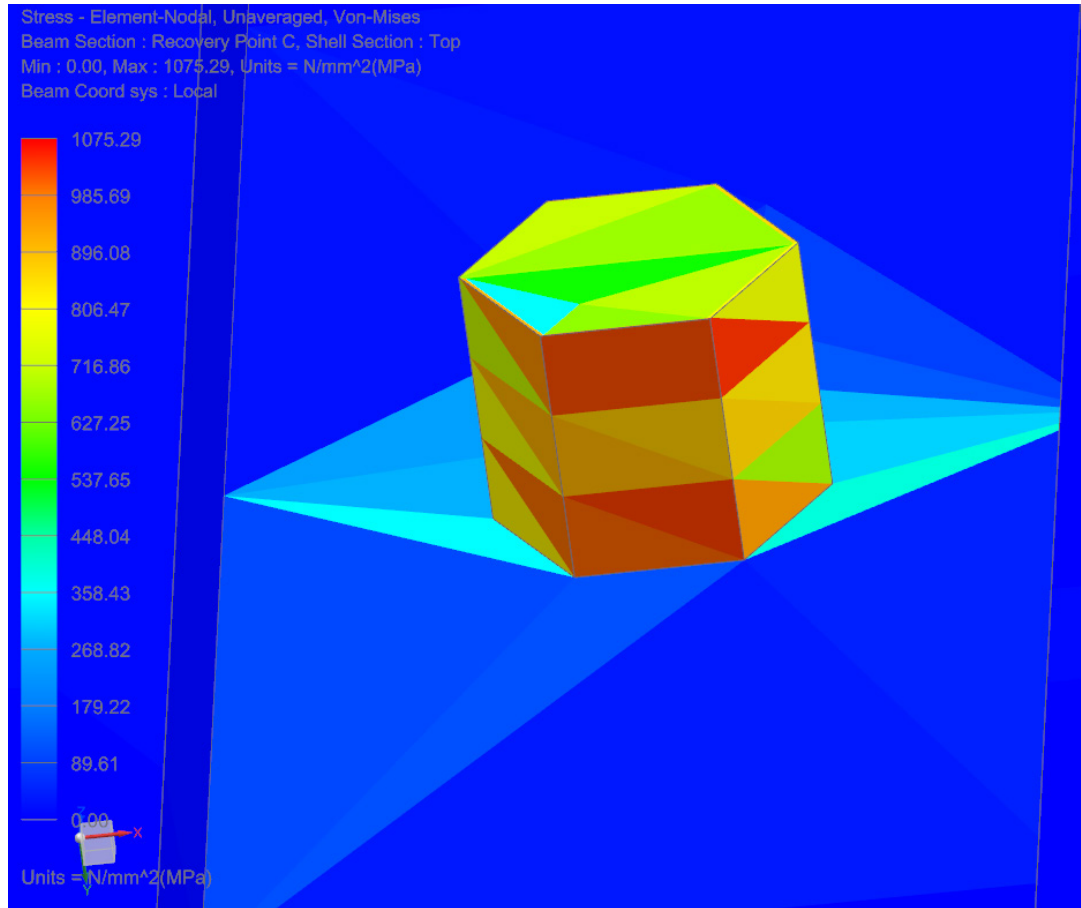


Figure 117: Suggested design pillar stresses

The second iteration of the suggested design does not include any pillars and shows an improved behavior compared to the first iteration. Figure 118 shows the Von-Mises stresses for the second iteration of the suggested design when the gauge pressure inside the switch is zero. The maximum stress is 671 MPa which is 78% of the compressive yield strength of the material. Consequently, an increase in the thickness of the wall might be necessary to reduce the stress. An optimization process would be necessary in order to determine the wall thickness that satisfies the minimum safety margin, while providing the minimum possible thermal conductance. Figure 119 shows the Von-Mises stresses when the gauge pressure is 1.5 bar. The maximum stress is 634 MPa, which is 74% of the yield strength. An important parameter of this analysis is also the relative displacement of the top and bottom faces of the switch. According to Figure 120, the maximum relative displacement is only 0.033 mm, an increase of 1.65%, which means that the gap distance does not change significantly with pressurization at 1.5 bar.

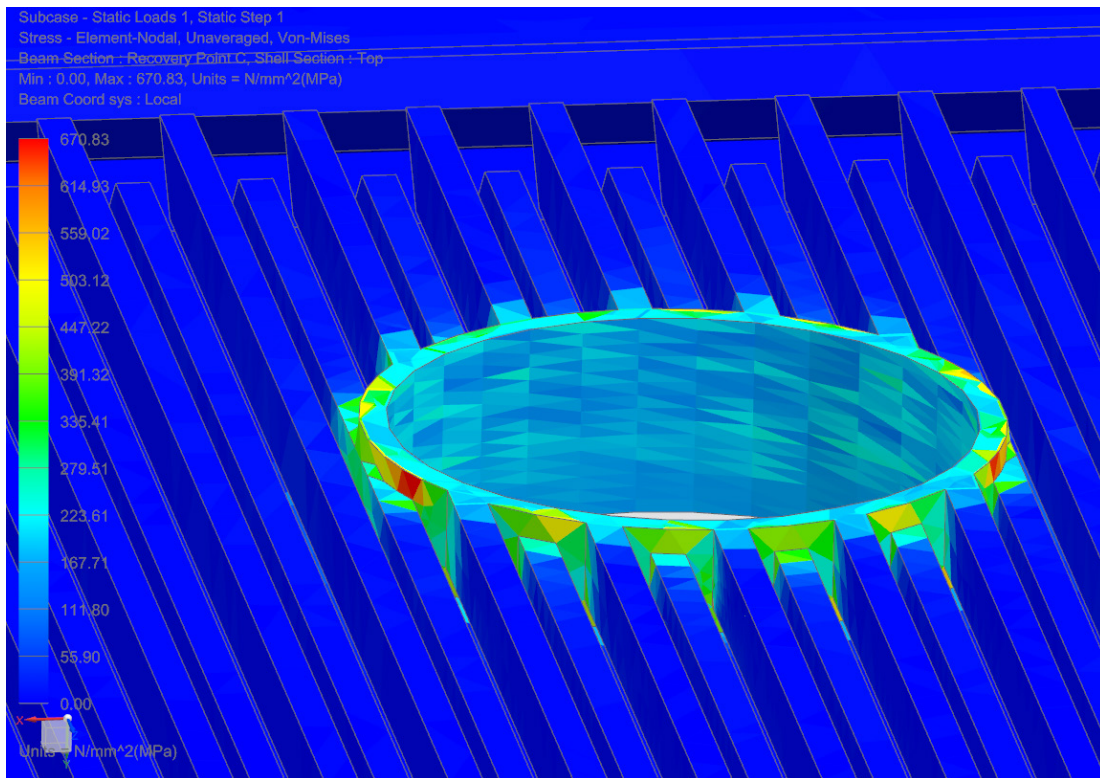


Figure 118: Suggested design maximum stresses (no pillars, $P_{gauge} = 0$ bar)

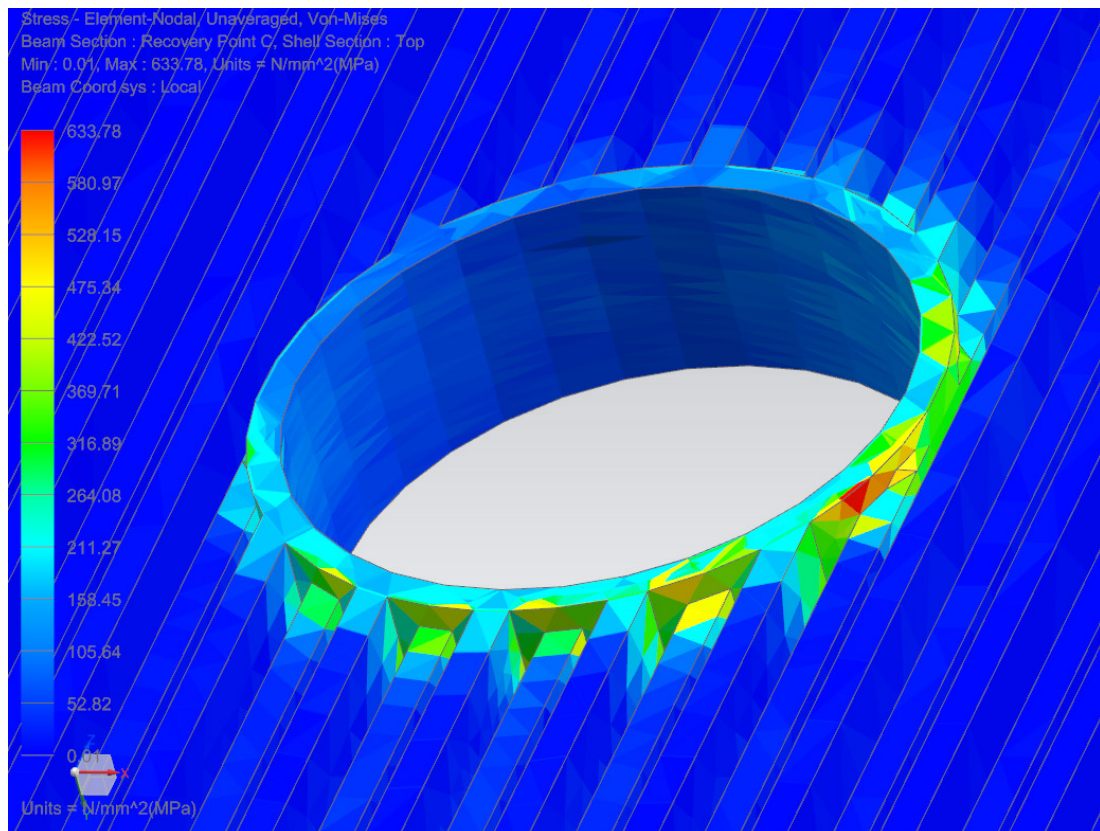


Figure 119: Suggested design maximum stresses (no pillars, $P_{gauge} = 1.5$ bar)

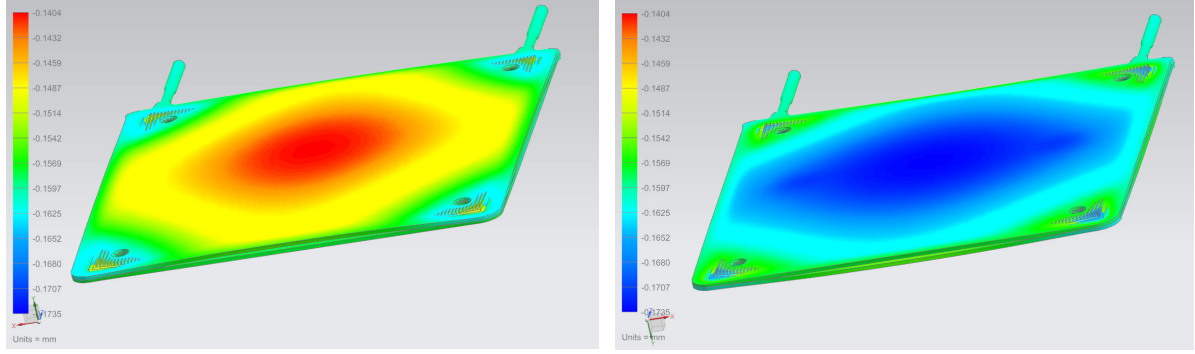


Figure 120: Vertical displacement at $P_{gauge} = 1.5$ bar

Of course, for a switch with a larger nominal surface area, the stresses and the relative displacement are going to increase, since the same pressure on a larger surface results in higher forces. In this case, the support pillars can be strategically placed near the center of the switch where the largest displacements are expected. Additionally, the pillars should be far enough from the mounting holes to avoid severe compressive stresses similar to Figure 117.

It should be noted that this design change provides an additional heat path for the OFF-case. The additional conductive coupling between the top and bottom face would be:

$$G_{hole} = \frac{k \cdot A}{L} = \frac{6.7 \cdot \frac{\pi}{4} (4.75^2 - 4.3^2) \cdot 10^{-6}}{2.2 \cdot 10^{-3}} = 0.0097 \frac{W/^\circ C}{bolt}$$

For a 20x20 cm² heat switch, using 6 bolts, this value corresponds nominally to an increase of the OFF-case conductive conductance by 14.8%. With conductive conductance representing about 60% of the total conductance, this translates to an increase of the total conductance by about 9%. However, if support pillars are removed, then this increase is nullified. It is even possible that the conductive conductance actually decreases if the number or the pillars removed is significant.

A further design improvement would be to minimize the thickness of the side walls from the current nominal of 0.4 mm. A decrease in this thickness results in a reduction in the parasitic conductance through the sides of the switch and a decrease in mass. This occurs at the expense of the stiffness of the walls. However, these side walls are not subjected to very high stresses under this mounting configuration.

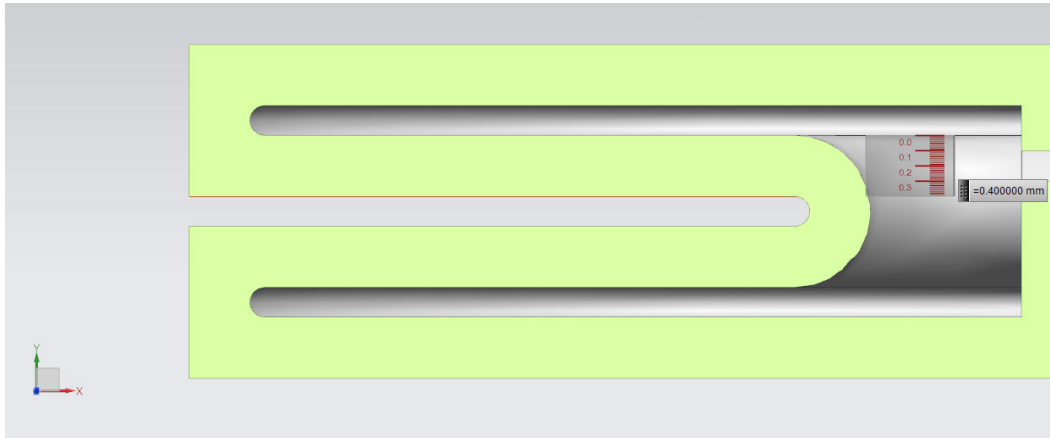


Figure 121: Side wall thickness

Figure 122 shows an isometric view of the mounting configuration on top of a honeycomb panel. Typically, the mounting on the honeycomb panel is done with the use of threaded inserts. The tubes can generate interference problems in certain cases, as shown in the figure. In these cases, a clearance between the tubes and the panels is necessary. This can be achieved by bending the tubes or by removing material from the panels.

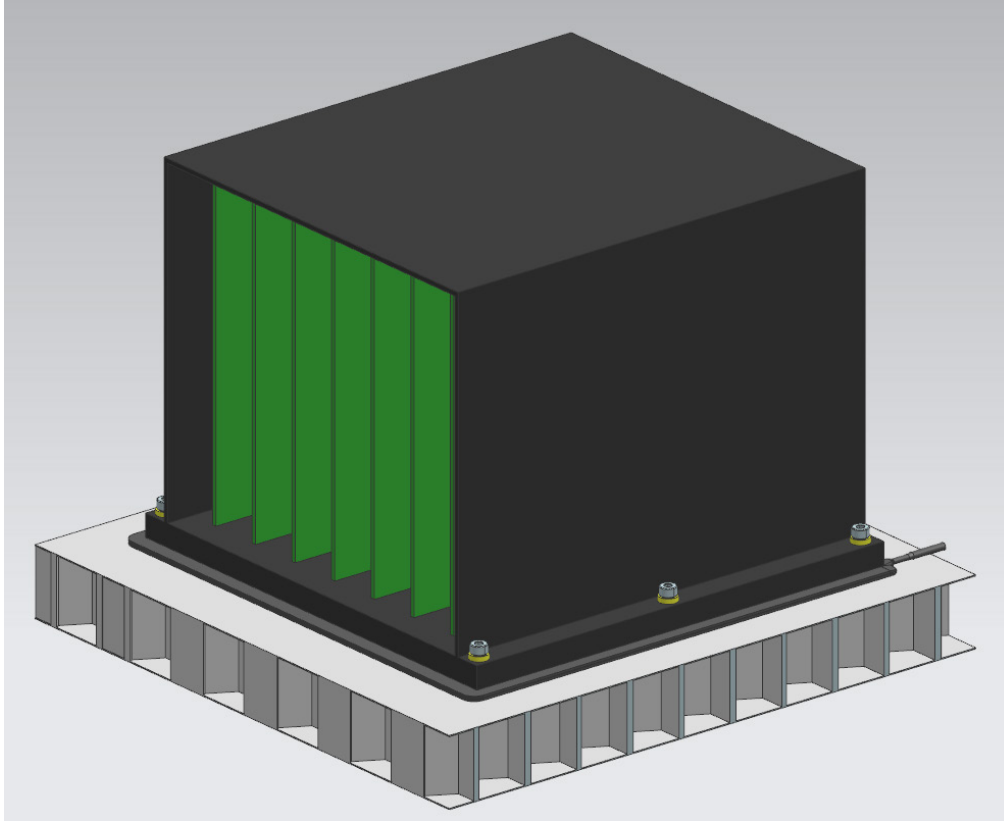


Figure 122: Mounting of heat switch and unit on honeycomb panel

11.3 Summary

There are several potential ways to improve the mountability, the performance and the manufacturability of the suggested gas-gap heat switch. The currently available 3D-printing technology is the most critical limiting factor for the production of a heat switch that respects manufacturing tolerances. Consequently, a lot of effort should be concentrated in manufacturing methods and processes. Furthermore, a simple modification in the mounting configuration of the heat switch seems to provide additional benefits, including smaller stresses and even a potential decrease in the thermal conductance for the OFF-case.

12 Conclusion & recommendations

12.1 Conclusions

Heat switches constitute a promising variable thermal conductance technology that could be implemented in space missions and especially those that are thermally-demanding. In such missions, the spacecraft experiences extreme variations of incident thermal fluxes and operates at different modes with varying internal power dissipations. Heat switches provide the means to tailor the losses to the environment according to the needs. The most important measures of effectiveness of a heat switch are the ON and OFF conductance and their ratio.

University of Twente has developed a gas-gap heat switch that is currently in its third design iteration. The behavior of this gas-gap heat switch is dependent on the temperature and pressure of the gas that occupies the internal gap of the device. The design of this gas-gap heat switch is innovative as it is one of the few heat switches designed for large electronic units and for room temperature applications. Most heat switches are designed for small components and for cryogenic temperatures. Compared to other similar heat switches, the idea behind the suggested gas-gap heat switch has the advantage of easy and quick manufacturing, without complex mechanisms and with a very light structure. A thorough analysis shows that in terms of thermal performance the ideal candidate gases are hydrogen and helium because of their high thermal conductivity relative to any other gas. The activation mechanism of the gas-gap heat switch has yet to be determined. The best available solution would be the use of sorber material, whose ability to adsorb the gas decreases with increasing temperature. This option would provide a totally passive thermal control means that does not have any power requirements and sophisticated activation mechanisms.

The produced prototypes of the heat switch were subjected to meticulous inspection, including emissivity measurements, leak tests and CT scans. The CT scans have shown significant deviations from the nominal dimensions that rendered the parts difficult to mount on the test setup and reduced the performance of the switch.

In order to objectively evaluate the performance of the heat switch, a representative test configuration was necessary that would minimize the uncertainties, mainly defined by heat losses via radiation and parasitic conductances through the fasteners. Detailed and reduced thermal models of the test configuration with the heat switch were developed and correlated with the experimental results. The second and third prototypes of the heat switch were tested. The second prototype exhibited better thermal behavior than the third and its ON and OFF conductance was within less than 20% from the theoretical one over a temperature range of -40 to +40°C. The performance of the third prototype deviated significantly from the theoretical values of the thermal models. This deviation is the result of the strong deviation of the produced prototype from the nominal dimensions.

Testing showed that the second prototype switch has an overall ON and OFF conductance (including thermal fillers) of 2.60 and 0.30 W/K respectively at a temperature of 20°C, yielding a ratio of 8.67. The theoretical values are 2.53 and 0.26 W/K for a ratio of 9.86. Similarly, the

third prototype, has an overall ON and OFF conductance (including thermal fillers) of 3.28 and 0.99 W/K respectively at a temperature of 20°C, yielding a ratio of 3.31. The theoretical values are 8.42 and 0.54 W/K for a ratio of 15.51. These values are for the case the heat switch is pressurized with Helium.

Based on the scale analysis of the third prototype and taking into account the use of Hydrogen, the overall ON heat transfer coefficient converges to a value of 241 W/m²·K and the OFF heat transfer coefficient to around 8.5 W/m²·K. This yields an overall ON/OFF ratio of 27.29 for an area larger than 0.1 m². The area density of the third prototype converges to a value of 8.16 kg/m² for an area larger than 0.1 m². Consequently, the performance requirements of the heat switch set in Table 1 are not respected and further design improvements are necessary. The overall ON heat transfer coefficient can be improved by applying a more uniform and higher contact pressure. With Sigraflex, a contact heat transfer coefficient of at least 1000 W/m²·K can be achieved with the appropriate contact conditions. This increase of 42.9% in the contact heat transfer coefficient leads to an overall ON heat transfer coefficient of 304 W/m²·K, a 26.1% increase.

A straw-man concept analysis was performed in order to determine the effects of the use of the developed gas-gap heat switch in Earth-Observation missions. The analysis model was based on the Sentinel-2 mission and showed that a decrease of 0.62% in the power budget can be achieved with an increase of the mass budget by 0.077% based on the experimental conductance values. Eventually, this mission does not show significant temperature fluctuations of the units throughout the orbit. Consequently, the impact of the heat switch is rather minimal. The impact of the heat switch should be investigated in other missions that are more thermally-demanding in order to have a clearer indication.

12.2 Remarks & recommendations

As mentioned earlier, inspection of the tested prototypes showed very loose tolerances with significant differences from the nominal design dimensions. The impact of these deviations was assessed in Chapter 8 and proved to be very critical, especially for the third prototype. The obvious conclusion to be drawn is that significant improvements are necessary in the manufacturing process of the 3D-printed heat switch for it to become a relatively cheap and viable solution as a means of satellite thermal control. It appears that even though the gas-gap heat switch a very promising technology, its application and performance is temporarily limited because of the limitations imposed by the currently available manufacturing technology.

An alternative solution to be investigated is the use of materials with similar thermal properties and potentially better manufacturing tolerances than Ti-6Al-4V. For example, aluminium or silver filled epoxies could be used. However, special attention shall be paid to diffusion through the material, its porosity and outgassing properties. At the moment, even stereolithography (SLA), the most precise and accurate additive manufacturing method for polymers does not seem to be able to provide the needed tolerances for this specific application.

Another important parameter to be taken into account is the leakage rate of the switch. A proper sealing must be applied on the tubes of the switch in order to minimize the gas losses. As a first solution, materials with matching CTE should be used to minimize the relative displacement of the components with changes in temperature. Furthermore, interference problems between the tubes and the panels shall be taken into account. A potential solution would be the bending of the tubes at a 90° angle, facing away from the panel.

Once an efficient and accurate manufacturing process has been established, for better understanding of its behavior, the heat switch shall be subjected to thermal fatigue tests. This is to determine the thermal cycles it can undergo before failure in order to determine its survivability during a real-life mission. Accelerated thermal cycling with sharp temperature fluctuations could be used. Creep refers to the deformation of materials at elevated temperatures when they are exposed to static mechanical stresses [41]. Because the heat switch is not expected to reach very high temperatures ($T < 0.4T_{\text{melting}}$ [K]), creep should not be an issue, unless the switch is used on hot space structures.

Appendix A Sentinel-2 units

Table 25: Units power dissipation and temperature range

Unit	Dissipation Min [W]		Dissipation Max [W]		Operational Temperature Range [°C]	
	Sun	Eclipse	Sun	Eclipse	Min	Max
COMS	69	27.6	70	28.3	-10	+50
Batteries	0	10	0	22.5	+9	+35
PCDU	83	52	95	60	-20	+55
SBT	33.6+6.7	33.6+6.7	33.6+6.7	33.6+6.7	-15	+88
WDE	19.4	19.4	30.4	30.4	-20	+50
MMFU	39	30	50	37	-20	+45
ICU	89	14.6	99	16.3	-20	+50
GPS	9.6	9.6	12.4	12.4	-20	+50
OBC	23	23	24.2	24.2	-20	+50
RIU	41.5	41.5	47.3	47.3	-20	+50

Table 26: Acronyms, dimensions and thermal capacitance of Sentinel-2 units

Unit	Acronym	Base Dimension [mm]		Thermal Capacitance [J/K]
		Length	Width	
COMS	Communications	1000	950	10000
Batteries	-	360	280	25066
PDCU	Power Conditioning and Distribution Unit	510	330	27400
SBT	S-Band Transponder	180	170	2461
WDE	Wheel Drive Electronics	270	240	7689
MMFU	Mass Memory and Formatting Unit	330	300	9068
ICU	Instrument Control Unit	360	360	24600
GPS	Global Positioning System	310	220	2765
OBC	On-board Computer	200	220	9000
RIU	Remote Interface Unit	460	210	14160

Appendix B Orbital heating fluxes

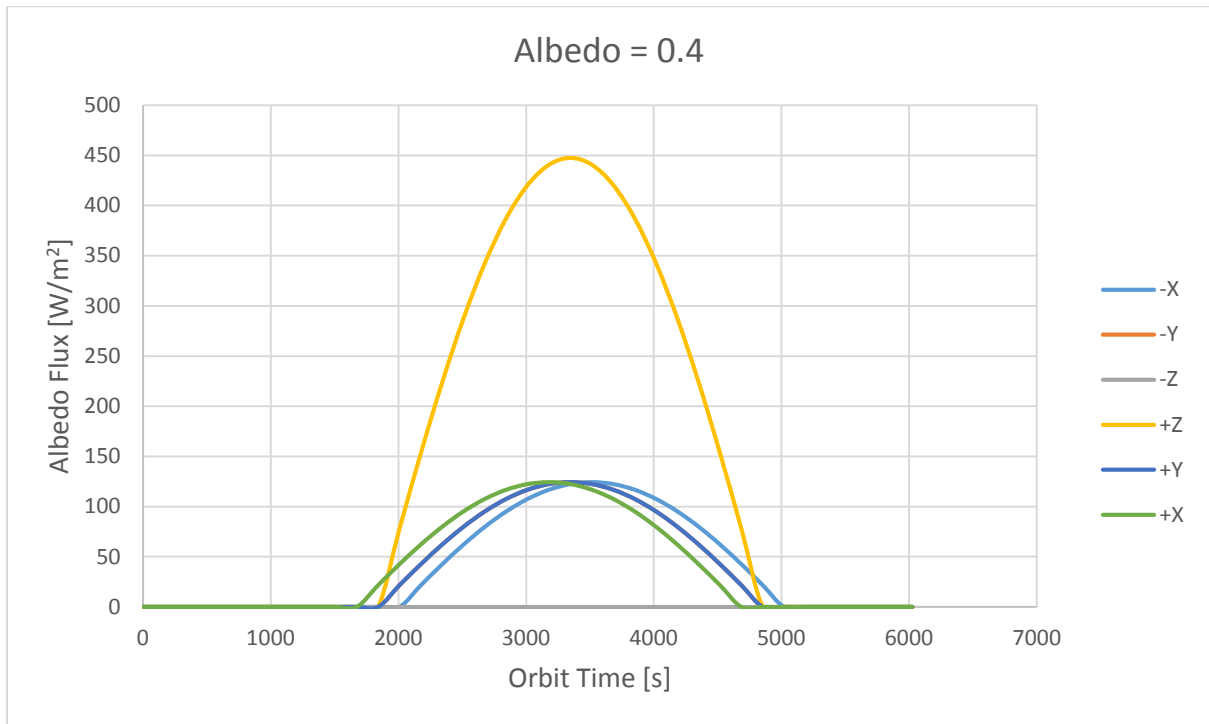


Figure 123: Incident Albedo flux in Worst Hot

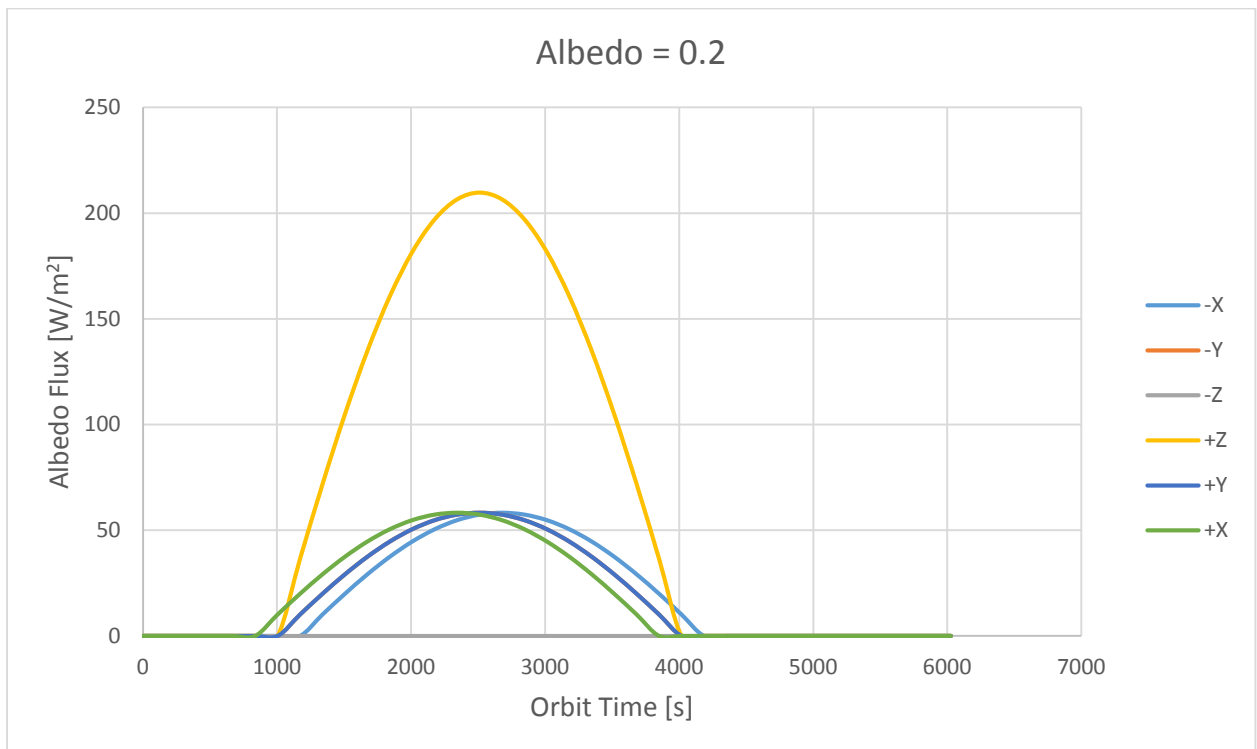


Figure 124: Incident Albedo flux in Worst Cold

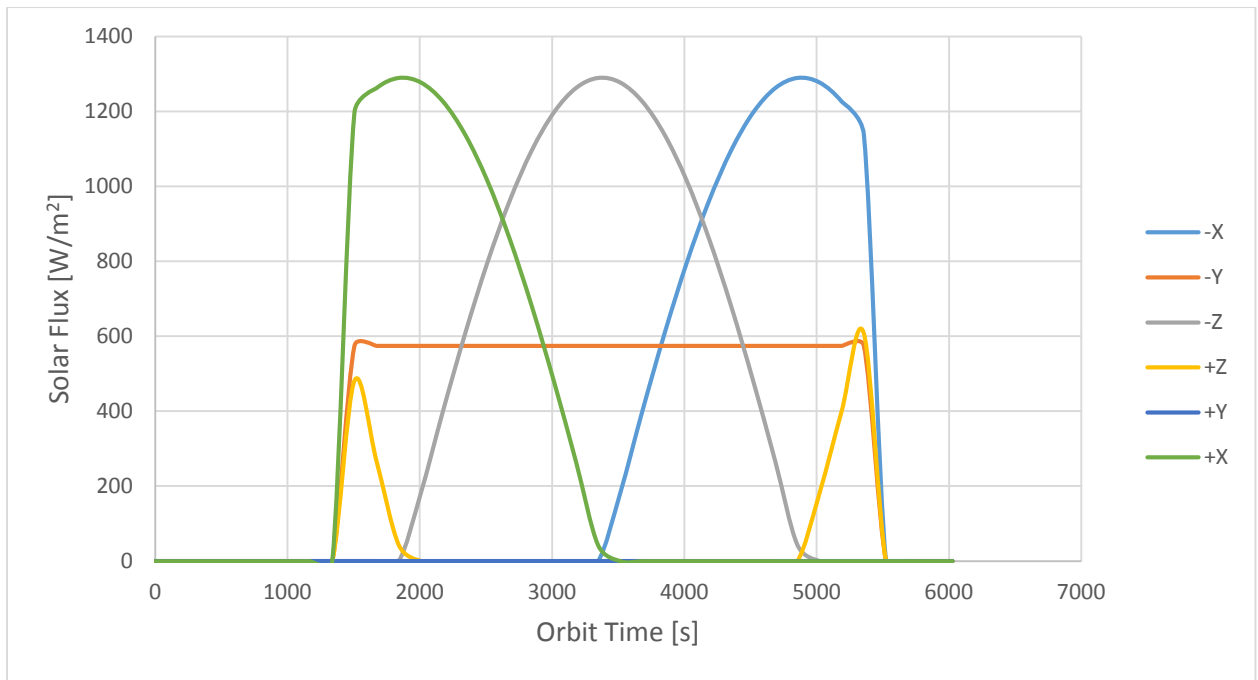


Figure 125: Incident Solar flux in Worst Hot

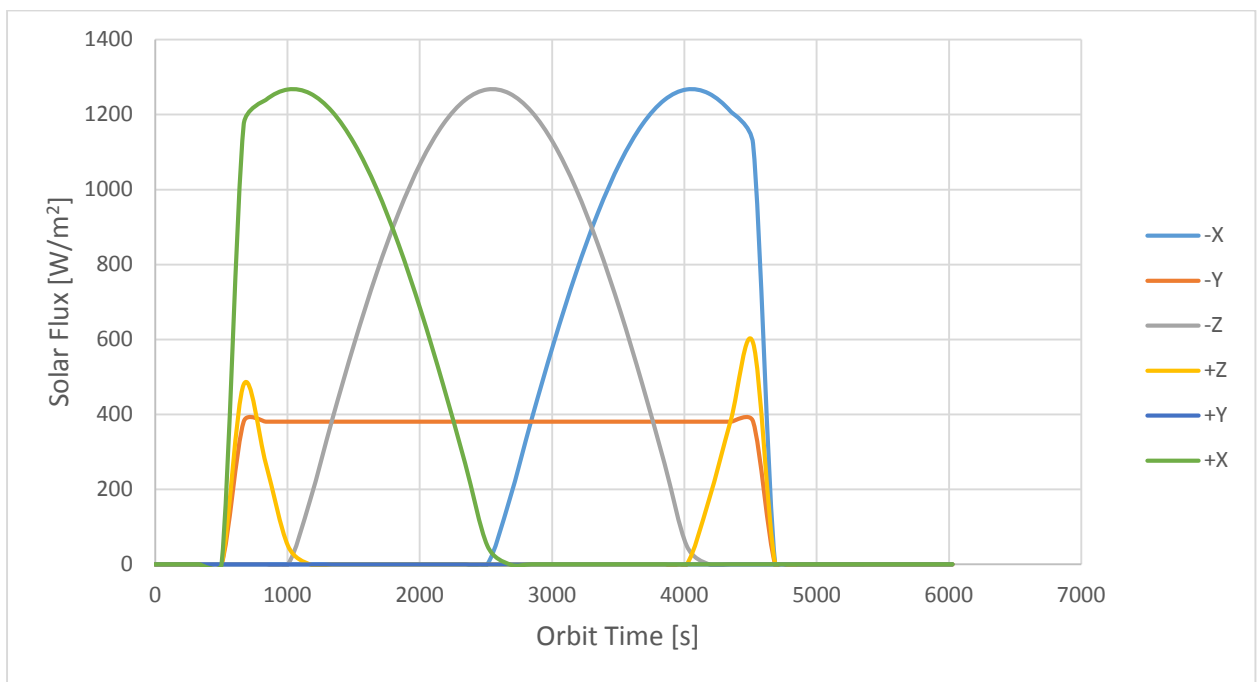


Figure 126: Incident Solar flux in Worst Cold

Appendix C Material transport properties

Table 27: Lennard-Jones constants and molecular weights of selected species [15]

<i>Species</i>	σ (Å)	ε/k_B (K)	$M \left(\frac{\text{kg}}{\text{kmol}} \right)$	<i>Species</i>	σ (Å)	ε/k_B (K)	$M \left(\frac{\text{kg}}{\text{kmol}} \right)$
Al	2.655	2750	26.98	H ₂	2.827	59.7	2.016
Air	3.711	78.6	28.96	H ₂ O	2.655 ^a	363 ^a	18.02
Ar	3.542	93.3	39.95	H ₂ O	2.641 ^b	809.1 ^b	
Br ₂	4.296	507.9	159.8	H ₂ O ₂	4.196	289.3	34.01
C	3.385	30.6	12.01	H ₂ S	3.623	301.1	34.08
CCl ₂ F ₂	5.25	253	120.9	He	2.551	10.22	4.003
CCl ₄	5.947	322.7	153.8	Hg	2.969	750	200.6
CH ₃ OH	3.626	481.8	32.04	I ₂	5.160	474.2	253.8
CH ₄	3.758	148.6	16.04	Kr	3.655	178.9	83.80
CN	3.856	75.0	26.02	Mg	2.926	1614	24.31
CO	3.690	91.7	28.01	NH ₃	2.900	558.3	17.03
CO ₂	3.941	195.2	44.01	N ₂	3.798	71.4	28.01
C ₂ H ₆	4.443	215.7	30.07	N ₂ O	3.828	232.4	44.01
C ₂ H ₅ OH	4.530	362.6	46.07	Ne	2.820	32.8	20.18
CH ₃ COCH ₃	4.600	560.2	58.08	O ₂	3.467	106.7	32.00
C ₆ H ₆	5.349	412.3	78.11	SO ₂	4.112	335.4	64.06
Cl ₂	4.217	316.0	70.91	Xe	4.047	231.0	131.3
F ₂	3.357	112.6	38.00				

^a Based on mass diffusion data.

^b Based on viscosity and thermal conductivity data.

Table 28: Collision integrals for diffusivity, viscosity, and thermal conductivity based on the Lennard-Jones potential [15]

$k_B T / \varepsilon$	Ω_D	$\Omega_\mu = \Omega_k$	$k_B T / \varepsilon$	Ω_D	$\Omega_\mu = \Omega_k$
0.30	2.662	2.785	2.70	0.9770	1.069
0.35	2.476	2.628	2.80	0.9672	1.058
0.40	2.318	2.492	2.90	0.9576	1.048
0.45	2.184	2.368	3.00	0.9490	1.039
0.50	2.066	2.257	3.10	0.9406	1.030
0.55	1.966	2.156	3.20	0.9328	1.022
0.60	1.877	2.065	3.30	0.9256	1.014
0.65	1.798	1.982	3.40	0.9186	1.007
0.70	1.729	1.908	3.50	0.9120	0.9999
0.75	1.667	1.841	3.60	0.9058	0.9932
0.80	1.612	1.780	3.70	0.8998	0.9870
0.85	1.562	1.725	3.80	0.8942	0.9811
0.90	1.517	1.675	3.90	0.8888	0.9755
0.95	1.476	1.629	4.00	0.8836	0.9700
1.00	1.439	1.587	4.10	0.8788	0.9649
1.05	1.406	1.549	4.20	0.8740	0.9600
1.10	1.375	1.514	4.30	0.8694	0.9553
1.15	1.346	1.482	4.40	0.8652	0.9507
1.20	1.320	1.452	4.50	0.8610	0.9464
1.25	1.296	1.424	4.60	0.8568	0.9422
1.30	1.273	1.399	4.70	0.8530	0.9382
1.35	1.253	1.375	4.80	0.8492	0.9343
1.40	1.233	1.353	4.90	0.8456	0.9305
1.45	1.215	1.333	5.00	0.8422	0.9269
1.50	1.198	1.314	6.00	0.8124	0.8963
1.55	1.182	1.296	7.0	0.7896	0.8727
1.60	1.167	1.279	8.0	0.7712	0.8538
1.65	1.153	1.264	9.0	0.7556	0.8379
1.70	1.140	1.248	10.0	0.7424	0.8242
1.75	1.128	1.234	20.0	0.6640	0.7432
1.80	1.116	1.221	30.0	0.6232	0.7005
1.85	1.105	1.209	40.0	0.5960	0.6718
1.90	1.094	1.197	50.0	0.5756	0.6504
1.95	1.084	1.186	60.0	0.5596	0.6335
2.00	1.075	1.175	70.0	0.5464	0.6194
2.10	1.057	1.156	80.0	0.5352	0.6076
2.20	1.041	1.138	90.0	0.5256	0.5973
2.30	1.026	1.122	100.0	0.5170	0.5882
2.40	1.012	1.107	200.0	0.4644	0.5320
2.50	0.9996	1.093	300.0	0.4360	0.5016
2.60	0.9878	1.081	400.0	0.4172	0.4811

Appendix D Gas thermal properties⁸

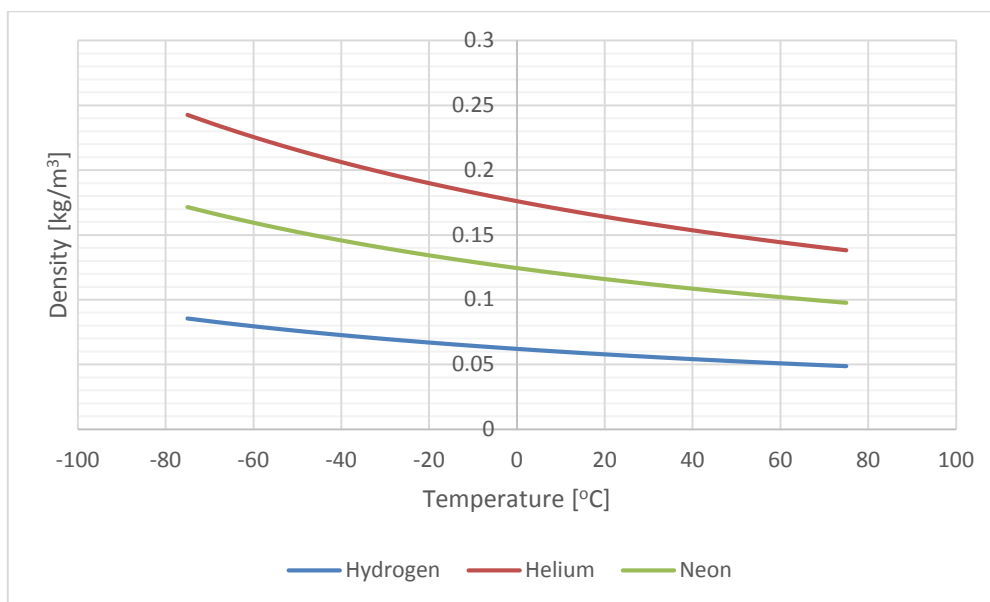


Figure 127: Gases thermal conductivity with respect to temperature

The uncertainty in the density is 0.2% for Hydrogen, 1.0% for Helium and 0.1% for Neon.

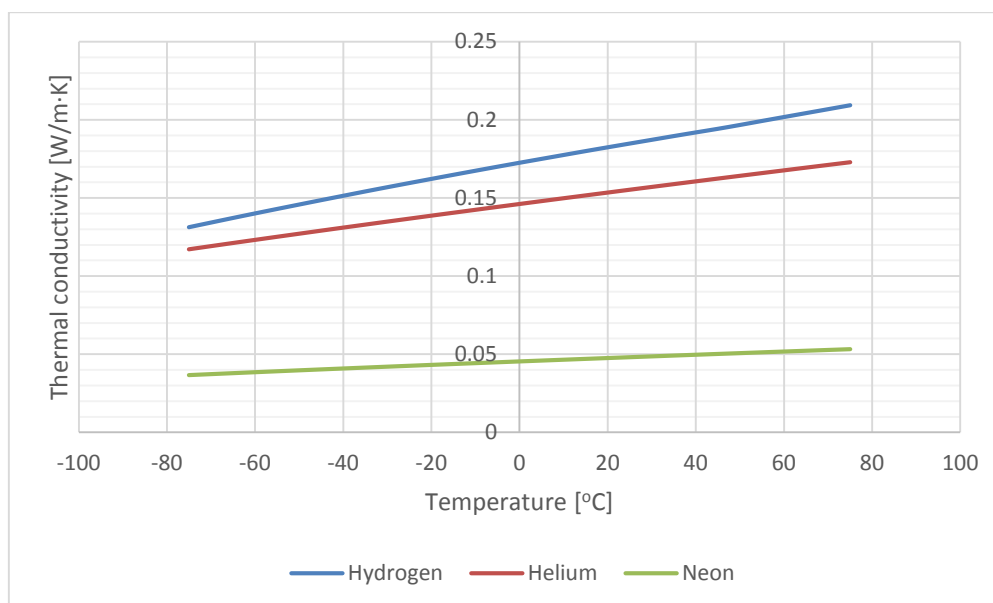


Figure 128: Gases density with respect to temperature

The uncertainty in the thermal conductivity is 10% for Hydrogen, 1.0% for Helium and 5% for Neon.

The properties were obtained at the theoretical continuum boundary of 700 mbar for Hydrogen, 1000 mbar for Helium and 140 mbar for Neon.

⁸ All properties are obtained from NIST Chemistry WebBook

Appendix E Radiation properties and VF

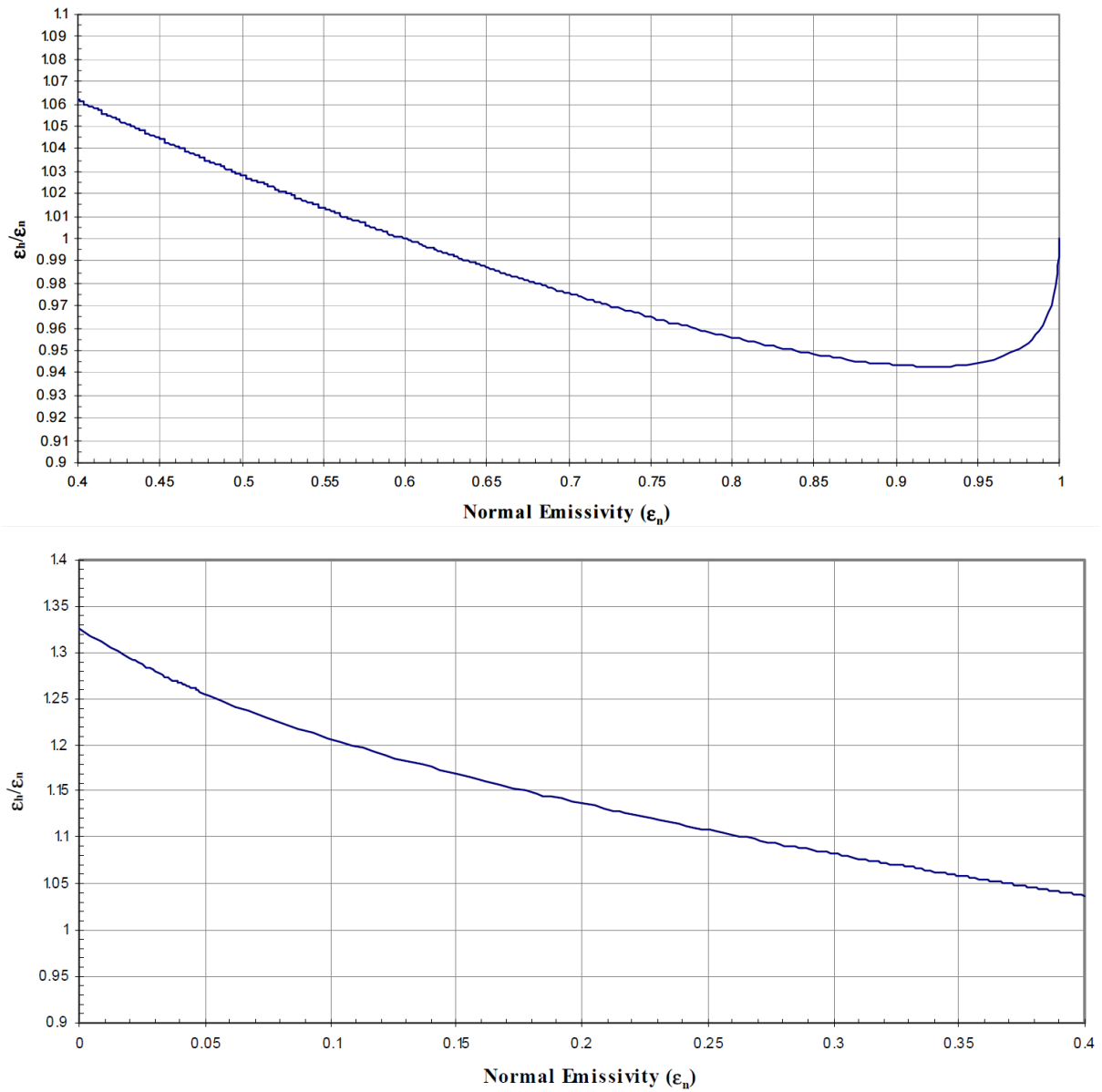


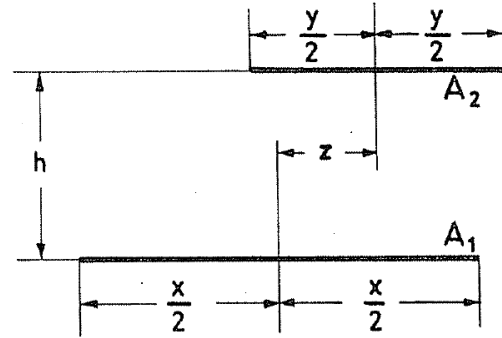
Figure 129: Ratio of hemispherical emissivity to normal emittance⁹

⁹ NASA/TP-2005-212792: Spacecraft Thermal Control Coatings References

$$X = \frac{x}{h}$$

$$Y = \frac{y}{h}$$

$$Z = \frac{z}{h}$$



Formula:

$$F_{12} = \frac{Y}{X} \quad F_{21} = \frac{1}{2X} \left[\sqrt{1 + \left(\frac{Y+X-2Z}{2} \right)^2} + \sqrt{1 + \left(\frac{Y+X+2Z}{2} \right)^2} - \right. \\ \left. - \sqrt{1 + \left(\frac{X-Y-2Z}{2} \right)^2} - \sqrt{1 + \left(\frac{X-Y+2Z}{2} \right)^2} \right] .$$

Figure 130: Two infinitely long parallel strips of unequal length¹⁰

¹⁰ ESA PSS-03-108 Issue 1 (November 1989)

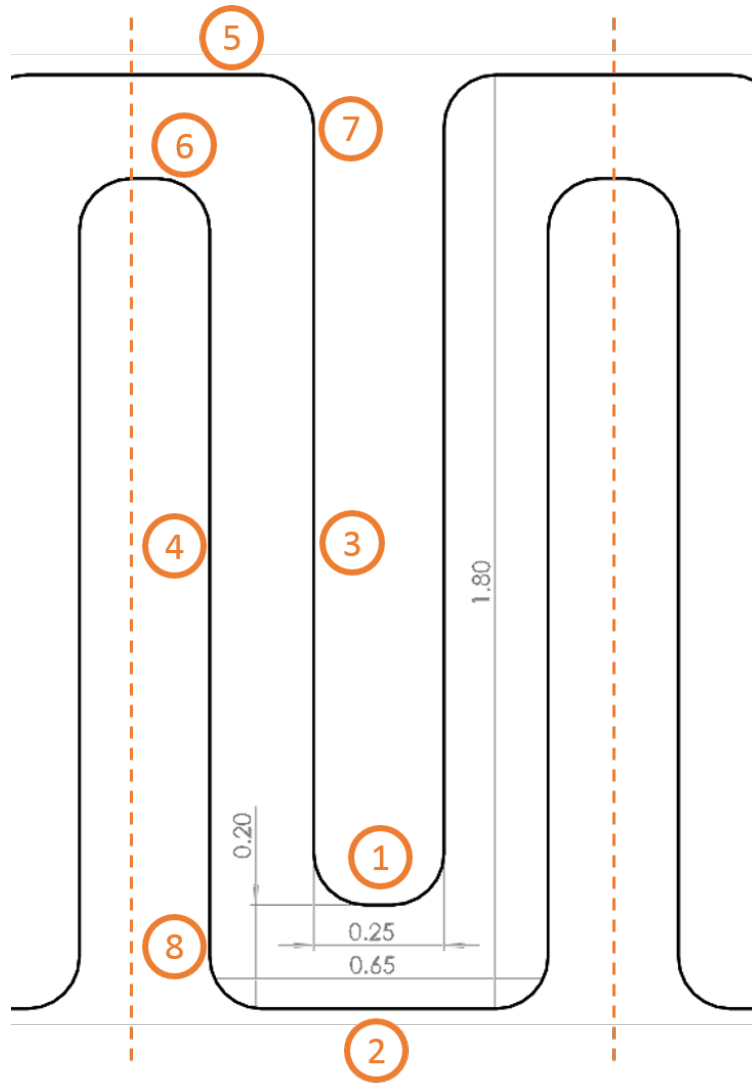


Figure 131: Second prototype fin profile

Table 29: Second prototype fin view factors

	View Factor	Area [m ²]
$F_{1 \rightarrow 2}$	0.8384	$2.5 \cdot 10^{-5}$
$F_{1 \rightarrow 8}$	0.1616	$2.5 \cdot 10^{-5}$
$F_{3 \rightarrow 4}$	0.8658	$1.4 \cdot 10^{-4}$
$F_{3 \rightarrow 8}$	0.0412	$1.4 \cdot 10^{-4}$
$F_{5 \rightarrow 6}$	0.1348	$3.25 \cdot 10^{-4}$
$F_{5 \rightarrow 4}$	0.1757	$2 \cdot 10^{-5}$
$F_{7 \rightarrow 4}$	0.0412	$2 \cdot 10^{-5}$
$F_{7 \rightarrow 6}$	0.1009	$2 \cdot 10^{-5}$

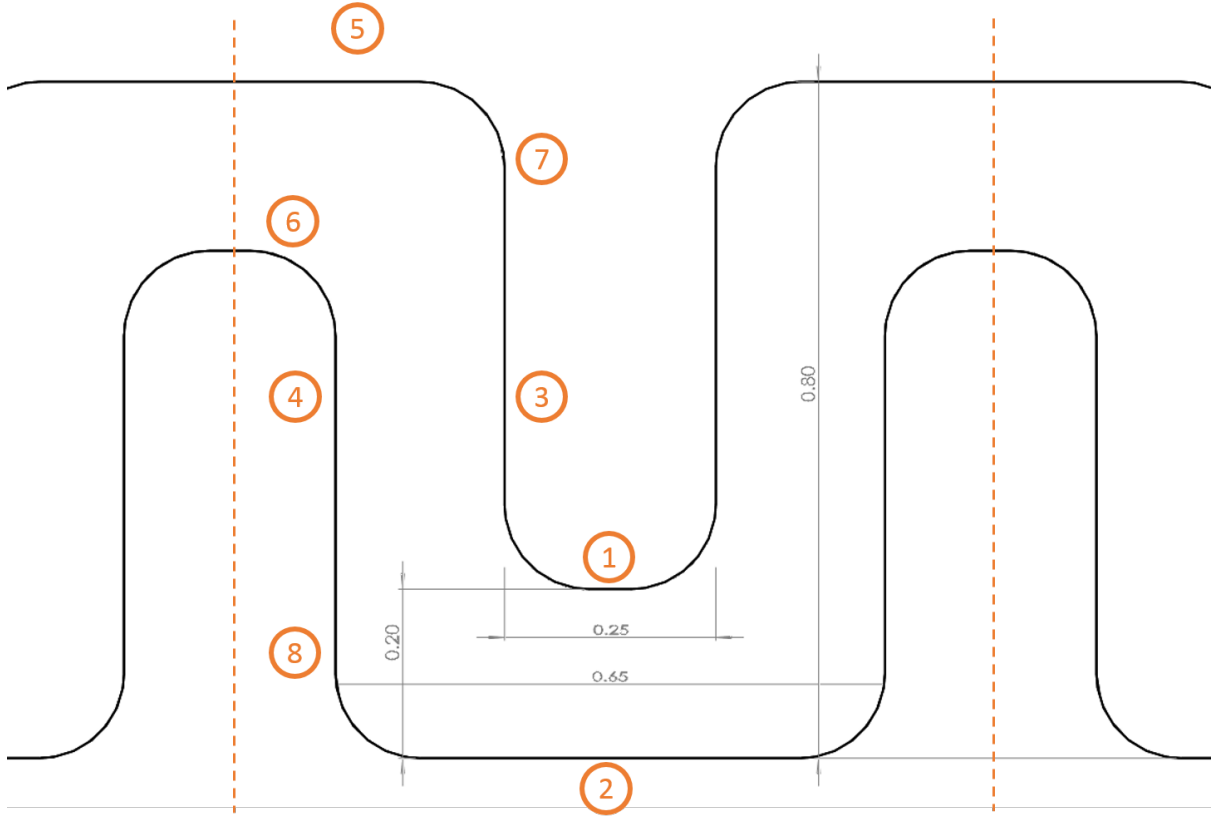


Figure 132: Third prototype fin profile

Table 30: Third prototype fin view factors

	View Factor	Area [m ²]
$F_{1 \rightarrow 2}$	0.8384	$5 \cdot 10^{-5}$
$F_{1 \rightarrow 8}$	0.1616	$5 \cdot 10^{-5}$
$F_{3 \rightarrow 4}$	0.6180	$8 \cdot 10^{-5}$
$F_{3 \rightarrow 8}$	0.1280	$8 \cdot 10^{-5}$
$F_{5 \rightarrow 6}$	0.1348	$6.5 \cdot 10^{-5}$
$F_{5 \rightarrow 4}$	0.1258	$4 \cdot 10^{-5}$
$F_{7 \rightarrow 4}$	0.1280	$4 \cdot 10^{-5}$
$F_{7 \rightarrow 6}$	0.1009	$4 \cdot 10^{-5}$

$$\sum_{i=1}^7 A_i F_{ij} = A_1 F_{12} + 2A_1 F_{18} + 2A_3 F_{34} + 2A_3 F_{38} + 2A_5 F_{54} + 2A_5 F_{56} + 2A_7 F_{74} + 2A_7 F_{76}$$

Appendix F Material properties

Table 31: Ti-6Al-4V chemical composition¹¹

Element	Percentage
Ti	89.734%
Al	6%
V	4%
Others	0.266%

Table 32: Inconel 718® chemical composition¹²

Element	Percentage
Ni	53%
Cr	20%
Fe	17%
Nb	5%
Mo	3%
Ti	1%
Others	1%

Table 33: Material thermal properties

Material	ρ [kg/m ³]	k [W/m · K]	C_p [J/kg · K]	α [1/K]
Aluminium 6061 ¹³	2,711	167	896	$22.38 \cdot 10^{-6}$
A2-70 SS ¹⁴	8,000	16.2	500	$17.3 \cdot 10^{-6}$
Ti-6Al-4V ¹⁵	4,430	6.7	526.3	$8.6 \cdot 10^{-6}$
Inconel 718	8,190	11.4	435	$13 \cdot 10^{-6}$

Table 34: Material structural properties

Material	ρ [kg/m ³]	E [GPa]	Poisson ratio ν	UTS [MPa]	YTS [MPa]
Ti-6Al-4V	4,430	121.0	0.342	845	805
Inconel 718	8,190	200.0	0.294	1375	1100
Aluminium 6061-T6	2,711	69.0	0.330	276	242

¹¹ From MatWeb: Titanium Ti-6Al-4V (Grade 5), Annealed

¹² From MatWeb: Special Metals INCONEL® Alloy 718

¹³ Values obtained at 20°C from NX 9.0 material library

¹⁴ From MatWeb: 304 Stainless Steel (Austenitic)

¹⁵ From NX 9.0 material library

A2-70 SS	8,000	190.0	0.300	700	450
PEEK	1,350	4.4	0.38	-	-

Note that the Shear Modulus for isotropic materials is calculated as [41]:

$$G = \frac{E}{2(1 + \nu)} \quad (12.2-1)$$

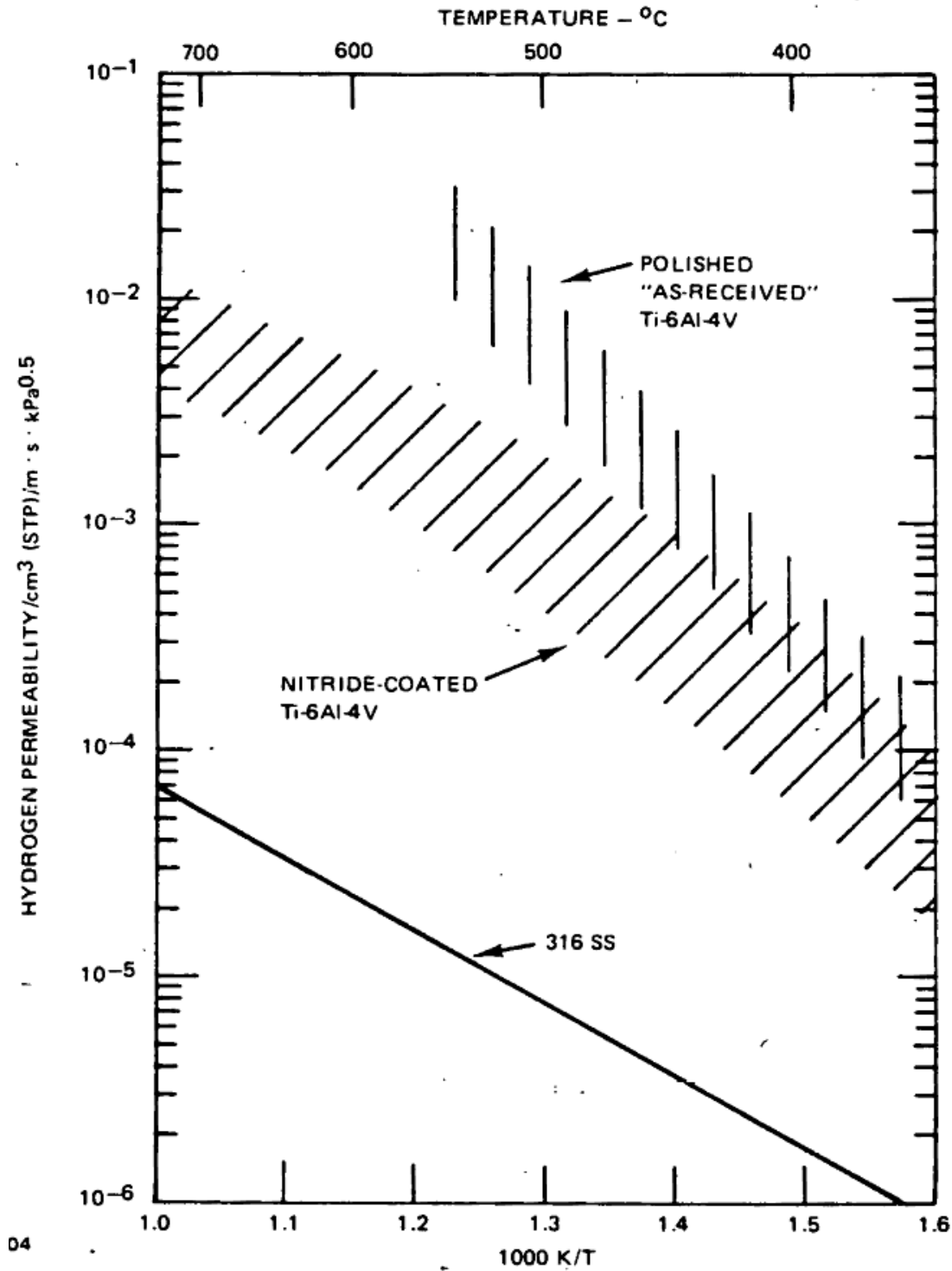


Figure 133: Hydrogen permeability versus temperature [42]

Appendix G Structural analysis results

Table 35: Classical rule-of-thumb safety factors [30]

Safety Factor	Criteria
$FS_{\text{material}} = 1.1$	Material properties known from a handbook or are manufacturer's values
$FS_{\text{stress}} = 1.3$	Nature of the load is defined in an average manner, with overloads of 20-50% and the stress analysis may result in error $< 50\%$
$FS_{\text{geometry}} = 1.1$	Manufacturing tolerances are not closely held
$FS_{\text{failure analysis}} = 1.0$	Failure analysis is derived for the state of stress, as for uniaxial or multiaxial static stresses or fully reversed uniaxial fatigue stresses
$FS_{\text{reliability}} = 1.2$	For a reliability of 95%

Maximum bolt preload

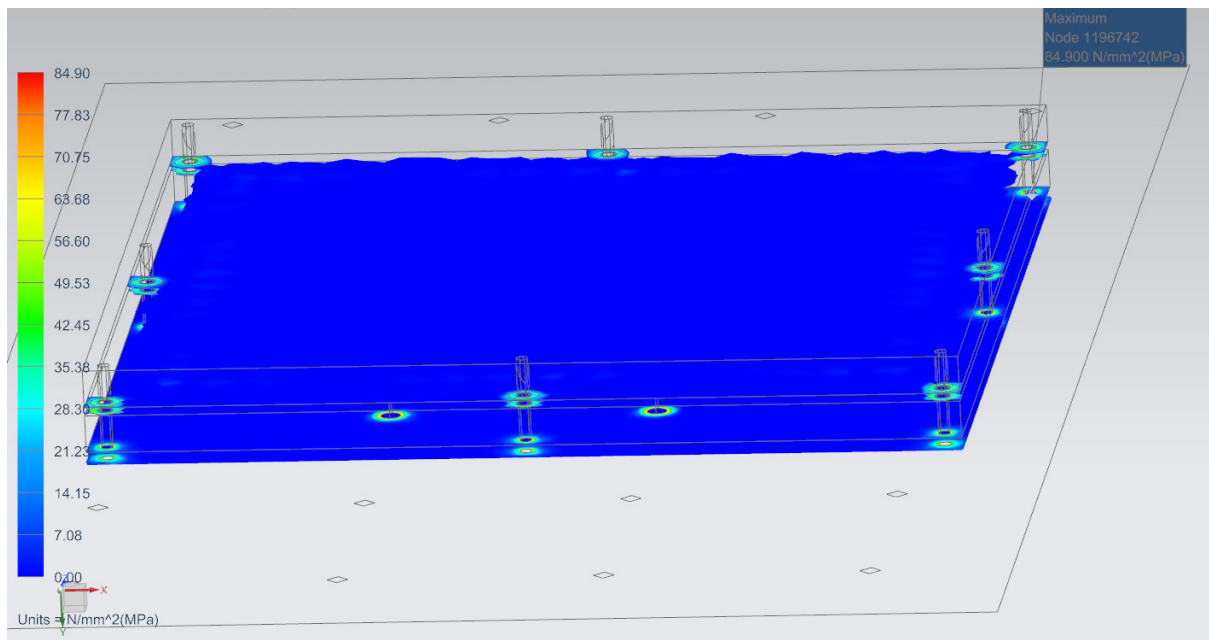


Figure 134: Bolted connections contact pressure

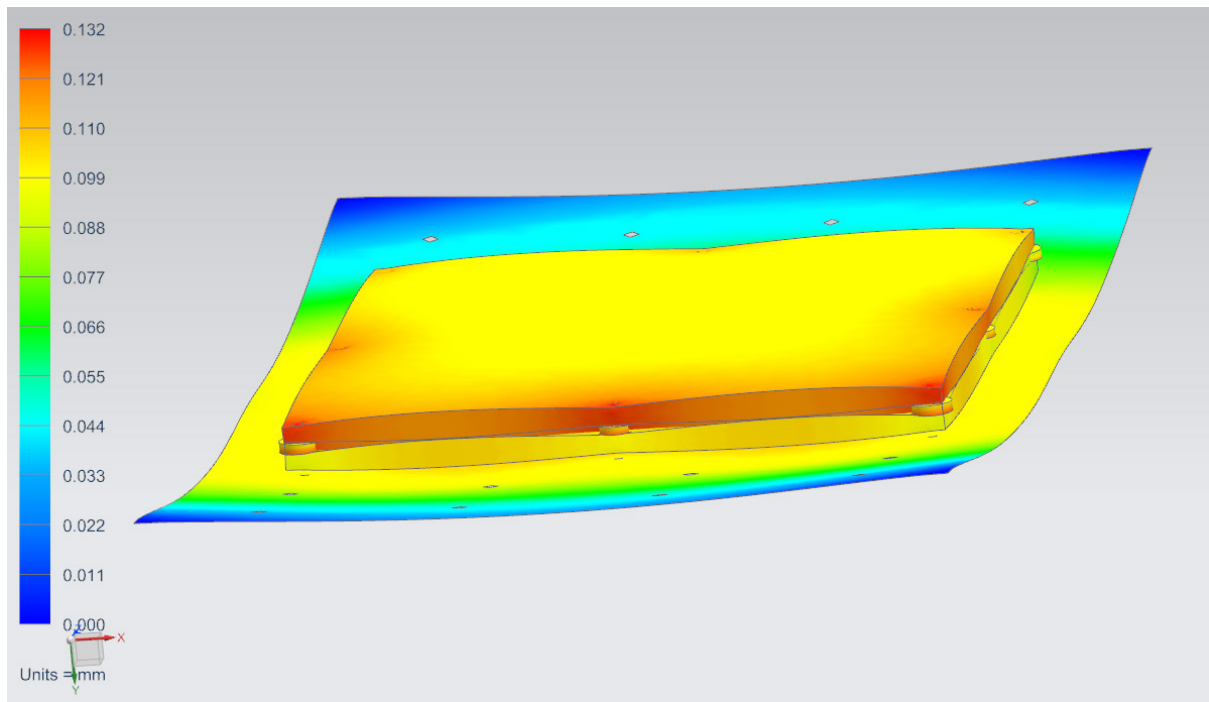


Figure 135: Test setup exaggerated displacement

Overpressurization

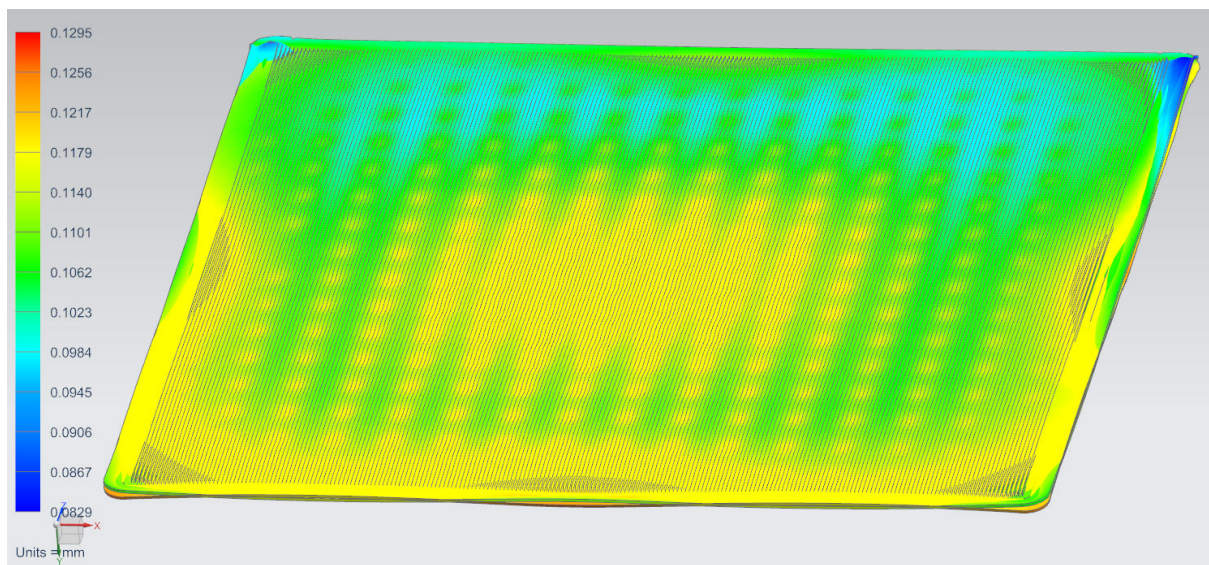


Figure 136: Switch exaggerated displacement [2.3 bar]

Appendix H Reduced TMM code

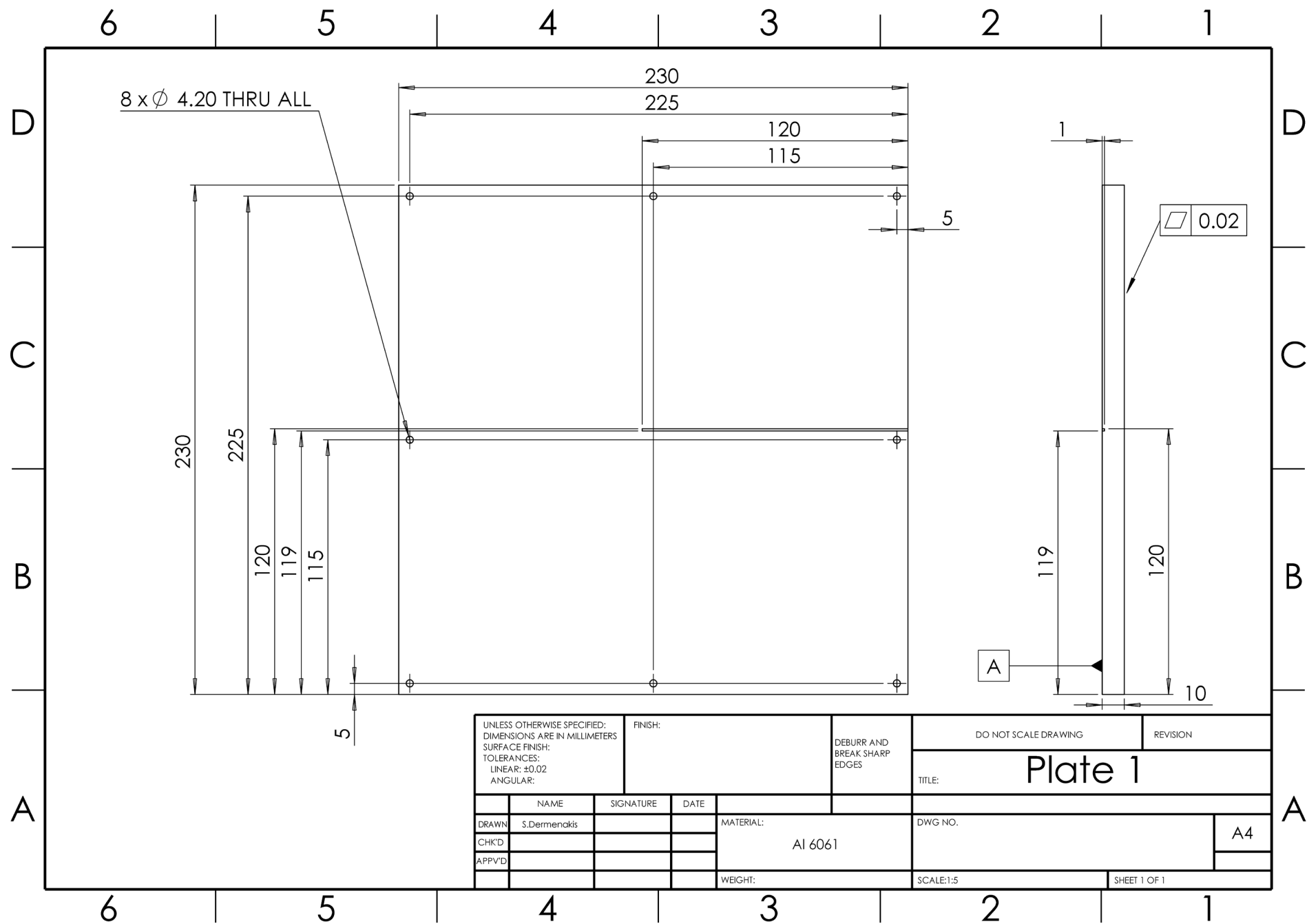
```
# ThermXL Export File for ON_state_SS (5/20/2016 2:59:53 PM)
#
# Cells containing formulas are exported as value only
# and the content is provided as a comment.
#
$MODEL ON_state_SS
#
$NODES
#
D10 = 'Plate 1 top', T = 20.00, C = 2.05E+2 # =896*2711*(0.01*0.13^2)/2
, QI = 4.00E+1;
D20 = 'Plate 1 bottom', T = 20.00, C = 2.05E+2 # =896*2711*(0.01*0.13^2)/2
;
D30 = 'Top switch', T = 20.00, C = 3.16E+1 # =526.3*4430*2.7067*10^-5/2
;
D40 = 'Bottom switch', T = 20.00, C = 3.16E+1 # =526.3*4430*2.7067*10^-5/2
;
D50 = 'Plate 2 top', T = 20.00, C = 2.05E+2 # =E4
;
D60 = 'Plate 2 bottom', T = 20.00, C = 2.05E+2 # =E5
;
D70 = 'Baseplate top', T = 20.00, C = 1.04E+3 # =896*2711*(0.006*0.285*0.5)/2
;
B80 = 'Baseplate bottom', T = 20.00;
D90 = 'MLI top', T = 20.00, C = 6.59E+0 # =390*H12
;
B100 = 'Shroud', T = 20.00;
#
$CONDUCTORS
#
GR(30, 40) = 1.37E-2; # =0.318*0.0432
GR(10, 90) = 2.37E-4; # =0.014*Nodes!H12
GR(100, 90) = 1.98E+0; # =0.9*Nodes!H13
GL(10, 20) = 2.82E+2; # =167*Nodes!H5/0.01
GL(20, 30) = 8.80E+0; # =727*Nodes!H6
GL(30, 40) = 6.56E+0;
GL(40, 50) = 7.83E+0; # =647*Nodes!H7
GL(50, 60) = 2.82E+2; # =D6
GL(60, 70) = 2.54E+1; # =1500*Nodes!H9
GL(70, 80) = 3.97E+3; # =167*Nodes!H10/0.006
GL(10, 90) = 3.21E-4; # =0.019*Nodes!H12
GL(10, 60) = 1.25E-2;
GL(60, 70) = 1.71E-2;
GL(50, 70) = 1.23E-1; # =0.0205*6
GL(10, 60) = 1.45E-2;
#
$CONSTANTS
#
$CONTROL
#
# Steady-state parameters
NLOOP = 10000;
RELXCA = 1.00E-6;
DAMPT = 1.00E+0;
# Preferences
TABS = 2.731500E+2;
STEFAN = 5.670510E-8;
```

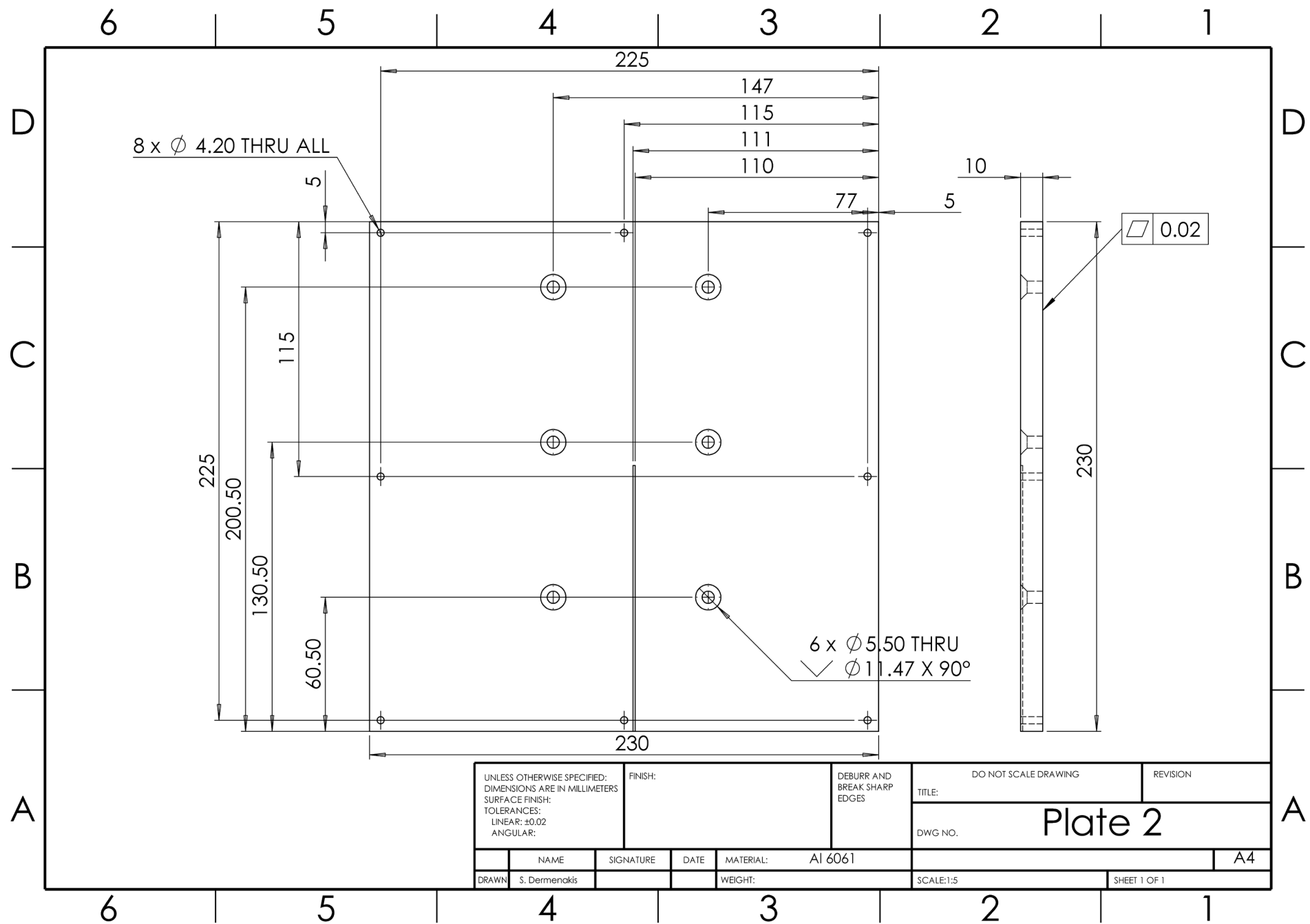
```

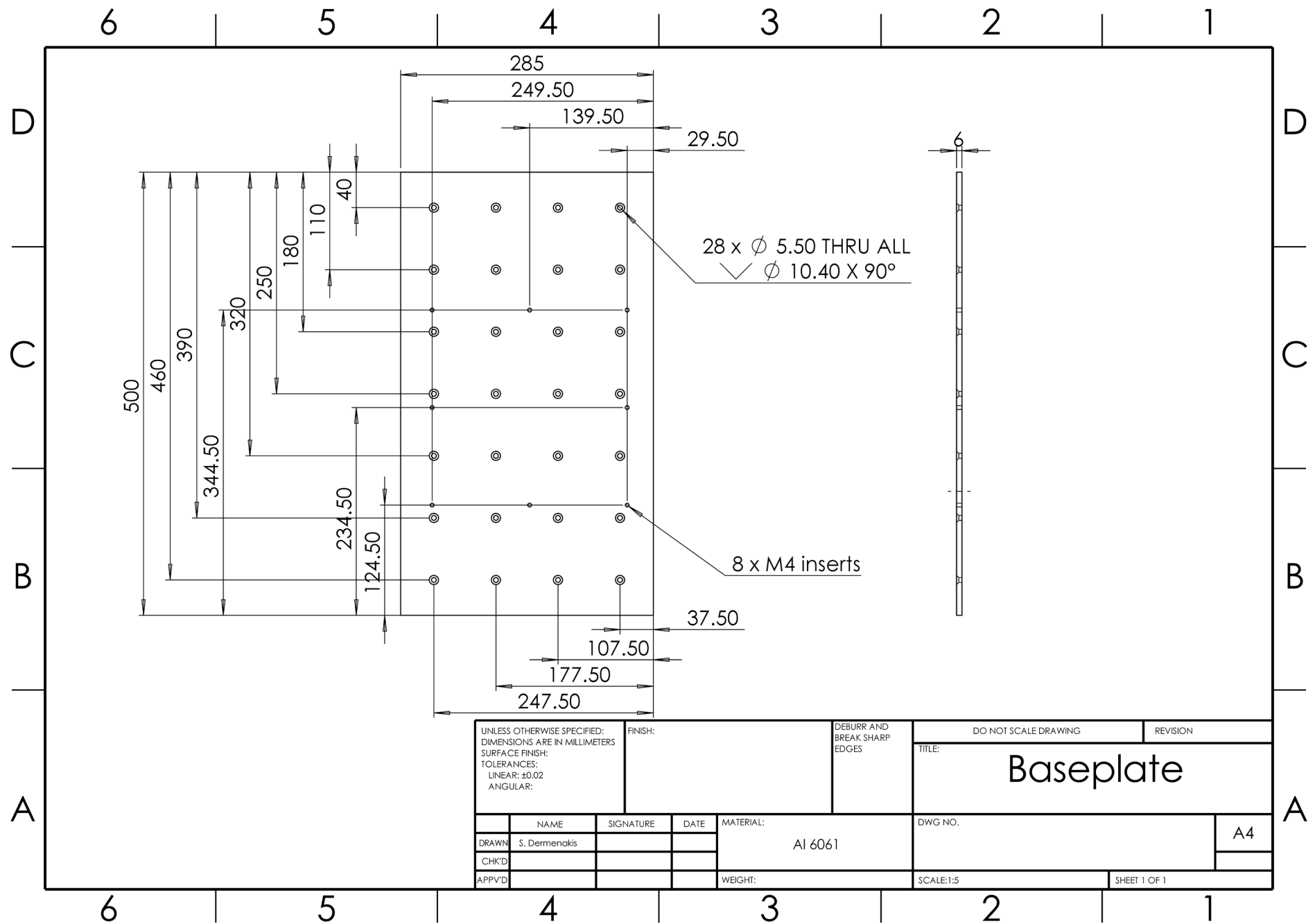
#
$EXECUTION
#
      CALL SOLVIT
      CALL DMPPTHM('STEADY_STATE') # Steady state model dump
#
$OUTPUTS
#
      FORMAT = 'E10.2'
      CALL PRQBAL(' ', CURRENT)
      CALL PRNDTB(' ', 'T,C,QS,QA,QE,QI', CURRENT)
#
$ENDMODEL ON_state_SS

```

Appendix I Technical Drawings







References

- [1] W. J. Larson and J. R. Wertz, Space Mission Analysis and Design, Microcosm Press and Kluwer Academic Publishers, 2005.
- [2] I. Catarino, G. Bonfait and L. Duband, "Neon gas-gap heat switch," *Cryogenics*, vol. 48, no. 1-2, pp. 17-25, 2008.
- [3] M. Krielaart, C. Vermeer and S. Vanapalli, "Compact flat-panel gas-gap heat switch operating at 295 K," *Review of Scientific Instruments*, no. 86, 2015.
- [4] J. C. Mankins, "Technology Readiness Levels," Office of Space Access and Technology - NASA, 1995.
- [5] European Cooperation for Space Standardization, ECSS-S-ST-00-01C - ECSS system - Glossary of terms, Noordwijk, the Netherlands: ESA Requirements and Standards Division, 2012.
- [6] Y. A. Cengel and A. J. Ghajar, Heat and Mass Transfer, McGraw-Hill, 2011.
- [7] J. R. Howell, R. Siegel and P. M. Menguc, Thermal Radiation Heat Transfer, New York: McGraw-Hill, 2010.
- [8] European Space Agency, "View Factors," European Space Agency, Noordwijk, the Netherlands, 1989.
- [9] J. Fatemi and M. H. J. Lemmen, "Effective Thermal/Mechanical Properties of Honeycomb Core Panels for Hot Structure Applications," *Journal of Spacecraft and Rockets*, vol. 46, no. 3, pp. 514-525, 2009.
- [10] B. Gebhart, Heat Transfer, McGraw-Hill, 1961.
- [11] C. Y. Han and J.-M. Choi, "Thermal Analysis of Spacecraft Propulsion System and its Validation," *KSME International Journal*, vol. 18, no. 5, pp. 847-856, 2004.
- [12] R. D. Karaman, Satellite Thermal Control for Systems Engineers, AIAA, 1998.
- [13] D. G. Gilmore, Spacecraft Thermal Control Handbook, The Aerospace Press, 2002.
- [14] J. J. Lissauer and I. de Pater, Fundamental Planetary Science: Physics, Chemistry and Habitability, Cambridge University Press, 2013.
- [15] J. H. Lienhard IV and J. H. Lienhard V, A heat transfer textbook, Cambridge, MA: Phlogiston Press, 2003.

- [16] E. Anglada and I. Garmendia, "Correlation of thermal mathematical models for thermal control of space vehicles by means of genetic algorithms," *Acta Astronautica*, vol. 108, pp. 1-17, 2015.
- [17] E. Tal-Gutelmacher and D. Eliezer, "Hydrogen-Assisted Degradation of Titanium Based Alloys," *Materials Transactions*, vol. 45, no. 5, pp. 1594-1600, 2004.
- [18] B. S. Yilbas, A. Coban, R. Kahraman and M. M. Khaled, "Hydrogen Embrittlement of Ti-6Al-4V Alloy with Surface Modification by TiN Coating," *International Journal Hydrogen Energy*, vol. 23, no. 6, pp. 483-489, 1998.
- [19] M. Ando, K. Shinozaki, A. Okamoto, H. Sugita and T. Nohara, "Development of Mechanical Heat Switch of Future Space Missions," in *44th International Conference on Environmental Systems*, Tucson, AZ, 2014.
- [20] D. Mishkinis, J. Corrochano and A. Torres, "Development of Miniature Heat Switch-Temperature Controller based on variable conductance LHP," in *Second International Conference "Heat Pipes for Space Applications"*, Moscow, 2014.
- [21] M. Pauken, E. Sunada, K. Novak, C. Philips, G. Birur and K. Lankford, "Development Testing of a Paraffin-Actuated Heat Switch for Mars Rover Applications," in *International Conference On Environmental Systems*, San Antonio, TX, 2002.
- [22] European Space Agency, "Sentinel-2: The operational Copernicus optical high resolution land mission," ESA, Noordwijk, the Netherlands, 2013.
- [23] E. E. Anderson and R. Viskanta, "Effective conductivity for conduction-radiation by Taylor series expansion," *Heat Mass Transfer International Journal*, vol. 14, pp. 1220-1224, 1971.
- [24] M. Kaviany, *Heat Transfer Physics*, Cambridge University Press, 2008.
- [25] B. R. Munson, D. F. Young, T. H. Okiishi and W. W. Huebsch, *Fundamentals of Fluid Mechanics*, John Wiley & Sons, 2009.
- [26] R. C. Reid, J. M. Prausnitz and B. E. Poling, *The Properties of Gases and Liquids*, New York: McGraw-Hill, 1987.
- [27] J. R. Thomas and D. P. Hasselmann, "Effect of Interfacial Separation on Composite Thermal Conductivity," in *28th International Thermal Conductivity Conference and the 16th International Thermal Expansion Symposium*, New Brunswick, Canada, 2005.
- [28] G. Springer, "Heat transfer in rarefied gases," in *Advances in Heat Transfer, Volume 7*, New York, Academic Press, 1971, pp. 163-218.

- [29] S. Song and M. M. Yovanovich, "Correlation of Thermal Accommodation Coefficient for 'Engineering' Surfaces," in *Twenty-fourth National Heat Transfer Conference and Exhibition*, Pittsburgh, PA, 1987.
- [30] F. P. Beer, R. E. Johnston Jr., J. T. DeWolf and D. F. Mazurek, *Mechanics of Materials*, McGraw-Hill, 2012.
- [31] C. Tien, "A correlation for thermal contact conductance of nominally-flat surfaces in a vacuum," in *Thermal Conductivity, Proceedings of the Seventh Conference*, 1968.
- [32] V. W. Antonetti, T. D. Whittle and R. E. Simons, "An approximate thermal contact conductance correlation," *Journal of Electronic Packaging*, vol. 115, pp. 131-134, 1993.
- [33] M. G. Cooper, B. B. Mikic and M. M. Yovanovich, "Thermal contact conductance," *International Journal of Heat Mass Transfer*, vol. 12, pp. 279-300, 1968.
- [34] G. Meyer and D. Strelow, "Simple Diagrams Aid in Analysing Forces in Bolted Joints," *Assembly Engineering*, pp. 28-33, 1972.
- [35] S. D. Rossides, "Behaviour of a Simple Tension Joint with Fasteners Tightened into Yield," British Aerospace Report, 1981.
- [36] D. G. Ullman, *The Mechanical Design Process*, New York: McGraw-Hill, 2010.
- [37] S. L. Rickman and E. K. Ungar, "A physics-based temperature stabilization criterion for thermal testing," in *Aerospace Testing Conference*, Manhattan Beach, CA, 2009.
- [38] E. Colizzi, "Thermal Balance Testing: A Rigorous Theoretical Approach to Stabilisation Criteria Based on Operative Re-Definition of Thermal Time Constant," in *42nd International Conference on Environmental Systems*, San Diego, CA, 2012.
- [39] S. Bell, *A Beginner's Guide to Uncertainty of Measurement*, Teddington, Middlesex, UK: National Physical Laboratory, 1999.
- [40] J. Black and R. A. Kohser, *De Garmo's Materials & Processes in Manufacturing*, John Wiley & Sons, 2008.
- [41] W. D. Callister and D. G. Rethwisch, *Material Science and Engineering*, John Wiley & Sons, 2011.
- [42] McDonnell Douglas Astronautics Company, "Hydrogen in Titanium Alloys," McDonnell Douglas Corporation, St Louis, 1981.
- [43] Y. A. Cengel and M. A. Boles, *Thermodynamics - An Engineering Approach*, McGraw-Hill, 2011.
- [44] J.-R. Tsai, "Overview of Satellite Thermal Analytical Model," *Journal of Spacecraft and Rockets*, vol. 41, no. 1, pp. 120-125, 2004.

